# Large Groups of Quasars
# in an Ultraviolet-Excess Survey

Peter Raymond Newman

A thesis submitted in partial fulfilment
of the requirements for the degree of
Doctor of Philosophy.

# Abstract

This thesis describes the objectives, design, construction and analysis of the Chile-UK Quasar Survey, a new wide-field spectroscopic redshift survey of ultraviolet-excess quasar candidates. The main objectives of the survey are the construction of a large, homogeneous catalogue of quasars with redshifts $0.4 \leq z \leq 2.2$, and the use of the catalogue to investigate the large-scale structure of the early Universe, particularly at large scales ($\sim 100~h^{-1}$ Mpc).

The survey covers 140 deg$^2$, with a $10° \times 10°$ programme area centred at $10^h40^m$, $+5°00'$, and a $6°3 \times 6°3$ control area centred at $11^h14^m$, $-29°00'$ (B1950 coordinates). Quasar candidates have been selected on $16 \leq b_J \leq 20$ and $(u_J - b_J) \leq -0.3$ from UK Schmidt Telescope photographic plates in the U and J bands digitized on the SuperCOSMOS machine at the Royal Observatory Edinburgh. The methods developed for astrometric and photometric calibration of the SuperCOSMOS data are described in detail. Positional uncertainties of $\Delta r = 0.69$ arcsec r.m.s. and magnitude uncertainties of $\Delta b_J = 0.10$ mag and $\Delta u_J = 0.12$ mag are achieved across the whole survey area. A function relating positional uncertainty to the efficiency of light collection for spectrographs with optical-fibre input is derived and used to show that the efficiency for this survey is $>80$ per cent.

Survey observations using a multi-object spectrograph with optical-fibre input on the 2.5-m du Pont telescope at the Las Campanas Observatory in Chile are reported. Spectra of 4588 candidates from 54 deg$^2$ of the survey area have been obtained in 12 nights of observations conducted in 1996 March, 1997 March and 1998 May. Of these spectra, 3134 have been analysed, resulting in the identification of 320 quasars with redshifts in the range $0.228 \leq z \leq 2.768$, and 93 narrow emission-line galaxies with redshifts in the range $0.015 \leq z \leq 0.397$. The distributions of the quasar and NELG samples as functions of position, redshift, apparent magnitude, colour and luminosity are described in detail. It is argued that the quasar sample is highly homogeneous and at least 70 per cent complete. Identifications of objects without emission lines are discussed.

A minimal spanning tree analysis of a homogeneous sample of 227 quasars drawn from the survey programme area catalogue identifies two large groups of quasars with high statistical significance. The first group contains 6 quasars with median

redshift $z = 1.236$ and mean separation $26 \pm 9$ $h^{-1}$ Mpc. The null hypothesis that the quasars in this group are distributed randomly is rejected by the $(m, \sigma)$ test of Graham et al. (1995) at the 0.0011 level, and the probability that this is a random significant event is 5 per cent. The shape of the group suggests a single filament with a length of $\sim 110$ $h^{-1}$ Mpc and a width of $\sim 15$ $h^{-1}$ Mpc. This group coincides with the core of the Clowes & Campusano (1991) group, the reality of which is confirmed by this independent survey. The second group is a new discovery. It contains 13 quasars with median redshift $z = 1.507$ and mean separation $32 \pm 7$ $h^{-1}$ Mpc. The $(m, \sigma)$ test finds that this group is significant at the 0.0020 level, and the upper limit on probability that this is a random significant event is 13 per cent. The shape of the second group resembles three intersecting filaments with an overall size of $\sim 150 \times 80 \times 85$ $h^{-3}$ Mpc$^3$, making it one of the largest structures in the Universe found so far.

The use of measures of the C IV $\lambda 1549$ broad emission line to determine the intrinsic luminosity of quasars is investigated, using spectra from a luminosity-limited sample of survey quasars. The observational evidence and theoretical basis for a power-law correlation between luminosity and equivalent width (the Baldwin Effect) are reviewed. A model that predicts a power-law correlation between luminosity and the velocity width of broad emission lines is described. The Baldwin Effect correlation is detected at the 2.4-$\sigma$ level. A positive slope for a luminosity-velocity width correlation is detected in agreement with the proposed model but at lower significance.

# Contents

# List of Tables

# List of Figures

# Collaborators

My work on the Chile-UK Quasar Survey is in collaboration with my thesis supervisors, Dr Roger G. Clowes (University of Central Lancashire) and Dr Luis E. Campusano (Universidad de Chile), and my colleague, Dr Matthew J. Graham (formerly at University of Central Lancashire, now at Imperial College, London). The original proposals and justification for the CUQS were produced by RGC and LEC. For the 1996 observations, MJG provided the photometric calibration (§3.4.4), and made the tessellation (§4.3.2). MJG also provided the standard-star photometric solutions as part of the 1997 calibration (§3.4.5). I made the spectroscopic survey observations at Las Campanas Observatory with LEC (§4.5), and LEC managed the conversion of my observing plans into plug-plate drilling instructions (§4.2). The identification and redshift measurements of emission-line objects (§5.2.1) were performed in parallel by myself and MJG, and disputes were resolved with help from RGC. Otherwise, all of the work reported here is my own.

# Acknowledgments

I must first offer sincere thanks to my director of studies, Roger Clowes, and my second supervisors, Luis Campusano and Gordon Bromage, for their instruction and guidance. I received financial support during this work from PPARC in the form of a research studentship and travel grants for observing trips and conferences. My studies made extensive use of computer hardware and software provided by the PPARC Starlink Project, the IRAF software from the U.S. National Optical Astronomy Observatories, and extensive data from NASA and the Centre de Données astronomiques de Strasbourg. The observations reported here were made while I was a guest observer at the Las Campanas Observatory in Chile courtesy of the Observatories of the Carnegie Institution of Washington. Much of the research was based on photographic plates from the UK Schmidt Telescope digitized on the Super-COSMOS machine at the Royal Observatory Edinburgh. Great thanks to everyone involved at those facilities for their help and for hospitality at the observatories, and to colleagues and friends at the University of Central Lancashire and elsewhere – you know who you are.

For SAB, who waited so long she became a Brit.

"Nature uses only the longest threads to weave her patterns, so each small piece of her fabric reveals the organization of the entire tapestry."
– R.P. Feynman, *The Character of Physical Law*

# Chapter 1

# Introduction

## 1.1  Thesis overview

This thesis describes the objectives, design and construction of a new study of the large-scale structure of the Universe: the Chile-UK Quasar Survey (CUQS), a redshift survey of ultraviolet-excess candidates designed to cover 140 deg$^2$ of sky to a limiting magnitude of $b_J = 20$. The remainder of this chapter provides an overview of the rôle of the CUQS in cosmology, and describes methods for the measurement of large-scale structure, the observational background to this study, and the foundations of the theory of structure formation. Chapter 2 describes in detail the objectives and design of the CUQS and the related observing programmes being undertaken.

Chapter 3 describes the digitized photographic plate data used for survey candidate selection and the new procedures used for astrometric and photometric calibration of the data. Excellent calibrations were achieved over the full survey area, with r.m.s. uncertainties of $\Delta(u_J - b_J) = 0.16$ mag in colour and $\Delta r = 0.69$ arcsec in position. Chapter 4 details the spectroscopic observations made. Spectra of 4588 survey candidates from $\sim$ 54 deg$^2$ of sky were obtained in 12 nights of observations at the Las Campanas Observatory in Chile, conducted in 1996 March, 1997 March and 1998 May. Chapter 5 describes the construction and properties of the catalogue of objects derived from the survey observations. Analysis of the first 3134 spectra has identified 320 quasars and 93 narrow emission-line galaxies.

Chapters 6 describes the search for large groups of quasars in the CUQS cata-

logue. A new $\sim 150\ h^{-1}$ Mpc group of 13 quasars has been discovered at redshift $z \simeq 1.53$, and a $\sim 110\ h^{-1}$ Mpc group of 6 quasars at $z \simeq 1.24$ has been confirmed.

Chapter 7 addresses a different cosmological problem: the accurate determination of the intrinsic luminosity of quasars. The possibilities of determining luminosities from spectral features, in the form of the Baldwin Effect and line width-luminosity correlations, are examined using a luminosity-limited sample of 89 CUQS quasars. Both correlations are found, although not with high significance. Finally, a summary of the conclusions and an outline of future work, are given in chapter 8.

*Thesis conventions.* All distances are stated in comoving coordinates, and assume a standard cosmology with parameters $k = 0$, $\Omega_0 = 1$, $q_0 = 0.5$. The Hubble constant is parameterized as $H_0 = 100\ h$ km s$^{-1}$ Mpc$^{-1}$. The calculation of comoving coordinate distances and separations is described in detail in appendix B. In equations, vector variables are denoted by bold face, e.g. $\boldsymbol{x}$. All celestial positions are in J2000 coordinates unless stated otherwise, and diagrams show north up and east to the left. Uncertainties are stated as $\pm 1\sigma$ where $\sigma$ is the standard error on the mean. Logarithms to base 10 are written as log and those to base $e$ are written as ln. A glossary of abbreviations, symbols and units appears in appendix D.

## 1.2 Cosmology with wide-field redshift surveys

The CUQS is one of a new generation of wide-field redshift surveys to faint limiting magnitudes that have been made feasible by two novel technical developments. First, the digitization of photographic sky surveys by measuring machines such as the APM facility in Cambridge (Kibblewhite et al. 1984), and the COSMOS, and more recently, SuperCOSMOS machines at the Royal Observatory Edinburgh (Miller et al. 1992), have enabled the photometric and astrometric calibration of very large numbers of objects ($\sim 10^3$ deg$^{-2}$ to $B \simeq 20$) with high accuracy ($\Delta m \simeq 0.1$, $\Delta r \leq 1$ arcsec), over wide areas ($> 5° \times 5°$). Second, multi-object 'pseudo-slit' spectrographs, fed by optical fibres positioned in the focal plane of a wide-field telescope, are making possible the collection of candidate spectra at rates of $\sim 10^3$ per night of observation with far better wavelength and flux resolution than was possible with objective-prism and other slitless spectroscopy methods. Examples

of such spectrographs include the Fruit & Fiber instrument on the 2.5-m du Pont telescope at Las Campanas Observatory (Shectman 1993), the 2dF instrument on the Anglo-Australian Telescope (Lewis & Glazebrook 1997) and the Sloan Digital Sky Survey instrument (Margon 1999), Combined, these two new technologies are creating a revolution in faint wide-field redshift surveys.

What aspects of cosmology do such surveys address? The present epoch (redshift $z \simeq 0$) distribution of galaxies is clearly structured into clusters, superclusters, and connecting filaments, with intervening voids of very low-density. In contrast, observations of the cosmic microwave background radiation (CMBR) suggest that, at early times after the Big Bang before the decoupling of matter and radiation ($z > z_{\rm dec} \simeq 1100$), the mass distribution was almost perfectly smooth on angular scales of $\sim 10°$ (White et al. 1994). Standard cosmological models each predict different evolutionary paths for the mass distribution between these two epochs, but observationally, the actual mass distribution is not fully measured, especially at redshifts $z \gtrsim 0.6$ and length scales between 100–1000 $h^{-1}$ Mpc (Colless 1997). Some of the key questions that wide-field redshift surveys of faint objects can address are thus: How has large-scale structure evolved? What are the quantifiable attributes of the structure at $z \gtrsim 0.6$? Are the observed structures consistent with the predictions of current cosmological models?

In overview, the main objectives of the CUQS are the construction of a large, homogeneous catalogue of quasars with redshifts $0.4 \lesssim z \lesssim 2.2$ (corresponding to fractional ages of the Universe in the range $0.6 \gtrsim t_z/t_0 \gtrsim 0.17$, where $t_z$ is the age of the Universe at redshift $z$, and $t_0$ is the present age of the Universe at $z = 0$), and the use of the catalogue to investigate the clustering properties of quasars at those epochs, particularly at large scales ($\sim 100\ h^{-1}$ Mpc).

## 1.3 The measurement of structure

### 1.3.1 Overview

The mass distribution of the Universe can be represented as a time-dependent continuous scalar field of the mass density contrast, $\delta$, defined by

$$\delta(\boldsymbol{x},t) = \frac{\rho(\boldsymbol{x},t) - \overline{\rho}(t)}{\overline{\rho}(t)}$$

where $\rho(\boldsymbol{x},t)$ is the density at position $\boldsymbol{x}$ and time $t$ and $\overline{\rho}(t)$ is the mean density at the same epoch. Similar representations can be made for measurements of point processes, by suitable smoothed reconstruction of the underlying continuous field.

Mathematical tools for analysing the $\delta$ map can be divided into three categories. The first group of tools *identify* structures. The second group measure the *strength* of clustering, for example, as a function of scale. The third group describe the *topology* of the distribution. For detailed mathematical treatments, see e.g. Peacock (1999), Coles & Lucchin (1995) or Peebles (1993). The tools considered here are those suitable for application to limited-area surveys like the CUQS, which excludes those suitable only for all-sky or near-all-sky surveys, such as spherical harmonic analysis (Scharf & Lahav 1993).

### 1.3.2 Structure identification methods

There are several methods for picking out significant structures from large catalogues, of which two, percolation analysis and minimal-spanning tree analysis, will be considered here. Percolation analysis was first developed to analyse the motion of charge carriers in semiconductors, but several variations have been used in analysis of clustering of astronomical objects (Zeldovich et al. 1982; Einasto et al. 1984; Komberg et al. 1996). The analysis proceeds as follows. Consider a set of points scattered in a cubic volume of space of side $L$ containing $N \gg 1$ objects. Surround each point by a sphere of radius $r = b\overline{l}/2$ where $b$ is a dimensionless percolation parameter and $\overline{l} = L/N^{1/3}$ is the mean inter-point distance. If the spheres around two points overlap, then they become 'friends', and chains of overlapping spheres connect 'friends of friends'. If $b$ is small, all points are isolated; if $b$ is large all points are joined. So, as $b$ increases, the number of separate groups decreases from $N$ to 1.

At some critical value, $b_c$, (at least) one group forms that bridges the sample cube (achieving "percolation"). The value of $b_c$ depends on $N$, $L$ and the geometry of the spatial distribution of points. For Poisson distributions of points with large $N$, it can be shown that the mean $b_c \simeq 0.87$ (Coles & Lucchin 1995). For a uniform distribution of points in a rectangular lattice with planes parallel to the sample cube, clearly $b_c = 1$. For a sheet-like distribution of the same number of points at separation $\lambda$ arranged in parallel planes of thickness $h \ll L$, each plane will percolate when $b_c = (h/\lambda)^{1/3} < 1$. For a distribution in straight 'strings' of diameter $h \ll L$, percolation along each rod will occur when $b_c = (h/\lambda)^{2/3} \ll 1$. For a hierarchical clustering of points in small cubes of side $h \ll L$ separated by distance $\lambda$, it can be shown that $b_c > 1$. Analysis of the groups formed by friend-of-friends at different values of $b$ both identifies and characterizes structures in the point set.

A minimal spanning tree (MST) is a tool from graph theory that can be used to quantitatively identify clusters of objects in a manner analogous to that performed by eye. It was introduced to astronomy by Barrow et al. (1985) and is finding wide application in clustering studies (Adami & Mazure 1999; Brodbeck et al. 1998; Coles et al. 1998; Graham, Clowes & Campusano 1995; Clowes & Campusano 1991; Martínez et al. 1990). The information contained in a percolation analysis is also contained in an MST analysis, and the MST analysis provides additional information more efficiently (Bhavsar & Splinter 1996). A spanning tree is defined as a graph of edges connecting all objects in a set with no closed paths. The edge lengths may be specified in the natural dimensions of the data (e.g. angular or linear separation distances), or they may be in some other dimensions that represent the strength of connection between objects (Krzewina & Saslaw 1996). An MST is a spanning tree such that the sum of the edge lengths is minimized. The tree can be pruned of short branches to highlight structural backbones. It can be divided into sub-trees by removing edges longer than some length, for example to maximize the number of sub-trees that appear. A powerful feature of MST analysis is that it can identify structures whose characteristic size is similar to the survey size. The application of MST methods to the CUQS catalogue and the determination of the statistical significance of identified structures is presented in detail in chapter 6.

## 1.3.3 Measures of global clustering strength

A common assumption is that fluctuations in the mass distribution (i.e. the $\delta$ field) are uncorrelated and have a Gaussian distribution. If that is true, then the distribution is completely specified by any one of: the variance of counts in cells, $\sigma^2(r)$, the autocorrelation function, $\xi(r)$, or the power spectrum, $P(k)$.

Counts of objects in regular cells [e.g. Hubble (1934), de Vaucouleurs (1971)] can in principle give all the moments of the distribution of objects, but reveal nothing about the morphology because the analysis does not include directional information. For randomly-placed objects (i.e. a Poissonian distribution), the mean number of objects in a small cell, $\bar{n}$, is equal to the variance between cells. The ratio of the measured variance of an observed distribution to the mean count in cells, $\sigma^2/\bar{n}$, is therefore a measure of the departure from randomness of the clustering pattern.

The spatial two-point autocorrelation function of the density contrast for a *continuous* mass distribution over a given volume $V$ is $\xi(\boldsymbol{r}) = \overline{\delta(\boldsymbol{x})\delta(\boldsymbol{x}+\boldsymbol{r})}$ where $\boldsymbol{r}$ is a separation vector and the average is over the volume (i.e. over all positions $\boldsymbol{x}$). The 3-point and higher correlation functions are similarly defined. Note that $\xi(\boldsymbol{r}) = \xi(r)$ for an isotropic distribution. For a $\delta$ field with a Gaussian distribution and uncorrelated modes, the Fourier transform of $\xi(\boldsymbol{r})$ is the power spectrum, $P(\boldsymbol{k}) \equiv \overline{\tilde{\delta}(\boldsymbol{k})\tilde{\delta}^*(\boldsymbol{k})}/V$ where $\boldsymbol{k}$ is the wave vector, $\tilde{\delta}(\boldsymbol{k}) \equiv \int_V \delta(\boldsymbol{x})e^{i\boldsymbol{k}\cdot\boldsymbol{x}}d^3x$ and the $^*$ means complex conjugate (Peebles 1993, p. 509). Note that the complex phases of the Fourier modes of $\tilde{\delta}$ are randomly distributed for a Gaussian field, and $P(\boldsymbol{k}) = P(k)$. Analysis of the amplitude and shape of $P(k)$ at some epoch constrains models of primordial density fluctuations [see e.g. Peacock (1991)].

An alternative definition of $\xi(r)$ for a distribution of *discrete* objects is the joint probability that two objects are found in two volume elements $dV_1$ and $dV_2$ at linear separation $r$, $dP = \bar{n}^2 dV_1 dV_2[1 + \xi(r)]$ where $\bar{n}$ is the global mean space density of objects (Peebles 1993, p. 213). This is the same as the conditional probability of finding an object in a small volume at a distance $r$ from a given object, $dP = \bar{n}[1 + \xi(r)]dV$. For a given catalogue of objects, $\xi(r)$ can be estimated by comparing the positions of catalogue objects with a random distribution of points formed under the same selection function and boundary conditions. A simple and

commonly-used estimator in this case is

$$\xi(r) \simeq \frac{n_{cc} n_{rr}}{n_{cr}^2} - 1$$

where $n_{cc}$ is the number of pairs of catalogue objects within radius $r$, $n_{rr}$ is the number of pairs of random points, and $n_{cr}$ is the number of catalogue-random pairs (Coles & Lucchin 1995). However, the best unbiased estimator with minimum variance is

$$\xi(r) = \frac{n_{cc} - 2n_{cr} + n_{rr}}{n_{rr}}$$

where the $n_{cr}$ term reduces noise effects from the survey boundaries (Landy & Szalay 1993; Szapudi & Szalay 1998).

Both $\xi(r)$ and $P(k)$ are popular tools, but they reveal little detail about structures. In particular, the filaments and sheets that are obviously evident in maps of the galaxy distribution are not highlighted at all. Indeed, Szalay (1999, see also Martínez et al. 1990) has shown dramatically that two visually very different distributions, one an apparently chaotic field, the other a highly ordered Voronoi tessellation, can have *identical* $\xi(r)$ statistics, differing only in the organization of the modes of the power spectrum, the first random, the second ordered. This distinction may be lost in the measured statistics. Clearly, better measures of the observed density field are needed to distinguish between these different distributions. $\xi(r)$ and $P(k)$ are also particularly poor statistics for surveys with dimensions similar to the scales of interest. $\xi(r)$ and $P(k)$ are dependent on the particular volume considered, because their approximations rely on local rather than global mean densities (Börner 1993), and therefore have very weak statistical power for measuring structures with sizes similar to the sample scale. Measuring $P(k)$ from surveys of galaxies is further complicated by the need to convolve the true $P(k)$ with the Fourier transform of the spatial window function of the survey (Feldman et al. 1994; Vogeley 1995). Recently, Kerscher (1998) has shown that is is possible to find statistics based on a combination of percolation and void probability distributions that have more power than $\xi(r)$ in detecting the form of clustering.

### 1.3.4 Topological and geometric measures

Very large N-body simulations have shown clearly that different cosmological models and different choices of parameters produce different forms of structure and evolution of structure of the mass density field. Low density universes tend to produce structure earlier than high density universes. The nature of the dark matter (for example, cold weakly-interacting massive particles, relativistic 'hot' neutrinos, or some mix), the value of the cosmological constant, the shape and tilt of the power spectrum of primordial density fluctuations and the presence of cosmic strings and textures, all leave different imprints on the form of structure of the subsequent mass density distribution [see e.g. White (1997) for a review].

To quantify the *form* of the large-scale structure, as opposed to merely its clustering strength, the topology of the mass distribution can be measured and how the topology varies with scale can be determined. The set of measures known as Minkowski Functionals is sufficient to provide a complete description of the topology (Mecke et al. 1994). For a 3-dimensional distribution, there are four Minkowski Functionals: the area, volume, integrated curvature and genus. These have been shown to be powerful discriminants between cosmological models for relatively small data sets of $\sim 10^3$ galaxy clusters (Schmalzing et al. 1997). The topology and evolution of clustering can also test the validity of the assumption of Gaussian initial density fluctuations (Yess & Shandarin 1996). The genus alone – or the equivalent Euler-Poincaré characteristic – has been used in several studies to (partially) compare the topology of observed galaxy distribution such as that found in the *IRAS* 1.2 Jy catalogue (Protogeros & Weinberg 1997) with various N-body simulations (Coles et al. 1996; Sahni et al. 1997). Other morphological (i.e. topology-plus-geometry) characteristics, such as the general shape descriptors (Luo & Vishniac 1995) or specific descriptors such as 'filamentarity' (Davé et al. 1997) can be used to make similar useful comparisons between observed and theoretical distributions.

### 1.3.5 Summary – What is "clustering"?

While the foregoing is by no means a complete review of all analysis methods for describing clustering, an important lesson to be drawn is that there is no single,

precise, definition of "clustering". Each analysis method provides a different measure of clustering, based on a different definition of the term and on different assumptions. Each method has different statistical power to test hypotheses on the nature of clustering, depending, for example, on the nature of the data set being analysed. Nevertheless, what makes any structure analysis method scientifically useful is that it can provide a comparison between observed and theoretical mass (or mass-tracer) distributions, and thereby provide a test of structure formation theories. Each of the methods described meets this criterion.

## 1.4 Observational background

### 1.4.1 Mapping large-scale structure

The observational problem in the study of large-scale structure is to construct the actual $\delta$ map of the Universe, and to determine how it has evolved with time. Of course, knowledge of the evolution of large-scale structure is severely limited by the short period over which the Universe has been observed. This is one reason why the Cosmological Principle (§1.5.1) is required: it is assumed that the *local* large-scale structure – seen at or close to the present epoch – is a representative end-point of the evolution of the *distant* large-scale structure, seen at much earlier epochs.

If the characteristic size of a galaxy cluster is defined using percolation analysis on volume-limited samples of galaxies, two things immediately become clear about the local Universe: $\gtrsim 97$ per cent of galaxies are members of clusters, and clusters tend to be linked by filaments, forming larger supercluster aggregations (Bhavsar & Ling 1988, and references therein). If the standard assumption that light traces mass (see §1.5.2) is then made, then it is found that clusters contain most of the mass of the Universe, while occupying $\sim 5$ per cent of the volume (Einasto et al. 1984).

For nearby clusters of galaxies, $\delta$ can be mapped directly from observations of gravitational lensing of background galaxies. It can also be mapped from the gravitational potential inferred from the orbital motions of galaxies within a cluster. However, lensing methods rely on bright background sources, which are not always available, or on very deep imaging, which is expensive in telescope time over large

areas. For widely-separated objects, the galaxy motions method suffers from problems of confusion between redshift due to expansion and redshift due to peculiar motions, and in any case only gives line-of-sight information directly.

For larger volumes over wide areas of the sky, the 2-dimensional or 3-dimensional positions of luminous objects must be mapped instead, and then an appeal must be made to some model of the mass-to-light ratio as a function of object attributes (type, environment, age, etc.) in order to infer the $\delta$ map. The basic methods for creating catalogues of object positions over large volumes of the Universe are well understood, but the procedures remain difficult. Low signal-to-noise ratios, incomplete candidate selection functions and poor understanding of the evolution of luminosity and number density of the objects observed all contribute to the problem.

## 1.4.2 Large-scale structure at $z < 1$

The existence of large density fluctuations in the local galaxy distribution with sizes of $\gtrsim 50 \ h^{-1}$ Mpc has been known since the discovery of the Boötes void (Kirshner et al. 1981, and references therein). Geller & Huchra (1989) subsequently reported the discovery of the Great Wall of galaxies with an extent of over $170 \ h^{-1}$ Mpc. At redshifts $z \lesssim 0.1$, filaments and walls with scales of $\sim 100 \ h^{-1}$ Mpc are now recognized as a common component of large-scale structure, as seen, for example, in results from the Century (Geller et al. 1997), Las Campanas (Doroshkevich et al. 1996; Tucker et al. 1997) and Durham/UKST (Ratcliffe et al. 1996) galaxy redshift surveys. Superclustering on these scales has long been seen in analyses of galaxy cluster catalogues (Oort 1983; Tago, Einasto & Saar 1984; Einasto et al. 1997).

Out to $z \simeq 0.3$, Broadhurst et al. (1990) found that counts of galaxies as a function of distance in a narrow-angle 'pencil beam' survey in the directions of both galactic poles show a repetitive pattern, with peaks spaced at $\sim 128 \ h^{-1}$ Mpc separation. This pattern was supported by similar findings in pencil beams to the same depth but in different directions (Ettori, Guzzo & Tarenghi 1997). Peaks in the number counts from pencil-beam surveys have insufficient statistical power to distinguish between cosmological models or to significantly constrain cosmological parameters (Kaiser & Peacock 1991; Tegmark 1995). Nevertheless, the spacing of the peaks is close to that seen in the local supercluster network (Einasto et

al. 1994). Bahcall (1992) found a distribution coincident with the Broadhurst et al. (1990) results in the Bahcall & Soneira (1984) catalogue, and argued that the narrow peaks in the Broadhurst et al. (1990) results are consistent with flattened superclusters of 20 Mpc width. More recent results (Ratcliffe et al. 1996) suggest the true story is more complex, but support the impression of a cellular structure on 50–100 $h^{-1}$ Mpc scales. There are suggestions that superclusters with similar scales exist in the galaxy distribution at $z \simeq 0.5$ (Connolly et al. 1996).

The clusters that constitute a supercluster may show a tendency to have their long axes aligned. For example, the Coma cluster is aligned with both Abell 1367 and NGC5056, and the latter is also elongated in the same direction (Oort 1983). Remarkably, the major axes of individual powerful radio sources tend to point in the direction of neighbouring quasars and radio galaxies for separations up to $\sim 45$ $h^{-1}$ Mpc (West 1991), giving tentative evidence of a filamentary pattern of superclustering at $z \sim 1$, and suggesting that the radio axes reflect the large-scale clustering pattern of the early Universe (West 1994; Bond et al. 1996).

### 1.4.3 The galaxy distribution at $z > 1$

The number-redshift, $N(z)$, histograms of recent high-redshift narrow-angle galaxy surveys strongly suggest that galaxies are also clustered at $z > 1$ on at least $\sim 10$ $h^{-1}$ Mpc scales. Wang et al. (1998) found peaks in the $N(z)$ distribution from 3-colour $(U - B, B - V, V - I)$ estimates of the redshift of galaxies in the first (northern) Hubble Deep Field (Williams et al. 1996). Using a highly-successful multi-colour $(U - G, G - R)$ method to select Lyman-break galaxy candidates in the range $2.5 \lesssim z \lesssim 3.5$, Steidel et al. (1998a; 1998b) found highly significant excesses of galaxies in some redshift bins at $z \simeq 3$, measuring at least $20 \times 14$ $h^{-1}$ Mpc on the sky, and concluded that Lyman-break galaxies must be much more clustered than the overall mass distribution on scales of $\sim 10$ $h^{-1}$ Mpc for any reasonable cosmological model, suggesting a high bias (see §1.5.2). These new results are tantalizing but, as with the Broadhurst et al. (1990) measurements, the extreme pencil-beam shape of the volumes surveyed means they do not have the statistical power to discriminate well between different cosmological models or to constrain the model parameters (Bagla 1998; Wechsler et al. 1998).

11

### 1.4.4 Quasars as mass tracers

To distinguish between different models using $P(k)$, its shape, amplitude and evolution at a wide range of scales and redshifts are needed. At present there are not sufficient measurements at scales between those measured by the wide-field (low redshift) galaxy surveys, $\lambda \lesssim 100 \ h^{-1}$ Mpc, and those measured by the CMBR measurements made by the *COBE* satellite, $\lambda \gtrsim 1000 \ h^{-1}$ Mpc (Colless 1997).

The luminosity of normal galaxies limits all feasible galaxy surveys to either wide fields at low redshift ($z \lesssim 0.15$, equivalent to $t_z/t_0 \gtrsim 0.8$ – see Fig. 1.1), or to highly anisotropic pencil beams at higher redshifts. As noted above, clustering statistics measured from pencil-beam surveys lack the power to distinguish between cosmological models or to significantly constrain cosmological parameters. What is needed is a more luminous class of objects which can be observed at high redshift but which trace the mass distribution as well as galaxies. Quasars seem to fit this bill well.

The much higher luminosity of quasars ($\sim 10^2$ times that of galaxies) allows their use as probes of the large-scale structure of the Universe to $z \simeq 4$ ($t_z/t_0 \simeq 0.1$). The $\sim 100 \ h^{-1}$ Mpc structures found in the $z \lesssim 0.2$ galaxy distribution are still in the linear stage of gravitational collapse, so a similar (comoving) scale should probably be measurable in the distribution of high-redshift objects. Therefore, one should expect the existence of a $\sim 100 \ h^{-1}$ Mpc typical scale in the quasar distribution if high redshift quasars trace the same high peaks in the mass density field as galaxies and clusters of galaxies. Oort (1983) was among the first to suggest that distant superclusters might be discovered in this way.

There is, indeed, evidence that quasars and other active galaxies can be used to trace the mass density distribution in place of galaxies. Pairs of quasars with small angular separation often show Ly$\alpha$ absorption in the spectrum of the more distant quasar close to the redshift of the nearer quasar, suggesting that quasars are located in regions of high gas density, plausibly clusters of galaxies (Shaver & Robertson 1983). At low redshifts, $z \lesssim 0.05$, Longo (1991) found that active galaxies trace the same large structures as normal galaxies. Engels et al. (1999) reported that the $\sim 14000$ AGN discovered by *ROSAT* are organized into clusters and filaments on $\sim 50$–$100 \ h^{-1}$ Mpc scales. Deng, Xia & Fang (1994) found that the scale length of
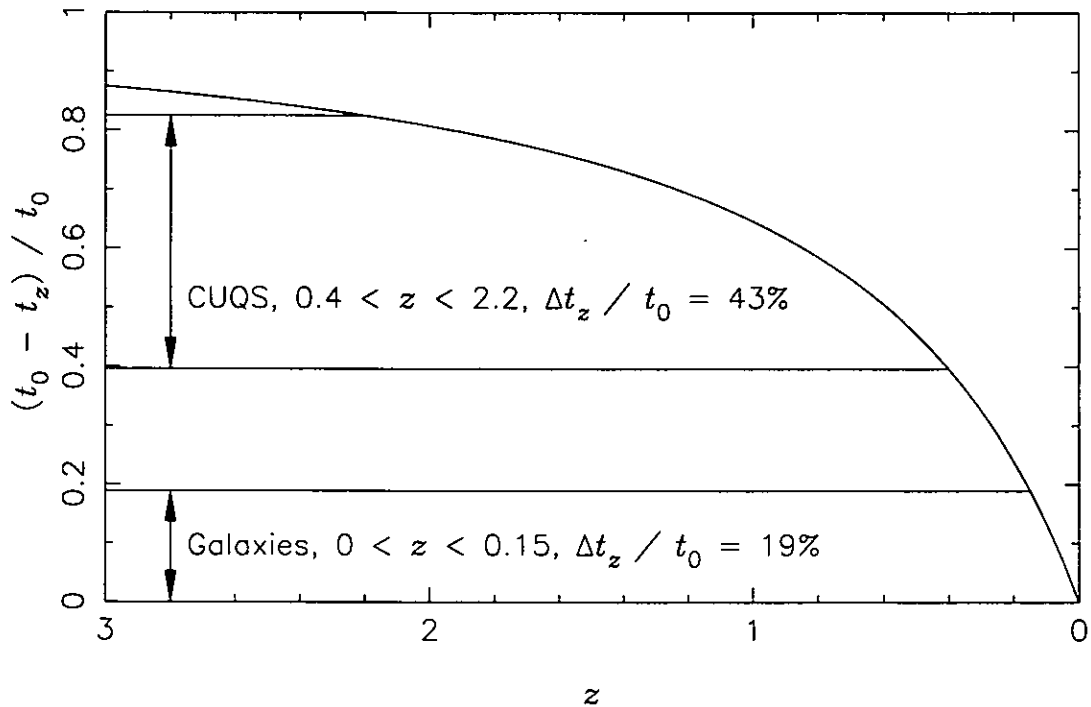
**Figure 1.1.** Comparison of the fractional look-back time probed by a typical wide-field galaxy survey (covering redshifts $0 \leq z \leq 0.15$) with that probed by the CUQS ($0.4 \leq z \leq 2.2$). The curve shows the look-back fractional time for a flat Einstein-de Sitter model where $t_z/t_0 = (1+z)^{-3/2}$. The horizontal lines show the boundaries probed by the galaxy and quasar surveys. As indicated, an ultraviolet-excess quasar survey probes more than twice the range of ages probed by a typical wide-field galaxy survey.

the bend in the global quasar power spectrum supports the view that quasars trace the same large-scale density field as galaxies and clusters. The quasar-galaxy cross-correlation function shows that radio-quiet quasars (the large majority) at $z \lesssim 0.6$ have constant bias with respect to galaxies and probably reside in small clusters of $\sim 10$ galaxies (Bahcall & Chokshi 1991; Mo & Fang 1993; Shanks & Boyle 1994; Fisher et al. 1996). It is also possible to relate the richness of host galaxy clusters to the properties of radio-loud quasars (Green & Yee 1988; Yee 1990; Bahcall & Chokshi 1991). There are suggestions that the quasar-galaxy correlation shows no evolution to at least $z \simeq 1.5$ (Smith, Boyle & Maddox 1995; Croom 1997; Smith 1998), although this relative bias is by no means certain at large redshifts (Fang & Jing 1998). Liu (1995) found a significant excess in the number of Ly$\alpha$ absorption line systems around quasars at $z \simeq 2.1$, suggesting that quasars are already in dense, virialized clusters by that epoch.

It may be concluded, at least tentatively, that quasars are probably good tracers of the mass density field out to $z \simeq 2$, but that the exact details of the bias between quasars and mass at $z \gtrsim 1$ needs further refinement. Although not addressed further in this thesis, it should be noted that quasars can also provide data for $\delta$ mapping at lower $z$ by acting as bright background illumination: absorption lines in quasar spectra can reveal protogalactic clouds of gas (and, indeed, galaxies) in the line of sight. The redshift, density, temperature and clustering of the clouds can be deduced from the wavelength, profile and equivalent widths of absorption lines. Cross-correlation of the absorption line redshifts from close groups of quasars can reveal the tangential extent of the clouds. The wavelength resolution of the CUQS is too low for such detailed studies, but the survey will provide an input catalogue for high-resolution spectroscopic study of absorption-line correlations.

## 1.4.5  Quasar clustering and large groups

Since the first identification of quasars as high-redshift objects (Hazard et al. 1963; Schmidt 1963), there have been many reports of small, isolated groups of quasars with spacing $\lesssim 50$ Mpc. See e.g. Burbidge et al. (1980) and Oort et al. (1981) for early collations. As these were generally from very limited samples, they were of little use in the study of large-scale structure. Subsequent studies of quasar clustering from more useful samples found that, with the possible exception of an occasional anomaly, quasars seemed to be unclustered (Osmer 1981). Deeper samples and a clear detection of clustering (Shanks, Boyle & Peterson 1988) then led to a revision in which quasars were thought to be weakly clustered on small scales ($\lesssim 10\ h^{-1}$ Mpc), while at larger scale they are scattered uniformly and randomly [for more recent references, see Shanks & Boyle (1994), where they present similar results for a combined sample of $\sim 700$ quasars]. Evolution became a possible complication with some tentative evidence for the existence of this small-scale clustering only at redshifts $z \lesssim 1.5$ (Iovino & Shaver 1988; Iovino et al. 1991). Now, the recent discoveries of several large quasar groups at $z > 1$ might be leading to a further revision.

The number of known large groups of quasars with supercluster-scale sizes has been slowly increasing, limited mainly by a shortage of deep, wide-field, homoge-

neous samples. Webster (1982) was the first to report detection of a large group, consisting of four quasars within a radius of $\sim 75\ h^{-1}$ Mpc at redshift $z = 0.37$ in an otherwise unclustered sample. Crampton, Cowley & Hartwick (1987; 1989) found the second large quasar group, in which 23 quasars at $z \simeq 1.1$ form a group with a size of at least $60\ h^{-1}$ Mpc. Then, Clowes & Campusano (1991) found the third group of 13 quasars at $z \simeq 1.3$. The Clowes & Campusano group has since been shown to contain at least 18 quasars (Clowes, Campusano & Graham 1995), with a size of $\sim 200 \times 35 \times 100\ h^{-1}$ Mpc. However, the Clowes & Campusano group extends to the boundaries of their discovery survey, so its total extent and membership were not fully determined by that survey.

Graham, Clowes & Campusano (1995), in attempting to overcome some of the limitations of the standard clustering tests, developed a graph theoretical method using the MST of a quasar catalogue for finding candidate large quasar groups and assigning them a statistical significance. The application of this method to six surveys over continuous areas, three of them with claims of detection of quasar groups, resulted in the recovery of the three known structures and the finding of a new candidate group in the Osmer & Hewett (1991) survey, consisting of 10 quasars at $z \simeq 1.9$ and with minimum dimensions $120 \times 90 \times 20\ h^{-3}$ Mpc$^3$. The group of Clowes & Campusano (1991) was recovered in a 3-dimensional MST test at a level of significance of 0.016 and with a minimum associated size of $150 \times 100 \times 60\ h^{-3}$ Mpc$^3$. From finding only four quasar groups in a rather large surveyed volume, Graham et al. (1995) suggested that large quasar groups might indeed be rare events.

Crampton, Cowley & Hartwick (1989) suggested that all clustering of quasars, even on small scales, is localized in such groups. Komberg, Kravtsov & Lukash (1996) reported finding 12 groups of $\geq 10$ quasars in the Véron-Cetty & Véron (1991) compilation of quasar and AGN catalogues using a friend-of-friends cluster-finding algorithm. They suggested that the space density of large quasar groups is comparable with that of large galaxy superclusters in the local Universe, and that large quasar groups might represent high-redshift equivalents of the Great Attractor and Great Wall. However, the heterogeneous nature of the compilation catalogue used by Komberg et al. introduced some problems in the interpretation of the significance of their groups.

As described in more detail in chapter 6, the CUQS so far has confirmed the reality of the Clowes & Campusano (1991) group, and has identified a new, fifth, large group of 13 quasars at redshift $z \simeq 1.5$ (Newman et al. 1998a; Newman et al. 1998b). The known large quasar groups are so large, and formed so early $(t_z/t_0 \simeq 0.25$ at $z = 1.5)$, that they may challenge the standard hypothesis that large-scale structure formed from gravitational collapse of a primordial density field with a Gaussian distribution (Szalay 1999; White 1997; Silk & Weinberg 1991).

### 1.4.6 The mass distribution at $z > 4$

Better knowledge of the $\delta$ map beyond $z \simeq 4$, where very few individual luminous objects have so far been detected, would also further constrain the choice of cosmological model. It may be possible to map the mass density contrast at the decoupling redshift, $z_{\text{dec}} \simeq 1100$, from observations of temperature anisotropies, $\delta_{\text{T}} = \Delta T/T$, in the cosmic microwave background radiation (CMBR). However, this is probably impossible at high resolution, because re-ionization of the inter-galactic medium by an early generation of hot objects would have blurred the fine details (Górski 1992; Sciama 1993; White et al. 1994; Tegmark et al. 1997; Gaztañaga et al. 1998). In particular, the intense ultraviolet radiation from an early generation of quasars at $z \simeq 10$ would have produced density fluctuations $\delta_{\text{T}} \simeq 10^{-5}$ on $1°$ scales, through the kinetic Sunyaev-Zeldovich (SZ) effect. These would be indistinguishable from primordial anisotropies (Aghanim et al. 1996). Massive stars at $z \simeq 10$–$20$ may produce similar, although smaller, effects on $10°$ scales through the thermal SZ effect (Loeb 1997). Anisotropies in the primordial abundance of light elements might trace density fluctuations back to $z > 1500$, before the surface of last scattering of the CMBR (Copi et al. 1995; Jedamzik et al. 1995), but the observational difficulties with this method would seem to rule it out for the foreseeable future.

# 1.5 Theoretical background

## 1.5.1 Formation and growth of structure in the Universe

Standard theoretical Big Bang cosmology is founded on a set of interrelated models that attempt to explain three key sets of observations of the Universe:

- The approximately linear relationship between distance and redshift for extragalactic objects that implies that the Universe is expanding (Wirtz 1924; Robertson 1928; Hubble 1929; Leibundgut et al. 1996).

- The CMBR, with an almost perfect blackbody spectrum and a temperature of 2.73 K that is isotropic to $\sim 10^{-5}$, which implies that the Universe was hotter in the past and had an almost isotropic mass distribution at $z \simeq z_{dec}$ (Dicke et al. 1965; Penzias & Wilson 1965; White et al. 1994).

- The particular ratios between the abundances of the light elements that constrain baryon density and other conditions in the very early Universe at $z \gg z_{dec}$ (Alpher et al. 1948; Schramm 1993).

The physical assumptions underlying these models are that gravitation is described by the General Theory of Relativity [see e.g. Weinberg (1972) or Peebles (1993)], and that the Cosmological Principle holds true. On scales larger than the quantum regime, general relativity is probably the best-tested of all physical theories, so the larger of these assumptions is the Cosmological Principle, which holds that there are no preferred places in the Universe. This implies that, when averaged over sufficiently large scales, the Universe is both isotropic (looks the same in all directions) and homogeneous (has the same physical properties everywhere). The Cosmological Principle is still for the most part an assumption, but it appears to be a reasonable one. There are no scientific reasons to suppose otherwise: the Milky Way is a large but otherwise unremarkable spiral galaxy; isotropy is apparent in deep sky maps; and global tests (based, for example on the origin and abundances of the light elements) suggest the Universe is homogeneous, although this is not strictly proven (Peebles 1998).

In current standard cosmology, the structure of the mass density field was formed by the gravitational collapse of primordial fluctuations which arise naturally in the-

ories of the very early, inflationary, Universe (Guth 1981). In this paradigm, primordial density fluctuations are generated by fluctuations in quantum fields during the inflationary phase. The wavelength of the fluctuations is stretched by the general expansion of the Universe until they represent modes outside the particle horizon. When the period of inflation ends, the horizon grows faster than the expansion, and the fluctuations "reenter" the horizon, and subsequently evolve under the rules of general relativity. In particular, inflation theory predicts that the power spectrum of the primordial fluctuations will be adiabatic with a Gaussian distribution, and will be scale-free ($P(k) \propto k$ where $k$ is the wavenumber) for small $k$ (large scales), turning over to $P(k) \propto k^{-3}$ for large $k$ (small scales). See e.g. Ostriker (1993), White et al. (1994) and Turner (1997) for reviews.

In the era before the decoupling of matter and radiation, $z > z_{\mathrm{dec}}$, fluctuations on mass scales $M \lesssim 10^{15} M_\odot$ are damped by photon viscosity, although clusters with $M \gtrsim 10^{15} M_\odot$ would survive. After $z \lesssim z_{\mathrm{dec}}$, the Universe has cooled enough for neutral gas to form, and the consequent removal of free electrons makes the Universe transparent, leading to a dramatic decrease in the sound speed and hence the removal of the photon damping. This permits the collapse of regions of $M \simeq 10^{5.5} M_\odot$, possibly leading to the initial formation of globular clusters. Objects of galaxy and larger sizes then form by aggregation at $z \simeq 10\text{--}3$. On the scales of interest here ($\gtrsim 100\ h^{-1}$ Mpc), the density contrast remains small enough that linear approximations of perturbation theory can be used to study the gravitational formation of structure (Rees 1992). The typical velocity dispersion of clusters in a supercluster is $\sim 300$ km s$^{-1}$, which implies sound crossing times much longer than the present age of the Universe. This means that little mixing can have taken place on these scales, so superclusters should have largely retained their structure at their creation, and they are therefore very suitable structures for studying the large-scale primordial mass distribution. The linear approximation means that the density contrast evolves from time $t_1$ to time $t_2$ as

$$\delta(\boldsymbol{x}, t_2) = \delta(\boldsymbol{x}, t_1) \frac{D(t_2)}{D(t_1)}$$

where $D(t)$ is a linear growth factor that depends on the cosmological parameters. For $\Omega = 1$ and $\Lambda = 0$, the relationship is particularly simple, giving $D(t) \propto t^{2/3} \propto (1 + z)^{-1}$ (Weinberg 1995).

18

## 1.5.2 Biased formation of luminous objects

When a luminous extragalactic object (galaxy, cluster, quasar) is observed, how much mass is being looking at? How may the mass density distribution be derived from observations of luminous objects (galaxies, clusters, quasars)? The standard approach to answering these questions is to postulate that luminous objects form in peaks in the mass density distribution, and assume that similar objects trace similar peaks. The *object* density contrast, $\delta_o$, smoothed over a suitable radius $R_S$, is then taken to be some function of the *mass* density contrast, i.e. $\delta_o(\boldsymbol{x}, R_s) = f[\delta(\boldsymbol{x}, R_s)]$. Assuming $f$ is well behaved, then $\delta_o$ can be expanded in a Taylor series in $\delta$, i.e.

$$\delta_o = a + b_1\delta + \frac{b_2\delta^2}{2!} + \cdots$$

where $b_1 = f'(a), b_2 = f''(a)$ and so on. The constant is fixed as $a = 0$ by the requirement that $\overline{\delta_o} \to 0$ on large scales. In a linear approximation, $b_1$ describes the biasing of object formation, so that if the objects trace the peaks of density enhancements, $b_1 > 0$. The statistics of the objects tracing the density peaks can then be related to the statistics of the underlying mass density field. In particular, it can be shown that rare high peaks in $\delta$ will show enhanced correlations over lower peaks (Kaiser 1984; Bardeen et al. 1986).

Although the linear bias approximation is an easy first-order approximation to make, it is a very strong assumption to take $b_1$ to be constant everywhere. For galaxies, at least, this assumption is not supported by numerical modelling. In an extensive comparison between the APM Galaxy Survey and N-body simulations produced using several variants of the cold dark matter model (standard, open, low-density flat, and tilted power spectrum), Jenkins et al. (1998) found that the distribution of galaxies must be biased relative to the mass in a non-trivial, scale-dependent fashion for all of the models considered. Some recent studies (Tegmark & Bromley 1999; Tegmark & Peebles 1998; Blanton et al. 1998) go further and suggest that galaxy-mass bias depends not just on scale, but on luminosity, morphology, redshift and other factors as well. The problem of how to relate observations of luminous objects – be they galaxies or quasars – back to the mass distribution remains unsolved. Advances are needed both on the observational side, for example to improve the completeness and homogeneity of samples, and on the theoretical

side, to model the formation and evolution of objects in relation to the mass density field.

# Chapter 2

# The Chile-UK Quasar Survey

## 2.1 Chapter overview

This chapter describes the motivation, objectives and design of the CUQS and the related observations being carried out in parallel with the main survey.

## 2.2 Motivation and objectives

The original motivation for the CUQS was the discovery of a $\sim 200~h^{-1}$ Mpc quasar group at $z \simeq 1.3$ in a quasar redshift survey covering a $5° \times 5°$ field (Clowes & Campusano 1991; Clowes, Campusano & Graham 1995; Graham, Clowes & Campusano 1995, hereafter refered to as the CC91 group). The CC91 group extends to the boundaries of the sparsely-sampled discovery survey, so a more densely-sampled survey over a larger area of sky was clearly needed to determine the full extent and membership of this remarkable structure.

The first objective, then, of the CUQS is to construct a large, homogeneous sample of quasars in a programme area centred on the region of sky containing the CC91 group at $10^h 40^m$, $+05°00'$ (B1950 coordinates). For good statistical power in measuring structure, a survey must extend to larger than the largest wavelength of interest, and the coverage must be as close to isotropic as possible (Tegmark 1995). The $10° \times 10°$ programme-area dimensions are therefore twice those of the CC91 discovery survey. The square survey geometry provides almost isotropic coverage of the structural wavelengths of interest (at $z = 1$, $10° \simeq 300~h^{-1}$ Mpc, and $\Delta z =$

$0.1 \simeq 100 \ h^{-1}$ Mpc).

Candidates for the CUQS are chosen on ultraviolet excess to include quasar redshifts in the range $0.4 \lesssim z \lesssim 2.2$ (Véron 1983), so that a large range of redshifts either side of the CC91 group is observed. Spectroscopic redshifts of all quasar candidates in the area are being obtained. The total number of quasars in the full programme area is expected to be $\sim 950$ from the surface density to an effective limit of $B \simeq 19.7$ (Boyle et al. 1990).

The background quasar density at the redshift of a large quasar group is required in order to determine the density contrast of the group. For this purpose, the survey also includes observations of a control area centred at $11^h14^m$, $-29°00'$. This is at an angular separation of $\sim 35°$ from the programme area, which is assumed to be sufficiently large that no group spans both areas. The control area is a square covering 40 deg$^2$ and its full catalogue is expected to contain $\sim 380$ quasars, providing in addition a substantial independent sample.

The primary objectives in analysing the survey quasar catalogue are then to:

- Identify statistically-significant large groups of quasars, using MST $(m,\sigma)$ analysis (see §6.2 for details) and 3-dimensional power spectrum analysis (Webster 1982; Feldman et al. 1994, hereafter 3DPSA). The MST $(m,\sigma)$ method finds groups in an objective manner with parameters completely determined from the characteristics of the survey. The reality of the CC91 group will be confirmed if it is also found in this independent survey.

- Determine whether or not the identified large quasar groups are consistent with formation by gravitational collapse from Gaussian primordial density fluctuations. The density contrast of a group, $\delta_q$, for its characteristic size, $\lambda_g$, can be measured as the contrast for a sphere of diameter $\lambda_g$ centred on the group, with the mean background density at the group's redshift determined from the control area. $\delta_q$ can then be compared with the r.m.s. density contrast expected at the group's epoch from the density fluctuation power spectra predicted by theoretical models. If the large quasar groups are found to be inconsistent with the models, then either non-Gaussian fluctuations, or other non-gravitational mechanisms for structure formation would be suggested.

- Measure the strength of clustering of quasars using 3DPSA. The fraction of the total survey volume likely to be occupied by large groups is $\lesssim 5$ per cent (the CC91 group occupies $\lesssim 2$ per cent). Therefore, the global 3-dimensional density fluctuation power spectrum is unlikely to be significantly biased by the presence of such groups. This assumption can be tested by, for example, excluding the wave vectors corresponding to the orientation of the groups from the power spectrum analysis, or by excluding the corresponding redshift intervals.

- Test the hypothesis made by Crampton et al. (1989) that all of the observed small-scale ($\lesssim 10\ h^{-1}$ Mpc) clustering of quasars is attributable to large groups. In the formation of structure by gravitational instability, large groups would be expected to be collapsing into a collection of smaller-scale clumps. Such sub-clustering is fairly clear in the group detected by Crampton et al. (1989), and is tentatively indicated in the CC91 group. The CUQS should detect a sufficient density of quasars to show any sub-clustering unambiguously.

- Further constrain the cosmological models compatible with large-scale structure at high redshift by characterizing the topology of the quasar distribution, as measured by Minkowski Functionals (Mecke et al. 1994).

Any quasar candidate selection method can be expected to include non-quasar 'contaminants'. In the case of selection on ultraviolet excess, these are mainly other objects with hard optical spectra such as narrow emission-line galaxies and hot galactic stars. Emission-line diagnostics (e.g. Rola, Terlevich & Terlevich 1997) can be used to distinguish between star-burst, LINER and other classes of active galaxies, to study their relative abundances. The spatial clustering of narrow emission-line galaxies in the catalogue will be studied. By cross-correlating the positions and redshifts of the narrow emission-line galaxies with (normal) galaxy survey catalogues, the results of Longo (1991), that suggest that active galaxies trace the same structures as normal galaxies, can be tested.

The major galactic contaminants of ultraviolet-excess quasar selection are white dwarf stars. The CUQS will therefore produce two large serendipitous catalogues of faint ($B \lesssim 20$) white dwarfs at the galactic latitudes of the programme and

23

control areas ($b \simeq 52°$ and $b \simeq 29°$), which may be used as probes of the structure of the Galaxy. Less useful contaminants are variable stars, where the uncorrelated magnitude changes between the epochs of the different photographic plates used (see next section) led to an erroneous assigned colour.

## 2.3  Survey design

The CUQS is designed to use multi-object spectrographs on telescopes of 2.5m or larger aperture. All observations to date have been made with the 2.5-m telescope at Las Campanas Observatory (see chapter 4), but the candidate selection process can be adapted to other instruments. Survey candidates are chosen from direct UK Schmidt Telescope plates digitized on the SuperCOSMOS measuring machine at the Royal Observatory Edinburgh. The programme area is covered by a $3 \times 3$ grid of UKST survey fields. The control area is covered by a $2 \times 2$ grid (Fig. 2.1 and table 2.1).

Two U and two J plates per UKST field are used. Each scanned plate produces a database of $\sim 10^5$ objects. The objects in the databases from the plates in each UKST field are then paired, resulting in a final database of $\sim 3 \times 10^4$ objects that are common to all the plates in that field. This process eliminates virtually all of the spurious detections in the individual plate scans due to satellite and meteor trails, emulsion faults, etc. (Cannon et al. 1985), while improving the photometric calibration of the final candidate lists by weighted averaging of the individual plate photometry. Photometric and astrometric calibration of the SuperCOSMOS data is described in detail in chapter 3. After calibration, candidates for spectroscopy are those objects with ultraviolet-excess colour $(u_J - b_J) \leq -0.3$ and apparent magnitudes in the range $16 \leq b_J \leq 20$. The completeness of the actual quasar sample that has been selected by this colour limit is discussed in detail §5.4. For observations with larger instruments such as the 400-fibre 2dF spectrograph on the 3.9-m Anglo-Australian Telescope, the magnitude limit could be extended to $b_J \leq 21$, which would increase the number of quasars detected by a factor of $\sim 3$ (Boyle et al. 1990), although some calibration problems are introduced (see §3.4.8).

24
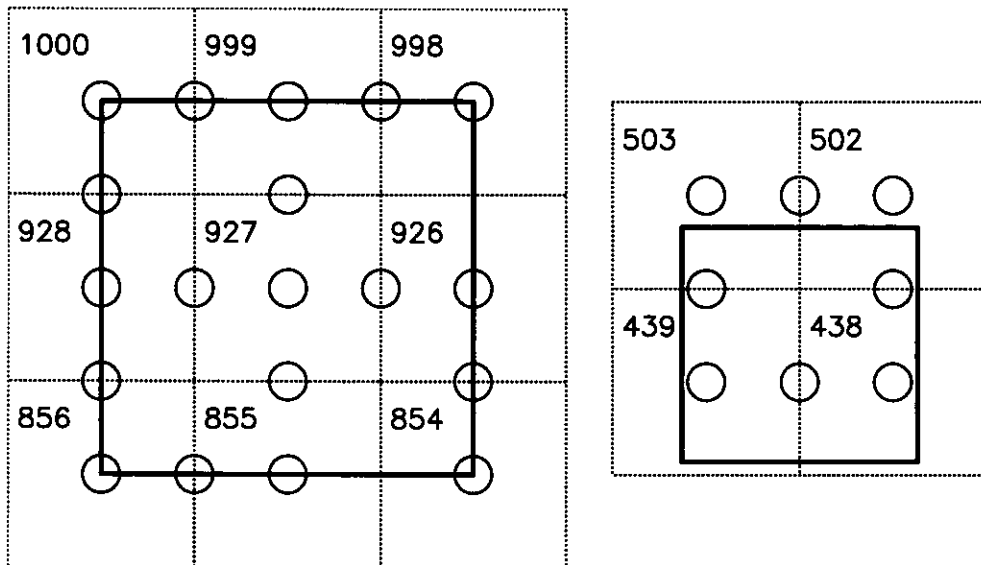
**Figure 2.1.** Schematic relationship between the CUQS areas (bounded by solid lines) and the UKST ESO/SERC sky survey fields (bounded by dotted lines and numbered). The UKST field centres are listed in table 2.1. The programme area (left) is $10° \times 10°$. The control area (right) is $6.3° \times 6.3°$. Circles show the positions of photometry sequences; those on boundaries are common to the plates from adjoining fields. North is up and east is to the left.

**Table 2.1:** Positions of the centres of the UKST ESO/SERC sky survey fields for the CUQS programme and control areas, as shown in Fig. 2.1, plus the F345 complete sample field described in §2.4.2.

| Field | B1950 | | J2000 | |
|-------|-------|-------|-------|-------|
| No. | $\alpha$ ($^h\!:^m\!:^s$) | $\delta$ ($°\!:'\!:''$) | $\alpha$ ($^h\!:^m\!:^s$) | $\delta$ ($°\!:'\!:''$) |
| 854 | 10 : 20 : 00 | +00 : 00 : 00 | 10 : 22 : 34 | −00 : 15 : 11 |
| 855 | 10 : 40 : 00 | +00 : 00 : 00 | 10 : 42 : 34 | −00 : 15 : 44 |
| 856 | 11 : 00 : 00 | +00 : 00 : 00 | 11 : 02 : 34 | −00 : 16 : 10 |
| 926 | 10 : 20 : 00 | +05 : 00 : 00 | 10 : 22 : 36 | +04 : 44 : 49 |
| 927 | 10 : 40 : 00 | +05 : 00 : 00 | 10 : 42 : 36 | +04 : 44 : 16 |
| 928 | 11 : 00 : 00 | +05 : 00 : 00 | 11 : 02 : 35 | +04 : 43 : 50 |
| 998 | 10 : 20 : 00 | +10 : 00 : 00 | 10 : 22 : 39 | +09 : 44 : 49 |
| 999 | 10 : 40 : 00 | +10 : 00 : 00 | 10 : 42 : 38 | +09 : 44 : 16 |
| 1000 | 11 : 00 : 00 | +10 : 00 : 00 | 11 : 02 : 37 | +09 : 43 : 50 |
| 438 | 11 : 07 : 00 | −30 : 00 : 00 | 11 : 09 : 25 | −30 : 16 : 17 |
| 439 | 11 : 30 : 00 | −30 : 00 : 00 | 11 : 32 : 29 | −30 : 16 : 34 |
| 502 | 11 : 00 : 00 | −25 : 00 : 00 | 11 : 02 : 26 | −25 : 16 : 09 |
| 503 | 11 : 22 : 00 | −25 : 00 : 00 | 11 : 24 : 29 | −25 : 16 : 29 |
| 345 | 22 : 32 : 00 | −40 : 00 : 00 | 22 : 34 : 54 | −39 : 44 : 28 |

## 2.4 Related programmes

### 2.4.1 Survey byproducts

As mentioned above, the survey selection criteria essentially selects all faint hot objects. This will result in the detection of any non-quasar objects with blue colours, including narrow emission-line galaxies and galactic white dwarfs. The survey construction process is also naturally producing a large collection of photometrically and astrometrically calibrated SuperCOSMOS databases (see chapter 3), which contain all classes of objects within the plate magnitude limits. Further uses of these data are outside the scope of this thesis, but it is anticipated that they will form the basis of other lines of research.

### 2.4.2 The F345 complete sample

The allocation of telescope time at Las Campanas Observatory for the 1998 observations was such that the CUQS fields moved beyond the maximum observable zenith angle before the end each night. To make good use of the remaining time, an additional programme of observations was developed with the objective of constructing a complete spectroscopic sample of all objects in the range $17 \leq b_J \leq 20$ in a 1°5-diameter field. This sample will be a useful tool in computing the completeness of different candidate selection methods, including ultraviolet excess. The need for such complete samples has been noted by Graham et al. (1999), who have highlighted problems with results based on surveys with systematic incompleteness.

The field centre, $22^h 30^m$, $-40°00'$ (B1950) was chosen as a compromise between zenith angle and moon distance for the observing run during 1998 May 17-21. The field lies at the centre of the UKST ESO/SERC survey field F345. Candidates were selected from one J plate and one R plate solely on $b_J$ magnitude, digitized on SuperCOSMOS as for the CUQS observations. Calibration of this data is again described in detail in chapter 3.

# Chapter 3

# Calibration of SuperCOSMOS data

## 3.1  Chapter overview

The source and calibration of the data used to construct the CUQS and related observing plans are described. The uncalibrated position and brightness data were taken from UK Schmidt Telescope (UKST) plates digitized by the SuperCOSMOS machine at the Royal Observatory Edinburgh (ROE). The characteristics of the plates and the digitized data, the quality assurance checks made on the data and the problems of star-galaxy classification are each discussed. The astrometric and photometric calibrations applied to the machine positions and magnitudes are then described in detail. Positional uncertainties of $\Delta r = 0.69$ arcsec r.m.s. and magnitude uncertainties of $\Delta b_J = 0.10$ mag and $\Delta u_J = 0.12$ mag were achieved across the whole CUQS area. The residual errors and possible future improvements to the calibration are discussed.

## 3.2  SuperCOSMOS data

### 3.2.1  UKST photographic source material

The 1.2-m UKST at Siding Spring Observatory produces photographic images of the sky on glass plates or film. Each plate is 356 mm square (in the following, 'plate'

**Table 3.1**: UKST plates used in the programme area. Exposure time is in minutes. Grade is the UKST quality grade. Object positions for pairing J plates with U plates are taken from plates marked with an asterisk.

| Field | Plate | | Substrate | Epoch | Emulsion | Filter | Exposure | Grade |
|-------|-------|---|-----------|-------|----------|--------|---------:|-------|
| 854 | J10147 | * | Glass | 1985/05/11 | IIIa-J | GG395 | 65.0 | AIE3 |
| | J12465 | | Glass | 1988/03/13 | IIIa-J | GG395 | 120.0 | AI2 |
| | U15979 | * | Film | 1994/03/11 | 4415 | UG1 | 90.2 | aIE |
| | U16579 | | Film | 1995/03/25 | 4415 | UG1 | 120.0 | aI |
| 855 | J9309 | | Glass | 1984/05/25 | IIIa-J | GG395 | 60.0 | AE2 |
| | J16076 | * | Glass | 1994/05/12 | IIIa-J | GG395 | 110.0 | a |
| | U9173 | | Glass | 1984/04/03 | IIIa-J | UG1 | 180.0 | a |
| | U16600 | * | Film | 1995/04/06 | 4415 | UG1 | 90.0 | a |
| 856 | J8487 | | Glass | 1983/04/17 | IIIa-J | GG395 | 60.0 | AID3 |
| | J15984 | * | Glass | 1994/03/12 | IIIa-J | GG395 | 70.0 | aD |
| | U12972 | * | Glass | 1989/02/11 | IIIa-J | UG1 | 175.0 | a |
| | U16939 | | Film | 1996/01/29 | 4415 | UG1 | 90.0 | a |
| 926 | J15926 | * | Glass | 1994/01/19 | IIIa-J | GG395 | 100.0 | aE |
| | J16931 | | Glass | 1996/01/27 | IIIa-J | GG395 | 60.0 | a |
| | U15931 | * | Film | 1994/01/20 | 4415 | UG1 | 120.0 | a |
| | U16927 | | Film | 1996/01/26 | 4415 | UG1 | 120.0 | a |
| 927 | J10063 | * | Glass | 1985/04/09 | IIIa-J | GG395 | 90.0 | a |
| | J10128 | | Glass | 1985/05/08 | IIIa-J | GG395 | 60.0 | a |
| | U10082 | * | Glass | 1985/04/12 | IIIa-J | UG1 | 180.0 | a |
| | U11076 | | Glass | 1986/04/29 | IIIa-J | UG1 | 180.0 | aI |
| 928 | J16021 | * | Glass | 1994/04/05 | IIIa-J | GG395 | 90.0 | aE |
| | U17045 | * | Film | 1996/04/18 | 4415 | UG1 | 120.0 | a |
| 998 | J15970 | * | Glass | 1994/03/05 | IIIa-J | GG395 | 70.0 | a |
| | J16935 | | Glass | 1996/01/28 | IIIa-J | GG395 | 60.0 | a |
| | U16964 | * | Film | 1996/02/25 | 4415 | UG1 | 120.0 | a |
| | U17482 | | Film | 1997/03/31 | 4415 | UG1 | 120.0 | aI |
| 999 | J16974 | | Glass | 1996/03/11 | IIIa-J | GG395 | 60.0 | a |
| | J17508 | * | Glass | 1997/04/08 | IIIa-J | GG395 | 60.0 | aID |
| | U16061 | * | Film | 1994/05/08 | 4415 | UG1 | 120.0 | aI |
| | U16936 | | Film | 1996/01/28 | 4415 | UG1 | 120.0 | a |
| 1000 | J16115 | * | Glass | 1994/05/30 | IIIa-J | GG395 | 110.0 | aI |
| | J17034 | | Glass | 1996/04/15 | IIIa-J | GG395 | 60.0 | aD |
| | U16593 | * | Film | 1995/04/03 | 4415 | UG1 | 120.0 | a |
| | U17095 | | Film | 1996/05/15 | 4415 | UG1 | 120.0 | a |

**Table 3.2**: UKST plates used in the control area. Columns as for table 3.1.

| Field | Plate | | Substrate | Epoch | Emulsion | Filter | Exposure | Grade |
|-------|-------|---|-----------|-------|----------|--------|----------|-------|
| 438 | J3905 | | Glass | 1978/02/10 | IIIa-J | GG395 | 70.0 | A2 |
| | J11668 | * | Glass | 1987/02/27 | IIIa-J | GG395 | 90.0 | AE3 |
| | U14209 | * | Glass | 1991/03/14 | IIIa-J | UG1 | 146.2 | a |
| | U14315 | | Glass | 1991/04/18 | IIIa-J | UG1 | 180.0 | a |
| 439 | J4829 | | Glass | 1979/02/27 | IIIa-J | GG395 | 70.0 | BI3 |
| | J5697 | * | Glass | 1980/02/20 | IIIa-J | GG395 | 65.0 | A1 |
| | U14231 | * | Glass | 1991/03/21 | IIIa-J | UG1 | 210.0 | a |
| | U14277 | | Glass | 1991/04/09 | IIIa-J | UG1 | 180.0 | aE |
| 502 | J4012 | | Glass | 1978/03/15 | IIIa-J | GG395 | 75.0 | A2 |
| | J16019 | * | Glass | 1994/04/04 | IIIa-J | GG395 | 60.0 | aU |
| | U14274 | * | Glass | 1991/04/08 | IIIa-J | UG1 | 180.0 | a |
| | U14976 | | Film | 1992/05/23 | 4415 | UG1 | 180.0 | aI |
| 503 | J2346 | * | Glass | 1976/05/30 | IIIa-J | GG395 | 60.0 | A0 |
| | J14227 | | Glass | 1991/03/20 | IIIa-J | GG395 | 70.0 | bI |
| | U14309 | | Glass | 1991/04/16 | IIIa-J | UG1 | 180.0 | aI |
| | U17502 | * | Film | 1997/04/05 | 4415 | UG1 | 120.0 | aE |

**Table 3.3**: UKST plates used in the F345 field. Columns as for table 3.1.

| Field | Plate | | Substrate | Epoch | Emulsion | Filter | Exposure | Grade |
|-------|-------|---|-----------|-------|----------|--------|----------|-------|
| 345 | J3585 | * | Glass | 1977/09/16 | IIIa-J | GG395 | 75.0 | AT2 |
| | OR13849 | * | Glass | 1990/09/21 | IIIa-F | OG590 | 75.0 | AIE3 |

**Table 3.4**: UKST plates measured on SuperCOSMOS but not used. Columns as for table 3.1, plus reason for rejection in the last column. Plates rejected as 'low grade' were replaced by another plate of the same field with a better grade.

| Field | Plate | Subst. | Epoch | Emul. | Filter | Exp. | Grd. | Why rejected |
|-------|-------|--------|-------|-------|--------|------|------|--------------|
| 503 | U14206 | Glass | 1991/03/12 | IIIa-J | UG1 | 180.0 | bI | Low grade. |
| 855 | J9241 | Glass | 1984/04/28 | IIIa-J | GG395 | 60.0 | BI3 | Low grade. |
| | U7714 | Glass | 1982/04/26 | IIIa-J | UG1 | 120.0 | bTI | Low grade. |
| 856 | U16003 | Film | 1994/03/21 | 4415 | UG1 | 120.0 | bE | Low grade. |
| 926 | J16485 | Glass | 1995/01/11 | IIIa-J | GG395 | 65.0 | bXU | Double exposure. |
| | U16609 | Film | 1995/04/27 | 4415 | UG1 | 12.6 | bUF | Density gradient. |
| 928 | J17074 | Glass | 1996/05/08 | IIIa-J | GG395 | 60.0 | aU | Under exposure. |
| | U16552 | Film | 1995/03/09 | 4415 | UG1 | 109.0 | cI | Low grade. |
| 998 | U15983 | Film | 1994/03/12 | 4415 | UG1 | 120.0 | aE | Emulsion streaks. |
| 999 | J16018 | Glass | 1994/04/03 | IIIa-J | GG395 | 110.0 | bX | Low grade. |

will be used to mean both glass and film substrates), and covers $\sim 6°\!.5 \times 6°\!.5$ of sky with an unvignetted radius of $2°\!.7$. The material used for this study includes standard ESO/SERC Southern Sky Survey and northern extension survey plates, plus additional plates exposed specifically for the CUQS or for other projects. The UKST unit at ROE designate standard numbered telescope fields that are spaced to tile the sky at $\sim 5°$ intervals, so that plates from adjacent fields overlap by $\sim 1°\!.5$. The arrangement of fields that cover the area of the CUQS is shown schematically in Fig. 2.1, and the field centres are listed in table 2.1.

The plates digitized on SuperCOSMOS and used in the CUQS are listed in table 3.1 (programme area) and table 3.2 (control area). The plates used for the F345 complete sample are listed in table 3.3. Plates measured but not used are listed in table 3.4 with the reason for their rejection. Plates recording images in three passbands have been used in this study, designated U, J and R, each indicating a different combination of emulsion and filter. All of the emulsions used were produced by Eastman-Kodak. The IIIa-J emulsion responds to wavelengths from ultraviolet to $\sim 5400$ Å. The 4415 (Tech Pan) and IIIa-F emulsions cover ultraviolet to $\sim 6900$ Å. In each case, the atmosphere adds an effective ultraviolet cut-off at $\sim 3200$ Å. The IIIa-J and IIIa-F emulsions are fine grained, and the 4415 is very fine grained. The filters used here are all uncoated glass produced by Schott. The UG1 filter passband covers $\sim 3200$–$3900$ Å; GG395 covers $\sim 3950$ Å to far red; OG590 covers $\sim 5900$ Å to far red. All emulsions used were hypersensitized prior to exposure. For exposures made since 1982 December, the plates were also flushed with dry nitrogen during exposure to suppress desensitization by the air. The J plates all use IIIa-J emulsion on glass substrates exposed through a GG395 filter, giving a combined passband of $\sim 3950$–$5400$ Å and a typical limiting magnitude of $B \simeq 22.5$ (which is $\sim 1.5$ mag fainter than the limiting magnitude of the objective-prism plates used by CC91). The U plates all used filter UG1 but different emulsions: IIIa-J on glass and 4415 on film, both giving a combined passband of $\sim 3200$–$3900$ Å, with typical limiting magnitudes of $U \simeq 21.0$. One R plate was used for the F345 sample, using the IIIa-F emulsion on a glass substrate and exposed through an OG 590 filter (the plate number is prefixed with 'O' to indicate this filter), giving a combined passband of $\sim 5900$–$6900$ Å and a limiting magnitude of $R \simeq 21.5$.

All plates are checked by the UKST Unit at ROE and are assigned a quality grade as shown in the tables. The first letter of the grade (in capitals for survey plates) indicates the overall quality of the plate from A (best) to C (worst). Subsequent letters indicate specific plate defects, as follows:

D : high density
E : emulsion blemish
F : over-exposure or high chemical fog
I : image sizes greater than 40 microns
T : image elongation
U : under-exposure (relative to exposure time)
X : other defects.

Survey plates are also given a grade number. The lower the number, the better the quality. Cannon et al. (1985) give a comprehensive description of plate grading.

## 3.2.2 SuperCOSMOS measurements

The SuperCOSMOS machine at ROE converts large-format (up to 500 mm square) photographic plates (glass or film) into a digitized format (MacGillivray 1998; Hambly & Miller 1997; Miller et al. 1992). The basic output from SuperCOSMOS are 'mapping mode' data, which consist of high-precision (15-bit) transmission density measurements with 10 $\mu$m spatial resolution, equivalent to 0.67 arcsec for UKST plates (Hambly et al. 1998). The data used for this study were further reduced at ROE from mapping mode to 'image analysis mode' (IAM), using the COSMOS crowded-field analysis software (Beard et al. 1990). IAM data as delivered from ROE are in the form of a file containing a record for each object detected above a specified threshold in the central $\sim 6° \times 6°$ of each UKST plate. For each object in the database, 32 parameters are stored (Kelly 1995; Hambly 1998a) including object position in plate and sky coordinates, instrumental magnitude, area and the software's determination of object class (star, galaxy, etc.). Object classification is discussed in §3.2.4. The astrometric calibration is described in §3.3. The definition of the detection threshold, the instrumental magnitude and its photometric calibration are described in §3.4.

All of the SuperCOSMOS data used for this study were subjected to further quality control checks on receipt from ROE. For each plate, a histogram of the $N(m_{sc})$ counts (where $m_{sc}$ is the SuperCOSMOS instrumental magnitude) was plotted to
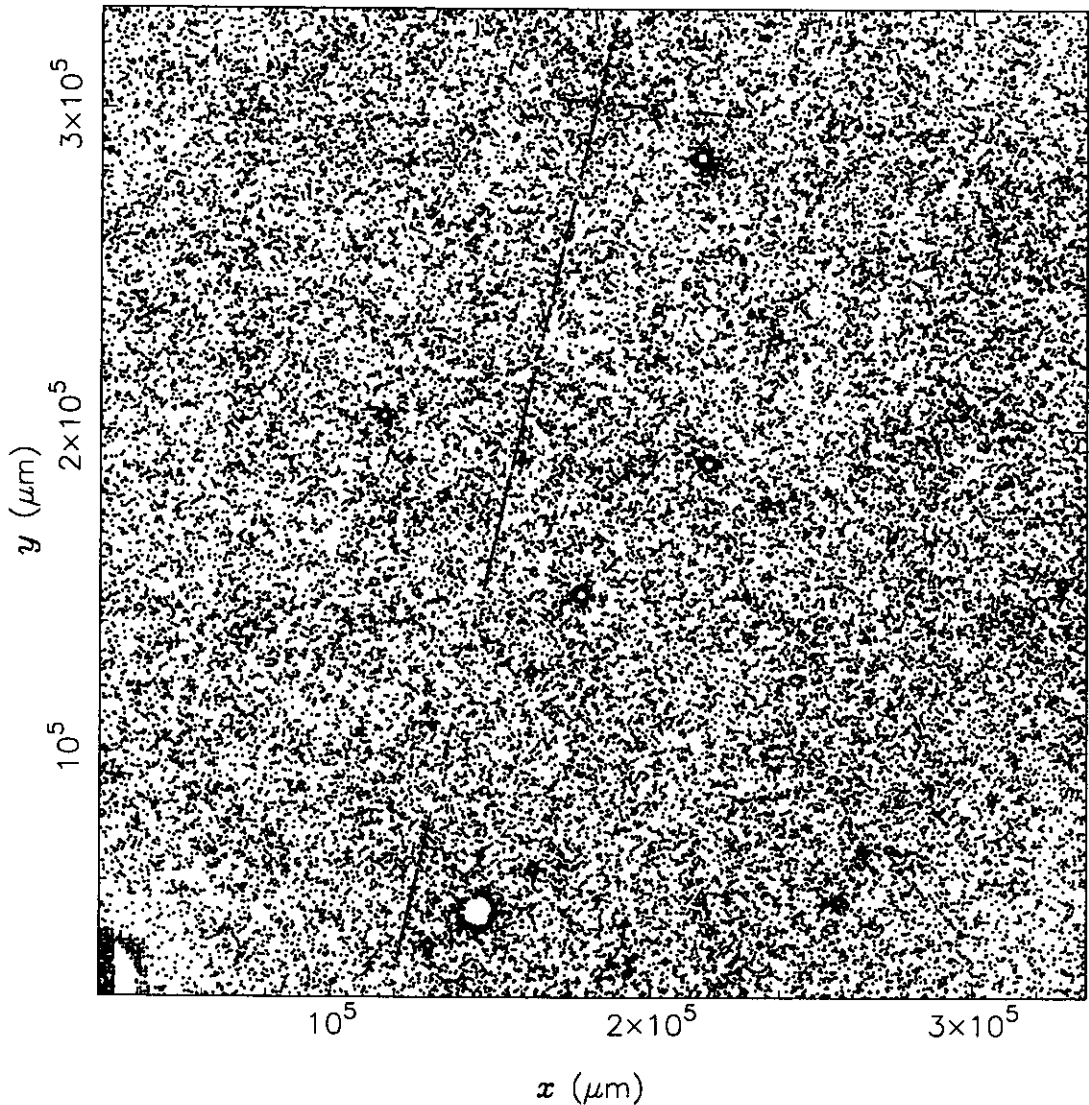
**Figure 3.1.** Positions in plate coordinates of faint objects in the SuperCOSMOS IAM database for plate J16115 (ESO/SERC field 1000), selected on the SuperCOS-MOS instrumental magnitude $-21 \leq m_{sc} \leq -20$ (corresponding to photometric magnitudes $21.5 \lesssim b_J \lesssim 22$). There are 49380 objects shown, of which many are artifacts (the total number of objects in this plate database is 205084). The large empty circles are due to bright stars, which show concentrations of artifacts at their boundaries. The two almost-parallel lines running from top to bottom are probably satellite trails. The short, nearly horizontal lines near the top centre are probably due to a meteor. The smudge in the bottom left-hand corner is due to the plate densitometry step wedge. The magnitude range shown here has been deliberately chosen to be fainter than that observed to emphasize the artifacts, although examination of the data in the observed magnitude range also shows the presence of artifacts. Compare this figure with Fig. 3.2.

determine the range of instrumental magnitudes in the data and to check for anomalies. Slices through the data, cut over small magnitude ranges at bright and faint magnitudes, were plotted to look for number-count density inhomogeneities, emulsion flaws and any other major defects not amenable to calibration. Nearly every plate was found to have some obvious defects, examples of which can be seen in Fig. 3.1. In cases where the data were found to be unacceptable, our approach was to request re-measurement of the plate or re-reduction of the mapping-mode data (with different thresholds, etc.) until better-quality data were obtained. If insufficient improvements were achieved, then a different plate of the same field was tried. If no existing plate was available, a new exposure was requested.

For the 1996 and 1997 observations, plate measurements were made during the commissioning phase of the SuperCOSMOS project, and some of the problems apparent in the SuperCOSMOS data could not be resolved. In particular, its ability to successfully measure consistent instrumental magnitudes from plates with high photographic density was poor. Some of these problems were traced to faulty electronics, while others were resolved when the plate illumination lamp was improved (H.T. MacGillivray, private communications, 1995 December 5, 1996 January 22, 1998 February 5). Subsequent re-measurement of the problematic plates was commenced for the 1998 observations, with a dramatic improvement in the quality of the magnitude data. This is discussed further in §3.4.

### 3.2.3 Pairing of plate databases

Despite an excellent ability to identify all real celestial objects above the plate magnitude limit, many records (often the majority) in an individual SuperCOSMOS plate database come from artifacts, e.g. diffraction spikes around bright stars, satellite trails, plate densitometry step wedges and photographic flaws, as seen in Fig. 3.1. To isolate just the celestial objects, the logical intersection of the sets of objects in the SuperCOSMOS databases from the four plates of each field was formed by using the Starlink CATPAIR code (Davenhall 1998a) to 'pair' the objects that coincide within a 2 arcsec radius on each of the plates. First the J plates were paired, then the U plates, then the paired J and U databases were paired on the 'master' J and U pair positions (see tables 3.1–3.3 for the choice of master plates used). This resulted
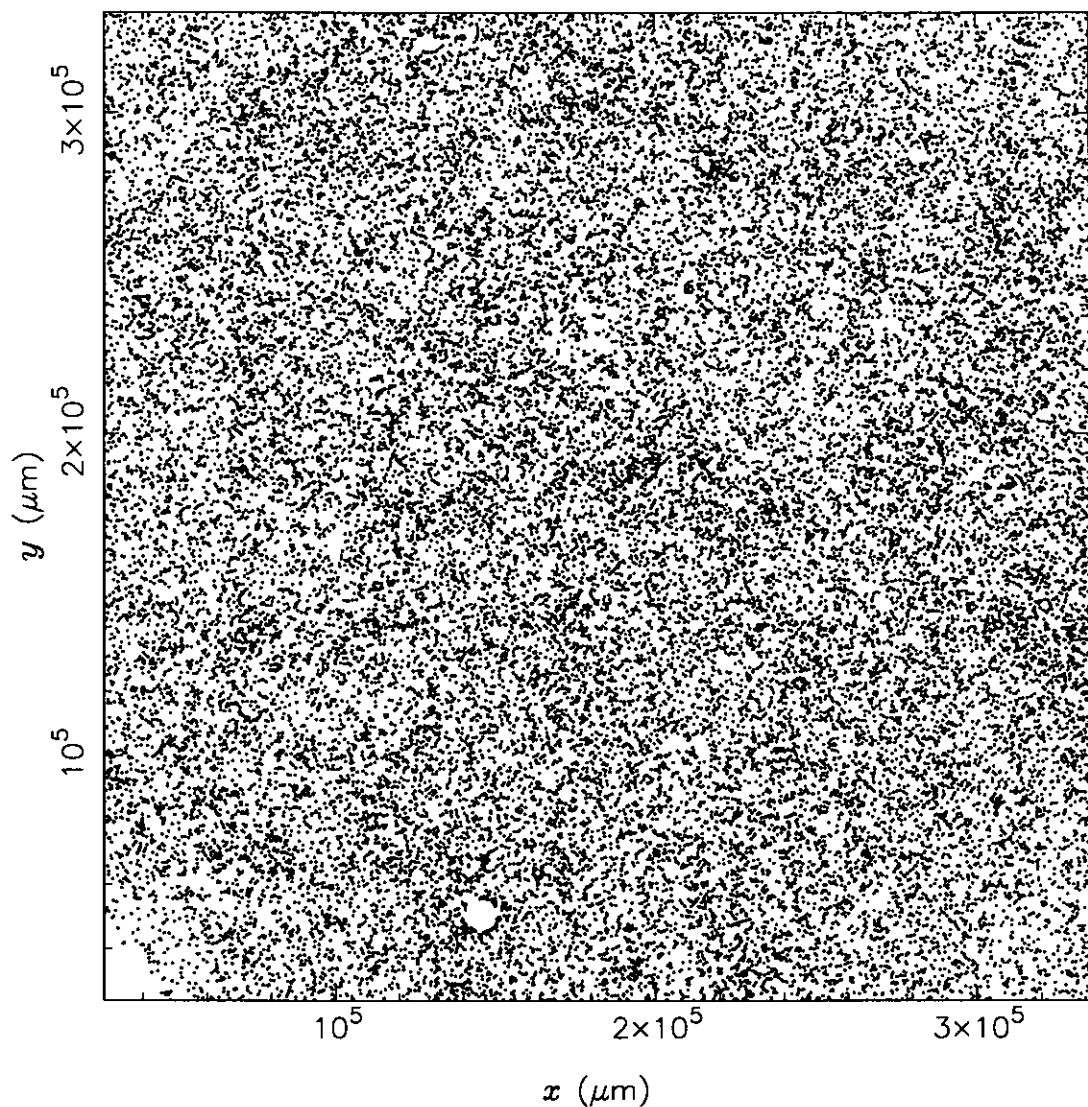
**Figure 3.2.** Positions in plate coordinates of faint objects in the SuperCOSMOS database resulting from pairing plates J16115 and J17034, selected on the same instrumental magnitude range as the objects shown in Fig. 3.1. There are 36523 objects shown out of a total of 151154 objects in the paired database. Note how almost all of the artifacts obvious in Fig. 3.1 have been removed, leaving a very high fraction of points marking celestial objects.

in final databases of 'stacked' plates holding $\sim 5 \times 10^4$ objects per field, where each object was detected on all of the four plates in the stack. It is very unlikely that an artifact position on one plate is correlated with an artifact position on all of the other plates in the stack, so this process removed almost all artifacts and left only celestial objects. This is clearly seen by comparing Figs. 3.2 and 3.1, which shows the effect of pairing the J plates.

### 3.2.4 Star-galaxy separation

An original defining characteristic of a quasar was that it has a *quasi-stellar* (i.e. star-like) image, so in order to optimize the use of telescope time, it has been common practice to try to exclude objects with non-stellar images from optically-selected spectroscopic surveys for quasars. Where the optical source material has been digitized, the usual process has been to reject objects that the measuring machine image analysis software has classified as non-stellar in appearance. As examples, this method was used to create input catalogues from APM measurements for the FIRST (Gregg et al. 1996) and 2dF (Croom 1997) surveys, from COSMOS measurements for the FOCAP (Boyle et al. 1990), Edinburgh Multicolour (Goldschmidt et al. 1991) and MEFOS (La Franca et al. 1998) surveys, and from MAMA measurements for the NGP ultraviolet-excess (Moreau & Reboul 1995) survey. Is this a sensible approach, and are star-galaxy separation methods reliable?

Rejection of candidates with non-stellar appearances may select against quasars, because (a) the host galaxies of $z \lesssim 0.5$ quasars might be visible on plates with faint limiting magnitudes such as those used here, (b) the quasar might be gravitationally lensed into multiple but unresolved components or (c) the quasar might lie close to a foreground object. Any of these situations could lead to a non-stellar classification [see e.g. Hewett et al. (1995), Köhler et al. (1997)]. It is less likely that $z \gtrsim 0.5$ quasar host galaxies would be visible, so this selection bias would be small in the CUQS which is designed in any case to select quasar candidates with redshifts in the range $0.4 \leq z \leq 2.2$. However, where the quasar is unresolved from a galaxy, the stellar photometric calibration used here can give erroneous magnitudes because point images are in general centrally saturated while galaxy images are not.

The reliability of star-galaxy separation methods was examined by considering two methods applied to a single UKST plate: J10128, a high-grade ESO/SERC survey plate in field 927 used in the CUQS (see table 3.1). The SuperCOSMOS analysis software classifies an object as a star or galaxy based on its position in a 3-dimensional parameter space based on measures of image geometry, area and surface brightness profile (Heydon–Dumbleton et al. 1989). The APM facility uses a similar approach but based on an 11-D parameter space: integrated object magnitude, area measured at 8 isophotal levels, peak intensity and image radius of gyration (Maddox

**Table 3.5**: Comparison of object classification made by the SuperCOSMOS and APM methods for plate J10128, for objects found in common by both machines. The upper table is arranged by SuperCOSMOS classification, and the lower table by APM classification. The percentages in the left half of the tables are the relative fractions of total objects classified, e.g. in line 1, 17 per cent of the objects were classified by SuperCOSMOS as galaxies. The percentages in the right half of the tables are the corresponding fraction for the other classification scheme, e.g. in line 1, APM classified as stellar 28 per cent of the 28297 objects that SuperCOSMOS classified as galaxies.

| SuperCOSMOS classification | No. of objects | % of total | APM Classification | | | | | | | |
| --- | --- | --- | --- | --- | --- | --- | --- | --- | --- | --- |
| | | | Stellar | | Non-stellar | | Merged | | Noise | |
| | | | No. | % | No. | % | No. | % | No. | % |
| Galaxy | 28297 | 17 | 8014 | 28 | 17563 | 62 | 2696 | 10 | 24 | <1 |
| Star | 63145 | 38 | 50358 | 80 | 6438 | 10 | 3407 | 5 | 2942 | 5 |
| Faint | 73313 | 44 | 42292 | 58 | 22578 | 31 | 5420 | 7 | 3023 | 4 |
| Junk | 11 | <1 | 2 | 18 | 4 | 36 | 1 | 9 | 4 | 36 |
| Substructure | 402 | <1 | 120 | 30 | 33 | 8 | 242 | 60 | 7 | 2 |
| Total | 165168 | | 100786 | | 46616 | | 11766 | | 6000 | |

| APM classification | No. of objects | % of total | SuperCOSMOS Classification | | | | | | | | | |
| --- | --- | --- | --- | --- | --- | --- | --- | --- | --- | --- | --- | --- |
| | | | Galaxy | | Star | | Faint | | Junk | | Substr. | |
| | | | No. | % | No. | % | No. | % | No. | % | No. | % |
| Stellar | 100786 | 61 | 8014 | 8 | 50358 | 50 | 42292 | 42 | 2 | <1 | 120 | <1 |
| Non-stellar | 46616 | 28 | 17563 | 38 | 6438 | 14 | 22578 | 48 | 4 | <1 | 33 | <1 |
| Merged | 11766 | 7 | 2696 | 23 | 3407 | 29 | 5420 | 46 | 1 | <1 | 242 | 2 |
| Noise | 6000 | 4 | 24 | <1 | 2942 | 49 | 3023 | 50 | 4 | <1 | 7 | <1 |
| Total | 165168 | | 28297 | | 63145 | | 73313 | | 11 | | 402 | |

et al. 1990). A SuperCOSMOS scan of J10128 identified 216856 objects on the plate, while an APM scan identified 189744 objects. Pairing the two databases using the Starlink CATPAIR code found 165168 object identifications with positions common to ≤ 2 arcsec. A summary of the classifications of these common objects is shown in table 3.5. It is immediately clear that a high proportion of objects were given contradictory classifications. In particular, of the 28297 objects classed as galaxies by SuperCOSMOS, APM found 8014 to be stellar. Conversely, of the 46616 objects classed as non-stellar by APM, SuperCOSMOS found 6438 to be stellar. The differences suggest that one or both of the star-galaxy separation methods is producing erroneous results at the 15–30 per cent level.

These results suggest that simple acceptance of either the SuperCOSMOS or the APM stellar classifications could lead to considerable incompleteness in the final survey due to missed stellar objects, in addition to any quasars excluded because

of their truly non-stellar appearance. Indeed, this might be a source of some of the incompleteness detected by Graham et al. (1999) in earlier surveys. Boyle et al. (1987) estimated that $< 5$ per cent of the APM stellar classifications were incorrect based on a visual examination of some of the source plates used for the FOCAP survey, which points at the SuperCOSMOS classifications as being problematic, but it is not obvious how to conclusively decide which method is the better without extensive observational testing – the F345 complete spectroscopic sample may provide some clues.

It was decided that the SuperCOSMOS object classification would not be used as a candidate selection criterion. Instead, the available surface density of fibres provided by the Fruit & Fiber instrument at Las Campanas Observatory (see chapter 4) was exploited to observe *all* ultraviolet-excess candidates regardless of SuperCOSMOS star-galaxy classification. In the future, artificial neural network classifiers, working directly on the SuperCOSMOS mapping-mode data, may provide a more reliable solution [see e.g. Bazell & Peng (1998), Bertin & Arnouts (1996) and Odewahn et al. (1993)]. However, the volume of data in SuperCOSMOS mapping mode ($> 2$ gigabytes per plate) is several orders of magnitude larger than in image analysis mode, so it may make sense for these classifiers to be integrated into the SuperCOSMOS system itself.

## 3.3 Astrometric calibration

### 3.3.1 Accuracy required for fibre-input spectroscopy

What accuracy is required in the positions of candidates for observations using fibre-input spectrographs? More specifically, what are the effects on signal collection efficiency of astrometric inaccuracies and seeing conditions? Surprisingly, no formal analysis of these questions was found in the literature, so they will be addressed here first.

With perfect astrometry, telescope guidance and seeing conditions, and sufficiently wide fibres, essentially all the incident energy in the image of a survey candidate will fall into the appropriate spectrograph input optical fibre whose aperture is located in the telescope focal plane. In practice, the fibre size has been chosen

as a compromise influenced by factors which include the telescope focal ratio, the expected seeing disk size and the desire to minimize contamination of the object spectra with sky light. The focus of this analysis is therefore on the effects of seeing disk size and position errors for given fibre sizes.

First, an expression for the fraction of the image energy falling into a circular fibre of radius $R$ centred at position $(0,0)$ is derived. A telescope point spread function in the form of a 2-dimensional Gaussian, $g(x,y)$, centred at $(x_c, 0)$, with circular cross section and unit integral is assumed. Note that this ignores coma and other distortions in the telescope image. The standard deviation of the Gaussian, $\sigma$, is determined by the size of the seeing disk. The fraction of the total incident energy falling into the fibre, $f(x_c)$, is then given by the integral of $g(x,y)$ over the fibre aperture, i.e.

$$f(x_c) = \int_{x=-R}^{R} \int_{y=-\sqrt{R^2-x^2}}^{+\sqrt{R^2-x^2}} g(x,y)\, dy\, dx \tag{3.1}$$

where

$$g(x,y) = \frac{1}{2\pi\sigma^2} \exp\left(\frac{-(x-x_c)^2}{2\sigma^2}\right) \exp\left(\frac{-y^2}{2\sigma^2}\right).$$

Eqn. 3.1 can be simplified to

$$f(x_c) = \frac{1}{\sqrt{2\pi}\sigma} \int_{-R}^{R} \exp\left(\frac{-(x-x_c)^2}{2\sigma^2}\right) \operatorname{erf}\left(\frac{\sqrt{R^2-x^2}}{\sqrt{2}\,\sigma}\right) dx \tag{3.2}$$

where erf is the error function. There is no analytic solution to Eqn. 3.2, so it must be evaluated numerically.

For the LCO instrument, the fibre diameter is 320 $\mu$m, or 3.5 arcsec on the sky (Shectman 1993). Fig. 3.3 shows $f(x)$ for the typical seeing disk sizes of 1.8 $\pm$ 0.4 arcsec FWHM[1] that were measured at LCO during CUQS observations. For good seeing, > 98 per cent of the energy from a centred image enters the fibre, but this is reduced to < 50 per cent for position errors of $\gtrsim$ 1.6 arcsec. This determines the required astrometric accuracy: in average seeing conditions at LCO, position errors of $\leq 1$ arcsec are sufficient to get $\geq 75$ per cent of the image energy into the fibre. Note that it is the rate of change in the position error across the 1°5-diameter observed telescope field that is important in this application. The mean cumulative position error for each tile is removed at the telescope by centring the tile on a

---

[1]Note that $\sigma = \text{FWHM}/2\sqrt{\ln 4}$.
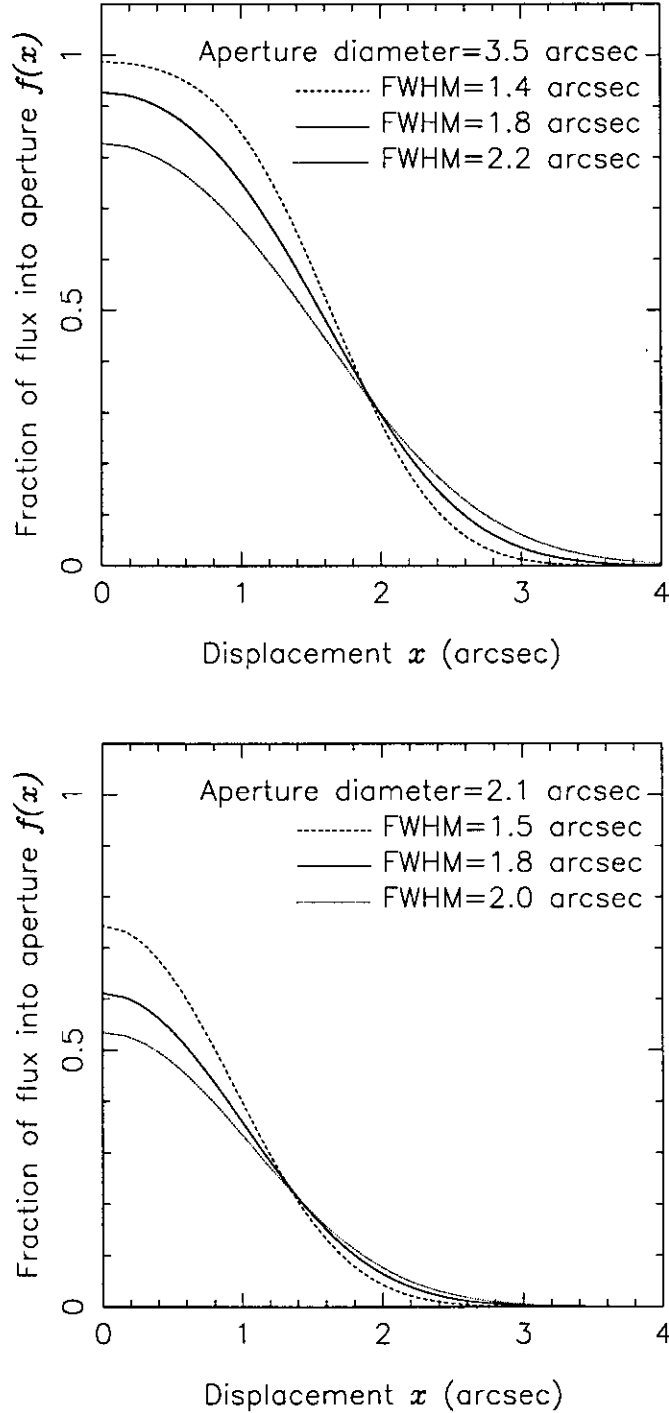
**Figure 3.3.** Fraction of light falling into a circular aperture from a displaced image with a Gaussian point spread function of circular cross section, as a function of displacement between the centres of the aperture and the image. The upper panel is for the 3.5 arcsec-diameter fibres used on the Fruit & Fiber instrument, with the range of seeing disk sizes recorded at Las Campanas Observatory during the observations reported in this thesis. The lower panel is for the 2.1 arcsec-diameter fibres used on the 2dF instrument on the Anglo-Australian Telescope, for the typical seeing disk sizes observed by Ryan & Wood (1995).

guide star. Note also that this defines the required accuracy of the fibre position in the telescope focal plane. The uncertainties in the final position come from many sources other than the SuperCOSMOS calibration, including the conversion from sky to plug-plate coordinates, the plug plate flex, centring and rotation on the telescope, differences between the temperature at which the plug plate was drilled and that at which the observations were made, differences between the planned and observed air mass and differential atmospheric refraction, and changes in plate scale with telescope focus (Barden & Massey 1988).

It is interesting to compare the LCO figures with those predicted by Eqn. 3.2 for the 2.1-arcsec fibres used on the 2dF fibre spectrograph on the AAT, using the typical 1.5–2.0 arcsec median seeing conditions recorded there (Ryan & Wood 1995). As can be seen in Fig. 3.3, the 2dF fibre size is too small to be efficient in all but the best seeing conditions recorded at the AAT, and that achieving even 50 per cent efficiency in average seeing conditions requires positions with $\lesssim$ 0.6 arcsec accuracy.

### 3.3.2 Sources of position error in digitized UKST data

There are at least four possible sources of errors in the positions assigned to objects on digitized Schmidt plates, most of which have been reviewed in detail by Evans (1988). First, there are errors introduced by the digitization process due to inaccuracies in the measuring machine. However, these errors are known to be very small ($\sim$ 0.15 $\mu$m equivalent to $\sim$ 0.1 arcsec) for SuperCOSMOS (Hambly et al. 1998).

Second, there are problems in determining the centroid of images on a Schmidt plate due to image shape distortion at the focal surface of the telescope, the bending of the plate during exposure, the nature of the emulsion and its developing process. This problem is acute for the relatively bright astrometric reference stars ($\lesssim$ 12 mag) which are saturated on the plates used here, and is naturally worse at the periphery of the plates, where the image shape distortion is greatest.

Third, the whole-plate astrometric fitting method inevitably means that the fit is better constrained in the centre of the plate than at the edges, because of the larger number of astrometric standard stars surrounding each point. This could possibly be improved upon by deriving separate fits for each observed tile, but the corresponding loss of accuracy because of the small number of standard stars in each

tile probably outweighs any gain.

Fourth, there are errors due to faults in the software that derives the $(x, y) \rightarrow (\alpha, \delta)$ mapping. Quality control checks applied to early SuperCOSMOS data showed an anomalous but systematic position error distribution that led to the discovery of incorrect proper-motion corrections in the SuperCOSMOS software (H.T. MacGillivray, private communication, 1996 January 31).

### 3.3.3 Calibration

The SuperCOSMOS data as delivered include J2000 $(\alpha, \delta)$ positions derived from a 9-parameter fit to the $(x, y)$ plate centroid positions of PPM catalogue stars (Röser & Bastian 1991; Bastian & Röser 1993). The astrometric solutions are found by a modified version of the algorithm used by the Starlink ASTROM code (Wallace 1994). A single fit is used for the whole plate (Davenhall 1998b), but the plate data do not include details of the stars used or the quality of the fit.

From a comparison of the positions assigned by SuperCOSMOS to common objects in the data from overlapping plates in adjacent fields, it was found that the position difference vectors varied smoothly in magnitude and direction across each plate and that the *mean* rate of change in position differences should have been small enough ($< 1$ arcsec deg$^{-1}$) to keep all the candidates on the fibers in each observed tile. For the 1996 observations, therefore, the positions used in the observations were all taken directly from the SuperCOSMOS plate catalogues. All of the 1996 tiles were near the centres of fields 927 (programme area) and 438 (control area), and show consistent signal levels across each tile.

A problem arose, however, at the plate boundaries, where the difference between the cumulative position errors from the two plates became important. For a single observed tile to cross the boundary between adjacent plates, positions must be taken from both plate databases. Such tiles were first observed in the 1997 observing run. The simplistic approach used for the 1997 observations was to choose straight lines of constant $\alpha$ or $\delta$ as the boundaries of data to be chosen from the separate plate databases (see §4.3.1 for details of the boundaries used). Object data from the rectangular bounded subsets were then merged, and survey candidates and guide stars were selected from the merged data set. In practice, the 1997 observa-

41

tions showed that this approach was unacceptable. Exposures of tiles 1997.2.1 and 1997.2.3 (which cross boundaries near the corner touched by fields 927, 928, 999 and 1000) produced almost no signal above sky. Tile 1997.3.1 (also near the same corner) produced detections only in the north-west quarter of the tile. See table 4.2 for the observational details of these exposures.

This plate-boundary problem may be formally characterized in terms of position difference vectors, defined as $\Delta P = \{(\alpha_A, \delta_A), (\alpha_B, \delta_B)\}$, where A and B identify two overlapping plates, and the $(\alpha, \delta)$ are the astrometric positions of a single object identified on those plates. The $\Delta P$ distribution for the SuperCOSMOS positions from typical plates has an r.m.s. vector length of 0.9 arcsec, which should have been marginally acceptable. However, a more detailed examination of the $\Delta P$ distribution as a function of position on the plate (Fig. 3.4) shows very steep local gradients, $\nabla . \Delta P \simeq 3$ arcsec deg$^{-1}$, which are $\sim 3$ times the mean gradient. Even with smoothing (Fig. 3.5), these gradients are too large to allow all the fibres across a tile of diameter $1^\circ\!.5$ to be simultaneously well illuminated. The gradients are strongest near the corners of the plates, in agreement with locations of the problematic tiles. The gradients cause further problems if the guide stars for a tile are chosen from the different plates (see §4.3.3).

Two methods to improve the astrometric calibration and circumvent this problem were tried. For both, the Tycho catalogue of highly accurate positions from the *HIPPARCOS* mission was used (Hog et al. 1997). The Tycho catalogue provides a greater surface density of standard stars than the PPM catalogue, e.g. in field 927, there are 268 suitable Tycho standards compared with the 173 PPM stars used by SuperCOSMOS. The Tycho catalogue also reaches fainter magnitudes than PPM, reducing the problems due to the difficulty of finding the centroid of saturated images. Only Tycho stars with complete data and high quality ($Q \leq 5$) were selected.

First, the Starlink ASTROM code (Wallace 1994) was used to obtain a plate solution. ASTROM uses the observed zenith distance to correct for differential atmospheric refraction, then makes a 9-coefficient fit (radial distortion; plate centre, zero points and scales in $x$ and $y$; orientation; non-perpendicularity) to the plate and reference positions of all the astrometric standard stars, then applies the fit to the
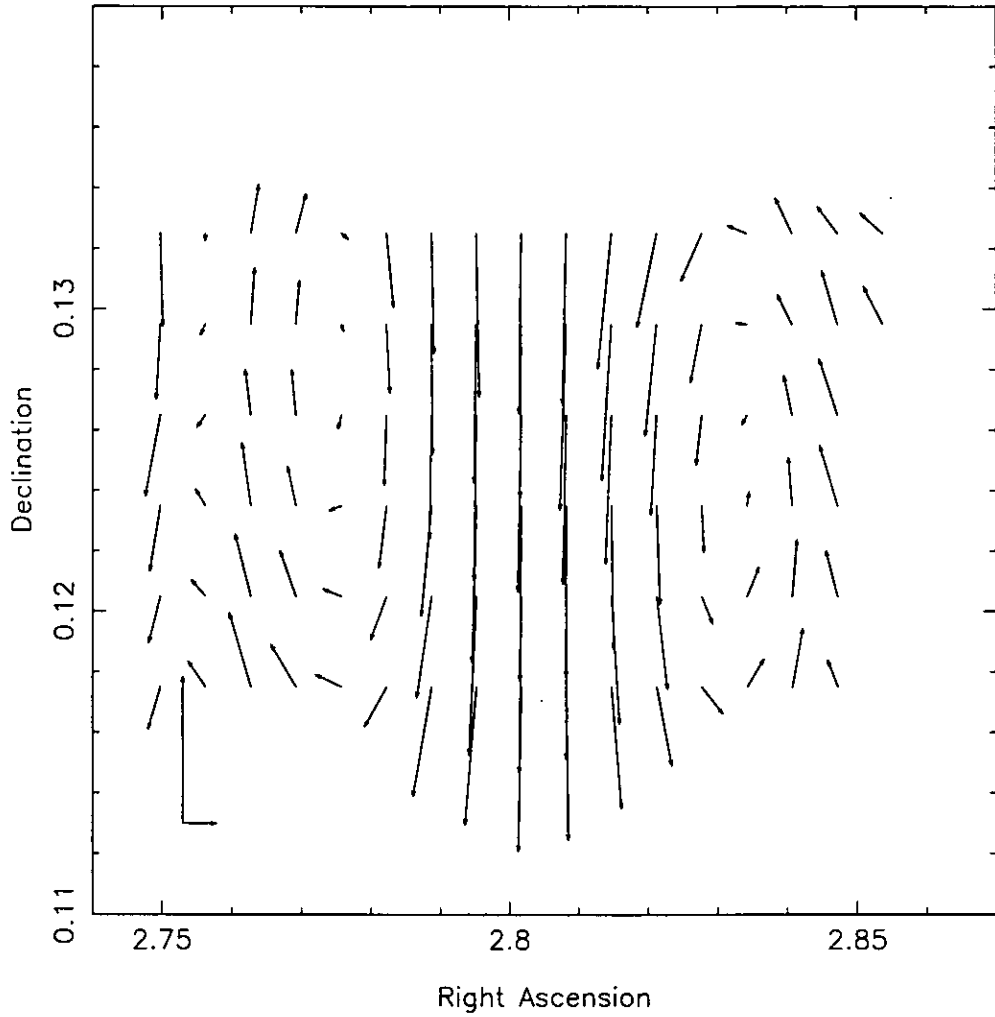
**Figure 3.4.** Mean $\Delta P$ for the SuperCOSMOS positions of 5397 objects in the overlap between fields 927 and 999. Each arrow shows the mean $\Delta P$ for a bin centred at the base of the arrow. The axes are marked in radians. Note that the scales in $\alpha$ and $\delta$ are different: the pair of arrows in the lower left corner are 1 arcsec in length and point in the positive $\Delta P$ direction.

Right Ascension fit          RA range =  2.752,  2.852
Smoothed                     Dec range =  0.117,  0.132
Degree of fit (X, Y) =  7,  3    Z range = -0.497,  0.207 arcsecs
Cells in (X, Y) = 20, 10     Plot elevation, rotation =  55, 230
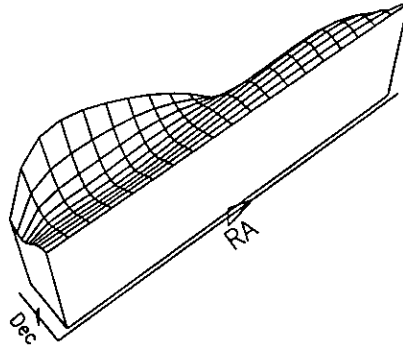


Declination fit              RA range =  2.752,  2.852
Smoothed                     Dec range =  0.117,  0.132
Degree of fit (X, Y) =  7,  3    Z range = -1.144,  0.319 arcsecs
Cells in (X, Y) = 20, 10     Plot elevation, rotation =  55, 230
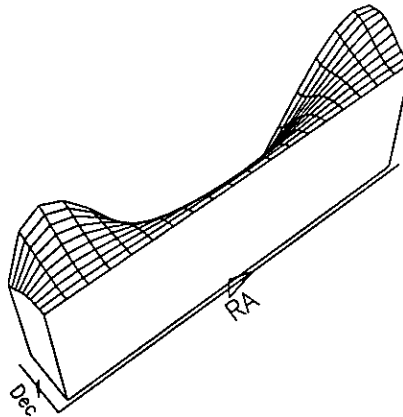


**Figure 3.5.** The smoothed $\Delta P$ values from Fig. 3.4. The $z$ axis shows the magnitude of the $\Delta P_{\text{smooth}}$ component in the $\alpha$ (upper panel) and $\delta$ (lower panel) directions. At the field 927 edge of the overlap (low $\delta$), $\Delta P_{\text{smooth}}$ is set to zero, and orthogonal polynomials have been fit in the $\alpha$ and $\delta$ directions to produce a surface that smoothly joins the positions from the two plates.

unknown object positions. The plate boundary position differences between plates calibrated by ASTROM are shown in Fig. 3.6. They follow the same pattern as the SuperCOSMOS differences, with little difference in amplitude or gradient.

The second method was based on the POLYASTR code (R.G. Clowes, private communication, 1997 December 5). POLYASTR fits an $n$-th degree polynomial in $x$ and $y$ to each of the $(\alpha, \delta)$ reference star positions, then applies the fit to the unknown object positions. This is sufficient for small areas of a plate, but leaves large uncorrected distortions when fit to the whole plate. To improve on this, the code was modified (POLYASTRX) to include the $x^m y^n$ ($m, n \geq 0$) cross terms in the polynomial. Fits of 4th degree polynomials (i.e. up to terms in $n + m = 4$) produced results comparable in form to the SuperCOSMOS and ASTROM methods, with amplitude almost identical to the ASTROM method (Fig. 3.6). The r.m.s. error between the standard and fit positions for the whole plate was 0.601 arcsec, but the maximum $\nabla.\Delta P$ was steeper than SuperCOSMOS. No significant improvement in the r.m.s. error was gained by increasing the polynomial to 5th degree, but this is clearly a function of the number of reference stars available. Robichon et al. (1995), using a similar approach to use Tycho stars to calibrate Schmidt plates digitized by the MAMA machine at the Centre d'Analyse des Images in Paris, found a significant improvement with 5-th degree polynomials when using $\sim 4$ times more reference stars. However, the plates used by Robichon et al. were short exposures ($\sim 15$ min) and so had more reference stars for which good centroids could be found. For polynomials of 6th or higher degree, the POLYASTRX fit was poorly constrained.

A separate limiting factor in the accuracy of the astrometry is the uncertainty in the proper motions in the Tycho catalogue, which are typically of the order of $\pm 0.05$ arcsec $\text{yr}^{-1}$. This is larger than the value of the proper motion for most of the reference stars. The parallax values are similarly uncertain for all but the brightest stars in the Tycho catalogue (Hog et al. 1997). The base epoch of the Tycho data is J1991.25. The epoch of the plates used here ranges from 1976.4 to 1996.2, so the cumulative uncertainty from proper motion is as large as $\sim 0.75$ arcsec (cf. the Robichon et al. plate epochs which range from 1992.9 to 1993.6). When the Tycho proper motions and parallaxes were included in the ASTROM fits, there was a strong correlation between the plate epoch and the r.m.s. error. Omitting
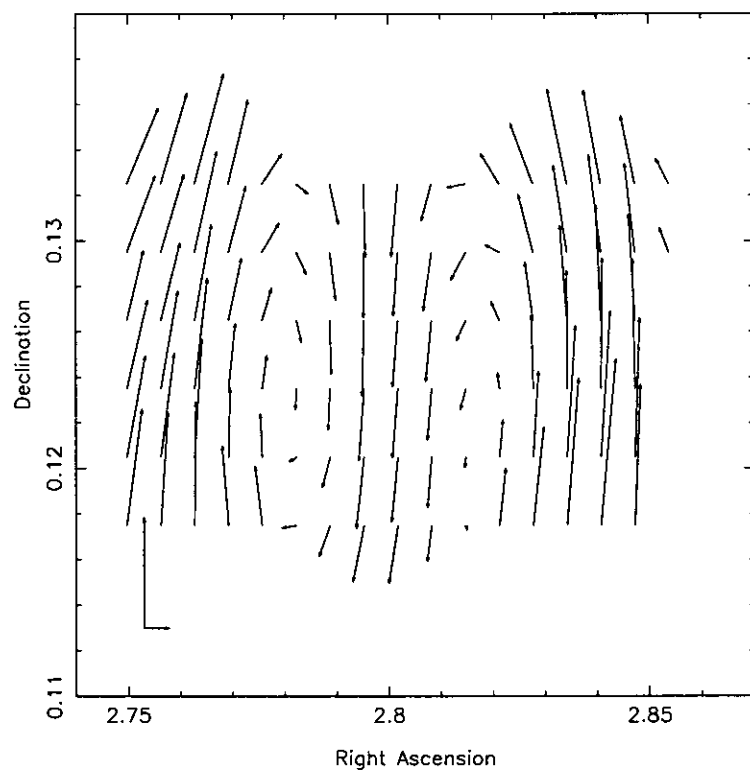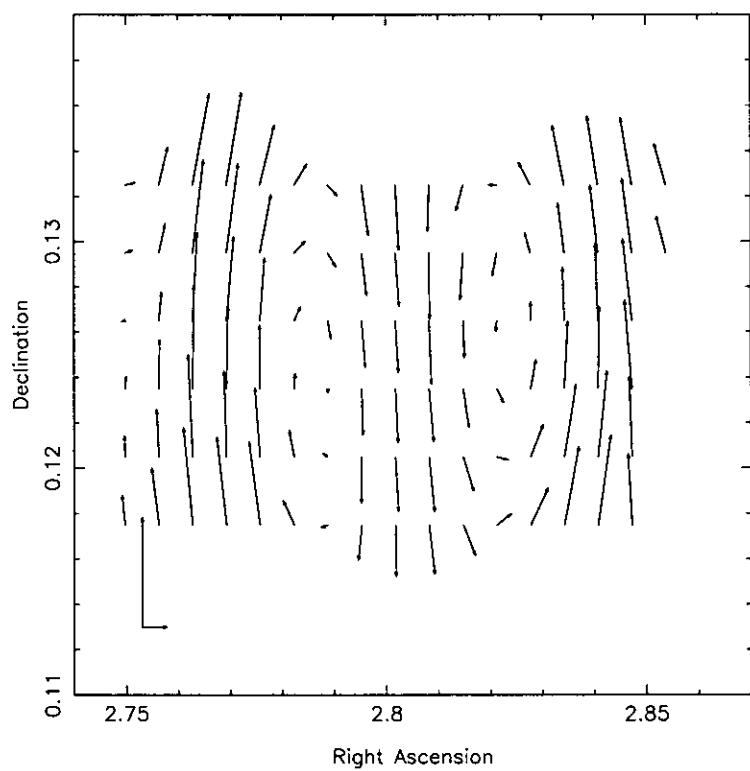
**Figure 3.6.** Mean $\Delta P$ for ASTROM positions (upper panel) and POLYASTRX positions (lower panel), as for Fig. 3.4.

46

the proper motions and parallaxes from the fit removed the correlation (Fig. 3.7) without significantly increasing the minimum r.m.s. error.

The principle conclusion is that none of the methods examined – SuperCOSMOS, ASTROM and POLYASTRX – is satisfactory for the task of astrometric mapping across plate boundaries. Each produces a maximum $\nabla.\Delta P$ in plate overlap areas that is too steep for use with tiles that overlap plate boundaries. A second conclusion is that simple and efficient polynomial fitting codes (with cross terms) provide positions almost as good as ASTROM-type methods which try to model the telescope field from an engineering point of view. It is interesting to note that the problem could have been eased if the ESO/SERC survey fields had been designed to have larger overlaps between adjacent fields. The current overlap is $\sim 0°\!.8$ (after digitization). A larger overlap, $\sim 1°\!.5$, would have allowed sufficient smoothing of the $\Delta P$ distribution to be useful here, at the cost of an increased number of UKST fields needed to cover the sky.

The final decision with respect to the 1998 observations was to avoid the problem entirely and have no observed tiles with positions taken from more than one plate (see §4.3.2). The ASTROM positions were chosen, because (a) it was known that problems had been encountered while using the SuperCOSMOS positions in the 1997 observations, (b) ASTROM provides better slightly absolute accuracy than SuperCOSMOS (mainly through the use of more and better standard star positions), and (c) the SuperCOSMOS method is still partially a 'black box' for which incomplete information was known, whereas the ASTROM method and data were well understood. The r.m.s. error between the standard and fit positions on each reference plate is $\leq 0.861$ arcsec and the mean for all plates is $0.69 \pm 0.09$ arcsec.

### 3.3.4 Future improvements

An underlying problem that has not been addressed here is the conflict between the magnitude of astrometric calibration stars and the saturation of bright stars on deep UKST plates. The same conflict arises in choosing telescope guide stars (§4.3.3). New and improving faint astrometric catalogues such as the USNO-A (Monet 1997) may provide one solution. Another solution would be to make short (and hence unsaturated) UKST exposures of the same field as the main survey plates, and use

47
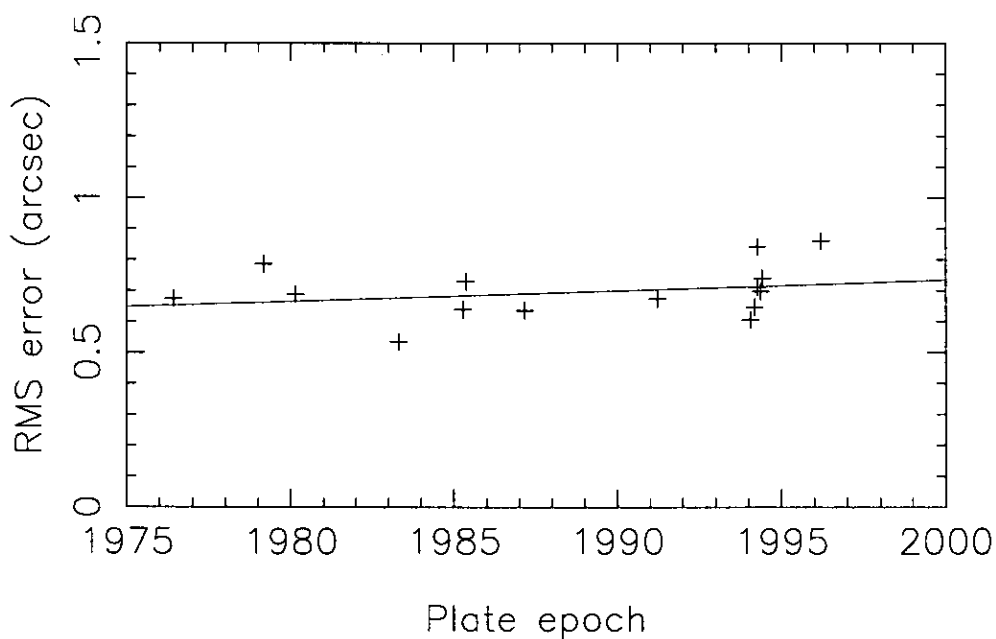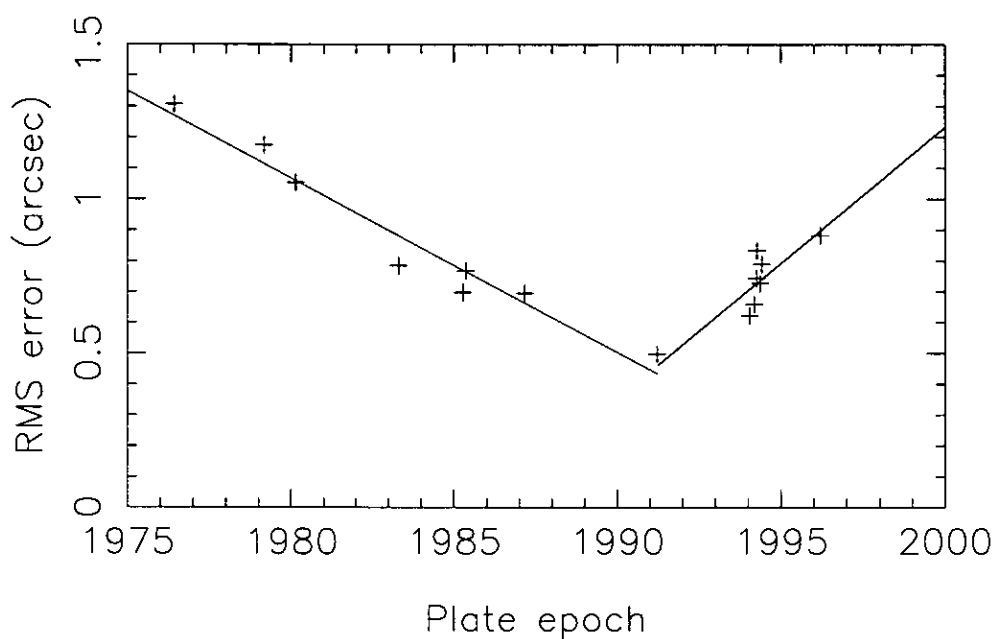
**Figure 3.7.** Upper panel: points show the ASTROM r.m.s. error for each master UKST J plate in the 15 ESO/SERC fields, against plate epoch, where the Tycho proper motions and parallaxes are included in the fit. The lines are least-squares fits to the points, divided into pre-1991.25 and post-1991.25 sets. Note that the lines cross almost exactly at 1991.25 – the Tycho catalogue epoch. Lower panel: points as upper panel, with proper motion and parallaxes excluded from the fit. The line is a least-squares fit to all the points.

these to bootstrap an astrometric solution for the deep plates. Given more time, it would also be interesting to pursue mathematically more complex methods for providing smooth astrometric calibration across plate boundaries such as those of Eichhorn (1960) and Taff et al. (1990).

A possible novel solution to the problem of finding the centroid of bright stars, yet to be tried, would be to fit low-order polynomials to the diffraction spikes that appear on the plates and then use the intersection of the curves to define the image centre.

## 3.4 Photometric calibration

### 3.4.1 Photometric systems and notation

The literature contains many vague definitions of the magnitude systems used in different studies, and there is a resulting lack of clarity in conversion of their measurements to standard photometric systems. A rigorous derivation of the system used here is presented to attempt to improve the situation.

The integrated flux, $\ell_f$, of an object is defined in terms of the intrinsic object flux density (corrected for atmospheric extinction), $\ell_I(\lambda)$, when measured through a specified passband, $f(\lambda)$, as

$$\ell_f = \int_0^\infty \ell_I(\lambda)\, f(\lambda)\, d\lambda \tag{3.3}$$

where $\lambda$ is the wavelength. The filtered astronomical magnitude, $m_f$, is then defined as

$$m_f = C_f - \frac{5}{2}\log \ell_f \tag{3.4}$$

where the constant $C_f$ sets the zero-point of the magnitude scale. A standard photometric system for communication of results in astronomy is Cousins' photoelectric $UBV$ system and its extensions, which is based on three specific filters with ultraviolet, blue and green (visual) passbands (Bessell 1990; Blair & Gilmore 1982, and references therein). For the $U$ and $B$ values of interest here, Eqn. 3.4 thus gives

$$
\begin{aligned}
U &= C_U - \tfrac{5}{2}\log \ell_U \\
B &= C_B - \tfrac{5}{2}\log \ell_B.
\end{aligned}
$$

The passbands of the filter and emulsion combinations for UKST plates used (§3.2.1) differ from the photoelectric passbands, leading to natural UKST magnitudes that will be denoted by $U_J$ and $B_J$, where the J is used here to indicate the use of the IIIa-J emulsion. These magnitudes are defined in like manner, as

$$
\begin{aligned}
U_J &= C_{U_J} - \tfrac{5}{2}\log \ell_{U_J} \\
B_J &= C_{B_J} - \tfrac{5}{2}\log \ell_{B_J}.
\end{aligned}
$$

The photometric sequences used in this thesis (§3.4.2) are calibrated to photoelectric $UBV$ magnitudes. Using photoelectric sequences to calibrate photographic observations, as done here, results in hybrid magnitudes, which will be denoted by $u_J$ and $b_J$. In this hybrid system, it is assumed that the integrated fluxes of calibration stars defined by the response of the UKST emulsion and filter passband combinations are equal to the integrated fluxes in the photoelectric system, i.e. $\ell_{B_J} = \ell_B$ and $\ell_{U_J} = \ell_U$ for each calibration star, but that the zero-points come from the photoelectric $U$ and $B$ systems. This gives the following hybrid relations, which are applied to both calibration stars *and* calibrated objects:

$$
\begin{aligned}
u_J &= C_U - \tfrac{5}{2}\log \ell_{U_J} = C_U - C_{U_J} + U_J \\
b_J &= C_B - \tfrac{5}{2}\log \ell_{B_J} = C_B - C_{B_J} + B_J.
\end{aligned}
\tag{3.5}
$$

The effect of the differences between the passbands of the photoelectric and photographic systems on the calibrated objects is now considered. In particular, for objects with typical stellar colours, there are well-calibrated equations that relate the natural UKST and $UBV$ systems (Blair & Gilmore 1982). For the passbands considered here, these are

$$
\begin{aligned}
U &= U_O + (0.03 \pm 0.05)(U - B), & -0.4 \le U - B \le 2.0 \\
B &= B_J + (0.28 \pm 0.04)(B - V), & -0.1 \le B - V \le 1.6
\end{aligned}
\tag{3.6}
$$

where the $U_O$ definition is based on IIa-O emulsion, not the IIIa-J (or 4415) emulsion on the U plates used here. The ultraviolet response of the IIa-O and IIIa-J emulsions is very similar (Boyle 1986), so the total passband of the images is principally defined by the UG1 filter and it is safe to take $u_J = U_O$. Also, note that the uncertainty in the $(U - B)$ colour factor is larger than the factor. Even though the colours of quasars, $-1.5 \lesssim U - B \lesssim -0.3$, are mostly outside the Blair & Gilmore (1982)

calibrated range, it is reasonable to assume that the colour term is still consistent with zero, so

$$U = u_J \tag{3.7}$$

can be adopted. On the other hand, the $B$ and $B_J$ passbands differ considerably. The $B$ passband peaks at $\sim 4300$ Å, is fairly symmetric and has a FWHM of $\sim 1000$ Å, while the $B_J$ passband peaks at $\sim 4000$ Å, is highly asymmetric (peaking on the short wavelength side), and has a FWHM of $\sim 1600$ Å. The colour term must therefore be included. Combining Eqns. 3.5 and 3.6 gives

$$B = b_J - (C_B - C_{B_J}) + 0.28(B - V). \tag{3.8}$$

Now, as noted above, a hybrid system is being used. In transferring the photoelectric calibrations to the photographic observations, the difference in the passbands have been ignored and $b_J = B$ has been taken for the calibration stars. The calibration stars have mean colour $(B_C - V_C)$. Hence Eqn. 3.8 gives

$$(C_B - C_{B_J}) = 0.28(B_C - V_C)$$

so

$$B = b_J + 0.28[(B - V) - (B_C - V_C)]. \tag{3.9}$$

The mode of the colour distribution of the actual calibration stars used here is $(B_C - V_C) = 0.7 \pm 0.1$. The final relation for this calibration of photoelectric $B$ magnitudes is then found by substituting this value into Eqn. 3.9,

$$B = b_J + 0.28(B - V - 0.7). \tag{3.10}$$

If a mean colour of $B - V \simeq 0.3$ is assumed for $z \lesssim 2.2$ quasars (Smith 1983; Boyle 1986), then Eqn. 3.10 gives the relations for CUQS quasars as

$$\begin{aligned} B &= b_J - (0.1 \pm 0.1) \\ U - B &= (u_J - b_J) + (0.1 \pm 0.1) \end{aligned} \tag{3.11}$$

where the uncertainties include an allowance for the considerable scatter about the mean $B - V$ colour due to the relative positions of emission lines and photometric passbands and the continuum properties of individual quasars (Boyle et al. 1990; Hewett et al. 1995). The $u_J$ and $b_J$ magnitudes will be deliberately used in the remainder of this thesis, as $(B - V)$ measurements for the objects observed in the CUQS are not available.

## 3.4.2  Photometric sequences

A primary objective of the CUQS is to produce a catalogue with a selection function that is homogeneous across the entire survey area, so it is critical that the photometric calibration of survey candidates is itself homogeneous. Sensitivity and vignetting variations across even a single UKST plate may require a position-dependent calibration, and where multiple UKST fields are covered, particular attention is required to achieve homogeneity across plate boundaries. The approach used here was to use position-weighted averages derived from multiple photometric calibration regions in each UKST field, with regions at the field boundaries that are common to the overlap area of plates from the adjacent fields, to achieve a consistent calibration across each of the CUQS areas with smoothly varying residual errors.

Observations for 27 new $UBV$ sequences were made in 1994 and 1996 with the Cerro Tololo Interamerican Observatory (CTIO) 1.5-m telescope. Fig. 2.1 shows the relationship between the UKST fields and the calibration regions. The positions and exposures are shown in table 3.6. The photometric sequences from the 1994 observations were derived by Dr Matthew J. Graham, and have been reported in Graham (1997). MJG also derived the $UBV$ solutions for the standard stars in the 1996 observations. A summary of the remainder of the reduction of the 1996 observations and the derivation of photometric sequences that were performed by the present author is given below. Full details of all of the photometric observations and data reduction will be reported in a forthcoming paper (Graham, Clowes, Campusano & Newman, in preparation).

The 1996 photometric sequence observations were reduced using IRAF tasks following similar procedures to those used for the 1994 observations. For each calibration region, normally three CCD exposures in each of $U$, $B$ and $V$ were used. All of the CCD images were first bias-subtracted and flat-fielded using CCDPROC and were inspected visually to check for major defects. All images were accepted. For subsequent processing, the images for each region were processed together. Image header information was edited to correct for known differences between recorded and actual exposure times. The air mass was calculated for the mean local sidereal time and zenith angle of the exposure using SETAIRMASS. All of the CCD images for the region were shifted so that the stellar images (approximately) coincided with

52

**Table 3.6**: Observations of photometric sequences for the programme area (upper group) and control area (lower group). The region name includes the UKST field number, with a suffix that identifies the approximate position within the field (C=centre, E=east, N=north; see Fig. 2.1). Each region covers 14.8 × 14.8 arcmin$^2$ centred at the position shown. The exposure times are the total for each filter, normally consisting of 3 equal exposures. The F926N observations are insufficient to obtain either $U$ or $B$ magnitudes. F439C has only been used for $B$ magnitudes. For completeness, the position of F854E has been listed although this region has not yet been observed.

| Region Name | Year observed | Position (J2000) $\alpha$ ($^h$:$^m$:$^s$) | $\delta$ ($^\circ$:$'$:$''$) | Exposure time (s) $U$ | $B$ | $V$ |
|---|---|---|---|---|---|---|
| F854C | 1996 | 10 : 22 : 25 | −00 : 16 : 35 | 1800 | 1800 | 720 |
| F854E | − | 10 : 32 : 29 | −00 : 16 : 51 | − | − | − |
| F854N | 1994 | 10 : 22 : 32 | +02 : 04 : 10 | 1800 | 980 | 250 |
| F855C | 1996 | 10 : 42 : 15 | −00 : 14 : 33 | 1800 | 1800 | 720 |
| F855E | 1994 | 10 : 53 : 27 | −00 : 15 : 52 | 1800 | 600 | 300 |
| F855N | 1996 | 10 : 42 : 45 | +02 : 11 : 14 | 1800 | 1800 | 720 |
| F856C | 1996 | 11 : 02 : 40 | −00 : 15 : 50 | 1800 | 1800 | 720 |
| F856N | 1996 | 11 : 02 : 57 | +02 : 12 : 38 | 1800 | 1800 | 720 |
| F926C | 1996 | 10 : 21 : 55 | +04 : 38 : 38 | 1800 | 1800 | 720 |
| F926E | 1996 | 10 : 32 : 26 | +04 : 49 : 44 | 1800 | 1800 | 600 |
| F926N | 1996 | 10 : 23 : 13 | +07 : 23 : 48 | − | 1200 | − |
| F927C | 1994 | 10 : 42 : 02 | +04 : 32 : 02 | 1800 | 600 | 740 |
| F927E | 1996 | 10 : 51 : 48 | +04 : 45 : 28 | 1800 | 1800 | 720 |
| F927N | 1996 | 10 : 42 : 44 | +07 : 13 : 27 | 1800 | 1800 | 720 |
| F928C | 1996 | 11 : 02 : 08 | +04 : 54 : 02 | 1800 | 1800 | 720 |
| F928N | 1994 | 11 : 02 : 25 | +07 : 14 : 19 | 1800 | 600 | 300 |
| F998C | 1996 | 10 : 23 : 21 | +09 : 35 : 29 | 1800 | 1080 | 720 |
| F998E | 1994 | 10 : 32 : 27 | +09 : 46 : 16 | 1800 | 600 | 240 |
| F999C | 1994 | 10 : 42 : 45 | +09 : 44 : 17 | 1800 | 630 | 250 |
| F999E | 1996 | 10 : 52 : 05 | +09 : 41 : 21 | 1800 | 1800 | 720 |
| F1000C | 1996 | 11 : 00 : 22 | +10 : 05 : 24 | 1800 | 1800 | 720 |
| F438C | 1996 | 11 : 09 : 53 | −30 : 22 : 50 | 1800 | 1800 | 720 |
| F438E | 1994 | 11 : 20 : 50 | −30 : 24 : 52 | 1800 | 630 | 250 |
| F438N | 1996 | 11 : 02 : 23 | −27 : 59 : 10 | 1800 | 1800 | 720 |
| F439C | 1996 | 11 : 33 : 32 | −30 : 30 : 22 | − | 1800 | 720 |
| F439N | 1996 | 11 : 23 : 48 | −27 : 33 : 56 | 1800 | 1800 | 720 |
| F502C | 1996 | 11 : 02 : 11 | −25 : 24 : 48 | 1800 | 1800 | 720 |
| F502E | 1994 | 11 : 13 : 31 | −25 : 09 : 56 | 1800 | 630 | 250 |
| F503C | 1996 | 11 : 24 : 50 | −25 : 25 : 03 | 1800 | 1800 | 720 |

the image with least air mass (which was chosen to be the 'master' image) using IMMATCH and IMSHIFT. IMEXAMINE was used to determine the mean FWHM of the stellar point-spread function (PSF) and the modal sky level for each image. The standard deviation of the sky was then calculated from (Massey & Davis 1992)

$$\sigma = \frac{(sp + r^2)^{1/2}}{p}$$

where $s$ is the measured sky mode in analogue-to-digital units (ADU), $r = 3.5$ is the CCD read noise in electrons and $p = 2.0$ is the CCD gain in electrons ADU$^{-1}$ (the values of $r$ and $p$ are appropriate for the CCD used at CTIO in the observed wavebands).

DAOFIND (in the DIGIPHOT.DAOPHOT package of IRAF) was used to locate the centroid of all objects detected at $3.5\sigma$ above the sky level in each image. These positions were input to PHOT to measure aperture-integrated magnitudes for all the objects detected. The aperture radii used – 15 pixels for $U$ images and 6 pixels for $B$ and $V$ images – were identical to those used for the 1994 observations (1 pixel = 0.44 arcsec). However, the FWHM of the 1996 PSF was smaller than for 1994 for the $U$ images, so these aperture sizes may have increased the uncertainties in the $U$ results slightly due to excess contamination from sky noise.

Aperture corrections were computed for each image using $\sim 10$ bright, isolated, unsaturated stars per image to determine the mean difference between the instrumental magnitudes determined from the PHOT aperture radius and the radius used for the standard star measurements (25 pixels). The photometric solutions from the standard stars were used to derive calibrated $U$, $B$ and $V$ magnitudes for each of the objects detected. Finally, the magnitudes from each of the multiple images were combined to calculate mean calibrated $U$, $B$ and $V$ magnitudes for each of the objects detected in all the images, together with uncertainties and CCD coordinates. This gave the final calibrated photometric sequences.

Each object in each photometric sequence was matched to the corresponding object in each SuperCOSMOS database, by finding a simple geometric transformation between CCD and sky coordinates using GEOMAP. The combined set of photometric and SuperCOSMOS values for the matched objects in each calibration region were then used to determine the photometric magnitudes of all the objects on each plate, as described in the following sections.

### 3.4.3 SuperCOSMOS instrumental magnitudes

The SuperCOSMOS instrumental magnitude of an object is defined as

$$m_{\mathrm{sc}} = -\tfrac{5}{2} \log \sum_{i=1}^{n} (I_i - I_{\mathrm{sky}})$$

where $n$ is the number of connected pixels above the detection threshold, $I_i$ is the intensity in pixel $i$, and $I_{\mathrm{sky}}$ is the local median sky intensity per pixel. There is a non-linear relationship between $m_{\mathrm{sc}}$ and the corresponding photometric magnitude due to the photographic emulsion response, the degree of image saturation and the absolute image density (Hambly 1998b). The threshold level is defined by

$$I_{\mathrm{thr}} = \frac{I_{\mathrm{sky}} \times (100 + p)}{100}$$

where $p \geq 0$ is a parameter chosen to match the plate photographic density characteristics (Hambly 1998a). Note that $I_{\mathrm{thr}}$ is a *multiplicative*, as opposed to additive, factor above the median sky local to the object. The effective sensitivity of UKST plates varies across the field due to optical vignetting and, on pre-1982 plates, variable desensitization during the exposure. Provided $p$ is well chosen, the use of a threshold that is a constant fraction above the local sky value leads to object detection rates that are independent of position on the plate. This is a considerable advantage over the APM system, which uses a threshold that is a constant additive factor above the local median sky value. As Croom (1997) noted, the APM threshold definition leads to object detection rates that are position dependent, requiring a complex correction strategy.

### 3.4.4 Calibration for 1996 observations

The calibration of the SuperCOSMOS databases for the initial spectroscopic observations was described in detail by Graham (1997), and is summarized here. Spectroscopy started in the centre of fields 927 and 438. At the time that the observing plan was prepared, only the F927C and F438E photometric sequences were available.

For each region-plate pair, a cubic spline of 2 or 3 pieces was fitted to the sets of $(m_{\mathrm{sc}}, m_{\mathrm{phot}})$ points, where $m_{\mathrm{phot}}$ is the $b_J$ or $u_J$ photometric magnitude as appropriate for the plate. The typical r.m.s. uncertainty in the fits was $\simeq 0.2$ mag for an individual plate. The fitted splines were then used to calculate $m_{\mathrm{phot}}$ for each object

on the plate. For SuperCOSMOS objects outside the range of the fitting, linear extrapolations based on the gradient of the spline at the limit of the fit were used. The simple unweighted means of the $m_{\rm phot}$ values for each object from the stacked pairs of U and J plates in the field were taken as the object's magnitudes, with an r.m.s. uncertainty on each object estimated as $\sim 0.15$ mag.

No corrections were made for position-dependent effects. Since all the candidates for these observations were chosen from single UKST fields, no boundary corrections were needed.

### 3.4.5 Calibration for 1997 observations

The need to use multiple calibration regions to correct for position-dependent photometric errors became apparent as soon as spectroscopic candidate selection moved away from the central zones of the plates. When a single calibration region was used, as in 1996, strong gradients were seen in the surface density of candidates chosen on $16 \leq b_{\rm J} \leq 20$ and $(u_{\rm J} - b_{\rm J}) \leq -0.3$ at distances $\gtrsim 1^{\circ}\!5$ from the calibration region. The gradients were found to be a reflection of the very varied $m_{\rm sc} \rightarrow m_{\rm phot}$ relations exhibited by the different photometric sequences on some plates as shown, for example, in Fig. 3.8. The SuperCOSMOS plate data and the physical plates in the UKST plate library at ROE were both examined in an effort to identify a characteristic that correlated with the $m_{\rm sc} \rightarrow m_{\rm phot}$ variations that would allow the calibration of the different regions to be brought into agreement. No correlation was found with the mean sky density in the vicinity of the calibration region [cf. Thackrah (1996)], although such as correlation has previously been found in APM data (Croom 1997).

A strong correlation *was* found, however, with the $(m_{\rm sc}, A_{\rm sc})$ relation, where $A_{\rm sc}$ is the SuperCOSMOS object area. This relation diverged for the calibration objects in different regions in the same manner as the $m_{\rm sc} \rightarrow m_{\rm phot}$ mapping. While $m_{\rm sc}$ and $A_{\rm sc}$ are not truly independent variables, what is of interest here is not their inter-relationship, but the form of their relationships with $m_{\rm phot}$. In particular, $A_{\rm sc}$ for any given object magnitude is expected to correlate with position due to image distortion variation in Schmidt plates. The fact that this problem was found only in some plate databases suggests that the source of the problem lay partly in poor
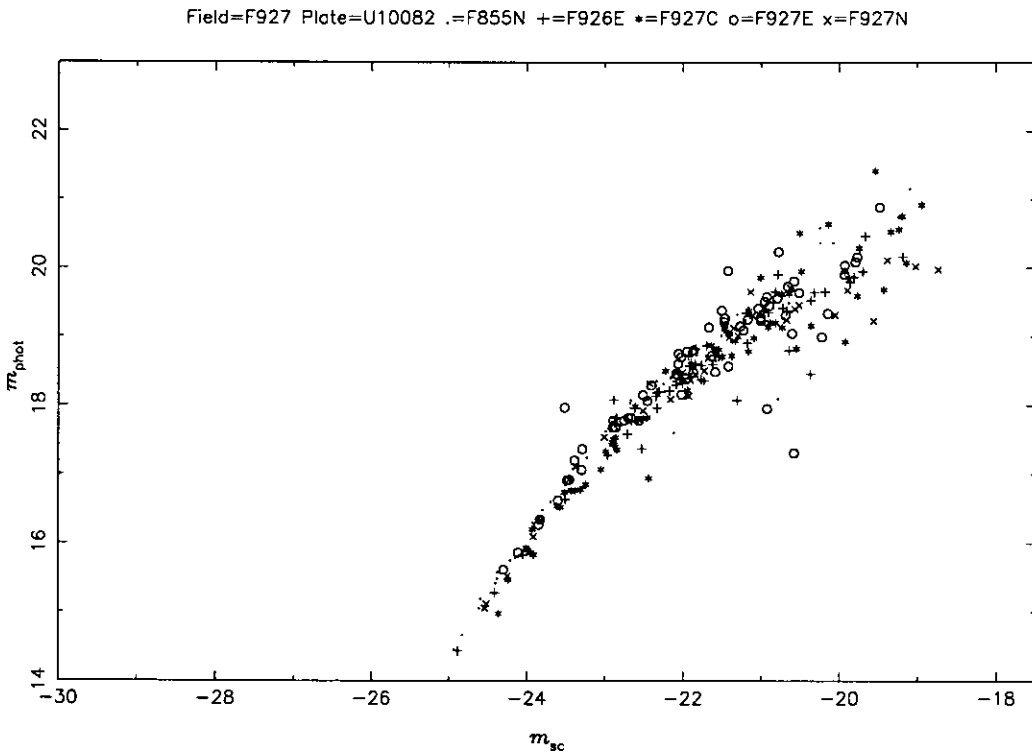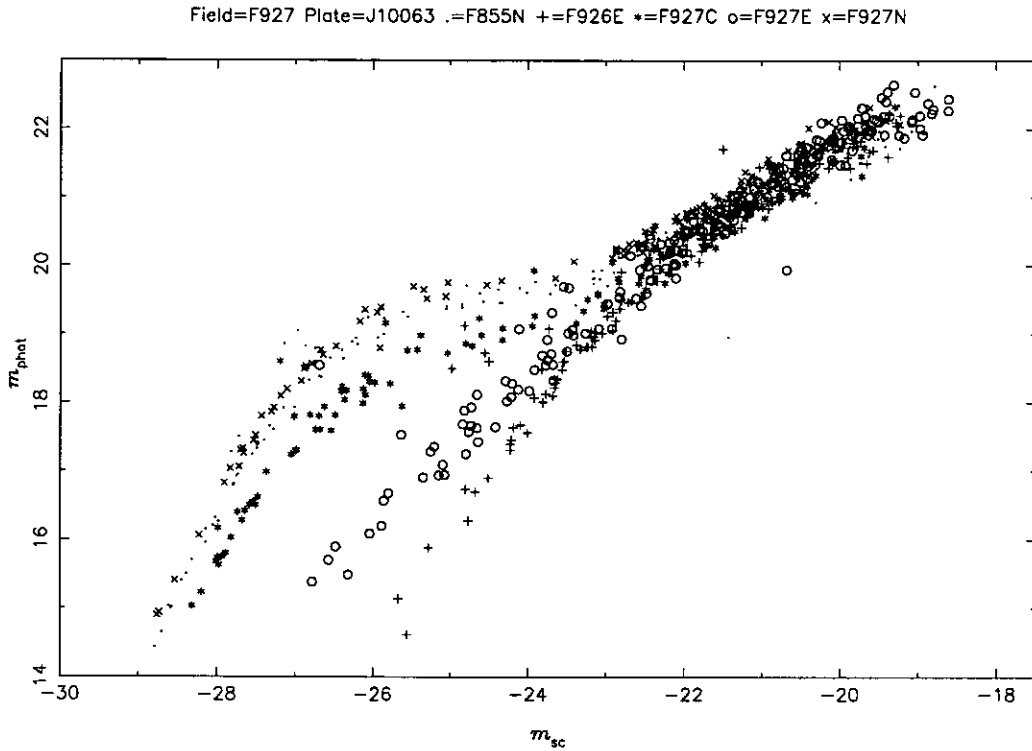
**Figure 3.8.** The $m_{sc} \rightarrow m_{phot}$ relations for plates J10063 (upper panel) and U10082 (lower panel), both in UKST field 927, before the 1997 observations. Each photometric region is plotted with a different symbol, shown in the legends. The same photometric data was used for both plates. The strong differences between the calibration curves are clear. J10063 is a 'very dark' plate; U10082 is not.

choices of $I_{\rm thr}$ in the SuperCOSMOS processing, especially for the high-density plates measured before the installation of a brighter lamp on SuperCOSMOS. The plate in which this effect is seen the worst, J10063, was 'very dark' for SuperCOSMOS (H.T. MacGillivray, private communication, 1995 December 5, and later confirmed by visual examination of the plate during a visit by the present author to the UKST Unit at ROE), in contrast to its UKST grade of 'a' which does not class it as overdense.

To make use of the correlation between $m_{\rm sc}$ and $A_{\rm sc}$ to correct the photometric calibration, a surface fitting code, 3DFIT, was written. This fitted a regular grid of bicubic splines to the $(m_{\rm sc}, A_{\rm sc}{}^{1/4}) \to m_{\rm phot}$ mapping. Taking the fourth root of $A_{\rm sc}$ has the effect of approximately linearizing the fitted surface between the low $m_{\rm sc}$, high $A_{\rm sc}$ limit and the high $m_{\rm sc}$, low $A_{\rm sc}$ limit, since magnitude is approximately proportional to the square root of the diameter of images on photographic plates. Examples of the fits for poor (J10063) and good (U10082) plates are shown in Fig. 3.9. The surface interpolated across the fitted bicubic splines was then used to calculate $m_{\rm phot}$ for all of the objects on the plate. Although the fitted surfaces tend to diverge rapidly outside the regions constrained by the calibration data, the remaining objects on each plate were found to lie within or sufficiently close to the constrained regions such that no problems due to poor extrapolation were introduced. The simple unweighted means of the $m_{\rm phot}$ values for each object from the pairs of U and J plates in the field were again taken as the candidate's magnitudes, with an r.m.s. uncertainty on each object again estimated as $\sim 0.15$ mag.

Candidates to be observed in 1997 were taken from UKST fields 927, 928, 999 and 1000 in the programme area, and field 438 in the control area. A comparison of the mean colours of candidates in the programme area fields showed that the field 999 objects were systematically more blue (i.e. $(u_{\rm J} - b_{\rm J})$ was more negative) than the field 927 objects, so that observed tiles (§4.3.2) overlapping the two fields contained candidates almost entirely from field 999. Field 927, being at the centre of the programme area, is the 'master' field for this survey, so a correction to the field 999 magnitudes was made. The objects in the overlap area of the two plates were paired and linear fits made to the differences in $b_{\rm J}$ and $u_{\rm J}$ magnitudes for objects in the range $16 \leq b_{\rm J}, u_{\rm J} \leq 20$. From these it was determined that the corrections

## J10063 (f927)

COSMAG range = { −28.500, −19.000} Smoothness = 30.000
AREA^0.25 range = { 1.8, 4.6} Interior COSMAG knots = 1
MAG range = { 14.000, 22.500} Interior AREA^0.25 knots = 1
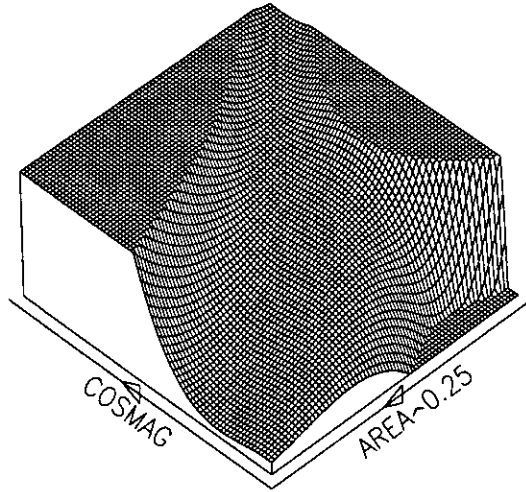


## U10082 (f927)

COSMAG range = { −24.500, −19.000} Smoothness = 11.800
AREA^0.25 range = { 1.7, 4.0} Interior COSMAG knots = 1
MAG range = { 13.000, 20.500} Interior AREA^0.25 knots = 1
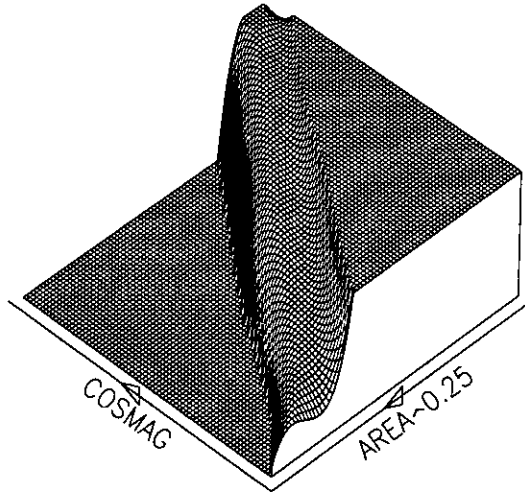


**Figure 3.9.** Surface fit to the $(m_{sc}, A_{sc}^{1/4}) \rightarrow m_{phot}$ mapping for plates J10063 (upper) and U10082 (lower), made with the 3DFIT code. The vertical axis is $m_{phot}$. The planar regions are where the fitted surface has been truncated outside the fitted points. Compare the spread of the fitted surface with the corresponding spread in the 2-dimensional $m_{sc} \rightarrow m_{phot}$ relations in Fig. 3.8.

59

required were

$$(b_{J927} - b_{J999}) = (-0.090 \pm 0.012)b_{J999} + (+1.410 \pm 0.225)$$
$$(u_{J927} - u_{J999}) = (+0.004 \pm 0.007)u_{J999} + (-0.187 \pm 0.124)$$

where the subscript identifies the field. Over the ranges of interest, $16 \leq b_J, u_J \leq 20$, the $b_J$ correction varies from $-0.04$ mag to $-0.40$ mag. The $u_J$ correction is almost constant, varying from $-0.12$ mag to $-0.10$ mag. The larger slope of the $b_J$ correction may be attributable to the use of a single J plate (J16974) for the 1997 observations, while the mean magnitudes from two U plates were used. The corrected magnitudes in the overlap area were then found to agree to within the uncertainties in the calibration ($\sim 0.1$ mag). No corrections were found to be necessary for fields 928 and 1000 to achieve a homogeneous candidate density.

### 3.4.6   Calibration for 1998 observations

Between the 1997 and 1998 observations, a number of improvements were made to the SuperCOSMOS facility as it moved towards the end of its commissioning phase. In the light of these improvements, a campaign was started to re-measure the plates with problematic photometric calibrations. The success of these improvements is shown dramatically by the 'before' and 'after' calibrations for plate J10063 shown in Figs. 3.8 and 3.10.

Most of the plate stacks were changed following re-measurements, so it was deemed necessary to recalibrate the photometry. As the $m_{sc} \rightarrow m_{phot}$ maps for the re-measured plates were almost coincident for the different regions, the 3DFIT method used for the 1997 observations was no longer appropriate because the range of the $A_{sc}$ fit was much narrower. Instead, simple 2-dimensional cubic spline curves were fitted to the $m_{sc} \rightarrow m_{phot}$ for each of the photometry regions, as for the 1996 calibration. Examples of the fitted curves for plate J10063 are shown in Fig. 3.11.

The mean photometric magnitudes assigned to objects were determined as follows. For each calibration region $i$ on plate $p$, the photometric magnitude of an object, $m_i$, was calculated from the spline fit for the object's $m_{sc}$. The weighted mean magnitude for the object for that plate, $m_p$, was found from the $n$ calibration
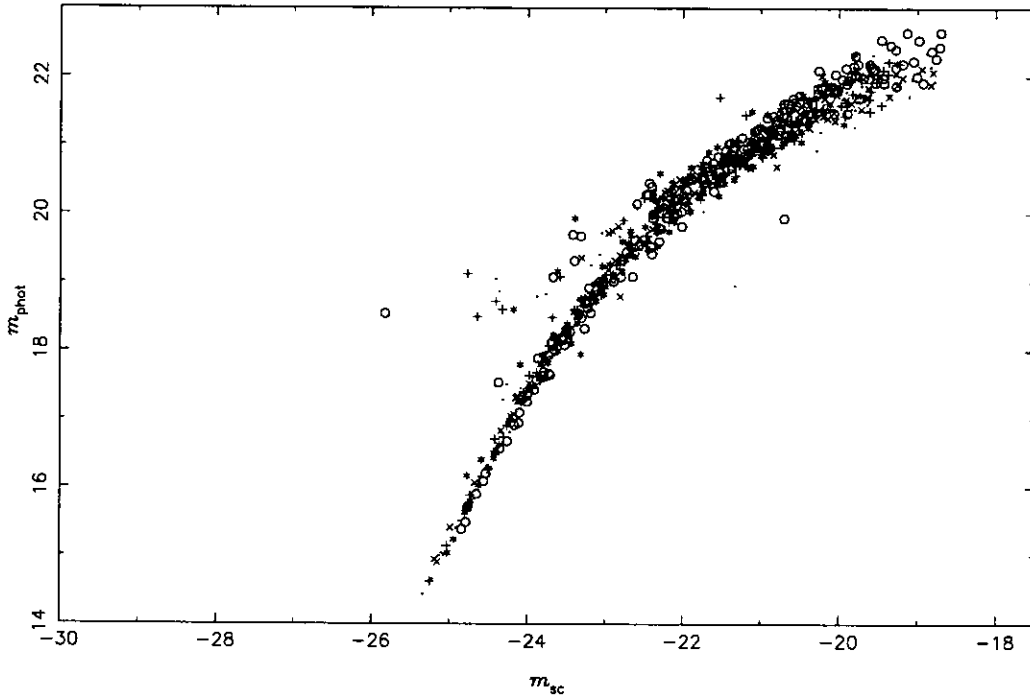
**Figure 3.10.** The $m_{sc} \to m_{phot}$ relations for plate J10063, before the 1998 observations, after re-measurement on SuperCOSMOS with improved illumination and thresholding, but with photometric calibration data identical to that used earlier. Note how the curves now almost coincide for all of the calibration regions.

regions, by

$$m_p = \frac{\displaystyle\sum_{i=1}^{n} m_i w_i}{\displaystyle\sum_{i=1}^{n} w_i}.$$

The weight for each calibration region, $w_i$, is based on the distance of the object from each of the *other* calibration regions, by

$$w_i = \prod_{j \neq i} (r_j)^{\alpha}$$

where $r_j$ is the Euclidean distance of the object from region $j$ and $\alpha$ is a smoothing parameter. This makes the nearest region the most strongly weighted, while maintaining a smooth variation in weights across the plate. For an object centred in one calibration region, the weights for the other regions will be zero, so the smoothed magnitudes are tightly tied to the calibration, thus ensuring smooth transitions through the calibration regions in the plate overlaps. The uncertainty in $m_p$ for a

61
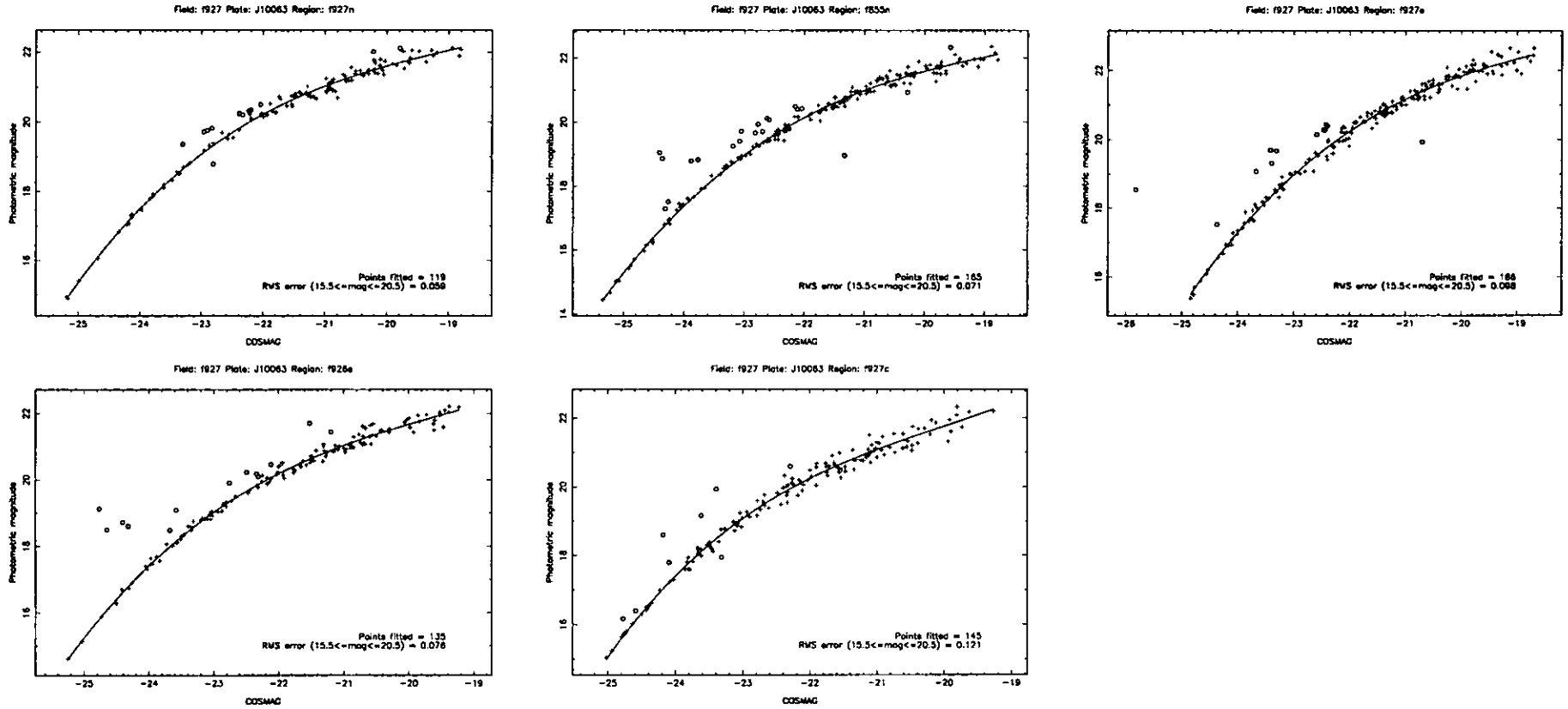
**Figure 3.11**: Typical photometric calibration curves, as fitted to the $m_{sc} \to m_{phot}$ maps for the five calibration regions on plate J10063 in UKST field 927. The $x$ axis is $m_{sc}$, the $y$ axis is $m_{phot}$. Crosses show points included in the fits, circles show excluded points. The number of points in each fit and the r.m.s. uncertainty of the fit over the range $15.5 \leq m_{phot} \leq 20.5$ are shown.

plate was taken to be the simple unweighted standard deviation, $\sigma_p$, of the $m_i$ for that plate. Suitable values for the parameter $\alpha$ were found by experiment and visual examination of the resulting isotropy of the magnitude distribution across each UKST field. Fields 854 and 928 required $\alpha = 2$; for all other fields, $\alpha = 1$ was sufficient. For the J plates in field 928, the 928C region was found to be anomalous and was omitted from the calibration. Plate U14315 in field 438 was found to have poor fits, so it was omitted from the photometric calibration pending re-measurement on SuperCOSMOS or replacement by a new plate.

The final adopted $b_J$ and $u_J$ magnitudes and their variance for each object were calculated from the variance-weighted mean of the magnitudes for each pair of J and U plates, i.e.

$$m = \frac{\sum m_p/\sigma_p^2}{\sum 1/\sigma_p^2}$$
$$\sigma_m^2 = \frac{1}{\sum 1/\sigma_p^2}$$

where the sums are over the pair of plates and $m$ is $b_J$ or $u_J$ as appropriate. The mean $\sigma_m$ in the adopted magnitudes for objects in a typical field are $\sigma_{b_J} = \pm 0.06$ and $\sigma_{u_J} = \pm 0.08$. These must be combined in quadrature with the r.m.s. uncertainty in the fitted calibration curves, which is typically $\pm 0.085$ mag, giving uncertainties in the adopted calibrated magnitudes and colours of

$$\Delta b_J = \pm 0.10 \text{ mag}$$
$$\Delta u_J = \pm 0.12 \text{ mag} \tag{3.12}$$
$$\Delta(u_J - b_J) = \pm 0.16 \text{ mag}.$$

The magnitudes assigned from this calibration were used for the 1998 observations (chapter 4), and were also used to re-calibrate the magnitudes of candidates observed in 1996 and 1997, so that the all entries in the survey catalogue (chapter 5) are consistent.

### 3.4.7 Calibration of field 345 plates

For the F345 complete sample (§2.4.2), no specific photometric calibration sequences were available in the UKST field 345. Instead, $B$ and $R$ magnitudes from the USNO-A V1.0 astrometric catalogue (Monet 1996; Monet et al. 1996) were used. At

63

Field: f345 Plate: J3585 Region: f345c

Points fitted = 9111
RMS error (15.5<=mag<=20.5) = 0.244

Field: f345 Plate: R13849 Region: f345c

Knot at COSMAG = −21.99242
Knot at COSMAG = −23.00016
Knot at COSMAG = −24.00790
Points fitted = 9008
RMS error (15.5<=mag<=20.5) = 0.318
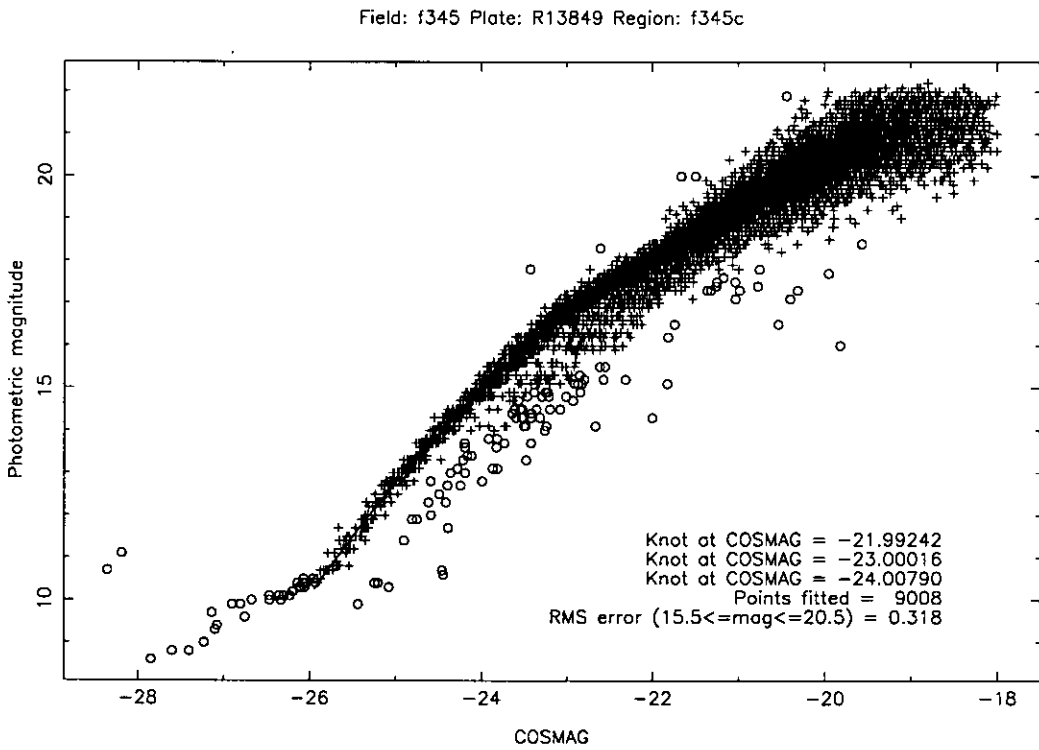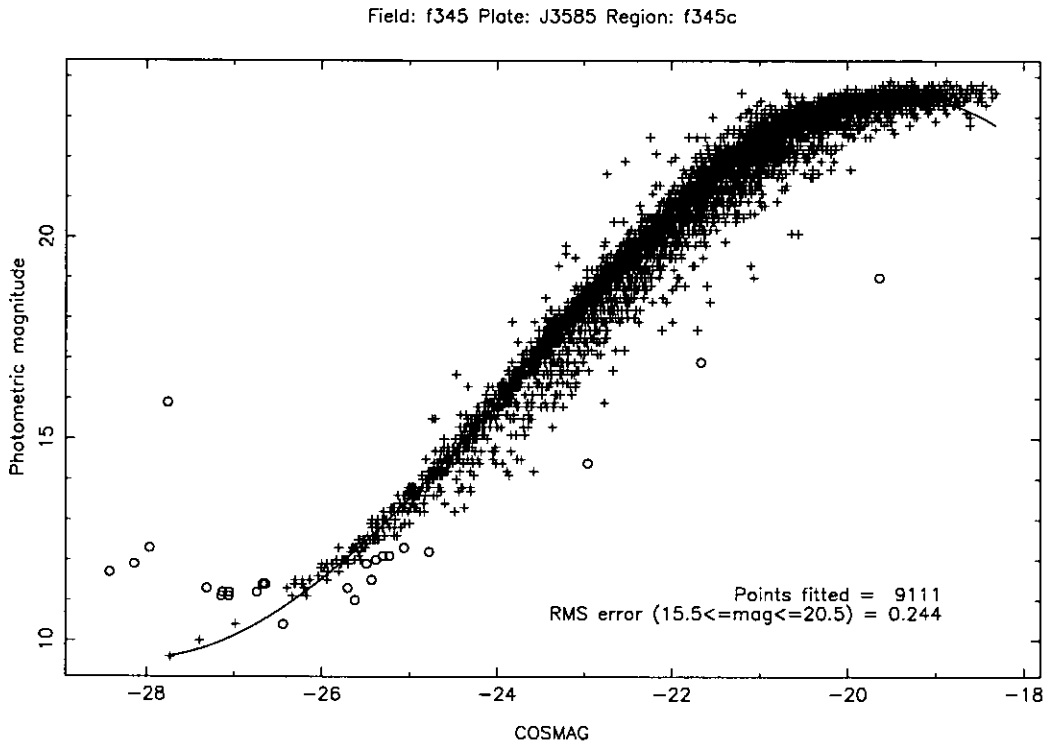
**Figure 3.12.** The photometric calibration points and the fitted $m_{sc} \rightarrow m_{phot}$ relations for plate J3585 (upper) and plate OR13849 (lower) in UKST field 345. The legend is the same as Fig. 3.11.

the declination of field 345, these are based on the UKST J and ESO R survey plates and are therefore in the same system as the plates used for these observations. In line with the conventions used here (§3.4.1), the R plate magnitudes will be denoted by $r_\mathrm{F}$.

All the objects in the SuperCOSMOS databases inside a central 2°-diameter circle were matched to objects in the USNO-A V1.0 catalogue and cubic splines were fitted to the $m_\mathrm{sc} \to m_\mathrm{phot}$ relations in the same manner as for the CUQS plates. The resulting fits are shown in Fig. 3.12. The r.m.s. uncertainty in the fits is $\sigma_{b_\mathrm{J}} = 0.244$ and $\sigma_{r_\mathrm{F}} = 0.318$, which are somewhat larger than the estimated measurement uncertainty in the USNO-A V1.0 catalogue of $\pm 0.15$ mag (Monet et al. 1996). However, since this is a secondary calibration from a catalogue whose primary purpose is astrometry, large uncertainties are not surprising. At the time of writing, no attempt to improve on these uncertainties has been made, but specific deep photometric sequences, as used for the main CUQS calibration, could clearly reduce the errors. As all of the observed objects are in a small central region of the plates, there should be no appreciable uncertainty from position-dependent calibration effects. The adopted uncertainties in the final calibration were therefore

$$
\begin{aligned}
\Delta b_\mathrm{J}(345) &= \pm 0.24 \text{ mag} \\
\Delta r_\mathrm{F}(345) &= \pm 0.32 \text{ mag}.
\end{aligned}
\tag{3.13}
$$

### 3.4.8 Future improvements

There is still considerable scatter in the $m_\mathrm{sc} \to m_\mathrm{phot}$ relations for a number of plates. These should be re-measured on SuperCOSMOS and recalibrated to achieve results as consistent as those for the (now) exemplary plate J10063. The standard-star calibration of the photometric sequences used have also been improved since the 1998 calibration (M.J. Graham, private communication, 1998 July 15). Both of these could reduce the uncertainties in the final CUQS catalogue to $\Delta(u_\mathrm{J} - b_\mathrm{J}) \simeq \pm 0.1$ mag across the entire survey area.

An issue that has not yet been fully addressed is the correction of the calibrated photometric magnitudes for galactic extinction. Recent advances by Schlegel et al. (1998) to trace galactic extinction using maps of dust emission from the *COBE* and *IRAS* satellites should make this task relatively simple. In galactic coordinates,

the CUQS programme area is centred $l \simeq 243°$, $b \simeq +52°$, and the control area is centred at $l \simeq 279°$, $b \simeq +29°$. An initial estimate of the extinction coefficients in the areas of sky around these positions gives $E(B - V) \simeq 0.025$ mag in the programme area and $E(B - V) \simeq 0.055$ mag in the control area. The differences between the corrected values of programme and control area magnitudes and colours due to differential galactic extinction are then estimated to be

$$b_{J\text{ctrl}} - b_{J\text{prog}} \simeq 0.12$$
$$(u_J - b_J)_{\text{ctrl}} - (u_J - b_J)_{\text{prog}} \simeq 0.04$$

using the coefficients of Schlegel et al. (1998) to convert $E(B - V)$ to $u_J$ and $b_J$ magnitude corrections. This implies that the $b_J \leq 20$ limit applied in candidate selection using uncorrected magnitudes will have been, in effect, 0.12 mag brighter in the control area than in the programme area. However, the colour difference is smaller than the uncertainties from other sources.

The possibility of extending the CUQS observations to fainter magnitudes (the 2dF fibre spectrograph on the 3.9-m AAT, for example, would enable candidates to $b_J \simeq 21$ to be observed) raises separate problems. The limit of the present $U$ photometry sequences is $U \simeq 20.5$. Beyond that, extrapolation would lead to a decrease in accuracy. In addition, detection limit of the UKST U plates is also reached at $U \simeq 21$, further complicating candidate selection (Boyle 1986). At these fainter magnitudes, poor photometric calibration can easily increase the contamination of the list of spectroscopic candidates due to galactic stars to unacceptable levels, leading to a poor, and poorly understood, survey selection function. Methods of reducing the stellar contamination, such as the linearization of the stellar ridge line in the candidate $(U - B)$ vs. $B$ relation might then be necessary (Boyle 1986; Croom 1997; Smith 1998).

# Chapter 4

# Observations and data reduction

## 4.1 Chapter overview

An overview is provided of the telescope and multi-object spectrograph used to make the spectroscopic observations for the CUQS at the Las Campanas Observatory[1] in Chile (LCO). The construction of the observing plans from the calibrated Super-COSMOS data is then described in detail, and the observations made are listed. The reduction and calibration of the observations is described, and examples of the reduced spectra are presented.

## 4.2 Telescope and spectrograph used

The 'Fruit & Fiber' multi-object spectrograph on the 2.5-m (100-inch) du Pont telescope at LCO has been used for all of the CUQS spectroscopic observations. An overview of the telescope and instrument is given here – both are more fully described by Shectman (1993, and references therein), who was largely responsible for the design and construction of the spectrograph and its use for the Las Campanas Redshift Survey of galaxies (Shectman et al. 1996).

The telescope is a reflector of Ritchey-Chrétien optical design with an $f/7.5$ Cassegrain focus. A corrector lens produces a 2°1 field of view that is $\sim 72$ cm in diameter at the slightly-curved focal surface. The field of view is essentially unvignetted over the central 1°5 diameter, increasing to $\sim 40$ per cent loss at the

---

[1] One of the Observatories of the Carnegie Institution of Washington (OCIW).

67

edges. The telescope was originally designed for wide-field astrophotography and has sub-arcsecond imaging quality.

The instrument (Shectman et al. 1992) uses 128 optical fibres to take light from images at the telescope focal surface to a floor-mounted grating spectrograph with an image-intensifier chain that ends in a 2D-Frutti position-sensing photon counter (Shectman 1984). Each optical fibre is 320 $\mu$m in diameter, which subtends 3.5 arcsec of sky at the focal surface. As discussed in §3.3, the fibre size is very well suited to the observed seeing disk sizes at LCO, which are typically 1.8 arcsec FWHM. The fibres are plugged by hand into an aluminium plate mounted on an instrument rotator and distorted by a pneumatic press into approximate agreement with the focal surface. Normally, 112 fibres are allocated to spectroscopic target objects and 8 fibres to sample the sky. This is the optimal allocation between targets and sky for accurate sky subtraction with sky-limited observations (Wyse & Gilmore 1992). The remaining 8 fibres installed on the instrument are known to be defective and are not used. The full system produces a useful response over the wavelength range $3200 \lesssim \lambda \lesssim 7400$ Å, peaking at $\sim 4250$ Å (the short-wavelength limit is principally due to atmospheric absorption). Derivation of the response curve for the CUQS observations is described in §4.6.4.

The positions of the holes into which the fibres are plugged are specified in the observing plan by precise J2000 $(\alpha, \delta)$ coordinates together with the planned date and time of exposure. Standard OCIW software corrects the positions for differential atmospheric refraction and converts them to physical plug-plate coordinates. This software also eliminates collisions between adjacent fibres – the minimum inter-fibre spacing is 55 arcsec – and lists the eliminated candidates. It is intended that the eliminated candidates will be observed at a later date. The plug plates are drilled by an OCIW sub-contractor in California using computer-numerically-controlled tools, and then shipped to LCO ahead of each observing run. The holes for up to five different observed fields ('tiles') can be drilled in the same plate, reducing or removing the need to change plates during the night. The lead time of 6–8 weeks between final specification of the observing plan and start of observations makes this instrument somewhat different to single-object spectrographs from the observer's point of view in that no modification of the plan at the telescope is possible.

The telescope guiding system requires that each tile is centred on an $R \simeq 13$–15 guide star (§4.3.3). The image of the guide star is led to a television camera via a 1-cm diameter coherent bundle of $\sim 10^3$ fibres, fixed in the centre of the plug plate. The telescope drive system uses the centroid of the guide star image to automatically guide the telescope during exposures. Two other four-fibre coherent bundles are positioned on $R \simeq 14$ stars near the edge of the field, which are used (a) to determine the correct rotation and centring of the plug plate, and (b) to determine the fine-tuning of the image plate scale by adjustment of the telescope focus. Careful rotational alignment of the plug plate for the first tile of each night has been found to be sufficient for subsequent tiles.

Once centred on a field to be observed, the spectrograph aperture is opened slowly in case an unacceptably bright object ($m \lesssim 14$) is illuminating one or more fibres, in which case the offending fibre or fibres are pulled from their assigned holes and added to the collection of sky fibres. The continuous read-out of the detector count rate is then used by the telescope operator to fine-tune the telescope pointing at the start of each exposure to maximize the illumination of the fibres. The central guide star image also gives a rough indication of changes in sky transparency, and provides a continuous measure of the FWHM of the seeing disk (calibrated by a seeing monitor sited nearby at LCO). Changing from one tile to the next (including changing fibres from one set of holes to the next, and acquiring the next target position) typically takes 35 min.

## 4.3 CUQS observing plans

### 4.3.1 Candidate selection

Candidates for spectroscopy were selected from the calibrated, stacked, SuperCOS-MOS databases (chapter 3). The initial selection of candidates for all years was on $16 \leq b_J \leq 20$. The colour selection was made during the tessellation of the survey area, as described in the §4.3.2. For the 1996 observing plan, all programme-area candidates were selected from the database for UKST field 927, and all control-area candidates were selected from field 438. No field boundaries were crossed. The 1997 and 1998 programme-area observations covered parts of fields 927, 928, 999

and 1000 (see Fig. 2.1). For the 1997 observations, the calibrated SuperCOSMOS databases for these fields were cut along boundaries of constant right ascension and declination, then merged into a single database from which candidates were selected. The boundaries, defined in radians by

$$
\begin{array}{llll}
927 & : & \alpha \leq 2.8405 & (\simeq 10^{\mathrm{h}}51^{\mathrm{m}}00^{\mathrm{s}}) & \delta \leq 0.13 & (\simeq +07^{\circ}26'54'') \\
928 & : & \alpha > 2.8405 & & \delta \leq 0.13 \\
999 & : & \alpha \leq 2.84 & (\simeq 10^{\mathrm{h}}50^{\mathrm{m}}53^{\mathrm{s}}) & \delta > 0.13 \\
1000 & : & \alpha > 2.84 & & \delta > 0.13
\end{array}
$$

were chosen to best avoid defects along the plate edges (the values in radians are the exact values used). In practice, this method caused problems with variations in astrometry across the field boundaries, as discussed in §3.3. Control-area candidates were again chosen solely from field 438. Candidates for the 1998 observations were selected from the same fields as for 1997. However, candidates for each exposure were chosen from the database for a single field instead of from a consolidated database. This avoided the steep astrometric error gradients that occurred at field boundaries.

## 4.3.2   Tessellation of the survey area

Candidates for 1996 were assigned to individual spectroscopic exposures by Graham (1997) using an adaptive tiling code called TESS. Candidates for 1997 and 1998 were assigned to individual exposures using a version of Graham's code revised and corrected by the present author and renamed TESSELLATE. Both codes are based on the following approach. The unvignetted telescope field of view is a $1°\!.5$-diameter disk. The most efficient covering of a plane by disks is the intuitive arrangement of a 'honeycomb' that places the centres of the disks on an equilateral triangular network (Kershner 1939; Conway & Sloane 1993, and references therein). This is also a reasonably efficient approximation for the relatively small area of the celestial sphere covered by the programme and control areas. The survey areas were initially tessellated on such a grid with a spacing of $1°\!.5$ between tile centres, giving the preferred tile positions shown in Fig. 4.1. The centre of each tile was then shifted from its preferred position to coincide with its chosen central guide star (see §4.3.3), and the radius of the tile was increased by the size of the shift to maintain continuous area coverage.

Each candidate in the magnitude-selected databases was then allocated to the
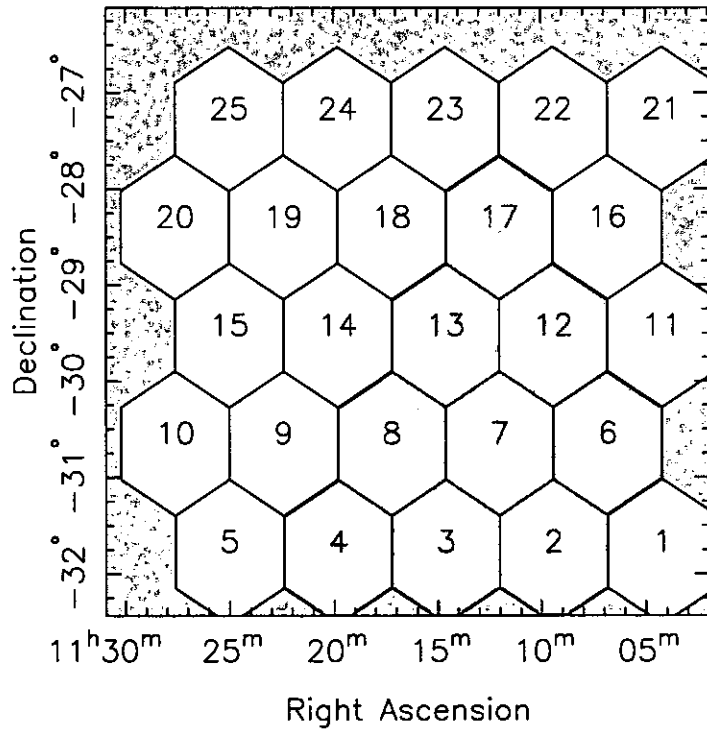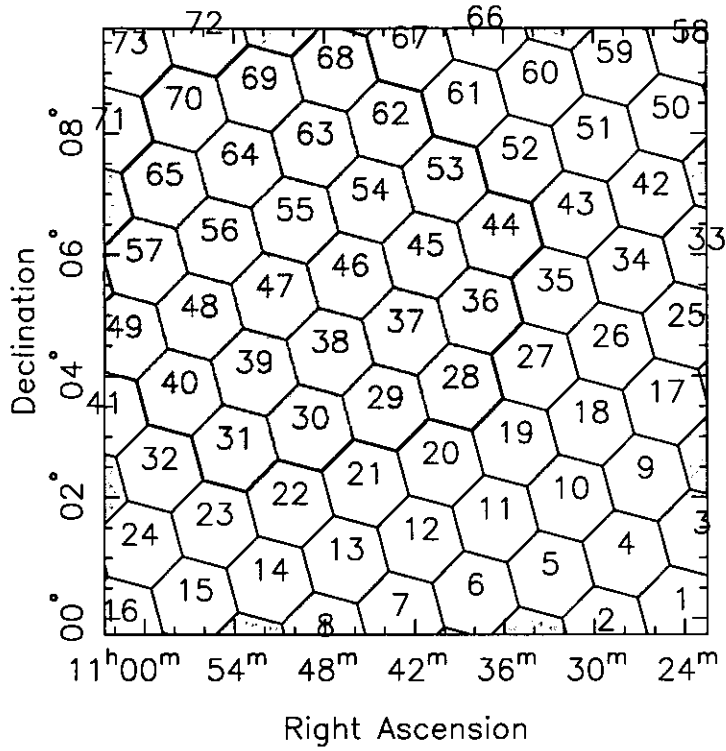
**Figure 4.1.** Positions of the preferred tiling for the $10° \times 10°$ programme area (upper panel) and the $6°3 \times 6°3$ control area (lower panel – note the different scales). The dark shaded tiles are those in the observing plans from 1996 to 1998, and the tile numbers give a cross-reference to the observing logs in tables 4.1–4.3.

nearest tile. Candidates that fell in the overlap between two tiles were allocated to the tile with the least number of candidates. The candidates in each tile were then sorted on ascending $(u_J - b_J)$ colour (i.e. most negative first). Finally, the first 112 candidates in each tile were assigned to fibres, after elimination of candidates that were too close ($\lesssim 55$ arcsec) for the fibre spacing in the plug plates. The actual candidates observed in each year, and the consolidated set for all observations are shown in Figs. 4.2 to 4.5.

The mean red limiting colour of the candidates in all of the tiles observed is $(u_J - b_J) = -0.36 \pm 0.09$, equivalent to $(U - B) = -0.26 \pm 0.09$ in the photoelectric magnitude systems (Eqn. 3.11). There are three principal sources of the tile-to-tile variations in the limiting colour: (a) the natural statistical variations in the colour of candidates, (b) the variations in observed surface density of candidates due to variations in tile size after centring on guide stars, and (c) residual errors in the photometric calibration. The standard error on the mean for all tiles, 0.09 mag, is smaller than the formal uncertainty in the colour calibration (Eqn. 3.12), supporting the conclusion that the photometric calibration has a high degree of homogeneity across the survey area.

However, the candidate selection is not perfect, and several minor flaws have been identified. The corners of all of the UKST fields suffer from two problems: they are worst affected by UKST vignetting, and they are furthest from the present calibration regions (Fig. 2.1). This has resulted in variations in the photometric errors leading in particular to the slight over-densities in the candidates near the western corners of field 928 visible in Figs. 4.4 and 4.5 (near $10^h 50^m, +3°30'$ and $10^h 50^m, +7°00'$). The addition of photometric sequences in the corners of all fields would allow considerable further reduction of the mean residual errors and improvement to the smoothness of the transitions between fields. Other flaws have been introduced in the construction of the observing plans from the calibrated data. Because of an error in the original TESS code, the programme-area tiles for the 1996 observations were incorrectly rotated, leaving small triangular areas unobserved, as can be seen in Fig. 4.2. In fact, no candidates lie in the missed areas, so analyses of the survey catalogue are not affected. A separate error in tile-size specification for the 1998 re-observation of a tile missed due to bad weather in 1997 led to candidates
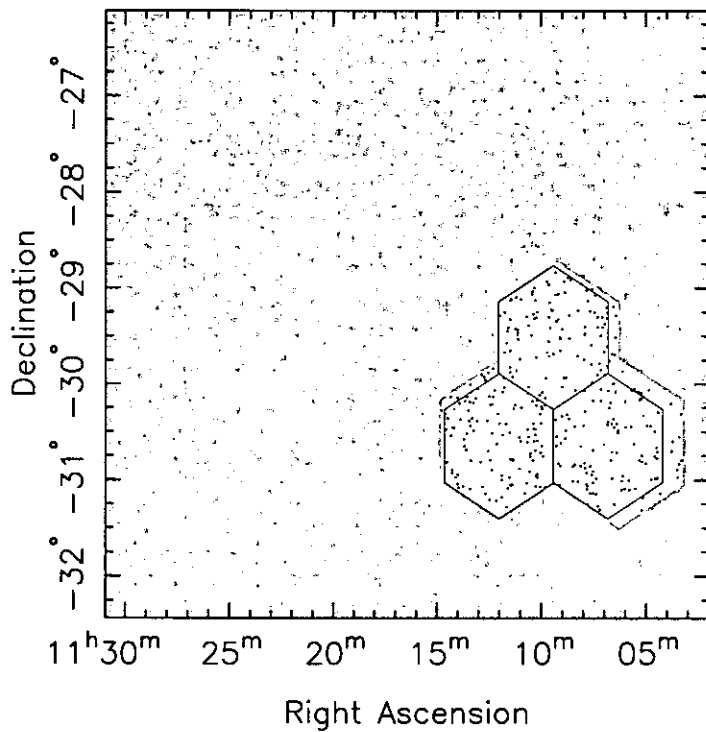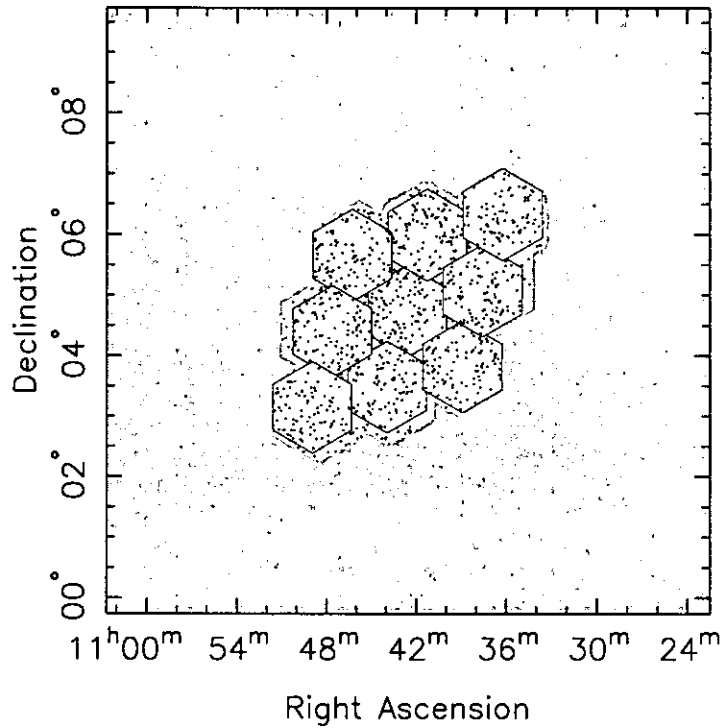
**Figure 4.2.** Positions of candidates for the 1996 observations in the programme area (upper panel) and control area (lower panel – note different scales). Dots show the positions of the candidates. Hexagons show the preferred positions of the tiles observed. The white areas show the actual areas of the observed tiles after shifting their centres onto guide stars. The shaded regions outline the whole of the CUQS area.
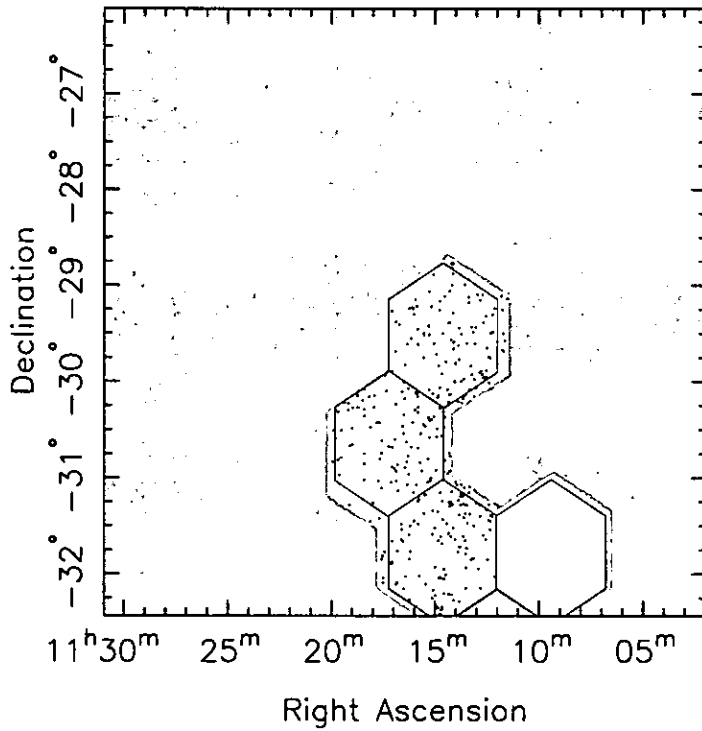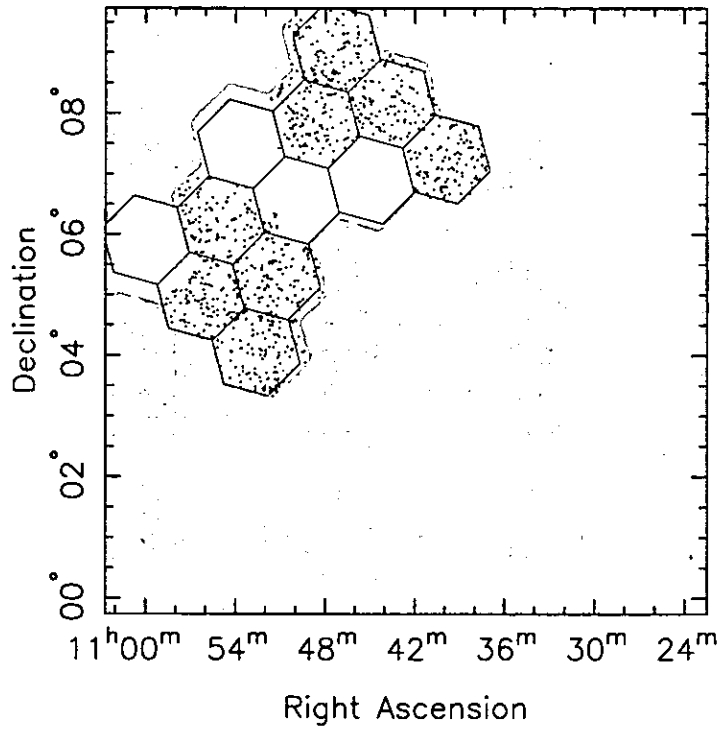
**Figure 4.3.** Positions of candidates for the 1997 observations. The legend is as for Fig. 4.2. Empty tiles were not observed due to bad weather, or the observations were abandoned due to bad astrometry (see §3.3), and were observed in 1998. A few candidates outside the survey area in tiles along the survey boundary have not been shown.

74
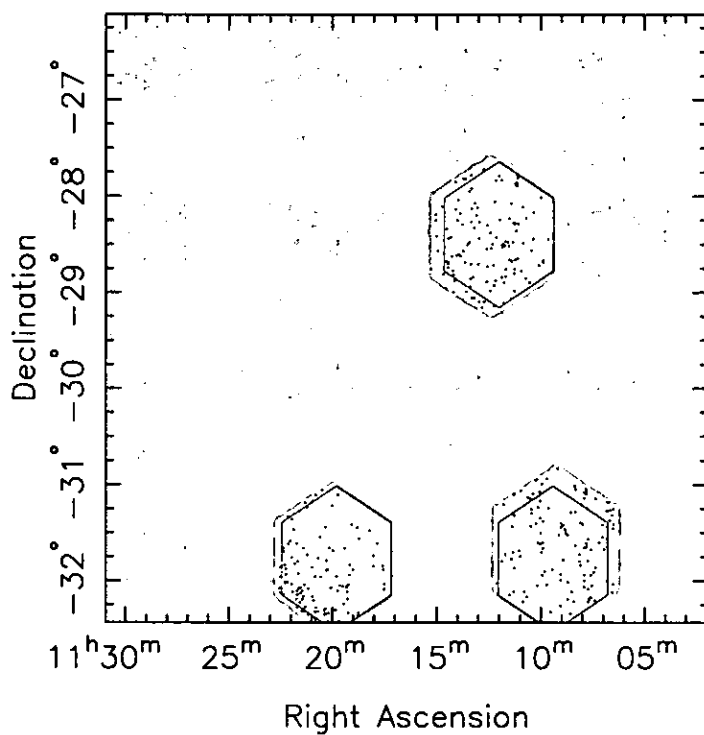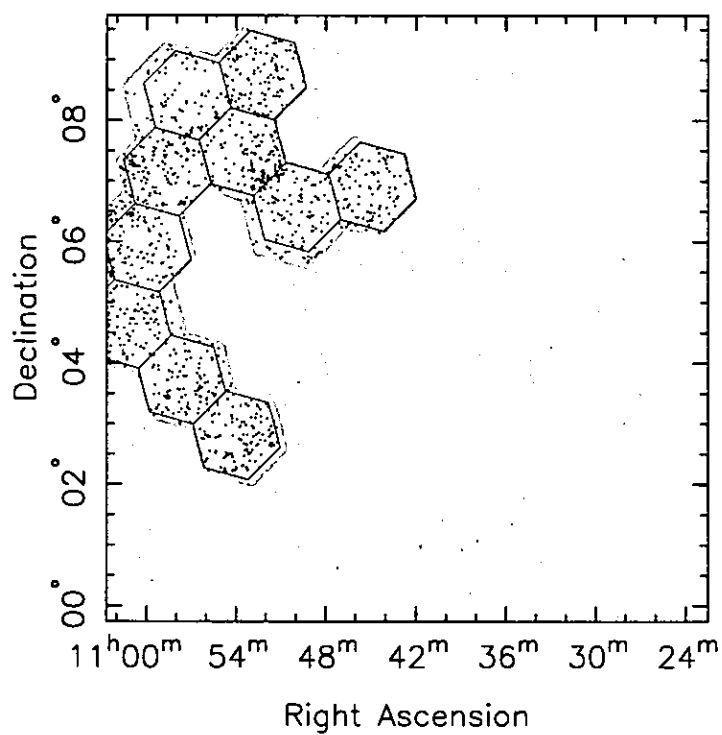
**Figure 4.4.** Positions of candidates for the 1998 observations. The legend is as for Fig. 4.2. A few candidates outside the survey area in tiles along the survey boundary have not been shown.
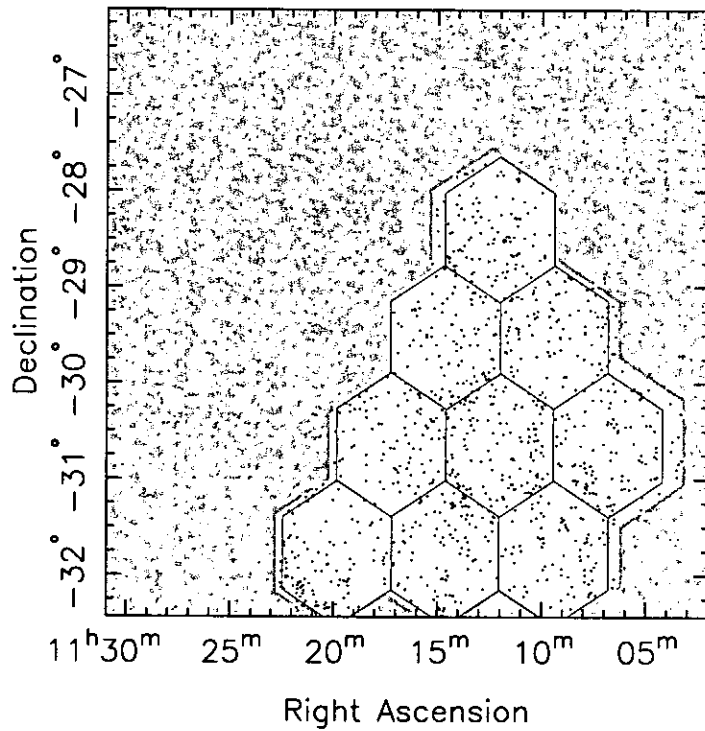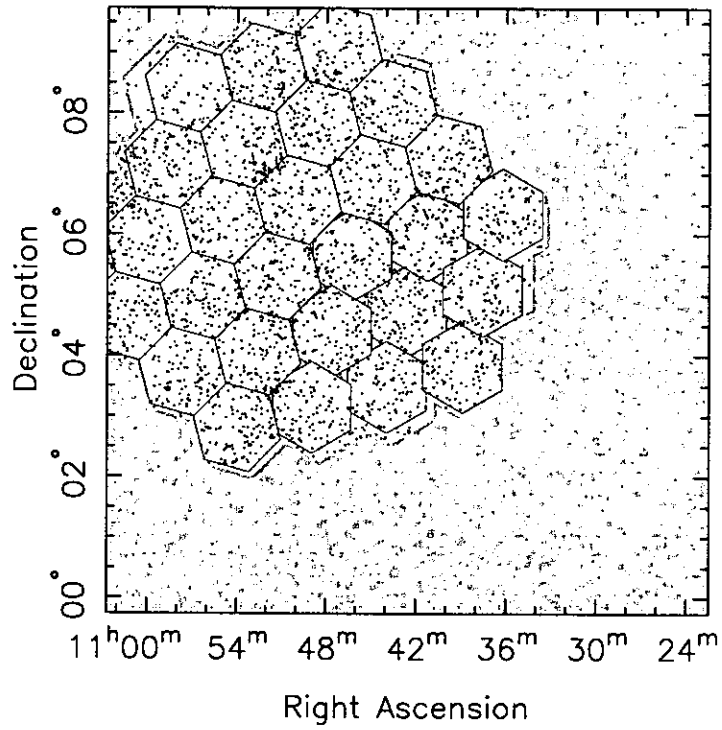
**Figure 4.5.** Consolidated positions of all candidates observed in 1996, 1997 and 1998. The legend is as for Fig. 4.2. A few candidates outside the survey area in tiles along the survey boundary have not been shown.

in a small region near $10^h58^m$, $+05°45'$ being omitted, as can be seen in Fig. 4.5. These missed candidates must be observed at a later date. However, the analysis of the quasar distribution presented here does not include the 1998 observations, and so again it is unaffected by this error.

### 4.3.3 Guide stars

Each exposure with the Fruit & Fiber spectrograph requires a field-centre guide star with a magnitude of $13 \lesssim R \lesssim 15$ (to suit the red-sensitive guiding system television camera). To check and correct field rotation and centring, at least two secondary guide stars with $R \simeq 14$ are needed on the periphery of the field (one to N or S of centre, and one to W or E). In practice, to allow for elimination of holes due to collisions with spectroscopic candidate fibres, two peripheral guide stars were chosen at each of the cardinal points of the field.

The identification of suitable central guide stars can be problematic. The telescope system requires that each observed field *must* be centred on a guide star. The surface density of magnitude 14 stars at the galactic latitude of the programme area ($b \simeq 50°$) is $\lesssim 150$ deg$^{-2}$ (Allen 1976, p.244), so the mean distance between suitable stars is $\gtrsim 5$ arcmin. A typical programme-area tile has to be offset from its preferred position by a similar distance. For the control area, at $b \simeq 30°$, the density of galactic stars is higher, so the shifts are generally smaller. As mentioned above, tile radii are increased by the offset from preferred centres, so the tile areas are increased and the surface density of observed candidates is decreased. The distribution of actual offsets for all of the observed tiles is shown in Fig. 4.6. The median observed shift is 5.4 arcmin, for which the decrease in surface density from the optimum (i.e. a 1°5-diameter field) amounts to 20 per cent. For the worst-case offset of 11.6 arcmin, the additional decrease in surface density from the median is 21 per cent. This distribution of shifts accounts at least in part for the variation in the limiting observed $(u_J - bj)$ colour per tile.

In identifying suitable guide stars, four additional problems arise. First, the magnitude range of acceptable guide stars is quite narrow. Stars that are too faint are not detectable by the auto-guiding system. Conversely, the guiding system has problems finding the centroids of stars that are too bright. It is therefore neces-

77
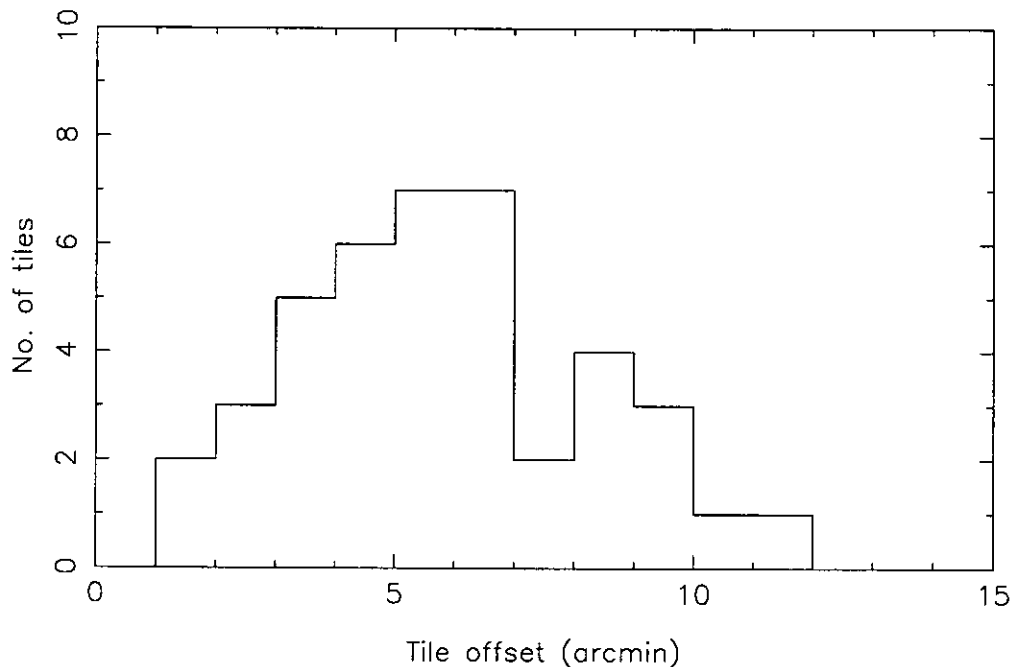
**Figure 4.6.** Distribution of offsets between preferred centres of tiles and actual centres after shift to nearest guide star for all observed tiles.

sary to choose guide stars with reliable magnitudes in a narrow range. Second, the photometric sequences used here cover the range $\sim$ 15–21 mag, so the photometric calibration of the SuperCOSMOS data at guide-star magnitudes is poor, and in any case does not include direct $R$ magnitudes. Third, it is critical that the guide stars and candidates be in exactly the same astrometric frame. The true astrometric positions are much less important than the relative positions, since errors in the former are removed when the telescope is centred on the guide star. Fourth, variable stars may change in magnitude between the catalogue epoch and the time of observation to fall outside the required magnitude range. However, significant variability is rare. For example, $\lesssim$ 7 per cent of stars in the *HIPPARCOS* catalogue are classified as variable at any level.

To try to avoid the first two of these problems (magnitude range and reliability), guide stars were selected from other catalogues with more reliable photometry at $R \simeq 14$. For the 1996 and 1997 observations, guide stars were selected from the HST Guide Star Catalogue (Lasker et al. 1990), which includes the $B$ magnitude and $(B - V)$ colour for each star, from which the stellar spectral type and hence $R$

magnitude were deduced. For the 1998 observations, the USNO-A V1.0 catalogue (Monet et al. 1996) was used, as it contains calibrated $R$ magnitudes. In all cases, a few of the guide stars were found in practice to be too faint for good automatic guiding, although it is not known if this was due to poor photometry or variability in the star. Telescope guiding for these tiles required heroic efforts from the telescope operators to keep the target fibres on objects being observed, for which thanks are due. To avoid the third problem (astrometric frame), each chosen guide star was matched to the corresponding object in the calibrated SuperCOSMOS data, and the positions from SuperCOSMOS (1996 and 1997 observations) or ASTROM (1998 observations) were used in the observing plan. This is a partial solution, since stars with these magnitudes are saturated on the UKST plates used, so the measured centroid may not be perfect (possible solutions to this problem were discussed in §3.3.4).

In all cases, stars of early spectral type were preferred, to maximize their distance for the required magnitude range and hence minimize any proper motion errors from the difference in epoch between the UKST plates and the spectroscopic observations ($\lesssim$ 20 yr). It is not clear how to avoid variable stars. Wide-field catalogues that include indications of variability, such as the Tycho catalogue (Hog et al. 1997), do not go faint enough, and a campaign to specifically identify variable stars to be avoided seems excessive. Choosing to use brighter stars only exacerbates the problem of increasing tile sizes because of their lower surface density.

### 4.3.4 Spectrophotometric flux calibration stars

Spectrophotometric flux calibration of the Fruit & Fiber spectrograph is naturally more complicated than for a standard slit spectrograph because it has 120 paths to calibrate. The instrument was designed principally to collect galaxy redshifts, for which accurate flux calibration was not required. The 2D-Frutti detector has an upper limit on the acceptable photon count rate that limits it to direct observations of stars of $m \gtrsim 14$, and there are presently no published spectrophotometric standard stars that faint that are accessible from Las Campanas. Accurate *absolute* flux calibration also relies on perfect centring of the standard and target objects on the fibre (§3.3), which cannot be guaranteed with this instrument.
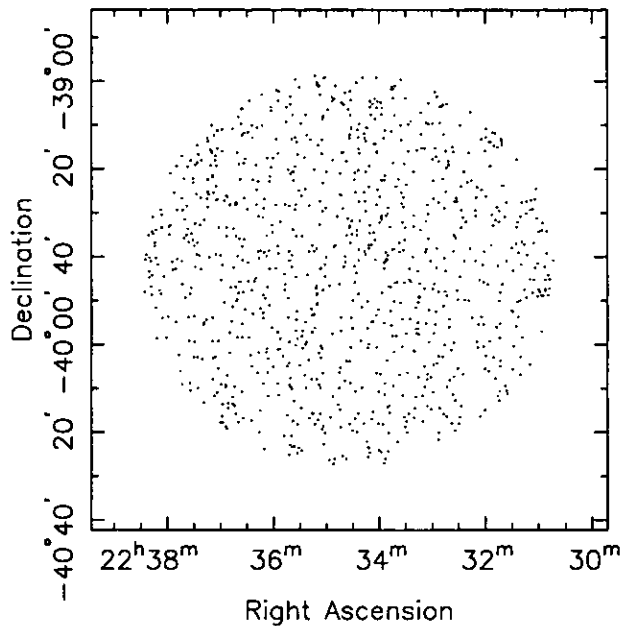
**Figure 4.7.** Positions of the 951 candidates in the F345 complete sample in the 1998 observing plan. This diameter of the circle containing the candidates is $1°5$.

If the probably reasonable assumption is made that all of the fibres have the same shape passband but differ in total throughput, then it is possible to use sky-line measurements to determine the relative throughput of the fibres (e.g. Lissandrini et al. 1994). The problem is then reduced to determining the shape of the instrument passband for a sample of fibres. An attempt to achieve this was made during the 1998 observations, and is described in detail in §4.6.4.

## 4.4 F345 observing plans

Candidates for observation in the F345 complete sample (§2.4.2) were selected from the SuperCOSMOS database from the paired J and R plate databases (table 3.3). The actual centre of the observed field, dictated by the guide star choice, was $22^h34^m35^s$, $-39°42'58'$ ($22^h31^m41^s$, $-39°58'29''$ in B1950 coordinates). All objects with $17 \leq b_J \leq 20$ in a $1°5$-diameter circle about the field centre were selected. Candidates were sorted into ascending $b_J$ magnitude, and allocated to tiles (all in the same sky position) for observation. After the initial allocation to tiles, much care was taken to ensure that a complete sequence of candidates was maintained after elimination of fibre collisions. The final range of candidates allocated to fibres covered $b_J = 17.0$ to $b_J = 19.10$. Their positions are shown in Fig. 4.7.

**Table 4.1**: CUQS observations in 1996 March 13–15. The tile centres are the central guide star positions. The tile names are as used in the catalogue and consist of the observed year, night and observing plan sequence numbers. The tile numbers refer to the programme area (P) and control area (C) tiles in Fig. 4.1. The FWHM seeing disk sizes were recorded by a monitor at the Swope telescope at Las Campanas Observatory. All tiles contain 112 candidates unless noted.

| Tile centre | | Tile | Tile | Exposure | Seeing | |
|---|---|---|---|---|---|---|
| $\alpha$ $(^{h}{:}^{m}{:}^{s})$ | $\delta$ $(^{\circ}{:}'{:}'')$ | Name | No. | time (s) | (arcsec) | Notes |
| $10:42:42$ | $+04:45:14$ | 1996.1.1 | P37 | $1800+1800$ | 1.6 | |
| $10:45:49$ | $+05:40:06$ | 1996.1.2 | P46 | $2400+2400$ | 1.2 | |
| $10:39:11$ | $+03:50:30$ | 1996.1.3 | P28 | $2400+2400$ | 1.5 | |
| $11:09:10$ | $-29:33:50$ | 1996.1.4 | C12 | $2700+2700$ | 1.6 | |
| $10:48:27$ | $+03:07:34$ | 1996.2.1 | P30 | $2700+2700$ | 2.9 | |
| $10:43:46$ | $+03:23:02$ | 1996.2.2 | P29 | $2700+2700$ | 1.6 | |
| $10:48:02$ | $+04:25:25$ | 1996.2.3 | P38 | $2700+2700$ | 1.7 | |
| $11:06:30$ | $-30:37:04$ | 1996.2.4 | C6 | $3000+3000$ | 2.1 | |
| $10:36:14$ | $+06:14:36$ | 1996.3.1 | P44 | $2400+2400$ | 2.9 | 111 cands. |
| $10:37:26$ | $+05:13:39$ | 1996.3.2 | P36 | $2700+2700$ | 1.7 | |
| $10:41:17$ | $+06:03:26$ | 1996.3.3 | P45 | $2700+2700$ | 1.6 | |
| $11:11:57$ | $-30:34:47$ | 1996.3.4 | C7 | $2700+3600$ | 1.9 | |

## 4.5 Spectroscopic observations

All observations with the Fruit & Fiber spectrograph were made using a grating with 300 lines mm$^{-1}$, blazed at 5000 Å, producing a mean dispersion of 6.1 Å pixel$^{-1}$. The grating angle used, 5°, put the full instrument response range of $\sim$ 3200–7400 Å onto the detector. Tables 4.1–4.3 give details of the exposures made in each year, which may be cross-referenced to Fig. 4.1 for their positions on the sky. In general, the tiles observed each year were ordered from west-most to east-most through the night to minimize the air mass through which the exposures were made.

Spectra for a total of 4588 CUQS candidates were obtained. Determining the area of sky observed is complicated by the tile shapes, the differences in sizes between tiles, and the degree of overlap between adjacent tiles. A Monte Carlo method, based on the actual tiles observed, was used to estimate the areas covered. For the 3144 spectra obtained in the 1996 plus 1997 observations, which are analysed together in the following chapters, the area observed was found to be 27.41 ± 0.02 deg$^2$ in the programme area and 8.38 ± 0.03 in the control area. Adding the 1444 spectra from the 1998 observations increases the total areas observed to 40.50 ± 0.05 deg$^2$ in the programme area and 13.50 ± 0.05 deg$^2$ in the control area.

**Table 4.2**: CUQS observations in 1997 March 11-14. Notes as for table 4.1. Where tile numbers are marked =, data were replaced by observations in 1998 (see text). Due to bad weather, tile 1997.2.1 was rescheduled and exposed on night 3, and tile 1997.4.3 was not exposed.

| Tile centre $\alpha$ ($^{\mathrm{h}}{:}^{\mathrm{m}}{:}^{\mathrm{s}}$) | Tile centre $\delta$ ($^{\circ}{:}'{:}''$) | Tile Name | Tile No. | Exposure time (s) | Seeing (arcsec) | Notes |
|---|---|---|---|---|---|---|
| 10 : 47 : 33 | +09 : 09 : 24 | 1997.1.1 | P68 | 2700 + 2700 | 1.3 | |
| 10 : 39 : 52 | +07 : 13 : 39 | 1997.1.2 | P53 | 2700 + 2700 | 1.3 | |
| 10 : 43 : 35 | +08 : 14 : 07 | 1997.1.3 | P62 | 2700 + 2700 | 1.3 | |
| 11 : 09 : 18 | −31 : 44 : 34 | 1997.1.4 | C2= | 2700 + 2700 | 1.4 | |
| 10 : 45 : 17 | +06 : 54 : 19 | 1997.2.1 | P54= | 3600 | 2.2 | 111 cands; N3. |
| 10 : 48 : 30 | +07 : 59 : 46 | 1997.2.2 | P63 | 2780 + 2700 | 1.4 | |
| 10 : 50 : 03 | +06 : 32 : 43 | 1997.2.3 | P55= | 2700 + 2700 | 1.4 | |
| 11 : 14 : 20 | −29 : 30 : 58 | 1997.2.4 | C13 | 2700 + 2700 | 1.4 | |
| 10 : 53 : 31 | +07 : 37 : 13 | 1997.3.1 | P64= | 2400 + 2400 | 2.2 | |
| 10 : 51 : 15 | +05 : 13 : 44 | 1997.3.2 | P47 | 2400 + 2400 | 1.5 | |
| 10 : 54 : 33 | +06 : 24 : 07 | 1997.3.3 | P56 | 2400 + 2400 | 1.5 | |
| 11 : 14 : 54 | −31 : 43 : 11 | 1997.3.4 | C3 | 2700 + 2700 | 1.9 | |
| 10 : 52 : 24 | +04 : 08 : 53 | 1997.4.1 | P39 | 2700 + 2700 | − | |
| 10 : 56 : 11 | +05 : 03 : 11 | 1997.4.2 | P48 | 2700 + 2700 | − | |
| 11 : 00 : 02 | +05 : 44 : 58 | 1997.4.3 | P57= | − | − | Not exposed. |
| 11 : 17 : 13 | −30 : 44 : 55 | 1997.4.4 | C8 | 2700 + 2700 | − | |

In addition, spectra for the brightest 768 candidates in the F345 sample were obtained in the 1998 observations. For this field, the area observed is simply a circle of diameter $1°5$ with an area of 1.77 deg$^2$. All objects in the range $17.00 \leq b_{\mathrm{J}} \leq 18.76$ were observed.

## 4.6  Spectral data reduction

### 4.6.1  Spectrum extraction

An example of one frame of raw spectroscopic data from the Fruit & Fiber spectrograph is shown in Fig. 4.8. The fibre input to the spectrograph, the image intensifier chain, and the 2D-Frutti detector, make these data quite different to those from a standard single-slit instrument with a CCD detector. Data reduction is therefore also quite different to 'normal' procedures. The photon counting system has zero bias, and experiments showed that the detector has an essentially zero dark count rate, so no bias or dark corrections are necessary. The detector system also discriminates against cosmic-ray hits, so no 'cleaning' is required during reduction. There

**Table 4.3**: CUQS and F345 complete sample observations in 1998 May 17-21. Notes as for table 4.1. Tiles numbered F are in the F345 complete sample. Due to bad weather, tile 1998.4.5 was rescheduled and exposed on night 5, and tiles 1998.5.3, 1998.5.4 and 1998.5.5 were not exposed.

| Tile centre $\alpha$ ($^h\!:\!^m\!:\!^s$) | $\delta$ ($^\circ\!:\!'\!:\!''$) | Tile Name | Tile No. | Exposure time (s) | Seeing (arcsec) | Notes |
|---|---|---|---|---|---|---|
| 10 : 53 : 46 | +02 : 47 : 05 | 1998.1.1 | P31 | 2700 | 1.0 | |
| 10 : 57 : 18 | +03 : 42 : 35 | 1998.1.2 | P40 | 5400 | 1.0 | |
| 11 : 09 : 15 | −31 : 39 : 56 | 1998.1.3 | C2 | 2700 | 1.0 | |
| 22 : 34 : 35 | −39 : 42 : 58 | 1998.1.4 | F | 4800 | 1.0 | 95 cands. |
| 22 : 34 : 35 | −39 : 42 : 58 | 1998.1.5 | F | 4800 | 1.0 | 96 cands. |
| 10 : 45 : 17 | +06 : 54 : 20 | 1998.2.1 | P54 | 5400 | 1.2 | 111 cands. |
| 10 : 58 : 50 | +07 : 07 : 23 | 1998.2.2 | P65 | 5400 | 1.2 | |
| 11 : 12 : 24 | −28 : 24 : 58 | 1998.2.3 | C17 | 3000 | 1.2 | |
| 22 : 34 : 35 | −39 : 42 : 58 | 1998.2.4 | F | 4200 | 1.2 | 101 cands. |
| 22 : 34 : 35 | −39 : 42 : 58 | 1998.2.5 | F | 5003 | 1.2 | 99 cands. |
| 10 : 50 : 12 | +06 : 26 : 48 | 1998.3.1 | P55 | 5400 | 1.0 | 111 cands; cirrus. |
| 11 : 00 : 20 | +06 : 01 : 13 | 1998.3.2 | P57 | 6000 | 1.0 | Cirrus. |
| 11 : 09 : 15 | −31 : 39 : 56 | 1998.3.3 | C2 | 4200 | 1.0 | Cirrus. |
| 22 : 34 : 35 | −39 : 42 : 58 | 1998.3.4 | F | 5400 | 1.0 | 94 cands. |
| 22 : 34 : 35 | −39 : 42 : 58 | 1998.3.5 | F | 5400 | 1.0 | 96 cands. |
| 10 : 53 : 40 | +07 : 26 : 06 | 1998.4.1 | P64 | 7200 | 2.0 | |
| 11 : 00 : 47 | +04 : 40 : 17 | 1998.4.2 | P49 | 5400 | 2.0 | Cirrus. |
| 11 : 12 : 24 | −28 : 24 : 58 | 1998.4.3 | C17 | 2700 | 1.5 | Cirrus. |
| 22 : 34 : 35 | −39 : 42 : 58 | 1998.4.4 | F | 5400 | 1.5 | 97 cands. |
| 22 : 34 : 35 | −39 : 42 : 58 | 1998.4.5 | F | 7200 | 1.0 | 90 cands; N5. |
| 10 : 52 : 31 | +08 : 45 : 01 | 1998.5.1 | P69 | 6900 | 1.5 | Variable cloud. |
| 10 : 57 : 43 | +08 : 18 : 15 | 1998.5.2 | P70 | 5400 | 1.5 | Variable cloud. |
| 11 : 19 : 60 | −31 : 46 : 19 | 1998.5.3 | C4 | − | − | Not exposed. |
| 22 : 34 : 35 | −39 : 42 : 58 | 1998.5.4 | F | − | − | Not exposed. |
| 22 : 34 : 35 | −39 : 42 : 58 | 1998.5.5 | F | − | − | Not exposed. |

is no manoeuvre on this instrument equivalent to widening the slit in a single-object spectrograph to illuminate wider regions on the detector with a flat-field image. Sky subtraction depends on the spectra in individual apertures (i.e. the portions of the image containing spectral information) whose fibres were pointed at (nominally) blank sky, instead of the outer portions of a single-slit aperture.

Variations in the instrument flat-field response are not completely static at the output pixel level, as with a CCD, because the detector position is continuously dithered through a raster pattern (with respect to the image intensifier output) during exposures to improve the post count-event recovery. Static defects in the image intensifier chain before the detector are spread over small areas of the output by the detector dither. There are several consistent flaws detectable in the raw
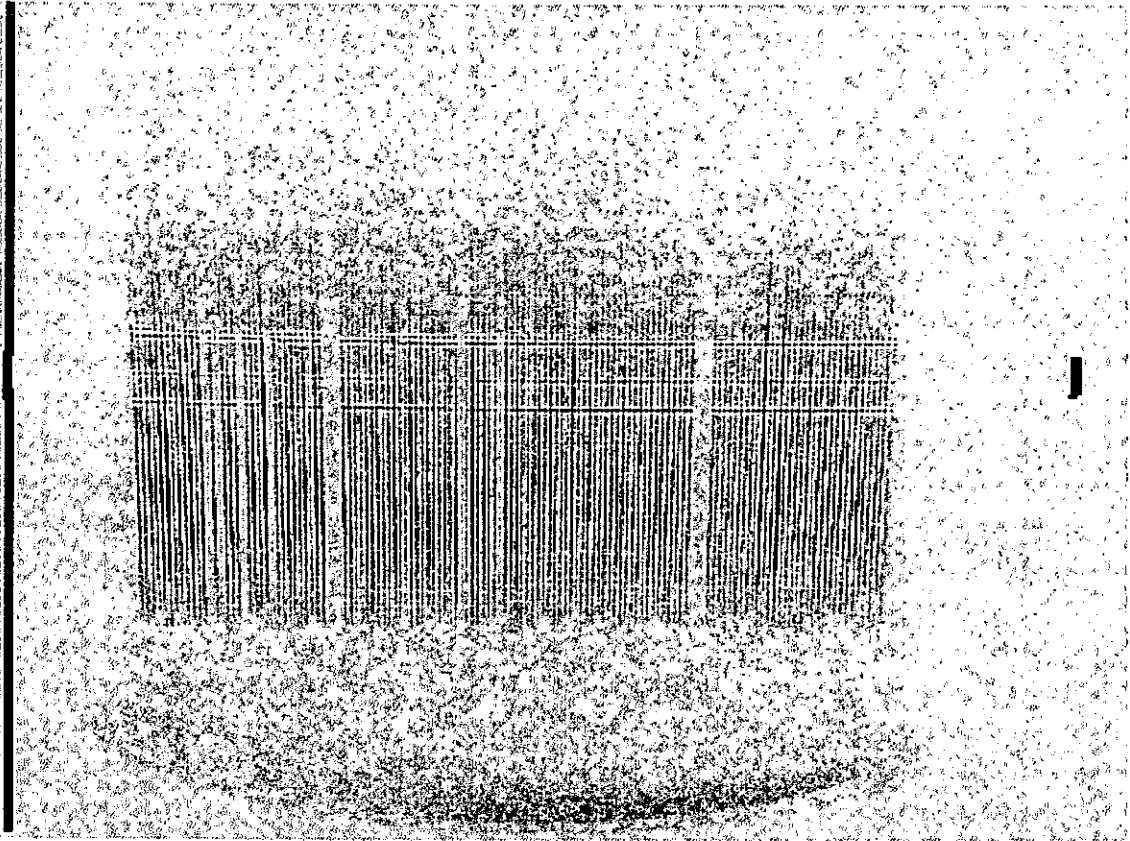
**Figure 4.8.** An example of raw spectroscopic data from the Fruit & Fiber instrument. Each exposure produces one data frame like this, each of which is 2048 by 1520 pixels in size. The image here is a negative, so darker means more counts. The vertical stripes are the 128 spectra, with the long wavelength end at the top. The horizontal dark bands across all the spectra are sky lines. The grey arc and the vertical dark lines are instrumental artifacts. The two broad gaps between spectra are a feature of the fibre spacing in the spectrograph slit, while the individual missing spectra correspond to broken fibres. Some resolution has inevitably been lost in this reproduction.

images. Rotating the grating to high order to provide more even illumination in the dispersion direction has the unfortunate side effect of shifting and rotating the apertures, thought to be due to a slight misalignment between the plane of the grating and the axis of the grating rotator assembly. These problems were not fully understood before the 1996 observations, and the flat-field images made that year were unusable because a different grating angle was used. The adopted procedure for the 1997 observations for removing flat-field variations in fibre apertures was to use the IRAF APFLATTEN task with flat-field images exposed with the grating angle unchanged from that used for the object exposures. The flattened flat looks very smooth, and clearly shows the removal of an image-wide horizontal defect around

6000 Å, several small isolated defect areas, and all pixel-level variations within the apertures.

Reduction of the flattened images was based on the sequence of the DOFIBERS task in the NOAO.IMRED.SPECRED package of IRAF (Valdes 1992). Essentially the same procedure was followed for each year's data, except as noted. The exposure-to-exposure (and, in 1997, night-to-night) stability of the images measured from the aperture traces and sky lines is excellent, with $\ll$ 1 pixel shifts. The aperture for each fibre was traced by fitting a polynomial to a sum of all images. Uncalibrated 1-D spectra were then extracted by unweighted summation of the pixels across each aperture.

## 4.6.2 Wavelength calibration

In the 1996 observations, a HeNe arc lamp was used for wavelength calibration. The wavelength axis of the extracted 1-D spectrum from each fibre was calibrated using long-exposure arcs to determine the dispersion function. A 6-term Chebyshev polynomial was fitted to the 21–24 arc lines identified in each aperture, with separate fitting parameters for each aperture in each of the long arcs. The mean dispersion was 6.1 Å pixel$^{-1}$ and the mean r.m.s. uncertainty in the fit to all apertures was 0.62 Å (maximum 0.94 Å). The wavelength range for identified lines was 3389–7439 Å. For night 1, only one long-exposure arc was recorded with the telescope at the zenith (i.e. $\delta = -29°$), which was used for all exposures from that night. For nights 2 and 3, a long arc exposure was recorded with the telescope at each of the field-centre declinations (i.e. $+5°$ for field 927, $-30°$ for field 438), and the appropriate arc was used for each tile. On each night, short-exposure arcs taken between the pair of exposures for each tile were used to check for zero-point shifts. Zero-point shifts were measured using three bright arc lines that were visible in all fibres. The shifts between the arcs at different declinations and between the zero-point checks were found to be $0.02 \pm 0.1$ pixels, all consistent with zero.

For the 1997 observations, a CuAr hollow-cathode lamp was used as a wavelength reference source. Similar procedures to those used in 1996 were followed for wavelength calibration. The CuAr lamp provided more lines than the HeNe lamp (typically 35 were identified in each aperture) over a wider wavelength range

(3248–8265 Å). The full range of r.m.s. errors between the measured and fitted CuAr wavelengths for all 120 working apertures was 0.45–0.98 Å, with a mean of 0.64 Å.

### 4.6.3 Sky subtraction

Wyse & Gilmore (1992) have provided a comprehensive discussion on the problems and methods associated with sky subtraction with fibre-input spectrographs. For example, the observed relative intensity of the night sky lines (e.g. the ratio of [O I] $\lambda5577$ to [O I] $\lambda6300$) clearly varies from exposure to exposure depending on air mass and sky conditions. The observations reduced here follow the Wyse & Gilmore recommendations to record the sky spectrum at the same time as the object+sky spectra on spatial scales within a few degrees of each other. However, no attempt was made in the observations to record the *variations* in sky across the field of view of the telescope. In addition, no attempt has been made in these reduction procedures to correct for the 'instrumental sky' due to scattered light between adjacent fibres. Examination of the raw data shows that the scattered light contribution in each aperture is only a few per cent for the faintest objects observed here.

A composite sky spectrum for each exposure was made from the sum of the spectra through the designated sky fibres. A standard sky subtraction method for Fruit & Fiber spectra, as used for the Las Campanas Redshift Survey (Shectman et al. 1996) and discussed in general by Lissandrini et al. (1994) and Cuby & Mignoli (1994), is to normalize the composite sky spectrum to each object+sky spectrum based on the flux in the [O I] $\lambda5577$ sky emission line in each fibre. This leads to the aesthetically pleasing removal of the strongest ([O I] $\lambda5577$) sky emission line, but at the possible cost of leaving a large total sky energy contribution across the rest of the wavelength range. A side issue, not noted in previous studies, is that relying on a single sky emission line for normalization, especially in automated procedures, is problematic for observations of emission-line object spectra, since there may be overlaps between the sky and object emission lines. In an attempt to improve the subtraction of the total sky energy, the sky and object exposures were therefore normalized to the sum of the flux in both the [O I] $\lambda5577$ and [O I] $\lambda6300$ lines, using an automated procedure to fit equal-width Gaussian profiles to those two lines. Every normalization was checked visually for problematic sky and object

emission coincidence and manual corrections were made in the few cases detected. The resultant sky-subtracted spectra show a residual flux in the 5577 Å line of $\lesssim 1$ per cent of the initial object+sky line flux, which is taken as representative of the net residual sky energy in the whole spectrum. The sky-subtracted sky spectra are similarly all close to zero with a mean variance per pixel of $\sigma^2 \simeq 10$.

## 4.6.4 Flux calibration

The CALIBRATE task was used to correct the individual wavelength-calibrated and sky-subtracted spectra for atmospheric extinction, using a standard CTIO extinction curve (no curve is available for LCO, but CTIO is nearby and at similar altitude).

As discussed in §4.3.4, flux calibration of Fruit & Fiber spectra is considerably more difficult than for conventional slit spectrographs. As an interim solution, an approximate instrument flux calibration curve was computed from the 1996 observations. A total of 19 quasars observed in the the 1996 CUQS run had previously been observed on a single-slit spectrograph and their spectra had been spectrophotometrically calibrated (L.E. Campusano & R.G. Clowes, private communication, 1996 May 29). The median ratio of the calibrated to uncalibrated spectra was calculated, and then smoothed by convolution with a Gaussian with a FWHM of 200 Å. The curve was then normalized to have unit integral over the range 3200–7250 Å. The result is shown in Fig. 4.9. The response covers the range $3000 \lesssim \lambda \lesssim 7400$ Å, peaking at $\sim 4250$ Å. This response curve has been used to calibrate all of the spectra in the survey.

An experiment was attempted in the 1998 observations to produce a more accurate response curve by illuminating circles of fibers with the de-focussed image of a spectrophotometric standard star, the $V = 11$ white dwarf EG274 (Hamuy et al. 1992). A white dwarf standard was chosen because it has sufficient near-ultraviolet emission to provide calibration down to the blue limit of the instrument response ($\sim 3000$ Å). The observing plans included specifications for a circle of holes in each fibre plug plate to take six fibres at a time. The circle radius, 0.25 inches, was calculated to be the radius of the output cone of the telescope at close to the maximum travel of the secondary mirror focussing drive. The intention was that the circle was first to be centred on the standard star by placing one of the plug-plate rotation
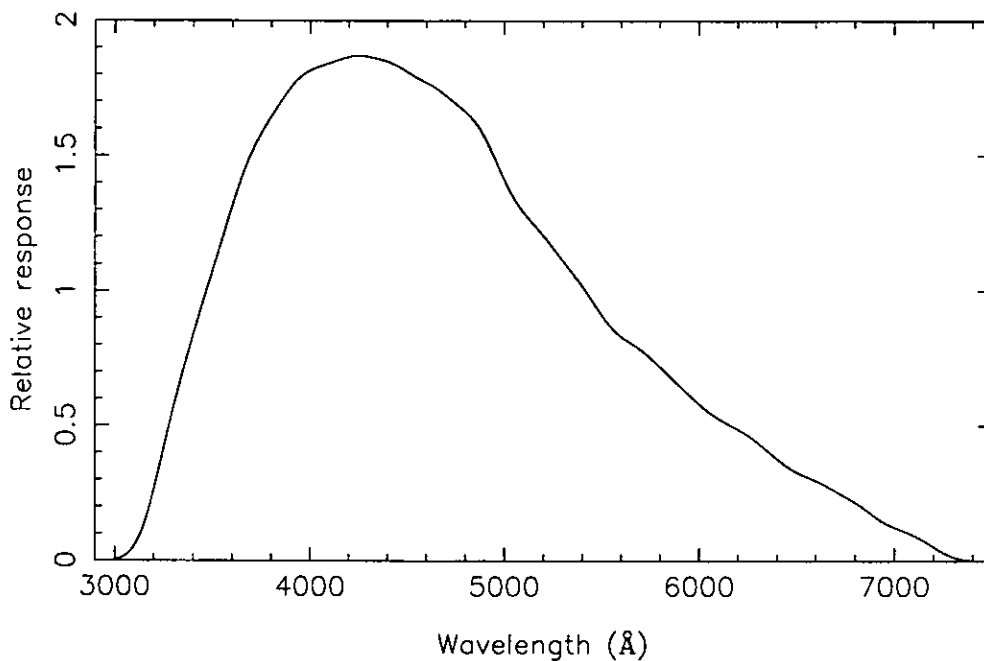
**Figure 4.9.** Response curve of the Fruit & Fiber instrument derived from the 1996 observations (see text).

adjustment fibre bundles in a hole in the centre of the circle and locating the star using the telescope guide camera. The telescope was then to be de-focussed until a signal was detected in the spectrograph from six object fibres placed in the holes on the periphery of the circle. Unfortunately, due to a mistake in the plate-drilling procedures, a circle of holes was drilled in only one of the five plates delivered to LCO. Examination of the image from the one test exposure made suggests that the procedure is successful, but the data have not yet been fully reduced and applied. Circle-of-fibres observations will be included in future CUQS observing plans, and the derived response will be used to recalibrate the earlier spectra.

### 4.6.5 Co-addition of calibrated spectra

In all cases where multiple exposures were made of the same tile, the spectra for each object from the separate calibrated spectra were co-added to produce the final reduced spectra. The reduced spectra were all re-binned to a linear 2 Å pixel$^{-1}$, and have a typical signal-to-noise (s/n) ratio of 8 pixel$^{-1}$. The wavelength range was trimmed to 3300–7000 Å (1996 observations) or 3200–7200 Å (1997 observations),

these being the reliable ranges for wavelength and flux calibration.

Examples of the spectra of quasars at a range of redshifts are shown in Fig. 4.10; examples of narrow emission-line galaxies are shown in Fig. 4.11 (see chapter 5 for details of redshift measurement and object classification). A full atlas of the spectra will be published once the survey is completed.
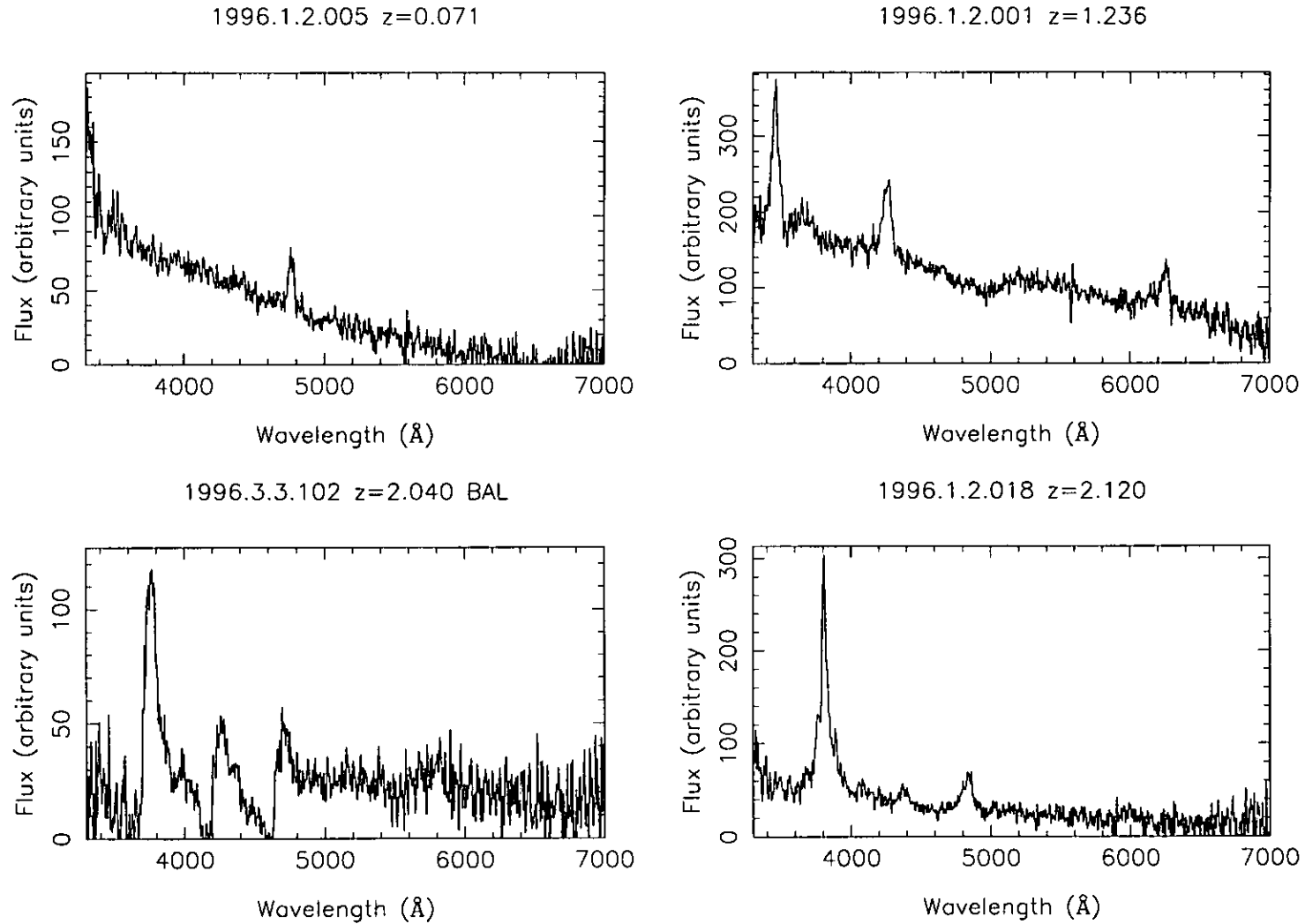
**Figure 4.10**: Examples of calibrated quasar spectra. Note the small residual flux in the [O I] $\lambda5577$ sky line in each spectrum, which has not been cropped in the plots. Top left: quasar at redshift $z = 0.701$; the main emission lines visible are Mg II $\lambda2798$ (measured at 4759 Å), and the red edge of the C III] $\lambda1909$ (near 3300 Å). Top right: quasar at $z = 1.236$; emission lines are C IV $\lambda1549$ (at 3464 Å), C III] $\lambda1909$ (at 4269 Å) and Mg II $\lambda2798$ (at 6257 Å). Bottom left: broad absorption-line quasar at $z = 2.04$; emission lines are Ly$\alpha$+N V $\lambda1216+1240$ (at 3770 Å), Si IV+O IV $\lambda1400$ (at 4259 Å) and C IV $\lambda1549$ (at 4698 Å). Bottom right: quasar at $z = 2.120$; emission lines Ly$\alpha$ $\lambda1216$ (at 3807 Å), N V $\lambda1240$ (at 3888 Å), Si IV+O IV $\lambda1400$ (at 4367 Å), C IV $\lambda1549$ (at 4835 Å), and C III] $\lambda1909$ (seen weakly at 5993 Å).
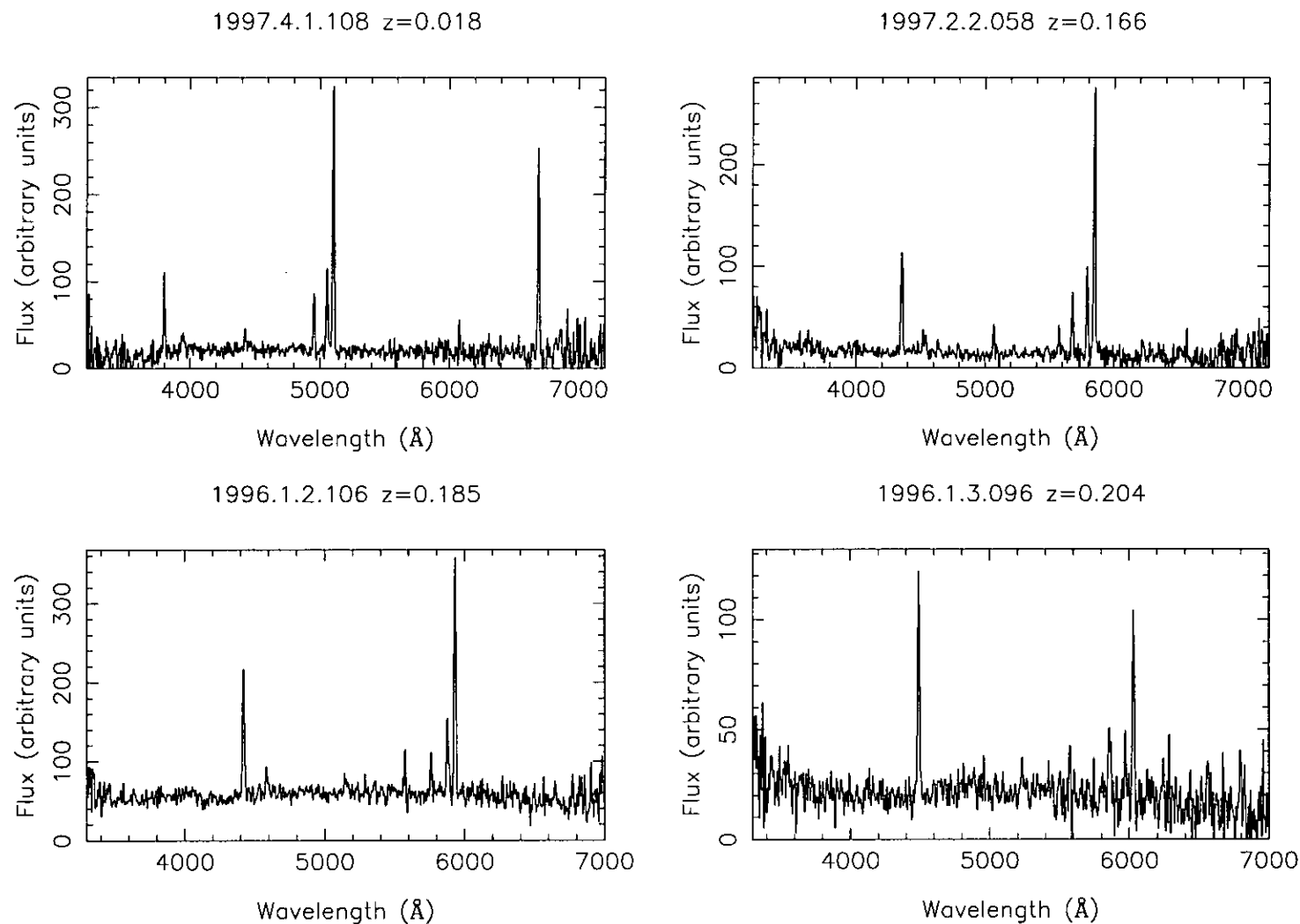
**Figure 4.11**: Examples of calibrated narrow emission-line galaxy (NELG) spectra. The main emission lines visible in each spectrum are [O II] $\lambda3727$, H$\delta$ $\lambda4340$, H$\gamma$ $\lambda4340$, H$\beta$ $\lambda4861$, the [O III] $\lambda\lambda4959$, 5007 doublet, and H$\alpha$ $\lambda6563$ (only visible in the top-left spectrum). These lines were measured at the mean redshifts indicated above each spectrum. Note the large variations in the line-strength ratios between the spectra.

# Chapter 5

# Properties of the CUQS catalogue

## 5.1   Chapter overview

Properties of the quasars and other emission-line objects in the CUQS catalogue after the analysis of the observations obtained in 1996 and 1997 are described. The methods used to identify emission-line spectra, to measure their redshifts and to calculate their absolute magnitudes are defined. The distribution of quasars and narrow emission-line galaxies on the sky and their number-counts as functions of redshift, colour and magnitude are presented and discussed. Finally, the identification of survey spectra of objects that do not show emission lines is briefly discussed.

## 5.2   Construction of the catalogue

### 5.2.1   Emission line identification and redshift measurement

The first step in the construction of the CUQS catalogue was to identify emission-line objects and to measure their redshifts. Plots of all of the reduced and calibrated spectra were visually inspected to identify objects showing, or suspected of showing, emission lines, and these spectra were subjected to further measurement. The positions of emission lines (both clear and suspected) were then measured, using the SPLOT task in IRAF. For approximately symmetric lines, SPLOT was used to fit a Gaussian profile to the line, to measure its central wavelength and FWHM. The continuum level was estimated from the line wings. For highly asymmetric lines and

**Table 5.1**: Laboratory wavelengths, $\lambda_0$, of the lines used to measure the redshifts of emission-line spectra (measured in vacuum for $\lambda_0 < 2000$ Å, in air otherwise). The approximate intensities relative to the combined Ly$\alpha$ and N v lines, applicable to broad-lined spectra, are taken from the composite quasar spectrum of Francis et al. (1991), except for H$\alpha$, which is take from Wills (1992).

| Source | $\lambda_0$ Å | Relative Intensity | Source | $\lambda_0$ Å | Relative Intensity |
|--------|--------|-----------|--------|--------|-----------|
| Ly$\alpha$ | 1216 | 100 | [O ii] | 3727 | < 1 |
| N v | 1240 | | H$\delta$ | 4102 | 3 |
| Si iv+O iv | 1400 | 19 | H$\gamma$ | 4340 | 13 |
| C iv | 1549 | 63 | H$\beta$ | 4861 | 22 |
| C iii] | 1909 | 29 | [O iii] | 5007 | 4 |
| Mg ii | 2798 | 34 | H$\alpha$ | 6563 | 50 |

lines showing strong adjacent absorption, the central wavelength was estimated by placing the SPLOT cursor on the peak of the line, as judged by eye, and the FWHM of the line was measured similarly from the line edges at the half-maximum above a visually estimated continuum level. A simple FORTRAN code was then used to find redshift correlations between the measured line positions and the positions predicted for red-shifted AGN emission lines. The lines used are listed in table 5.1.

This process of identification and measurement was performed independently by the present author and Dr Matthew J. Graham. Dr Roger G. Clowes then adjudicated on disputed identifications. Naturally, most of the disputes were in spectra with the lowest signal-to-noise ratios. To determine the efficiency of quasar detection, the individual identifications were subjected to a statistical analysis. The first person found 144 quasars, the second person found 141, and the third person found 144 quasars (not all the same). The sample common to the first two people contained 137 objects. The final catalogue contained 144 quasars. Application of the 'two-cut' method of Graham et al. (1999) then suggested that there are probably 148 quasars in total that *could* be detected in the spectra, so the detection efficiency is 144/148 = 0.97 (M.J. Graham, private communication, 1998 July 1). Failure to detect emission lines in the spectra is therefore not a likely source of significant incompleteness in the final catalogue.

As a convention, emission lines were defined as 'broad' if they had intrinsic (i.e. rest-frame) FWHM velocity of $v > 1000$ km s$^{-1}$, and 'narrow' otherwise. It was clear from the spectra that there were two populations of emission-line objects in

the survey: objects with spectra dominated by broad lines at redshifts $z \geq 0.228$, which were identified as quasars, and objects with narrow lines, at $z \leq 0.397$, which were identified as narrow emission-line galaxies (NELGs). There were two exceptions to this, both Seyfert 1-type spectra at low redshift showing a mix of broad and narrow lines: spectrum catalogue number 1997.1.1.047, with $z = 0.123$, and spectrum catalogue number 1997.1.2.012, with $z = 0.167$. These objects could be marginally included in the list of quasars on the basis of their line widths, but as their redshifts were $z \ll 0.4$, they were catalogued separately and excluded from the quasar analyses presented in chapters 6 and 7.

For each emission-line spectrum, the assigned redshift, $z$, and its standard deviation, $\sigma_z$, were calculated from all the identified lines. The r.m.s. spectrograph wavelength calibration uncertainty, $\sim 0.6$ Å, corresponds to a minimum redshift uncertainty $\Delta z \simeq 0.00012$ at the mean wavelength of the spectra ($\sim 5000$ Å). However, uncertainties due to the problems of finding the 'true' wavelength of asymmetric AGN lines, and the low s/n ratio for faint spectra, all considerably increase the redshift uncertainty for individual lines. In addition, AGN emission lines due to different ions probably originate in different physical regions of the quasar, adding Doppler shifts to the emission wavelengths due to local motions of the emitting gas (Corbin 1990), which results in each line in the spectrum from an AGN showing slightly different redshifts. If the redshift of two or more lines in a spectrum agreed, then the unweighted mean of the lines' redshifts was assigned to the object. Agreement between the redshifts from two or more lines was normally required. Where a single broad emission line was seen in the observed wavelength interval, the line was assumed to be Mg II $\lambda 2798$ and the uncertainty taken as $\sigma_z = 0.005$. For most quasars, the calculated uncertainty taking these factors into account was $\sigma_z \leq 0.005$. The worst uncertainties, for two quasars with highly asymmetric emission lines with adjacent broad absorption, was $\sigma_z = 0.03$. For all of the NELGs, $\sigma_z \leq 0.005$, and typically $\sigma_z = 0.002$. At the catalogue-mean quasar redshift, $z = 1.373$, the uncertainty in the comoving radial distance (appendix B) equivalent to $\sigma_z = 0.005$ is 4.1 $h^{-1}$ Mpc. For the NELGs, $\sigma_z \leq 0.002$ at mean $z = 0.135$ is equivalent to a radial uncertainty of 5.0 $h^{-1}$ Mpc. Note that the mean tangential positional uncertainty, $\Delta r = 0.69$ arcsec, corresponds to $\lesssim 0.01$ $h^{-1}$ Mpc at all redshifts in the survey.

## 5.2.2 Calculation of absolute magnitude

To examine the completeness of the survey sample and to construct volume-limited sub-samples, we need to know the luminosity of the objects in the survey, or equivalently, their absolute magnitudes. The absolute magnitude of each object, $M$, was calculated using

$$M = m - 5\log\frac{d_{\mathrm{L}}}{r_{10}} - k. \tag{5.1}$$

The first term on the right of Eqn. 5.1 is the $b_{\mathrm{J}}$ or $u_{\mathrm{J}}$ apparent magnitude taken from the photometric calibration of the survey input catalogue. The second term is the standard astronomical correction for the luminosity distance of the object, $d_{\mathrm{L}}$, to the distance for which absolute magnitudes are defined, $r_{10} \equiv 10$ pc. The calculation of $d_{\mathrm{L}}$ is explained in detail in appendix B, but note that $d_{\mathrm{L}}$ introduces cosmological parameters into the definition of $M$, for which we adopted the standard bland values ($\Omega_0 = 1$, $q_0 = 0.5$, $h = 1$, zero curvature). The third term is the $k$ correction, which corrects for the effect of redshift on filtered observations and depends on both the redshift of the object and its spectral energy distribution (SED). A full derivation of the general $k$ correction is given in appendix C. Here, we use the form applicable to spectra with a power-law SED, $f_\nu \propto \nu^\alpha$, where $\nu$ is the frequency, $f_\nu$ is the power per logarithmic frequency interval and $\alpha$ is a constant. This gives

$$k = -\tfrac{5}{2}(1 + \alpha)\log(1 + z).$$

The value of $\alpha$ must be determined from flux-calibrated observations. Here, we adopt the convenient value of $\alpha = -1$, which has been measured from the continuum of a high-resolution composite spectrum constructed from HST observations of 101 quasars with $0.3 \le z \le 3.7$ for intrinsic wavelengths $\lambda > 1038$ Å (Zheng et al. 1997). Note, however, that the literature contains a wide range of values for $\alpha$ in the ultraviolet to optical region of quasar spectra covering at least $-2.5 \lesssim \alpha \lesssim +2.0$ with no real fix on the origin of the differences (Francis et al. 1991; Natali et al. 1998; Wilkes 1999a). The spectrophotometric calibration of the CUQS quasars is not presently of sufficient quality to derive $\alpha$ accurately from these observations, so the specific choice of $\alpha$ used here is somewhat arbitrary. The additional small correction for the effect of quasar emission lines being redshifted through the filter passbands is dealt with in §7.4. No correction was made for galactic absorption.

## 5.3 Quasar selection function

An ideal survey would observe and identify all real quasars which meet the survey selection criteria. The ideal survey selection function, $S_I$, may be defined as the detected fraction of quasars such that $S_I = 1$ within the selection ranges and $S_I = 0$ otherwise. In reality, random uncertainties and systematic errors in the photometric and astrometric calibrations, source variability, adverse observing conditions and errors in data analysis all reduce the actual selection function from the ideal. Here, the expected effects of random uncertainties on the CUQS selection function are estimated by convolving the ideal 'rectangular' form of $S_I$ with Gaussian distributions of unit integral whose widths reflect the uncertainties in the variables.

For the CUQS, $S_I(b_J) = 1$ for $16 \leq b_J \leq 20$, $S_I(u_J - b_J) = 1$ for $(u_J - b_J) \leq -0.3$, and $S_I = 0$ outside those ranges. There are three principal stages at which $S_I$ is modified: during the selection of candidates, during observations, and during analysis of the spectra. In the selection of candidates, the largest uncertainties arise from photometric calibration and source variability. The uncertainties in the photometric calibration were derived in §3.4.6, finding $\Delta b_{J,cal} = 0.1$ mag and $\Delta(u_J - b_J)_{cal} = 0.16$ mag. Over the $\sim 10$ yr differences between the epochs of the UKST plates and the spectroscopic observations, quasars are known to show variations in flux with a standard deviation of $\sim 14$ per cent, equivalent to magnitude changes of $\Delta b_{J,var} = 0.16$ mag, and variations in colour with a standard deviation of $\sim 5$ per cent, equivalent to magnitude changes of $\Delta(u_J - b_J)_{var} = 0.06$ mag (Giveon et al. 1999). The standard deviation of the Gaussian, $g(b_J, \sigma)$, to be convolved with the $S_I(b_J)$ during candidate selection may be then estimated by

$$\sigma = \Delta b_{J,cal} + \Delta b_{J,var} = 0.26 \text{ mag}$$

which affects both the bright and faint ends of the $b_J$ selection range. The fraction of the integrated ideal selection function that remains after convolution is therefore

$$f_1 = \frac{\int_{16}^{20} S_C(b_J, \sigma = 0.26)\, db_J}{\int_{16}^{20} S_I(b_J)\, db_J} = 0.954$$

where the limits of integration are defined by the ideal selection range, and

$$S_C(x) = \int_{-\infty}^{+\infty} S_I(t)g(x - t, \sigma)\, dt$$

is the ideal selection function convolved with the errors. The result of this convolution is shown in Fig. 5.1. For the colour uncertainties, the standard deviation of the Gaussian to be convolved with $S_I(u_J - b_J)$ during candidate selection may be estimated by

$$\sigma = \Delta(u_J - b_J)_{cal} + \Delta(u_J - b_J)_{var} = 0.22 \text{ mag}$$

which affects the most-positive end of the $(u_J - b_J)$ selection. The fraction of the integrated ideal selection function that remains after convolution is therefore

$$f_2 = \frac{\displaystyle\int_{-1.7}^{-0.3} S_C(u_J - b_J, \sigma = 0.22)\, d(u_J - b_J)}{\displaystyle\int_{-1.7}^{-0.3} S_I(u_J - b_J)\, d(u_J - b_J)} = 0.947$$

where the lower limit of the integration was chosen to be the same as the most blue quasar observed and the upper limit is defined by the ideal selection criterion. The result of this convolution is also shown in Fig. 5.1.

During observations, the principal addition sources of incompleteness are the flux losses due to astrometric errors, source variability and adverse observing conditions, especially cloud and guiding errors. Each of these may cause the observed signal-to-noise ratio to fall below the minimum at which a spectrum may be identified as that of a quasar, which is taken here to be determined by $b_J = 20$. The effects of astrometric errors were discussed in §3.3. For the r.m.s. position errors in the CUQS astrometric calibration of 0.69 arcsec, it was shown that the fraction of light from a target object falling into the spectrograph fibre was 0.85, which is equivalent to a magnitude increase of $\Delta b_{J,ast} = 0.18$ mag. No formal measurement of the losses due to adverse observing conditions has been made, but most of the CUQS observations reported in chapter 4 were carried out in excellent sky conditions, although some problems were experienced with guiding, etc. The uncertainty in the losses due to adverse observing conditions is estimated, perhaps pessimistically, as $\Delta b_{J,obs} = 0.25$ mag. The standard deviation of the Gaussian to be convolved with $S_I(b_J)$ during observations may therefore be estimated by

$$\sigma = \Delta b_{J,ast} + \Delta b_{J,var} + \Delta b_{J,obs} = 0.59 \text{ mag}.$$
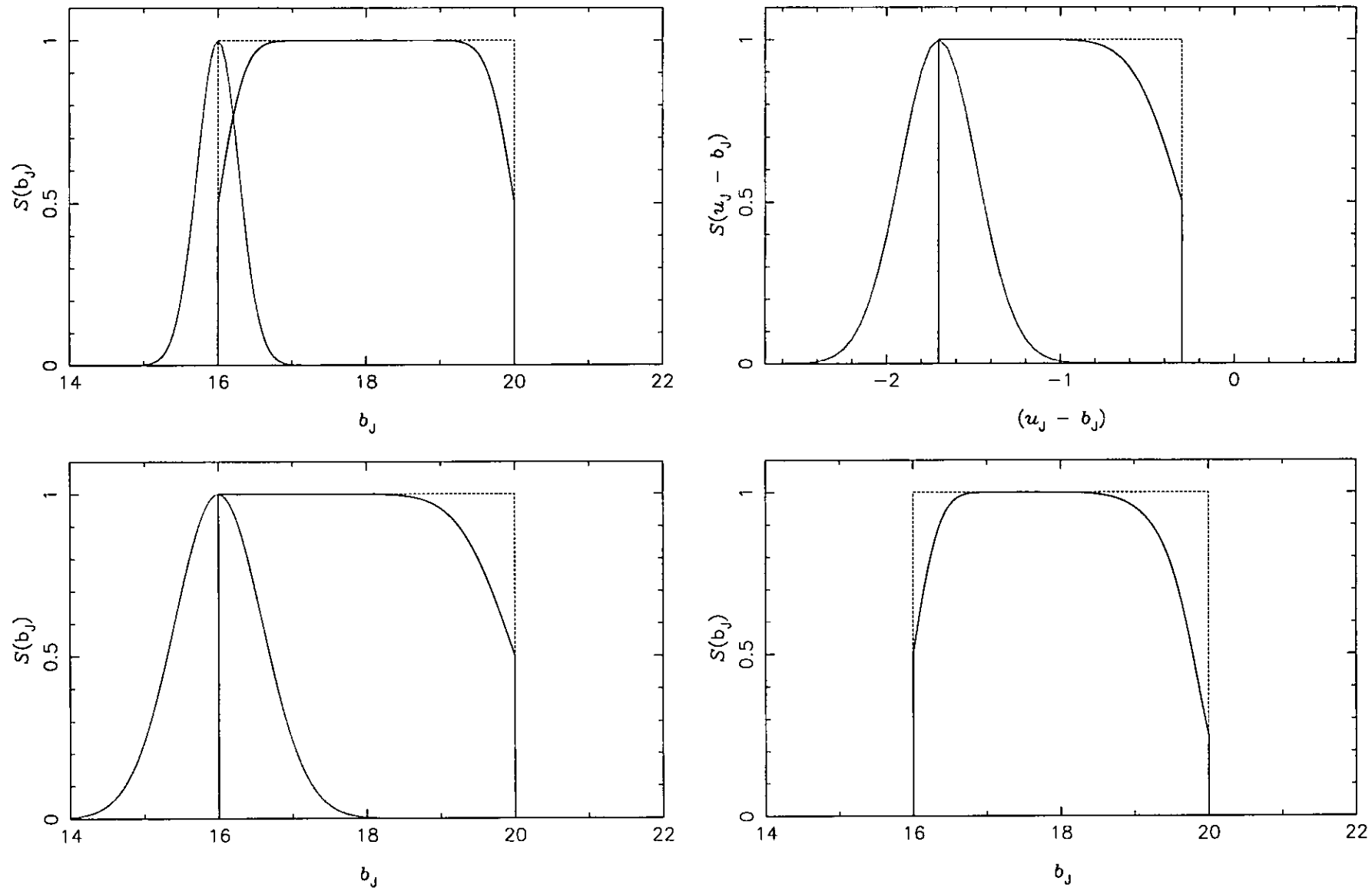
**Figure 5.1**: Deviations from the ideal survey selection function due to uncertainties in $b_J$ and $(u_J - b_J)$. In each panel, the ideal form, $S_I$, is shown by a dashed line, and the shape of the convolved Gaussian, $g$, is shown by the dotted line (shown here before normalization to unit integral). The solid line shows $S_C$, the convolution of $S_I$ with $g$ (see the text for details).

The result of this convolution is again shown in Fig. 5.1. The fraction of the observed candidates that reach the minimum signal-to-noise ratio may then be estimated by

$$
f_3 = \frac{\displaystyle\int_{16}^{20} S_C(b_J, \sigma = 0.59)\, db_J}{\displaystyle\int_{16}^{20} S_I(b_J)\, db_J} = 0.945.
$$

Combining the $b_J$ convolutions gives an integrated $S_C(b_J)$ selection fraction of $f_1 \times f_3 = 0.901$, the distribution of which is also shown in Fig. 5.1.

Finally, we must include the fraction of quasar spectra that were not identified as such during the data analysis. This was determined in §5.2.1 to be $f_4 = 0.97$. Combining all of these sources of incompleteness gives a total integrated fraction of $f_1 \times f_2 \times f_3 \times f_4 = 0.828$.

A good estimate of the maximum completeness of the CUQS after accounting for random uncertainties is therefore 83 per cent. Fig. 5.1 shows that incompleteness can be expected to most-strongly affect quasars with $b_J \gtrsim 19.5$. No attempt has been made at estimating incompleteness due to systematic errors. Variations in the quality of the photometric and astrometric calibrations with position in the SuperCOSMOS data, plus night-to-night variations in cloud, etc, could introduce tile-to-tile variations in completeness. The effects of such errors on the detection of quasar clustering is discussed in §6.9.

## 5.4 Properties of the quasar catalogue

The positions, magnitudes and redshifts of all 320 quasars detected in the 1996 and 1997 CUQS observations are tabulated in appendix A. Their distribution on the sky is shown in Figs. 5.2 (programme area) and 5.3 (control area). The combined distribution as functions of redshift, ultraviolet-excess colour and apparent and absolute magnitude are shown in Fig. 5.4. The sky distribution shows no obvious large-scale position-dependent inhomogeneities. The $N(z)$ distribution is similar to that found in other ultraviolet-excess surveys (Boyle et al. 1999; Croom 1997; Boyle et al. 1987) and is consistent with the expectation (Véron 1983) that $(U - B) \leq -0.3$ selects most quasars in the interval $0.4 \leq z \leq 2.2$ with rapid cut-off at $z > 2.2$. The median redshift of the quasars is $z = 1.41$. The $\log N(u_J - b_J)$ distribution shows that,
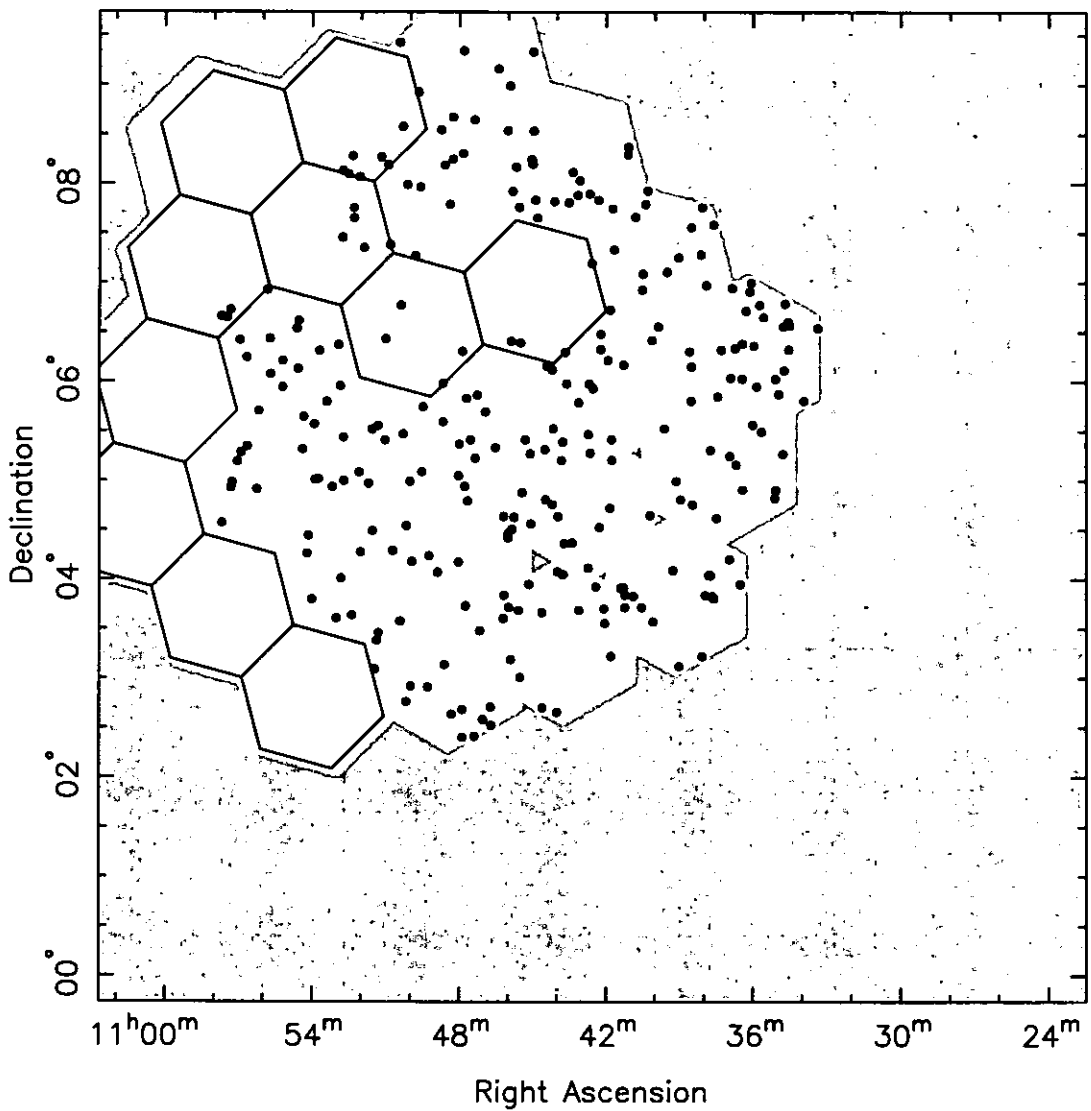
**Figure 5.2.** Positions of the 267 quasars in the programme-area catalogue from the 1996 and 1997 observations (dots). The white area shows the actual area observed in 1996, 1997 and 1998. The shaded area is the whole of the survey programme area. The outlined hexagons show the nominal positions of the tiles observed in 1998 that have not been analysed – the few quasars that appear in them come from the 1997 observations with astrometric problems (see §3.3) – and have been excluded from the analyses of structure. The actual area included in the structure analysis is shown in Fig. 6.2.

100
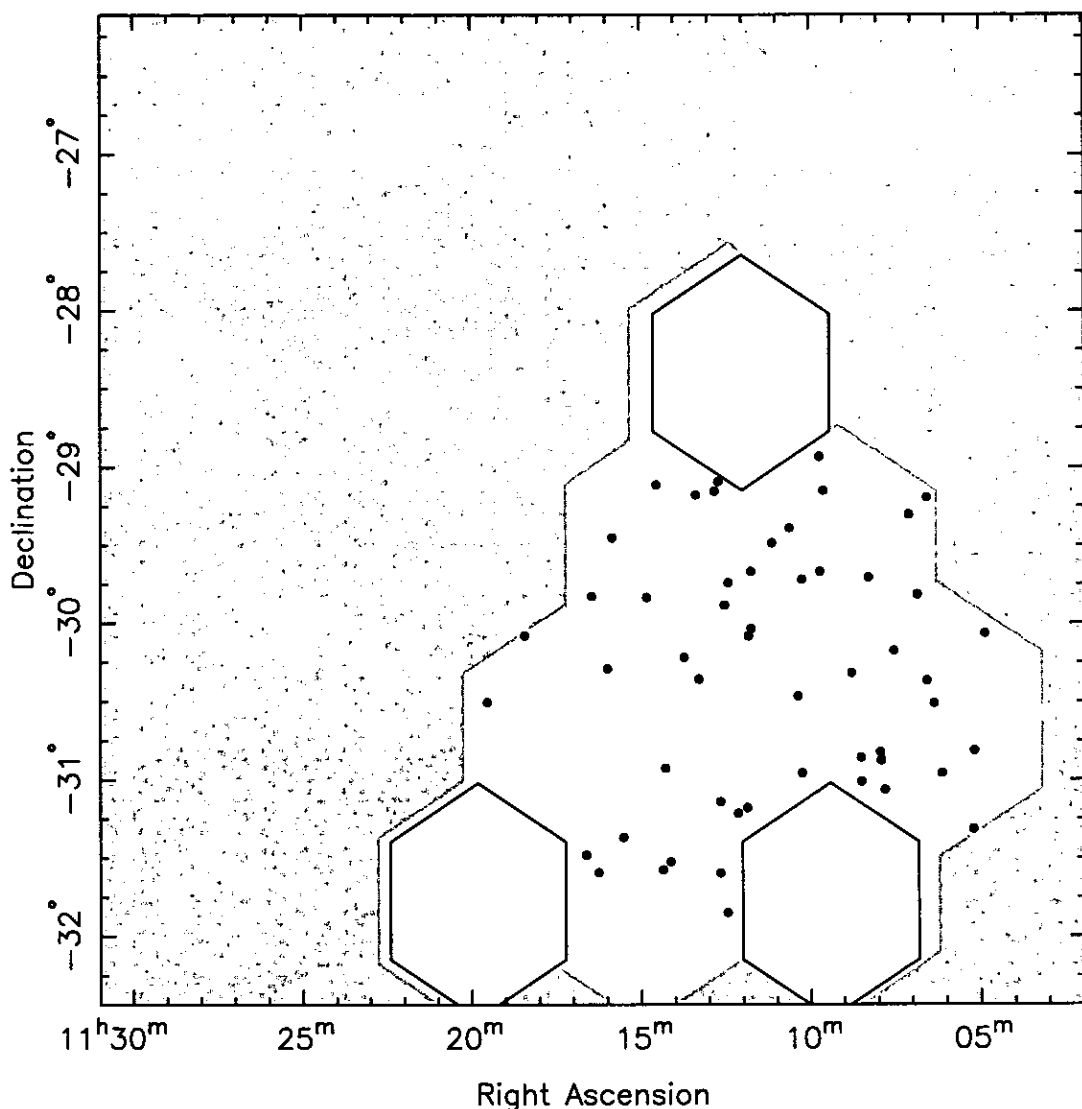
**Figure 5.3.** Positions of the 53 quasars in the control-area catalogue from the 1996 and 1997 observations. The legend is as for Fig. 5.2.

while the number of candidates continues to rise with increasing $(u_J - b_J)$ due to the increasing numbers of galactic stars included, the number of quasars detected falls rapidly at $(u_J - b_J) \gtrsim -0.9$. This suggests that few red quasars have been omitted from the survey candidate selection.

The expected selection function of quasars as a function of $b_J$ magnitude and $(u_J - b_J)$ colour has been discussed in §5.3. A preliminary analysis of the $\log n(b_J)$ and $\log N(u_J - b_J)$ distributions suggests that the observed distributions are close to those expected. The observed quasar absolute magnitude distribution peaks at $M_{b_J} = -24.5 \pm 0.1$. This is in excellent agreement with Eqn. 5.1, which predicts that all quasars with $z \leq 2.2$ and $M_{b_J} \leq -24.6$ should have apparent magnitudes

101
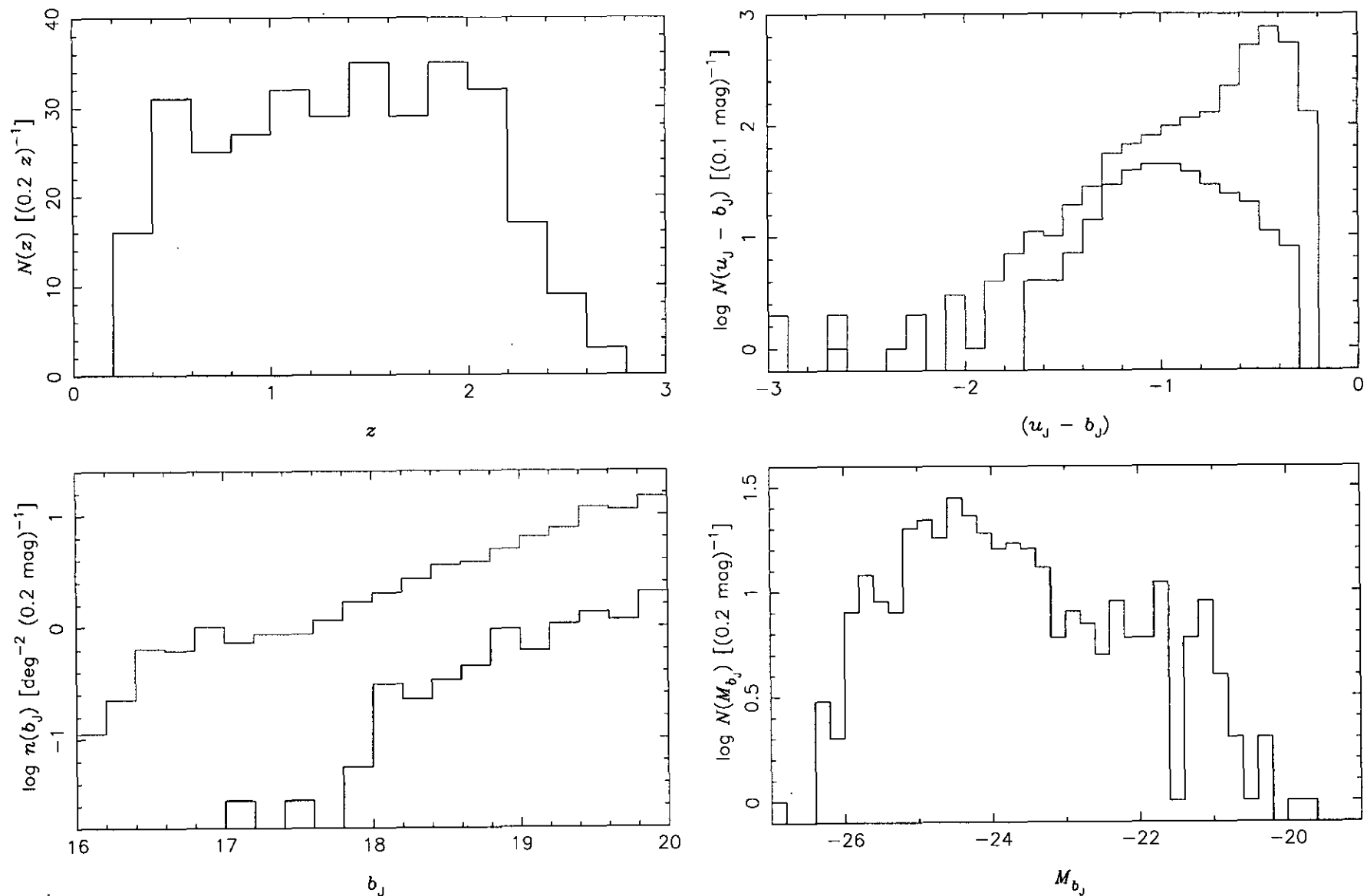
**Figure 5.4**: The distribution of the 320 quasars from the 1996 and 1997 observations as functions of: redshift $z$ (upper left); $(u_J - b_J)$ colour (upper right); apparent $b_J$ magnitude (lower left, expressed as a surface density); absolute $M_{b_J}$ magnitude (lower right). The solid lines relate to quasars and the dotted lines to observed candidates.

brighter than the survey candidate selection limit of $b_J = 20$, and suggests that there is no luminosity selection bias.

All of these conclusions suggest that the survey catalogue represents a homogeneous sample of the true quasar population for $0.4 \leq z \leq 2.2$. However, a single survey provides insufficient information to estimate the true completeness of the survey catalogue (i.e. the fraction of *all* quasars that have been detected), since there is no information about the distribution of quasars missed because of the colour and magnitude limits imposed. Nevertheless, the claim by Graham et al. (1999) that ultraviolet-excess surveys may be $\lesssim 70$ per cent complete because they select against low-luminosity quasars is only weakly supported here. If the Graham et al. hypothesis is correct, then a correlation between the $(u_J - b_J)$ colour and luminosity should be seen because less luminous objects should be expected to have more positive $(u_J - b_J)$. This might be seen as a natural consequence of the unified model for AGN (Antonucci 1993; Urry & Padovani 1995; Miller 1995), in which quasars that appear less luminous because they are seen edge-on will also have systematically more red colours, because of both extinction of light from the central engine by a dusty torus, and an increased fraction of the total luminosity being due to the host galaxy. Webster et al. (1995) claimed that the broad range of $(B - K)$ colours shown by a sample of quasars with flat radio spectra supported the view that dust extinction strongly affects quasar colours, with $A_B \simeq 5$ mag, and that perhaps 80 per cent of the true quasar population was being missed by optically-selected samples. This was challenged by Boyle & di Matteo (1995), who found that the extinction in $B$ due to dust in an X-ray selected sample of quasars was probably only $A_B = 1$. Benn et al. (1998) also argued that red $(B - K)$ colours in a radio-selected sample were due more to excess light in $K$ than to dust-induced deficit in $B$, and that this was not evidence that such quasars are necessarily red in $(U - B)$ colours.

For the CUQS sample, Fig. 5.5 shows that the $(u_J - b_J)$ colour of these quasars is not significantly correlated with $M_{b_J}$, with Pearson's correlation coefficient $\rho = 0.02$. The slope of the best-fit straight line is $0.006 \pm 0.01$, consistent with zero. The $(u_J - b_J)$ colour is, however, positively correlated with $M_{u_J}$, with $\rho = 0.23$ and a slope of $0.047 \pm 0.011$, more than $4\sigma$ from zero. It may therefore be said that the mean $(u_J - b_J)$ colour for the *observed* quasars becomes more red with increasing
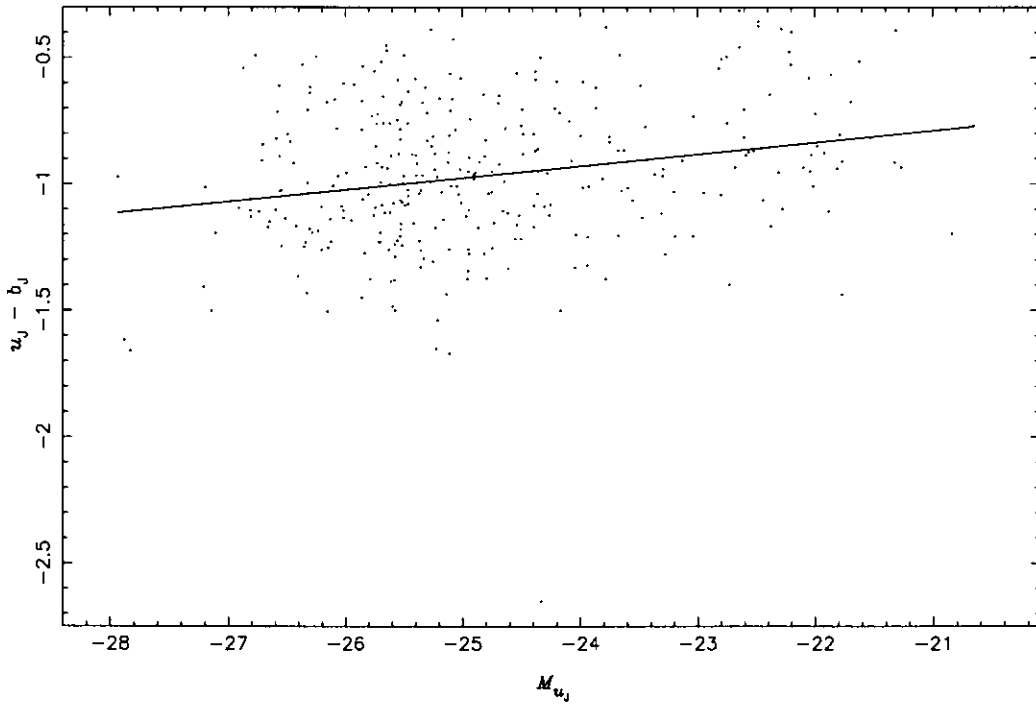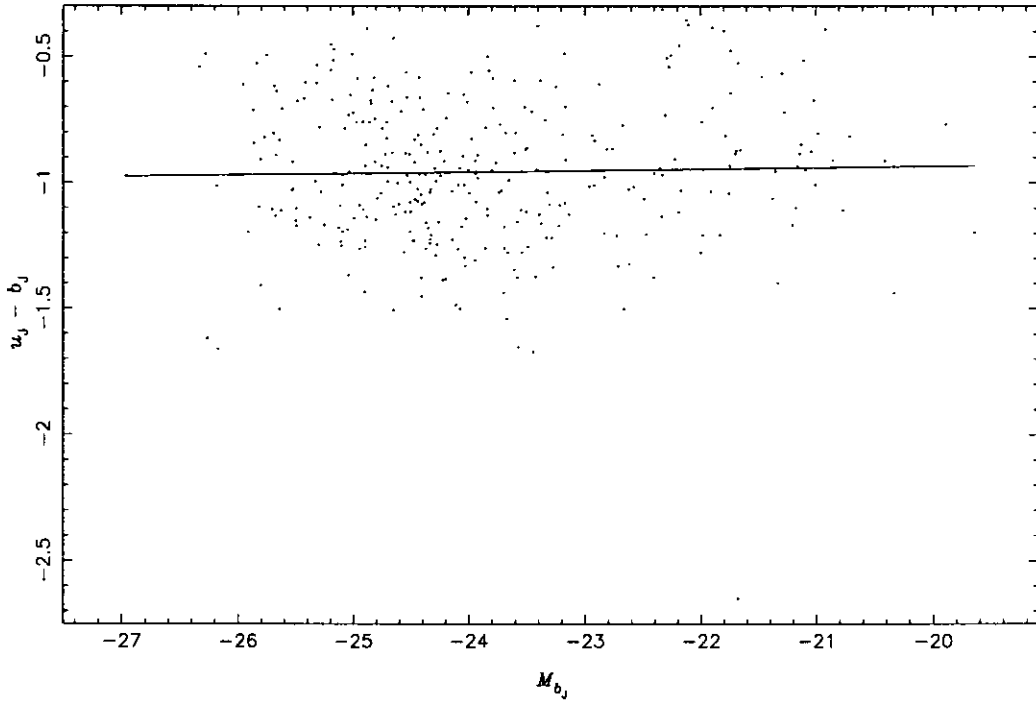
**Figure 5.5.** The $(u_J - b_J)$ relationships with $M_{b_J}$ (upper panel) and $M_{u_J}$ (lower panel) for the full quasar catalogue. Points show quasars. The straight lines are least-squares fits to the points.
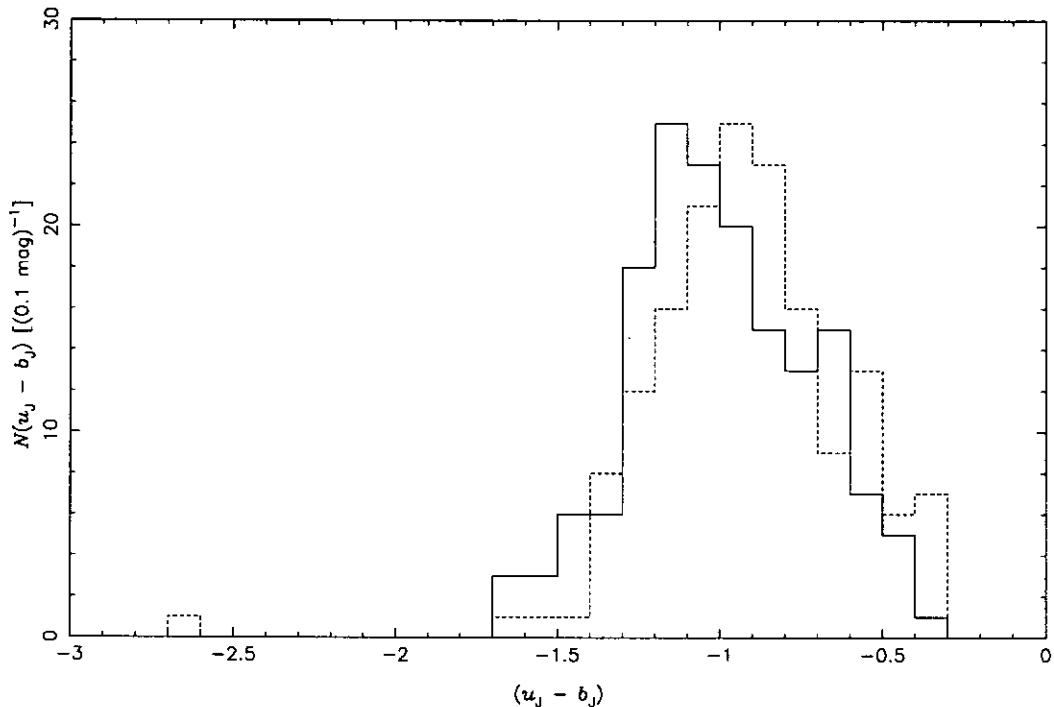
**Figure 5.6.** The distribution in $(u_J - b_J)$ for the bright and faint quasars, divided on $M_{u_J}$ into equal samples of 160 quasars each. The solid line shows the distribution for the bright half and the dashed line shows the distribution for the faint half.

$M_{u_J}$. This may be interpreted in one of two ways: (a) the mean $(u_J - b_J)$ colour for the true quasar population becomes more red with increasing $M_{u_J}$, or (b) the mean $(u_J - b_J)$ colour for the true quasar population is constant for all $M_{u_J}$, but the width of the distribution in $(u_J - b_J)$ decreases with increasing $M_{u_J}$, so that the $(u_J - b_J) \leq -0.3$ limit artificially shifts the mean observed colour towards the red with increasing $M_{u_J}$. To decide between these alternatives, the quasars are divided on $M_{u_J}$ into bright and faint samples of 160 quasars each. Examination of the distributions in $(u_J - b_J)$ colours in Fig. 5.6 shows that both distributions have very similar width, but that the faint distribution shifts to the red without significant truncation, consistent with interpretation (a). The shift is small, suggesting that this is a weak effect, consistent with Boyle & di Matteo (1995). It may therefore be concluded that few low-luminosity quasars in the redshift range $0.4 \lesssim z \lesssim 2.2$ are in fact missed by ultraviolet-excess selection, in agreement with the conclusions of Boyle et al. (1987). This argues in favour of the true completeness of the CUQS sample being at the high end of the Graham et al. (1999) estimates.

It may be noted that the Graham et al. (1999) statement that a survey that defines quasars as being more luminous than some specified limit, say $M_B \leq -23$, would also be biased against low-luminosity quasars, while of course true, might be misleading. Indeed, Schmidt & Green (1983) admitted that their own use of this limit (with $H_0 = 50$ km s$^{-1}$ Mpc$^{-1}$ and $q_0 = 0.1$) to separate 'quasars' from 'Seyfert 1 nuclei' made no fundamental sense because there is no reason to believe that there is a natural low-luminosity limit to the quasar phenomenon. If the unified AGN model is accepted, then the principal reason to make a luminosity cut should be to select a volume-limited sample, and the correct luminosity at which to make the cut can be determined theoretically from Eqn. 5.1 or observationally from the peak of the $N(M_{b_J})$ curve.

## 5.5 Properties of the narrow emission-line galaxy catalogue

The positions, magnitudes and redshifts of the 93 narrow emission-line galaxies (NELGs, but including the 2 low-redshift Seyfert 1 galaxies) detected in the 1996 and 1997 observations are tabulated in appendix A. Their distribution on the sky is shown in Figs. 5.7 and 5.8, and the redshift, colour and magnitude distributions are shown in Fig. 5.9.

The distribution of these NELGs on the sky is clearly not uniform. This is largely due to selection effects. It is considerably harder to distinguish between narrow emission lines and noise in spectra with low s/n ratios than it is to find broad lines. The identification efficiency for NELGs by the methods used here was therefore lower than for quasars (although the efficiency has not been quantified). Automated cross-correlation methods for matching a template NELG spectrum to the observed spectra would be better than the visual line-finding method used here in this regard. In addition, the $N(u_J - b_J)$ plot in Fig. 5.9 shows that there is a large incompleteness due to the $(u_J - b_J) \leq -0.3$ limit, so the small variations in the limiting $(u_J - b_J)$ colour from tile to tile (§4.3.2) have resulted in larger variations in the tile-to-tile counts for the NELGs than for the quasars. The distributions in redshift and $b_J$ are unremarkable. At the median $z = 0.129$, Eqn. 5.1 predicts a

106
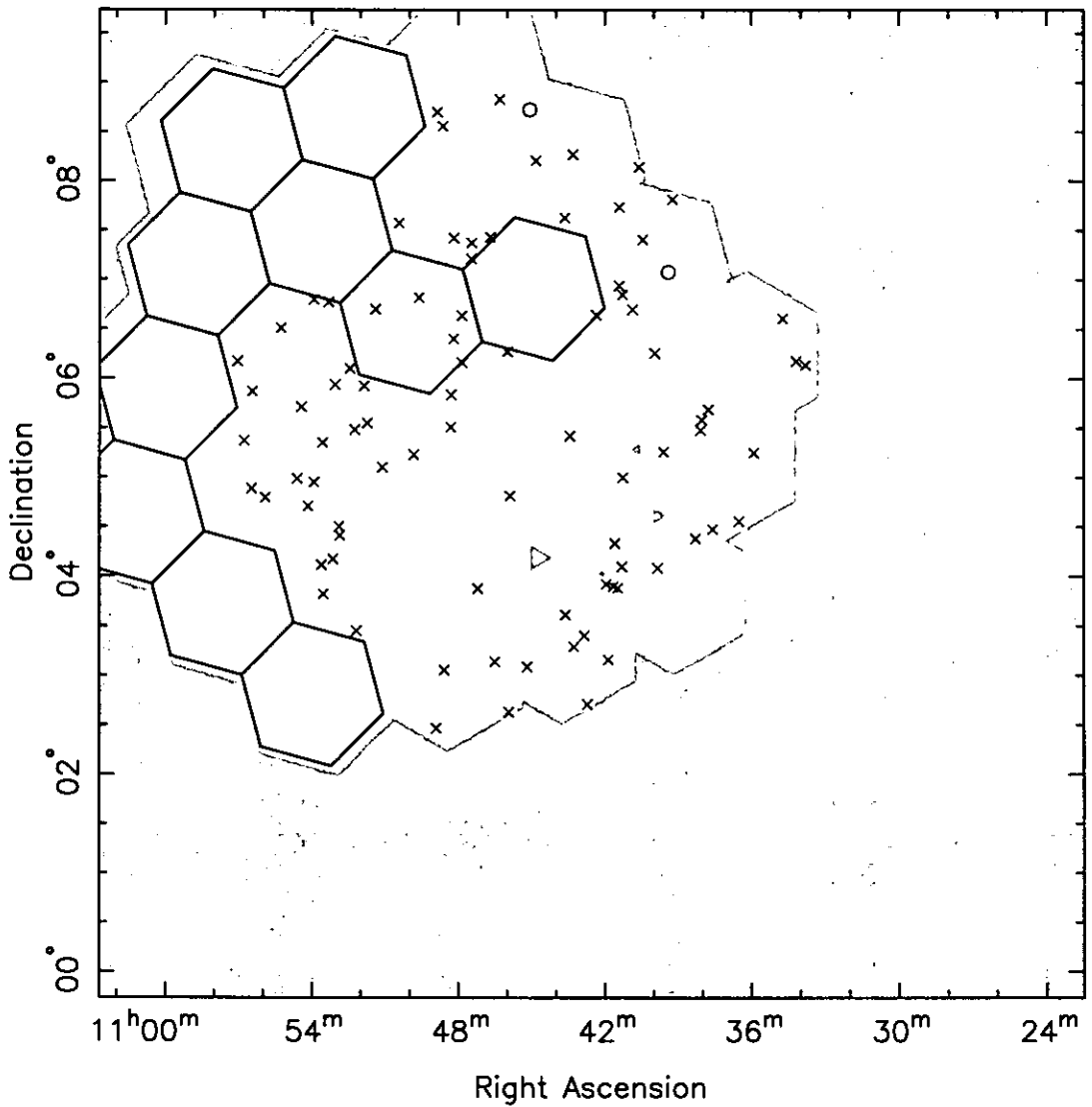
**Figure 5.7.** Positions of the 85 NELGs (crosses) and 2 low-redshift Seyfert 1 galaxies (circles) detected in the programme area spectra from the 1996 and 1997 observations. The shading and hexagons are as for Fig. 5.2.

volume-limited $M_{b_J} = -18.0$. This is within $\sim 0.5$ mag of the observed peak of the $N(M_{b_J})$ plot, suggesting that the magnitude limit is not the main source of incompleteness for these objects. Note that the same $\alpha = -1$ power-law form of the $k$ correction was used as was used for the quasars, which may also be justified for NELG spectra (Filipenko 1984).
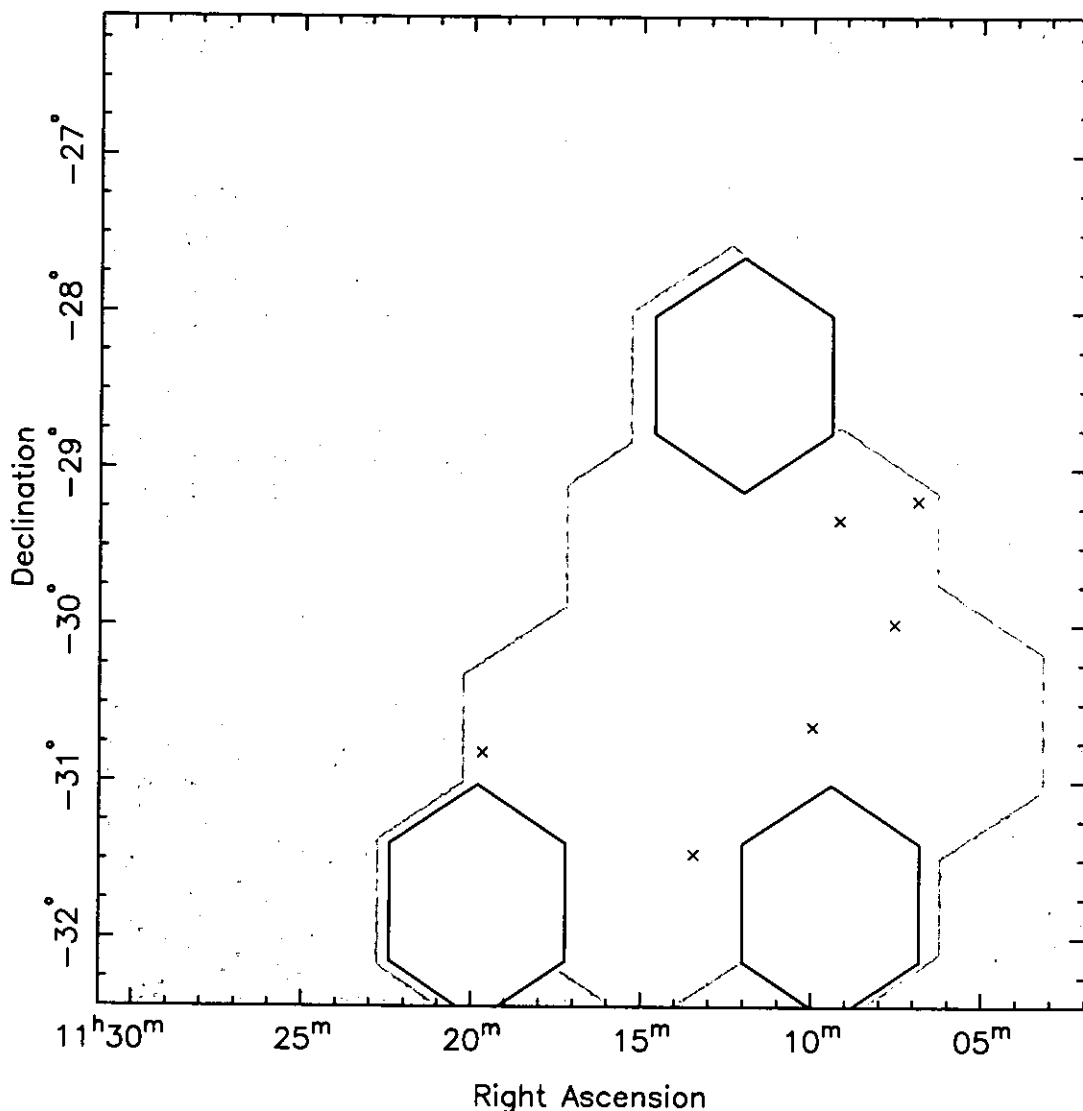
**Figure 5.8.** Positions of the 6 NELGs (crosses) detected in the control area spectra from the 1996 and 1997 observations. The shading and hexagons are as for Fig. 5.2.

## 5.6 Other objects identified

No attempt has yet been made at a complete identification of all spectra that do not show emission lines. Nevertheless, there are two classes of interesting non-AGN objects that have been identified so far in the CUQS spectra, but which have yet to be investigated in detail. The major contribution comes from hot galactic stars, especially white dwarfs, which meet all of the survey selection criteria and thus should provide a useful homogeneous sample. The white dwarf sample from the completed survey may form the basis for studies of galactic structure.
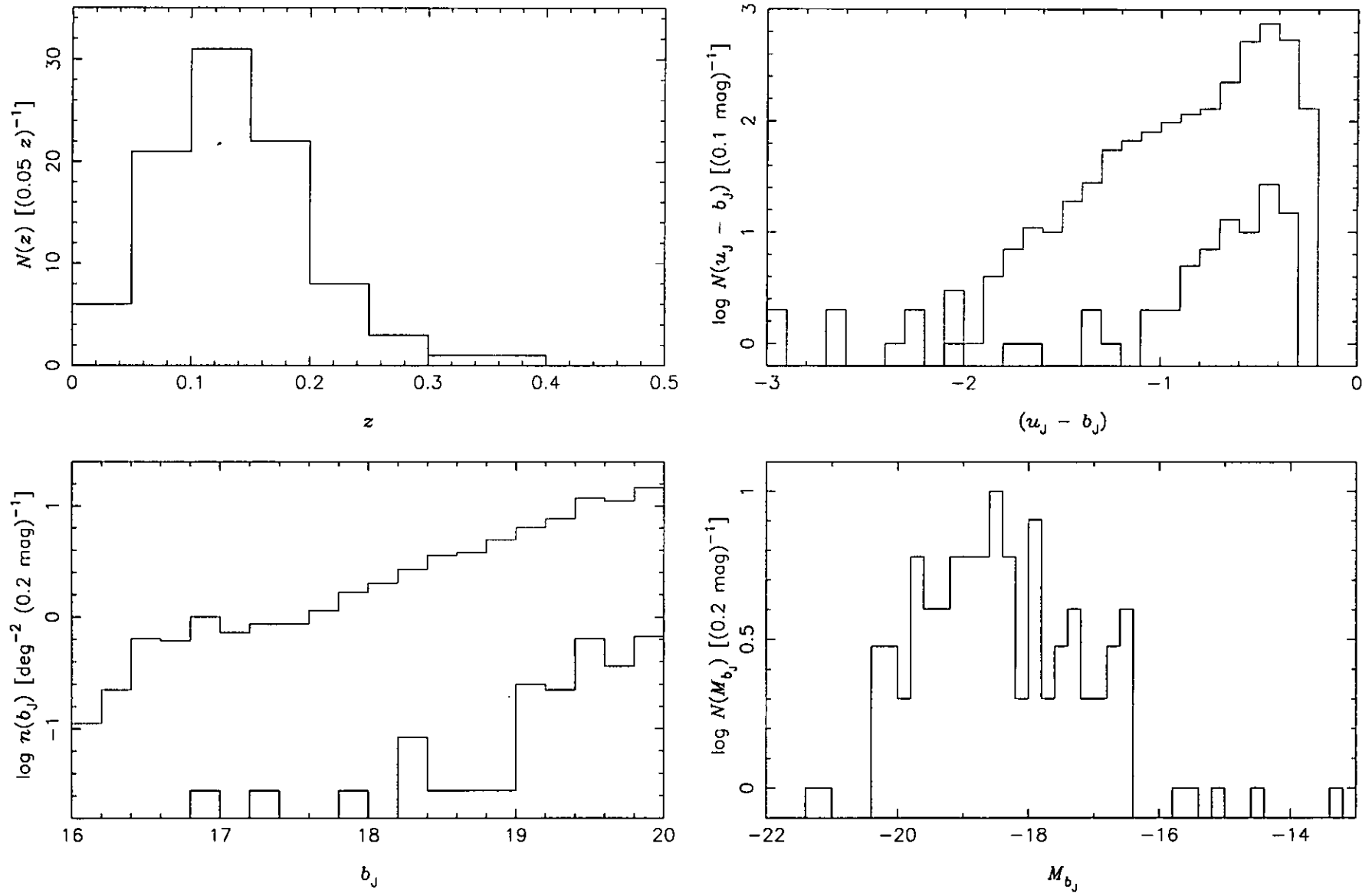
**Figure 5.9**: The distribution of the 93 narrow emission-line and Seyfert 1 galaxies from the 1996 and 1997 observations as functions of redshift (upper left), ultraviolet-excess colour (upper right), apparent magnitude (lower left) and absolute magnitude (lower right). The solid lines relate to narrow emission-line and Seyfert 1 galaxies and the dotted lines to observed candidates.

**Table 5.2**: Galaxies with blue colours but without emission lines detected in the 1997 observations, sorted by right ascension. The first column gives the CUQS spectrum reference number, consisting of tile name and aperture numbers. The positions, $b_J$ magnitude and $(u_J - b_J)$ colours are taken from the calibrated SuperCOSMOS data. The redshifts were measured as described in the text.

| CUQS No. | $\alpha$ ($^h$:$^m$:$^s$) | $\delta$ ($^\circ$:$'$:$''$) | $b_J$ | $(u_J - b_J)$ | $z$ |
|---|---|---|---|---|---|
| 1997.1.3.007 | $10:42:41.56$ | $+08:10:47.6$ | 17.12 | $-0.377$ | 0.096 |
| 1997.3.2.012 | $10:50:05.98$ | $+05:08:16.5$ | 17.70 | $-1.685$ | 0.122 |
| 1997.3.1.055 | $10:51:04.22$ | $+07:58:16.6$ | 19.05 | $-0.543$ | 0.025 |
| 1997.4.1.073 | $10:53:18.39$ | $+04:36:01.1$ | 19.71 | $-0.533$ | 0.090 |
| 1997.4.2.007 | $10:54:06.86$ | $+05:04:54.8$ | 19.66 | $-1.886$ | 0.079 |
| 1997.4.2.110 | $10:56:13.84$ | $+05:16:31.0$ | 19.35 | $-0.598$ | 0.042 |
| 1997.3.3.070 | $10:56:41.88$ | $+05:56:38.6$ | 19.24 | $-1.867$ | 0.063 |
| 1997.3.3.072 | $10:56:49.93$ | $+05:56:12.3$ | 19.00 | $-1.257$ | 0.063 |
| 1997.4.2.079 | $10:57:02.90$ | $+05:14:41.9$ | 17.80 | $-1.242$ | 0.051 |
| 1997.4.2.089 | $10:57:18.23$ | $+05:05:07.9$ | 18.90 | $-0.957$ | 0.056 |

A second interesting contribution comes from low-redshift galaxies with spectra absent of emission lines, first recognized during analysis of the 1997 observations. Those identified are listed in table 5.2 – the other years' data have yet to be checked. They were identified as galaxies by the presence of redshifted star-like spectral features including at least a distinct continuum break, which was assumed due to the Ca II H $\lambda3969$ and K $\lambda3934$ lines plus crowded hydrogen absorption lines close the the Balmer limit at 3646 Å. Most of these spectra also show weak absorption lines from other hydrogen Balmer series transitions (especially H$\delta$ $\lambda4102$ and H$\gamma$ $\lambda4340$) at redshifts that concurred with that measured from the continuum break, with an estimated uncertainty of $\Delta z \simeq 0.005$. All of the objects have faint extended images in the Digitized Sky Survey (DSS), suggesting confirmation of their identification as galaxies, although none of them are presently identified in the NASA Extragalactic Database. There were 10 galaxies found in the 1997 spectra out of a total of 1678 objects observed, a fraction of $10/1678 = 0.006$. Complete identification of the CUQS spectra without emission lines may increase the number slightly. By comparison, Boyle et al. (1990) identified $19/1409 = 0.014$ of their ultraviolet-excess spectra as "continuum" objects, in which they found no continuum break, no Ca II K and H lines, and no hydrogen Balmer lines at the $5\sigma$ level in their lower-resolution (14 Å) spectra. However, the DSS also shows faint extended images at the positions

of the Boyle et al. continuum objects, consistent with those found for the CUQS objects, suggesting that these objects may also be galaxies. It is not obvious why these galaxies should have $(u_J - b_J) \leq -0.3$, and most have colours sufficiently to the blue of that limit that it is not likely to be due to errors introduced by the stellar photometric calibration used here. They therefore probably warrant further investigation with spectroscopy and imaging at higher resolution.

# Chapter 6

# Large quasar groups in the CUQS

## 6.1 Chapter overview

A minimal spanning tree (MST) analysis is used to search for large groups in a homogeneous sample of quasars selected from the CUQS programme area catalogue. A concise definition of MSTs is given, with a simple example of a full and separated MST. The properties of the sample of quasars analysed are described. The method by which the critical distance used to separate the sample MST into candidate structures was chosen is defined. The methods used to calculate the significance of the candidate structures are also defined. Using these methods, two potentially significant large groups of quasars are found in the sample, one coinciding with a group found in earlier studies, and one a new discovery. Details of the groups identified are presented and their meaning from a cosmological standpoint is discussed.

## 6.2 Minimal spanning tree analysis

A minimal spanning tree is a concept from graph theory with applications in the analysis of the clustering properties of data from many branches of science. MST analysis was first used in an astronomical setting by Barrow et al. (1985), and has been shown to produce a superset of the information provided by a percolation analysis in a computationally more efficient manner (Bhavsar & Splinter 1996). A concise definition of MSTs, without proofs, is as follows. Consider a set of points in $n$-dimensional space, $\mathcal{P} \equiv \{p : p \in \Re^n\}$. Edges are defined as lines (not necessarily

Euclidean straight lines) that connect pairs of points in $\mathcal{P}$, $e \equiv (p_i, p_j : p_i, p_j \in \mathcal{P})$. Each edge as an associated 'length', denoted by $|e|$. The length of an edge can be defined in any way appropriate to represent the weight or strength of the connection between the points at the ends of the edge, but here it is assumed that shorter edges represent stronger connections. A *spanning tree* of $\mathcal{P}$ may then be defined as a set of edges, $\mathcal{T} \equiv \{e\}$, that connects all the points in $\mathcal{P}$ without closed loops. A $\mathcal{T}$ for which the sum of the edge lengths is minimal is called a *minimal spanning tree* (MST) of $\mathcal{P}$, and will be denoted $\mathcal{T}_{min}$. $\mathcal{T}_{min}$ thus embodies information about the strength of connections between the points in $\mathcal{P}$ in an efficient manner, and the clustering properties of $\mathcal{P}$ can be studied by analysis of $\mathcal{T}_{min}$. Here, analysis of the subtrees of a separated $\mathcal{T}_{min}$ is desired. Subtrees are defined as the set of non-empty connected subsets of $\mathcal{T}_{min}$, $\{\mathcal{S} : \mathcal{S} \subset \mathcal{T}_{min}\}$, generated by removal of all edges from $\mathcal{T}_{min}$ for which $|e| \geq d_{sep}$, where $d_{sep}$ is some separation length. Clearly, the elements of $\{\mathcal{S}\}$ are the more strongly connected regions of $\mathcal{T}_{min}$. An example of the full and separated MST for a random 2-dimensional point set is shown in Fig. 6.1. For more details on the properties and construction of MSTs and the operations that can be performed on them, see e.g. White (1984) or Dussert et al. (1986a; 1986b).

A separated MST was used to investigate clustering in a homogeneous sample of quasars from the CUQS programme area catalogue. The sample analysed is described in §6.3. The $(\alpha, \delta, z)$ positions of the quasars were used as the point set, and the comoving separations between pairs of quasars were used as the edge lengths. The calculation of comoving separation is given in detail in appendix B. A simple algorithm (Prim 1957; Dijkstra 1959) was used to construct the MST. Faster algorithms exist (Cheriton & Tarjan 1976), but their additional complexity is not warranted for the relatively small point sets analysed here. The method used to choose a characteristic value for $d_{sep}$ is explained in §6.4. Each subtree was then identified as a candidate quasar group, and its level of significance was determined. The null hypothesis[1] tested, $\mathcal{H}_0$, was that the positions of the quasars in each candidate group were drawn from a random distribution. The statistic calculated was the probability that the candidate group was more clustered than expected under $\mathcal{H}_0$. The 'degree of clusteredness' of each candidate group was

---

[1]Do not confuse the notation for null hypothesis, $\mathcal{H}_0$, with that for Hubble's constant, $H_0$.
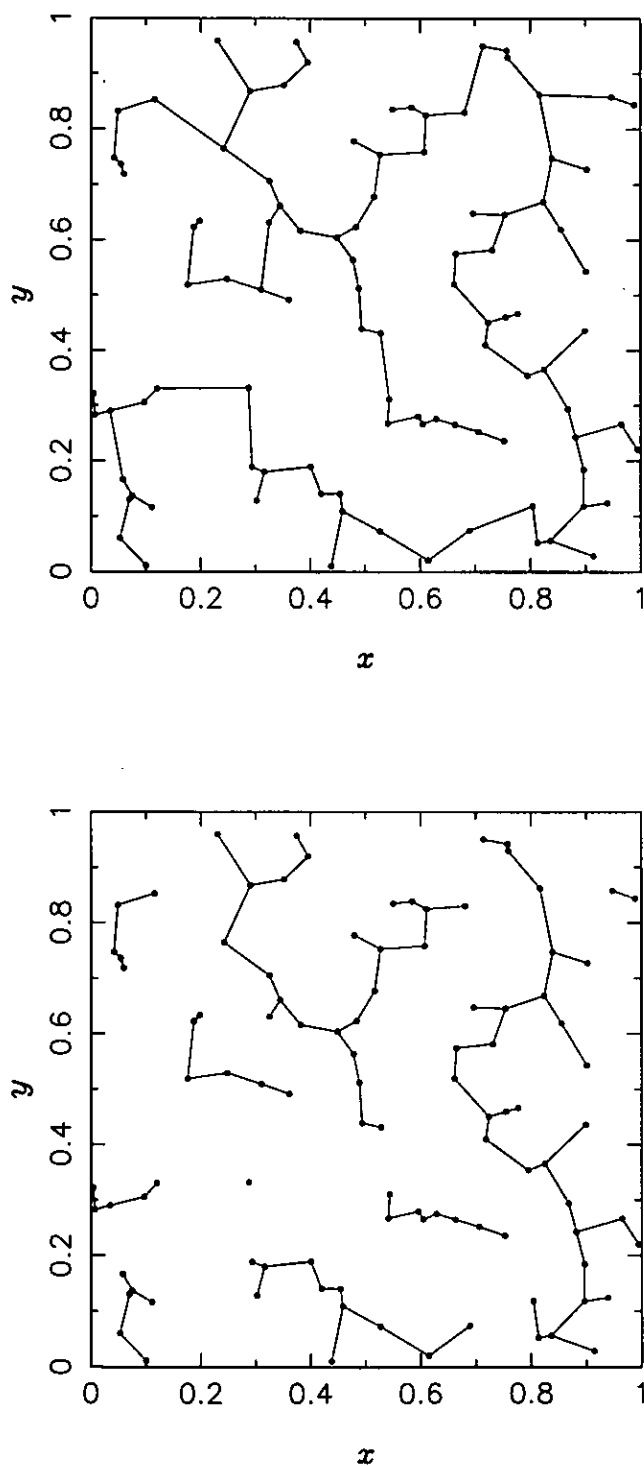
**Figure 6.1.** An example of a 2-dimensional MST for a set of 100 random points drawn from a uniform distribution over the range (0..1, 0..1). The points are marked by dots and the edges by lines. The upper panel shows the full MST. The lower panel shows the 9 subtrees and 1 isolated point that result from separation with the arbitrary choice of $d_{sep} = 0.12$.

measured by its $(m, \sigma)$ value (Graham, Clowes & Campusano 1995, see also §6.7), where $m$ is the mean normalized edge length for the candidate group and $\sigma$ is its standard deviation (i.e. the first and second central moments of the normalized edge length distribution). Dussert et al. (1986a; 1986b) have shown that clustered distributions have low values of both $m$ and $\sigma$ compared with the mean values from randomly-distributed point sets. The construction of the random point sets used to make this comparison are described in §6.6. Adami & Mazure (1999) extended the $(m, \sigma)$ statistic to include the third (skewness) and fourth (kurtosis) central moments, but showed that these higher moments are only marginally useful even with large point sets.

## 6.3   The sample analysed

There are 267 quasars in the programme area catalogue from the 1996 and 1997 observations. Of these, 32 have redshifts that were measured from a single emission line. As discussed in §5.2.1, this is most probably the Mg II $\lambda 2798$ line, implying $z \leq 0.875$. However, as other interpretations are possible, these 32 were excluded from this analysis[2]. The sample was then windowed by the good tiles from the 1996 and 1997 observations (i.e. excluding the tiles with astrometric problems – see §3.3.3). This excluded 8 more quasars, producing a final sample of 227 quasars. The sample distribution on the sky is shown in Fig. 6.2, and the distribution by redshift is shown in Fig. 6.3. The effect of the irregular sample shape is discussed in §6.10.1. Otherwise, the distribution on the sky is unremarkable. The $N(z)$ distribution shows a dip at $z \simeq 0.7$ compared with the full catalogue (Fig. 5.4), due to the omission of the single-line identifications, but is otherwise unremarkable. The area of the sample, calculated by the method in §4.5, is $27.41 \pm 0.02$ deg$^2$.

## 6.4   Critical separation distance

To be objective and appropriate, the choice of $d_{\text{sep}}$ must be based on some characteristic of the sample itself. Here, the value of $d_{\text{sep}}$ that maximizes the multiplicity,

---

[2]Inclusion of these single-line objects under the assumption that the line is indeed Mg II $\lambda 2798$, was shown to make no difference to the results discussed here.
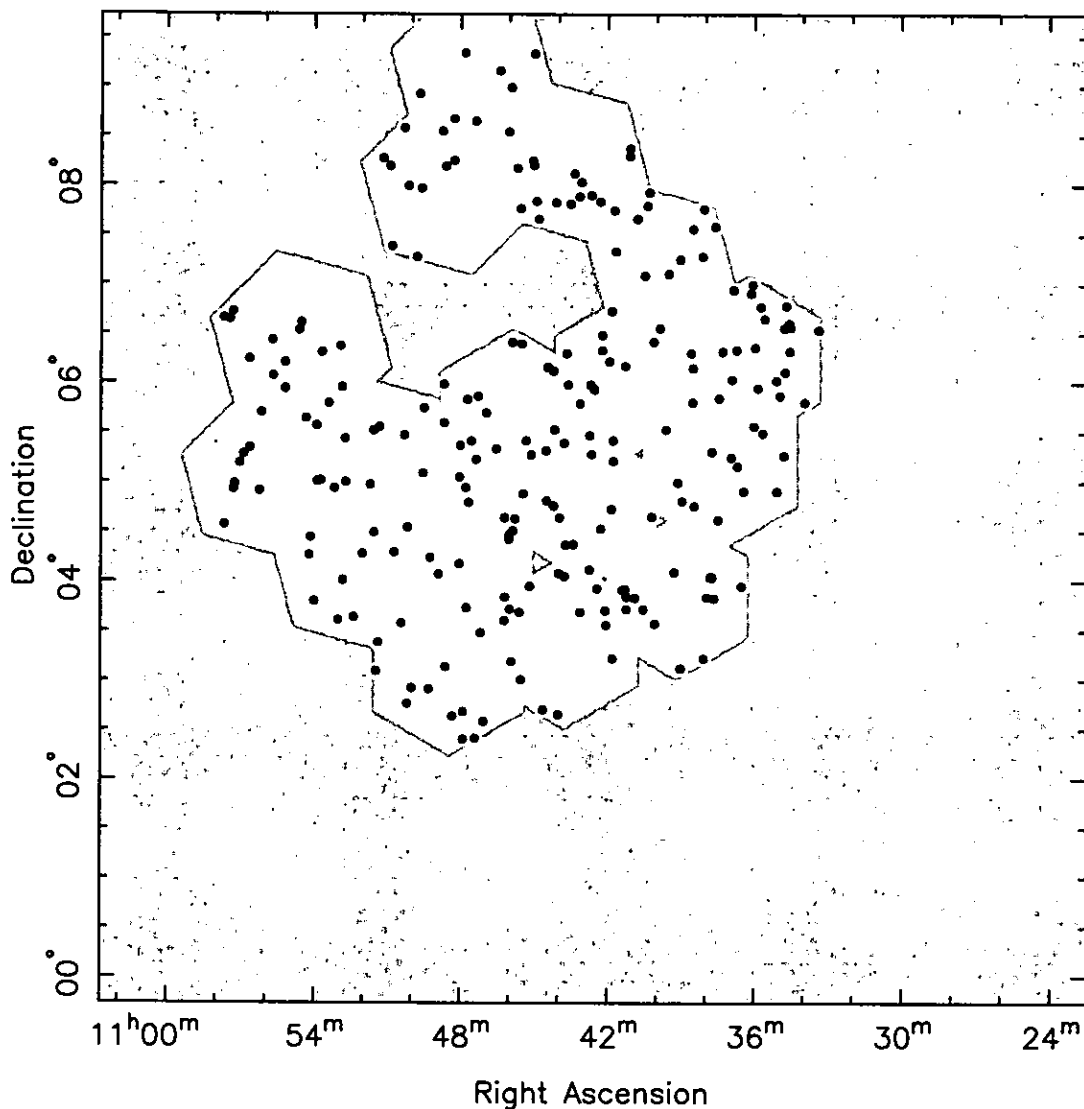
**Figure 6.2.** Positions of the quasar sample analysed. The shaded area is the entire CUQS programme area. The unshaded area is the area used for the analysis, and the points are the positions of quasars included in the sample.

$M(d_{sep})$, of the sample MST was used. $M(d_{sep})$ is defined as the number of elements in $\{S\}$ for that value of $d_{sep}$, i.e. the number of subtrees that result from the removal of all edges longer than $d_{sep}$ from $T_{min}$. Qualitatively, $M(d_{sep})$ may be expected to vary as follows. When $d_{sep} \leq \min(|e| \, \forall e \in T_{min})$, clearly $M(d_{sep}) = 0$ because all of the edges are removed and all of the points are isolated. As $d_{sep}$ increases above the minimum edge length so that some edges remain, so $M(d_{sep})$ initially also increases, as pairs and larger subtrees form[3]. As $d_{sep}$ increase further,

---

[3]Except for highly ordered distributions. For example, for points on a regular lattice, all of the points are joined at one value of $d_{sep}$.

116
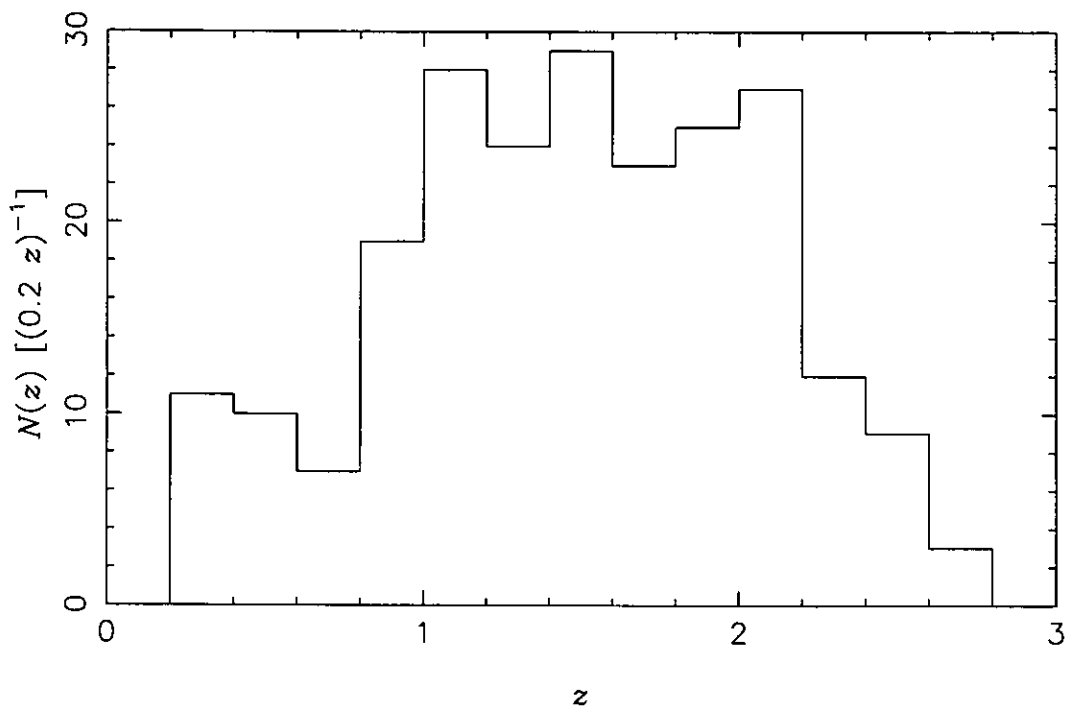
**Figure 6.3.** Redshift distribution of the quasar sample analysed.

$M(d_{sep})$ eventually reaches a maximum when the rate of subtree merger equals the rate of subtree formation. Finally, when $d_{sep} \geq \max(|e| \forall e \in \mathcal{T}_{min})$, $M(d_{sep}) = 1$ because no edges are removed and all of the points are connected in a single tree (i.e. $\mathcal{S}_1 = \mathcal{T}_{min}$).

The critical separation distance, $d_{crit}$, is then defined as the $d_{sep}$ that maximizes $M(d_{sep})$. The least $d_{sep}$ is chosen as there may be a range of $d_{sep}$ values that produce the same maximum $M(d_{sep})$, because $\mathcal{T}_{min}$ contains discrete edges, not a continuous distribution. The value of $d_{crit}$ from this method is therefore an objective choice of $d_{sep}$ for a particular sample. Using $d_{crit}$ as the characteristic length produces a maximal set $\{\mathcal{S}\}$ regardless of the morphology of the subtrees. In contrast, the percolation length and filling factor each characterize different global properties that do depend on the morphology of the clustering. However, the maximum diameter of the spheres circumscribing each of the subtrees of a separated MST as a function of $d_{sep}$ is analogous to the percolation length or the filling factor (Einasto et al. 1984; Yess & Shandarin 1996). In this analysis, $M(d_{sep})$ was calculated for a range of $d_{sep}$ values in 1 $h^{-1}$ Mpc increments. A more efficient and precise method would be to use the actual edge lengths in the MST as the values of $d_{sep}$ tested.

117
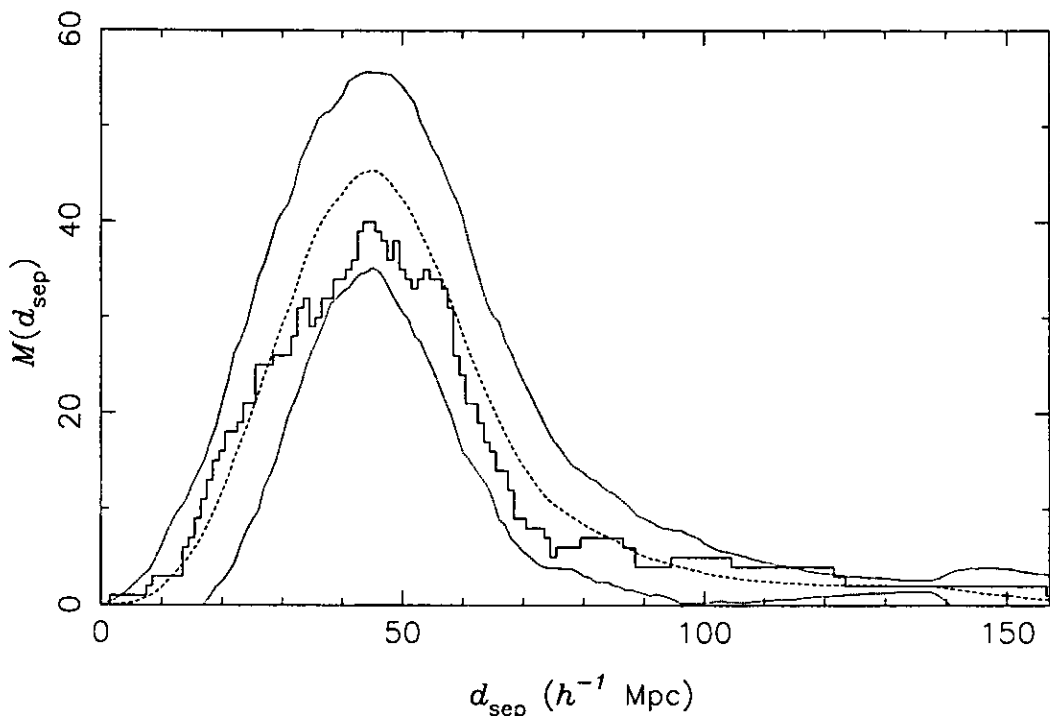
**Figure 6.4.** The multiplicity of $\mathcal{T}_{\min}$, $M(d_{\rm sep})$, against $d_{\rm sep}$ in steps of 1 $h^{-1}$ Mpc. The solid line shows $M(d_{\rm sep})$ for the present sample. The dashed line is the mean curve from 100 mock samples, and the dotted lines are the 3-$\sigma$ limits from the mock samples. The peak of the observed curve defines $d_{\rm crit}$.

The $M(d_{\rm sep})$ curve for the present sample is shown in Fig. 6.4. It is almost entirely within 3-$\sigma$ of the mean multiplicity curve from 100 mock samples (§6.6). The small > 3-$\sigma$ excess at $d_{\rm sep} \simeq 120$ $h^{-1}$ Mpc disappears if the single-line objects are included with redshifts that assume that the line is Mg II $\lambda2798$. For the observed sample, $d_{\rm crit} = 44 \pm 0.5$ $h^{-1}$ Mpc (where the uncertainty is due to the 1 $h^{-1}$ Mpc bin size). For the mock samples, the mean is $d_{\rm crit} = 44 \pm 3$ $h^{-1}$ Mpc. For unclustered samples, $d_{\rm crit}$ may be expected to be a simple function of the space density of quasars. The agreement seen here between the values for the observed sample and the mean of the mock samples indicates that the observed sample is, *on average*, not highly clustered.

## 6.5 Group size distribution

The distribution of group sizes after separation of the full MST at $d_{\rm crit}$ is shown in Fig. 6.5. While this is not used to formally determine the statistical significance of
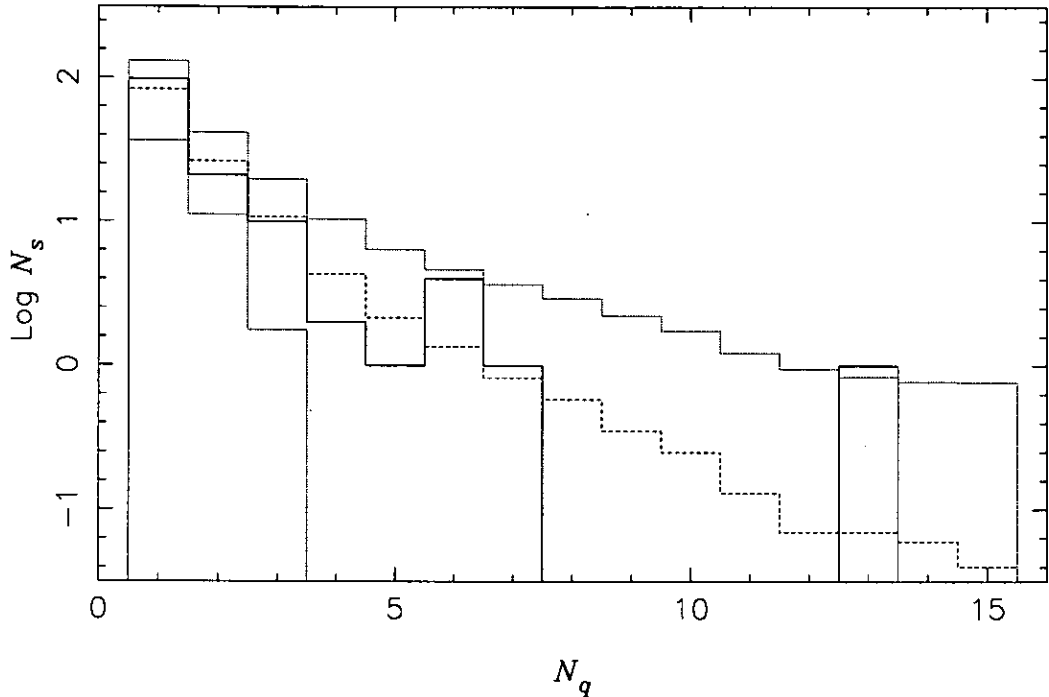
**Figure 6.5.** Number of groups, $N_s$, containing $N_q$ quasars, after separation of the MST at $d_{crit}$, for the present sample (solid line). The mean (dashed line) and 3-$\sigma$ limits (dotted lines) from 100 mock samples are also shown.

quasar groups, note that there is a $\sim$ 3-$\sigma$ excess of groups with 6 quasars above the mean number of such groups expected from mock catalogues, and a $>$ 3-$\sigma$ excess of groups with 13 quasars, corresponding to the sizes of the most significant groups discussed below. Approximately half of the quasars remain isolated (i.e. not in groups, $N_q = 1$) after separation.

## 6.6 Mock samples

The significance levels with respect to $\mathcal{H}_0$ of the candidate groups in the separated MST were calculated using mock samples generated by a Monte Carlo method. Each mock sample asserted $\mathcal{H}_0$ while duplicating the surface density and redshift distribution of the observed sample. Mock $\alpha, \delta$ values were each taken from a uniform distribution. These were windowed by the same tiles used to tessellate the observed sample, to ensure that the observed and mock catalogues used in the analysis covered identical areas. The distribution on the sky of the mock sample was thus random. Mock $z$ values were generated by permutation of the observed values. The mock
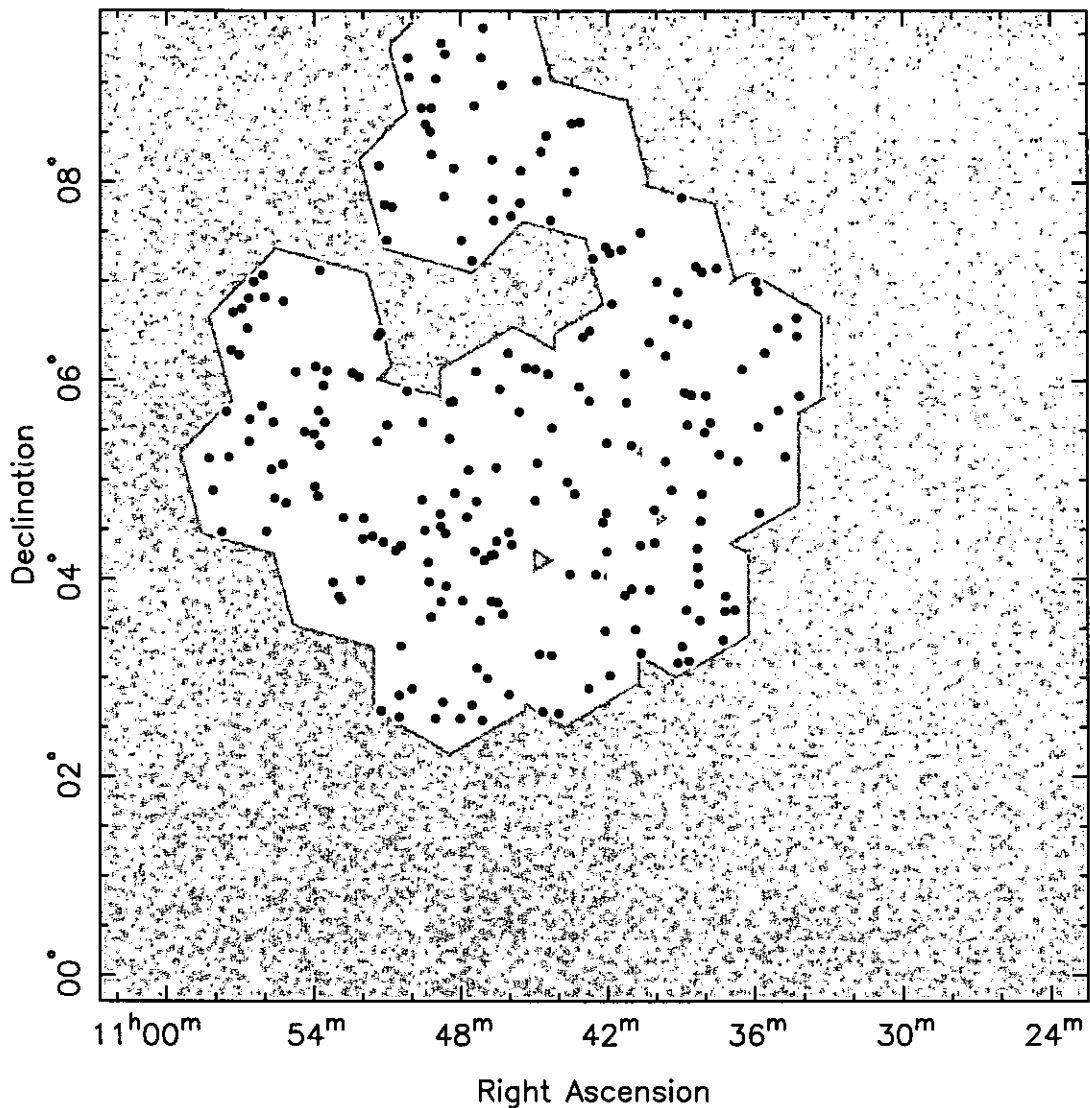
**Figure 6.6.** Positions of a mock sample based on the quasar sample analysed generated using the method described in the text. The legend is as for Fig. 6.2.

sample redshift distribution is thus identical to the observed distribution. Ideally, it would be preferably to use a functional description of the product of the true mean quasar redshift distribution with the survey radial selection function to generate mock $z$ values drawn from the same cosmic distribution as the observed values, but without (necessarily) being identical to the sample values. However, La Franca et al. (1998) have shown, for similarly-sized samples, that redshift permutation is statistically equivalent to function-fitting methods for the purpose of generating randomized comparison samples. An example of the positions on the sky of one instance of a mock sample is shown in Fig. 6.6.

# 6.7 Level of statistical significance

In the $(m, \sigma)$ method of Graham et al. (1995) for determining the statistical significance of quasar groups, the mean, $m$, and standard deviation, $\sigma$, of the edge lengths of each candidate group are calculated for the MST connecting all the quasars in the redshift range of the candidate. The observed $(m, \sigma)$ values are then compared with mock catalogues generated from randomizations of the same subset of quasars. Including only the quasars in the candidate group itself would lead to inductive (posterior) analysis, so Graham et al. added survey quasars in the candidate redshift interval but further than $d_{\mathrm{crit}}$ from the candidate, leading to what they termed a 'semi-posterior' analysis.

Here, an additional step was introduced to consider the occurrence of significant groups in the entire sample and so reduce the posterior nature of the analysis. First, following Graham et al. (1995), the observed $(m, \sigma)$ values for quasars in the redshift range of the candidate group were compared with the $(m, \sigma)$ values from $10^4$ mock versions of the quasars in the candidate redshift interval. In choosing the neighbouring non-group quasars, the redshift interval spanned by the candidate was expanded by $\Delta z = \pm 0.005$ to allow for the mean redshift uncertainty. Low values of both $m$ and $\sigma$ indicate clustered structures (Dussert et al. 1986b). The fraction of mock $(m, \sigma)$ values for each candidate group that were smaller than the observed $(m, \sigma)$ thus gave the significance level at which $\mathcal{H}_0$ was rejected *within that redshift interval*. The probability that the candidate group was a random significant event was then determined by the fraction of same-size groups in mock versions of *the entire sample* that were more $(m, \sigma)$-significant than the candidate group.

# 6.8 Results

### 6.8.1 Large quasar group A at mean $z \simeq 1.24$

Two potentially significant groups of quasars were found. Group A (Fig. 6.7) contains 6 quasars with median $z = 1.236$, and mean $|e| = 26 \pm 9 \ h^{-1}$ Mpc. The semi-posterior $(m, \sigma)$ test rejected $\mathcal{H}_0$ for group A at a significance level of $0.0011 \pm 0.0003$. In 100 instances of mock versions of the entire sample catalogue, 135 structures of
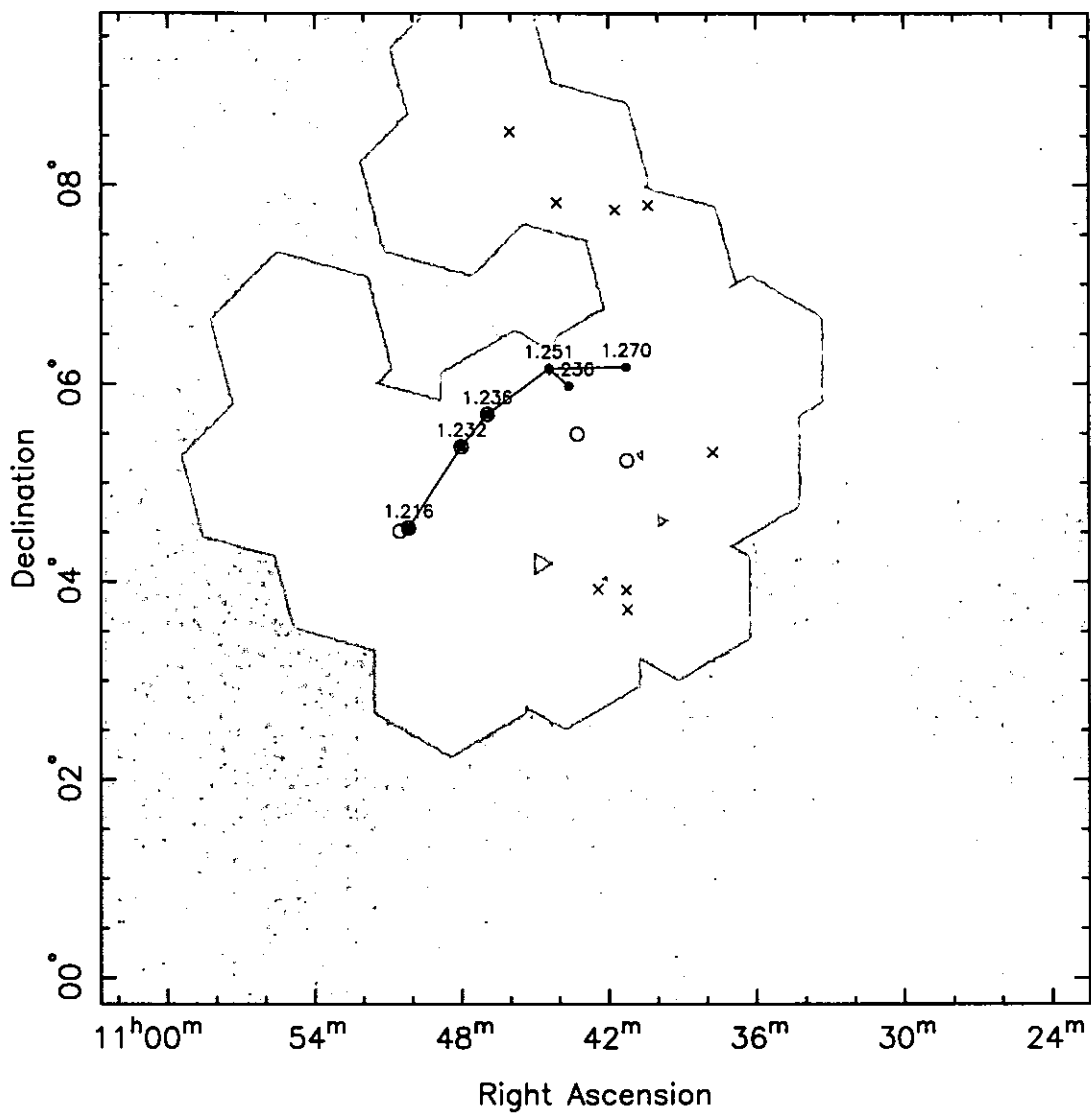
**Figure 6.7.** Quasar group A. Dots (labelled with redshifts) show the CUQS quasars in group A. Lines show 2D projections of the 3D MST edges, each shorter than $d_{crit}$. Crosses mark other CUQS quasars in the same redshift range but at larger separations. Open circles show the core MST group of 6 quasars from the CC91 objective-prism survey (Graham 1997). The shading is as for Fig. 6.2.

122

**Table 6.1**: Quasars from the sample analysed in the group A redshift interval. The upper part of the table lists the quasars in the group. The lower part of the table lists quasars in the same redshift interval as the group but farther than $d_{\rm crit}$ from the group. The first column gives the number of the quasar in the group. The second column gives the CUQS spectrum reference number, consisting of observed year, night, tile sequence and aperture numbers. The positions, $b_J$ magnitude and $(u_J - b_J)$ colours are taken from the calibrated SuperCOSMOS data. The redshifts and absolute magnitudes were determined as described in the text.

| Group No. | CUQS No. | $\alpha$ $(^{\rm h}.^{\rm m}.^{\rm s})$ | $\delta$ $(^\circ.'.'')$ | $b_J$ | $(u_J - b_J)$ | $z$ | $M_{b_J}$ |
|---|---|---|---|---|---|---|---|
| A.1 | 1996.2.3.094 | 10 : 50 : 10.11 | +04 : 32 : 48.3 | 18.86 | −1.24 | 1.216 | −24.34 |
| A.2 | 1996.1.2.068 | 10 : 48 : 00.44 | +05 : 22 : 09.8 | 19.69 | −1.28 | 1.232 | −23.54 |
| A.3 | 1996.1.2.001 | 10 : 46 : 56.72 | +05 : 41 : 50.4 | 18.62 | −1.00 | 1.236 | −24.61 |
| A.4 | 1996.3.3.083 | 10 : 43 : 36.59 | +05 : 58 : 48.5 | 19.91 | −1.22 | 1.236 | −23.33 |
| A.5 | 1996.1.2.054 | 10 : 44 : 25.80 | +06 : 09 : 25.4 | 19.58 | −1.26 | 1.251 | −23.69 |
| A.6 | 1996.3.3.002 | 10 : 41 : 17.13 | +06 : 10 : 17.5 | 17.04 | −1.62 | 1.270 | −26.26 |
| | 1996.3.2.117 | 10 : 37 : 44.83 | +05 : 18 : 33.5 | 19.94 | −1.33 | 1.224 | −23.27 |
| | 1996.2.2.054 | 10 : 42 : 25.61 | +03 : 55 : 37.7 | 18.95 | −1.24 | 1.227 | −24.27 |
| | 1996.1.3.091 | 10 : 41 : 16.77 | +03 : 55 : 10.6 | 19.95 | −1.08 | 1.243 | −23.30 |
| | 1997.1.3.099 | 10 : 44 : 06.75 | +07 : 49 : 31.7 | 18.73 | −0.66 | 1.250 | −24.53 |
| | 1997.1.3.029 | 10 : 41 : 44.23 | +07 : 45 : 01.8 | 19.22 | −1.17 | 1.254 | −24.06 |
| | 1996.1.3.086 | 10 : 41 : 14.03 | +03 : 43 : 11.1 | 18.95 | −1.02 | 1.259 | −24.33 |
| | 1997.1.1.063 | 10 : 46 : 01.54 | +08 : 32 : 34.6 | 19.15 | −1.03 | 1.268 | −24.14 |
| | 1997.1.2.075 | 10 : 40 : 23.33 | +07 : 47 : 50.8 | 19.03 | −0.78 | 1.268 | −24.27 |

**Table 6.2**: Edges in group A. Each edge is defined by the group quasars at its ends (see table 6.1) and the comoving separation between them.

| $i$ | $e_i$ | $|e_i|$ ( $h^{-1}$ Mpc) |
|---|---|---|
| 1 | A.1–A.2 | 36.9 |
| 2 | A.2–A.3 | 15.0 |
| 3 | A.3–A.5 | 30.1 |
| 4 | A.5–A.4 | 16.3 |
| 5 | A.5–A.6 | 32.1 |

**Table 6.3**: Positions and redshifts of the additional quasars in the core of the MST group from the CC91 survey found by Graham (1997) but too faint to be included in CUQS. The positions and magnitudes are from the CUQS astrometric and photometric calibration and the redshifts from Graham (1997). The last column gives the separation of the quasar from the nearest CUQS group A quasar.

| $\alpha$ $(^{\rm h}.^{\rm m}.^{\rm s})$ | $\delta$ $(^\circ.'.'')$ | $b_J$ | $(u_J - b_J)$ | $z$ | $M_{b_J}$ | $|e|$ ( $h^{-1}$ Mpc) |
|---|---|---|---|---|---|---|
| 10 : 50 : 30.78 | +04 : 30 : 54.8 | 20.33 | −1.33 | 1.215 | −22.87 | 3.3 |
| 10 : 43 : 16.56 | +05 : 29 : 47.1 | 20.72 | −1.24 | 1.259 | −22.56 | 26.1 |
| 10 : 41 : 15.56 | +05 : 13 : 44.5 | 20.05 | −1.12 | 1.253 | −23.22 | 36.3 |

6 mock quasars were found, so it is reasonable to expect one or two such structures in the observed catalogue. However, $\mathcal{H}_0$ was rejected by the $(m, \sigma)$ test at a more significant level than group A for only 7 of these 135 mock structures, so it may be said that the probability that group A is a random significant event is $7/135 = 5$ per cent.

The shape of group A suggests a curving filament with a short branch at one end with overall length $\sim 110\ h^{-1}$ Mpc and width $\sim 15\ h^{-1}$ Mpc. There are 8 other CUQS quasars in the same redshift interval as group A that are farther than $d_{\rm crit}$ from the group. The quasars in group A, and other quasars in the same redshift interval, are listed in table 6.1, and the edges in $\mathcal{S}_A$ are listed in table 6.2.

The quasars in group A coincide with the core of the CC91 group, as determined by Graham (1997) using a similar MST analysis on the CC91 data. Three quasars are common to both analyses. The other three quasars from the CC91 MST group that are not in the CUQS group are each within $d_{\rm crit}$ of the CUQS group, but are too faint to be in the present survey. These are listed in table 6.3. The omission of the three additional CUQS quasars from the Graham (1997) group is attributed to the sparse sampling of the CC91 survey: quasars A.5 and A.6 were classed as low-grade candidates by the CC91 selection method and were not observed, while quasar A.4 was not selected as a candidate, most probably because its objective-prism spectrum was overlapped and so was not considered further (R.G. Clowes, private communication, 1999 July 26). The reality of the CC91 group is therefore also indicated by the new data, although the significance level remains somewhat inconclusive.

## 6.8.2 Large quasar group B at mean $z \simeq 1.53$

Group B (Fig. 6.8) contains 13 quasars with median $z = 1.507$, and mean $|e| = 32 \pm 7\ h^{-1}$ Mpc. The overall size of the group is $\sim 150 \times 80 \times 85\ h^{-1}$ Mpc. For group B, the semi-posterior $(m, \sigma)$ test rejected $\mathcal{H}_0$ at a significance level the $0.0020 \pm 0.0004$. In 100 instances of mock versions of the entire sample catalogue, only 7 groups of 13 mock quasars were found, so finding just one such group in the observed catalogue is of interest. For none of these 7 mock groups was $\mathcal{H}_0$ rejected by the $(m, \sigma)$ test at the significance of group B, so an upper limit may be placed on the probability that

**Table 6.4**: Quasars from the sample analysed in the group B redshift interval, as for table 6.1.

| Group No. | CUQS No. | $\alpha$ ($^h:^m:^s$) | $\delta$ ($^\circ:':''$) | $b_J$ | $(u_J - b_J)$ | $z$ | $M_{b_J}$ |
|---|---|---|---|---|---|---|---|
| B.1 | 1997.3.2.108 | 10 : 51 : 18.56 | +05 : 33 : 32.0 | 19.81 | −1.26 | 1.477 | −23.86 |
| B.2 | 1996.3.3.116 | 10 : 41 : 55.71 | +06 : 12 : 56.6 | 19.29 | −1.08 | 1.480 | −24.38 |
| B.3 | 1996.3.3.095 | 10 : 43 : 40.25 | +06 : 17 : 51.3 | 19.60 | −1.01 | 1.486 | −24.09 |
| B.4 | 1997.2.3.058 | 10 : 48 : 40.34 | +05 : 59 : 12.4 | 19.85 | −1.13 | 1.487 | −23.84 |
| B.5 | 1997.3.3.104 | 10 : 56 : 10.78 | +05 : 42 : 23.4 | 19.76 | −1.07 | 1.490 | −23.93 |
| B.6 | 1997.3.3.078 | 10 : 57 : 42.37 | +06 : 39 : 43.0 | 19.15 | −0.88 | 1.495 | −24.54 |
| B.7 | 1996.1.2.109 | 10 : 45 : 52.74 | +06 : 24 : 36.8 | 18.08 | −0.83 | 1.507 | −25.64 |
| B.8 | 1997.3.2.093 | 10 : 52 : 43.95 | +05 : 26 : 22.9 | 18.03 | −0.80 | 1.510 | −25.69 |
| B.9 | 1997.3.3.027 | 10 : 54 : 20.60 | +05 : 38 : 46.4 | 19.36 | −1.04 | 1.545 | −24.41 |
| B.10 | 1997.3.3.012 | 10 : 52 : 51.69 | +05 : 57 : 33.8 | 18.65 | −0.55 | 1.590 | −25.20 |
| B.11 | 1997.3.2.126 | 10 : 51 : 41.84 | +04 : 58 : 31.8 | 19.94 | −0.98 | 1.598 | −23.92 |
| B.12 | 1996.2.3.127 | 10 : 49 : 14.38 | +04 : 14 : 27.6 | 19.49 | −0.96 | 1.604 | −24.37 |
| B.13 | 1997.3.3.003 | 10 : 53 : 41.66 | +06 : 18 : 51.6 | 19.90 | −0.56 | 1.605 | −23.97 |
| | 1996.3.1.023 | 10 : 34 : 35.01 | +06 : 36 : 29.3 | 19.67 | −0.95 | 1.480 | −24.00 |
| | 1996.3.1.111 | 10 : 36 : 05.22 | +07 : 00 : 08.6 | 19.68 | −0.68 | 1.490 | −24.01 |
| | 1996.2.2.076 | 10 : 45 : 59.37 | +03 : 43 : 09.3 | 19.43 | −0.99 | 1.500 | −24.28 |
| | 1997.1.2.123 | 10 : 40 : 29.91 | +07 : 05 : 28.2 | 19.45 | −0.94 | 1.524 | −24.29 |
| | 1996.1.3.103 | 10 : 40 : 04.52 | +03 : 34 : 26.3 | 19.82 | −0.95 | 1.528 | −23.93 |
| | 1996.1.1.014 | 10 : 41 : 50.80 | +04 : 43 : 32.7 | 20.00 | −0.92 | 1.534 | −23.76 |
| | 1997.2.2.120 | 10 : 50 : 08.09 | +07 : 59 : 43.2 | 19.35 | −0.85 | 1.537 | −24.41 |
| | 1996.2.2.128 | 10 : 45 : 54.21 | +03 : 11 : 24.9 | 19.85 | −0.96 | 1.549 | −23.94 |
| | 1997.1.3.035 | 10 : 41 : 05.95 | +08 : 22 : 35.1 | 18.94 | −0.67 | 1.549 | −24.85 |
| | 1996.3.3.119 | 10 : 42 : 13.58 | +06 : 19 : 42.7 | 19.50 | −0.81 | 1.559 | −24.30 |
| | 1997.1.3.118 | 10 : 45 : 00.29 | +08 : 12 : 03.8 | 19.41 | −0.81 | 1.590 | −24.44 |
| | 1996.3.3.027 | 10 : 41 : 46.85 | +05 : 25 : 01.6 | 19.91 | −0.91 | 1.591 | −23.94 |
| | 1997.1.2.051 | 10 : 38 : 04.83 | +07 : 45 : 52.7 | 18.87 | −0.49 | 1.606 | −25.00 |

**Table 6.5**: Edges in group B, as for table 6.2.

| $i$ | $e_i$ | $|e_i|$ ($h^{-1}$ Mpc) | | $e_i$ | $|e_i|$ ($h^{-1}$ Mpc) |
|---|---|---|---|---|---|
| 1 | B.4–B.1 | 30.9 | 7 | B.8–B.5 | 37.7 |
| 2 | B.1–B.8 | 28.9 | 8 | B.9–B.10 | 37.9 |
| 3 | B.8–B.9 | 31.4 | 9 | B.10–B.13 | 19.6 |
| 4 | B.4–B.7 | 34.7 | 10 | B.5–B.6 | 39.6 |
| 5 | B.7–B.3 | 26.8 | 11 | B.10–B.11 | 41.1 |
| 6 | B.3–B.2 | 17.5 | 12 | B.11–B.12 | 38.3 |
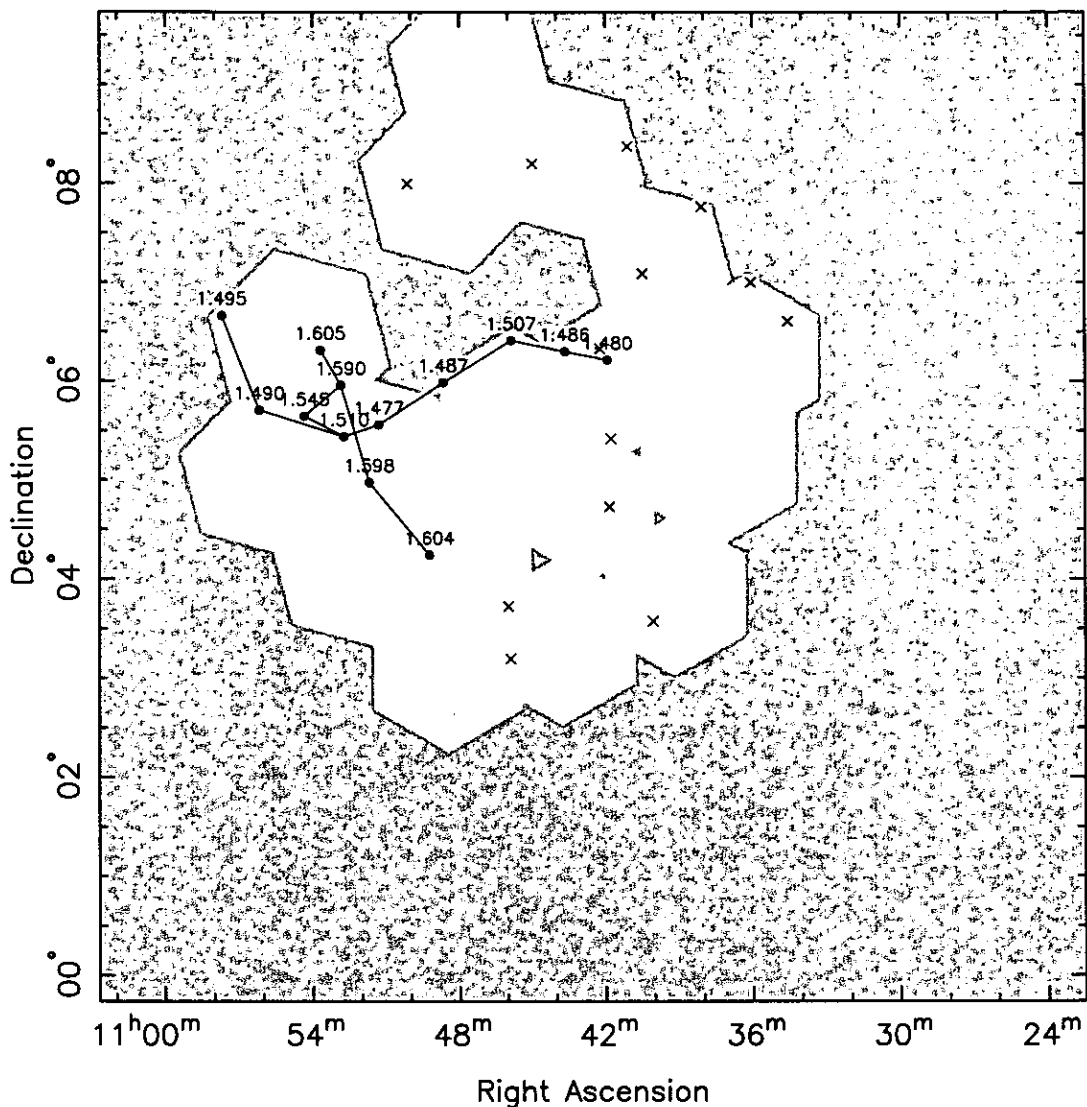
**Figure 6.8.** Quasar group B. Symbols are as for Fig. 6.7.

the observed structure is a random event at a level of significance of at most 1/8 or 13 per cent. Calculation of these significance values requires extensive computer resources, but further work should be able to better constrain this probability.

The shape of group B resembles three intersecting filaments. The first filament runs approximately east-west at $z \simeq 1.49$. A second filament runs from the first in a predominantly radial direction, joining the third, approximately north-south, filament at $z \simeq 1.60$. The size and shape are comparable to a network of galaxy superclusters (Einasto et al. 1997). There are 13 other CUQS quasars in the same redshift interval as group B that are farther than $d_{crit}$ from the group. Group B is a new discovery, and is one of the largest structures found so far. It lies partly outside

126

the eastern edge of the CC91 survey area, and so would not have been detected in that survey. The quasars in group B, and other quasars in the same redshift interval, are listed in table 6.4, and the edges in $\mathcal{S}_B$ are listed in table 6.5.

The relationship between groups A and B and all the other quasars in the programme area is shown in Fig. 6.9. The shortest comoving distance between the quasars in groups A and those in group B is $\sim 172\ h^{-1}$ Mpc $\simeq 4\,d_{\text{crit}}$, so it is unlikely that these two groups are part of a single very large group.

## 6.9 Sources and effects of error

The mean redshift uncertainty for all of the CUQS quasars is $\Delta z = \pm 0.005$. At the mean redshift of group A, this translates into a comoving radial distance uncertainty for each quasar of $\pm 4.5\ h^{-1}$ Mpc. At the mean redshift of group B, it is equivalent to $\pm 3.7\ h^{-1}$ Mpc. The r.m.s. uncertainty in the position on the sky, $\Delta r = 0.69$ arcsec, corresponds to a comoving tangential distance uncertainty of $\lesssim 0.01\ h^{-1}$ Mpc at all redshifts, so clearly the radial uncertainty dominates the errors in quasar separation. For group A, the longest edge is $|e_1| = 36.9\ h^{-1}$ Mpc (see table 6.2). If the mean redshift error is assumed in the worst case, so that the redshifts of the quasars on this edge are changed by $\Delta z_{A.1} = -0.005$ and $\Delta z_{A.2} = +0.005$, then the separation increases to $|e_1| = 41.2\ h^{-1}$ Mpc, which is still smaller than $d_{\text{crit}} = 44\ h^{-1}$ Mpc. Note that the increase in edge length, $4.3\ h^{-1}$ Mpc, is less than the maximum radial error because the edge is not purely radial, and that the actual redshift uncertainties for the specific quasars in question are $\Delta z_{A.1} = \pm 0.002$ and $\Delta z_{A.2} = \pm 0.003$, so the maximum edge length is, in fact, less. The interpretation that group A is real is therefore quite robust against redshift uncertainty.

The edge in group B (table 6.5) whose inclusion is most vulnerable to radial uncertainties is $e_8$. Assuming the survey-mean redshift uncertainty would increase its length from $|e_8| = 37.9\ h^{-1}$ Mpc to $|e_8| = 44.4\ h^{-1}$ Mpc, which is slightly larger than $d_{\text{crit}}$ (although within the limits of uncertainty for $d_{\text{crit}}$). Removing $e_8$ would break group B into two insignificant structures. However, if the *actual* measured redshift uncertainty of the quasars in question, $\Delta z_{B.9} = \pm 0.006$ and $\Delta z_{B.10} = \pm 0.001$, are used then $|e_8|$ increases to only $42.5\ h^{-1}$ Mpc, which is still less than $d_{\text{crit}}$. The
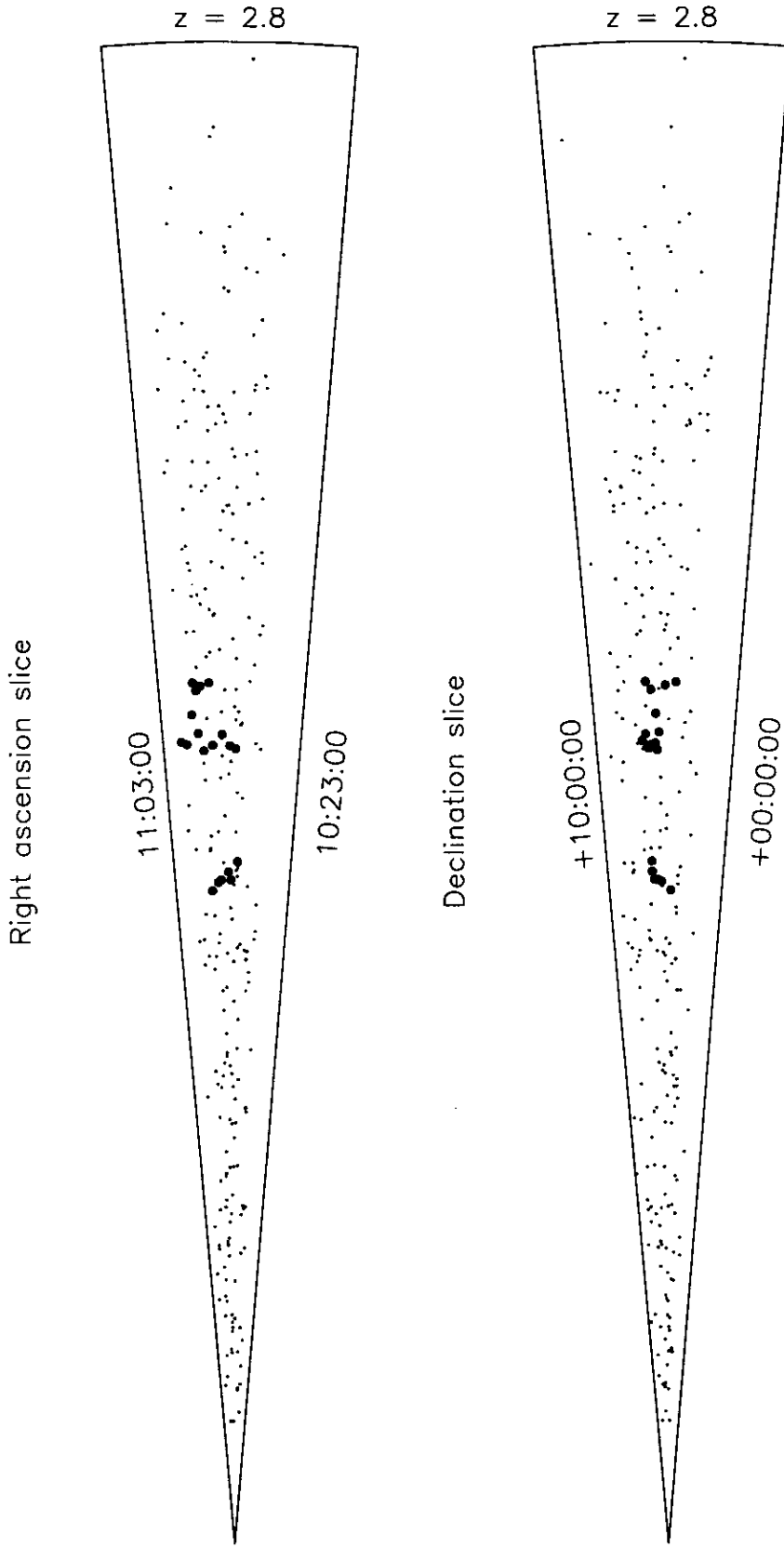
**Figure 6.9:** Quasars in the CUQS programme area, highlighting groups A and B. The upper panel shows the programme area sliced in right ascension (i.e. collapsed in declination) The lower panel shows it sliced in declination (collapsed in right ascension). Small dots show all 267 quasars in the programme area from the 1996 and 1997 observations. Large dots show the quasars in groups A and B. The apex of each slice is at $z = 0$. Note that the slices are not of constant thickness across their width because of the irregular area of sky observed.

interpretation that group B is real is therefore also robust.

As noted above, the mean astrometric uncertainty across the survey (§3.3) is negligible compared to the redshift uncertainty. However, astrometric errors reduce spectral s/n ratios because of the photons from a survey candidate that miss the spectrograph input fibre. When the s/n falls to $\lesssim 3$, the efficiency with which the spectrum may be identified as that of a quasar falls sharply. However, spatial correlation between astrometric errors over angles larger than a single observed tile ($\sim 1°5$) is not expected, because the mean error for each tile is removed when the observation is centred on the observed guide star. Group A spans $\sim 2°75$ and includes quasars from 3 tiles. Group B spans $\sim 4°0$ and includes quasars from 5 tiles. Hence it may be concluded that the interpretation of the groups as real structures does not depend strongly on astrometric errors.

Photometric errors should most affect the selection of candidates for those with $(u_J - b_J) \simeq -0.3$ or $b_J \simeq 20$. The most red quasar in group A has $(u_J - b_J) = -1.00$, and the most red quasar in group B has $(u_J - b_J) = -0.55$. Taking the uncertainties in magnitude and colour from Eqn. 3.12, it may be noted that the $(u_J - b_J)$ colours of the quasars in both groups are all more than $> 0.16$ mag from the $(u_J - b_J) \leq -0.3$ cut-off. Only group quasars A.4 and B.11 are within the uncertainty $\Delta b_J = \pm 0.10$ mag of the $b_J = 20$ limit. It may be concluded that the reality of the groups does not depend strongly on the photometric uncertainties.

## 6.10 Discussion

### 6.10.1 Biases due to the sample area and selection criteria

The shape of the present sample area is quite irregular, which might be seen as a cause for concern in the interpretation of the results of this analysis. However, the following points argue in favour of the usefulness of the results. First, $d_{crit}$ is not a strong function of the shape of the area analysed. For example, it is unchanged if the tiles north of $+06°24'$ (i.e. tiles 53, 56, 62, 63 and 68 in Fig. 4.1) are omitted, leaving a sub-area that is more closely convex. As far as they lie within this convex sub-area, the same groups of quasars are identified as candidate structures in a separated MST as in the full sample area. Second, the statistical significance of the groups is

129

calculated by comparison with mock samples with areas that have a shape identical to that of the observed sample, so that the significance of the groups is also not a function of sample shape. Nevertheless, is it recognized that group B, in particular, runs along the border of the present sample, so it is appropriate to suggest that its membership and significance should be re-evaluated once the observations of the remaining survey area can be included in the analysis. The minimum requirement for this is to fill in the 'hole' in the current sample area to the north of the identified groups, using the 1998 observations, but to achieve the original objective that the survey properly samples structures on 100 $h^{-1}$ Mpc scales, observations of the full survey area must be completed.

Of more concern is the use of a magnitude-limited sample in MST analysis. The value of $d_{\rm crit}$ for a volume-limited sample is a function of the sample survey density; for a magnitude-limited sample, it clearly also depends on the radial selection function (Dekel & West 1985). No allowance is made here for the radial selection function, so this analysis is biased against detecting structures at the high-$z$ end of the sample. Since the apparent magnitude-limited selection function naturally decreases with redshift (ignoring luminosity evolution), fewer quasars are detected at high redshift than at low redshift. If anything, this should imply distant groups detected here are *more* significant than nearby groups, because the mean comoving separation increases with radial distance as the detected fraction of quasars decreases (assuming constant comoving space density), and so $d_{\rm crit}$ should also be an increasing function of redshift. Developing the MST method to account for this could be a subject for future research, but a better approach would be to use a luminosity-limited sample, equivalent to volume-limited for no luminosity evolution. However, the space density of a luminosity-limited sample drawn from the present catalogue is too small for a useful MST analysis. Using the absolute magnitudes calculated in §5.2.2 and selecting on $M_{b_J} \leq -24.5$ produces a sample of only 91 quasars in the same area as that analysed here, and increases the critical separation distance to $d_{\rm crit} = 57\ h^{-1}$ Mpc. Increasing the apparent magnitude limit of the survey to $b_J \leq 21$ would increase the space density of a luminosity-limited sample to be similar to that of the magnitude-limited sample analysed here, making such an analysis more useful, at the cost of introducing the problems in photometric calibration and

candidate selection discussed in §3.4.8.

## 6.10.2  Cosmological significance of large quasar groups

As discussed in chapter 1, different cosmological models and different choices of cosmological parameters produce different forms of large-scale structure and different evolutionary paths, so the presence of large quasars groups in the early Universe can put constraints on acceptable choices of cosmological model. The known large quasar groups, including the two found here, are so large, and formed so early $(t_z/t_0 \simeq 0.25$ at $z = 1.5)$, that they may challenge the standard hypothesis that large-scale structure formed from gravitational collapse of a primordial density field with a Gaussian distribution (Szalay 1999; White 1997; Silk & Weinberg 1991).

However, a major obstacle to the use of quasars in such a challenge arises from the question of the bias between the quasar and mass distributions, as discussed in §1.5.2. If quasars have high bias – i.e. they only form in the deepest gravitational potential wells – then they will appear to be more strongly clustered than the underlying mass distribution. Worse, if quasar-mass bias depends on other environmental factors, then the relationship between quasar clustering and mass clustering will be complicated still further. Some means of attacking these problems, and hence enabling comparisons between the observed quasar distribution and the expected mass distribution, are outlined in §8.3.2.

# 6.11  Conclusions

An MST analysis of the quasars detected in the 1996 and 1997 CUQS observations has objectively identified two potentially-significant large group of quasars. The first group consists of 6 quasars at mean $z \simeq 1.24$ and spans $\sim 110\ h^{-1}$ Mpc. The second group consists of 13 quasars at mean $z \simeq 1.53$ with a maximum dimension of $\sim 150\ h^{-1}$ Mpc. Although their formal statistical significances are only $\sim 5$ per cent and $\lesssim 13$ per cent respectively, the interpretation that these groups are real is not affected by the known sources of error in the CUQS calibration or redshift measurements. Nevertheless, the first group has now been identified in three independent surveys – CC91, the CUQS, and in Mg II $\lambda 2798$ absorption (L.E. Campusano, G.M.

131

Williger & R.G. Clowes, private communication, 1998 October 23).

It might be tentatively concluded that these groups may indicate regions of space that have a high quasar density. Corrections to the analysis to account for the selection function and refinement of the quasar-to-mass bias function are required to be able to compare these results with theoretical expectations of the mass distribution. In any case, these remarkable structures and their environments warrant further investigation, for example using deep multi-colour imaging to identify galaxies at the same redshifts as the quasar groups.

# Chapter 7

# Luminosity indicators in CUQS quasars

## 7.1 Chapter overview

The equivalent width and the velocity width of the C IV $\lambda$1549 broad emission line are investigated as possible indicators of intrinsic quasar luminosity, using a luminosity-limited sample of 89 spectra drawn from the CUQS. The motivation for seeking quasar luminosity indicators is outlined, and the observational evidence and theoretical basis for them are discussed. The selection of a sample of quasar spectra from the CUQS and the methods used to measure the spectra and to fit the correlations are described in detail. The results weakly support the existence of both the equivalent width-luminosity correlation (i.e. the Baldwin Effect) and a velocity width-luminosity correlation. Finally, the results are discussed in the light of previous findings and models of the physical structure of quasars, with comments on the limitations of such correlations as cosmological tools.

## 7.2 Motivation

One of the standard observational tests of cosmology relates the deceleration parameter, $q_0$, to the shape of the redshift-magnitude, $m(z, q_0)$, relation (Hubble 1929; Sandage et al. 1995), provided the observations are of 'standard candles', i.e. objects with known intrinsic luminosity. The $m(z, q_0)$ relation for quasars would be partic-

133

ularly useful because they are seen to high redshift, $z \gtrsim 0.75$, where the deviation of $m(z, q_0)$ from linear with $q_0$ becomes significant.

However, the unified scheme for AGN, which is highly successful at explaining many observed attributes of quasars (Antonucci 1993; Urry & Padovani 1995; Falcke et al. 1995, and references therein), suggests that deriving intrinsic quasar luminosities from observations is difficult, because it pictures quasars as having a complex axisymmetric structure, where the continuum emission, the broad emission lines, and the narrow emission lines each originate in physically separated regions. In particular, in unified models, the continuum emission comes from a hot disk of material accreting onto a central black hole of mass $M_{BH} \simeq 10^7$–$10^9$ $M_\odot$ (Haehnelt et al. 1998). The broad-line region (BLR) consists of many small, optically-thick gas clouds, possible the envelopes of $\sim 5 \times 10^4$ 'bloated stars' (Alexander & Netzer 1997), orbiting at a radius $R_{BLR} \lesssim 1$ pc (Shields 1992) from the central black hole. The BLR clouds reprocess ionizing radiation from the continuum source into line emission in a manner similar to stellar H II regions. The accretion disk and BLR may be partially or completely obscured by a physically large and optically thick, dusty, torus approximately co-axial with the accretion disk.

Derivation of the intrinsic luminosity of a quasar from observations will clearly require corrections to account for this complex structure and for the inclination angle between the axis of symmetry and the line of sight. How might such corrections be made? For galaxies, which can be spatially resolved in imaging and spectroscopy, the corresponding corrections are relatively straightforward: for example, the Tully-Fisher relation (Öpik 1922; Tully & Fisher 1977) combines the observed rotation rate of spiral galaxies with the observed inclination angle to predict the intrinsic galaxy luminosity. Willick (1999) provides a review of such relations for deriving the luminosities of different classes of normal galaxies. For quasars, which are not normally resolvable in images, some other observable indicator is required to derive intrinsic luminosities. Here, correlations between continuum luminosity, the equivalent width of the C IV $\lambda 1549$ line (the Baldwin Effect) and the line velocity FWHM are explored as possible solutions.

## 7.3 Background

### 7.3.1 Equivalent width as a luminosity indicator

**Observational evidence**

As first reported by Baldwin (1977, hereafter B77), the Baldwin Effect (BE) is an apparent correlation between the intrinsic continuum luminosity, $L_{cont}$, of quasars and the equivalent width, $W_\lambda$, of their C IV $\lambda$1549 broad emission line [see e.g. Osmer & Shields (1999) for a recent review]. Simply put, $W_\lambda$ for an absorption line is the width in wavelength units of a line to zero intensity with a rectangular profile that has an area equal to that of the observed line. $W_\lambda$ is formally defined by[1]

$$W_\lambda = \int_{line} \left[ \frac{f_c(\lambda) - f(\lambda)}{f_c(\lambda)} \right] d\lambda \tag{7.1}$$

where $f(\lambda)\, d\lambda$ is the measured flux in the wavelength interval $\lambda \to \lambda + d\lambda$, $f_c(\lambda)\, d\lambda$ is the corresponding continuum flux in the absence of the line, and the integral is over the line width. Hence for emission lines, $W_\lambda \propto L_{line}/L_{cont}$, where $L_{line}$ is the line luminosity above the continuum and $L_{cont}$ is the continuum luminosity measured across the width of the line. B77 found evidence of a correlation represented by a power law of the form

$$W_\lambda \propto L_{cont}{}^\beta \tag{7.2}$$

with the index found to be $\beta \simeq -0.64$. An equivalent expression, used in some studies, is $L_{line} \propto L_\lambda{}^b$, where $L_\lambda$ is the specific continuum luminosity at the line centre (so $b \simeq 1 + \beta$).

The B77 result was based on an heterogeneous sample of quasars selected on radio attributes, with flat spectrum, steep spectrum and radio quiet sub-samples, and Baldwin noted that it was not clear to what extent the apparent correlation may have been due to selection effects. Baldwin et al. (1978, hereafter BEA78) found a similar correlation to B77 in a different (but still heterogeneous) sample, modifying the relationship to be expressed as $W_\lambda \propto L_\lambda{}^\beta$. Both the B77 and BEA78 results were, indeed, criticized as being hampered by selection effects. Jones & Jones (1980)

---

[1]Note that $W_\lambda$ is formally defined to be negative for emission lines. Since logarithms are required here, the absolute values of $W_\lambda$ are assumed throughout this chapter.

pointed out that faint quasars with weak emission lines would be difficult to observe, artificially enhancing the apparent BE. Murdoch (1983) noted that samples chosen with flat radio spectra, which are in general highly variable, would cause similar artificial correlations. Nevertheless, further positive results supporting the existence of the BE for the C IV line, with a range of power-law slopes, have been found by other studies such as Kinney et al. (1990), $\beta \simeq -0.17$; Campusano (1991a; 1991b), $\beta = -0.63$; Zamorani et al. (1992), $\beta \simeq -0.13$; Osmer et al. (1994), $\beta \simeq -0.25$. Several of these studies also reported similar relationships for the Ly$\alpha$ $\lambda$1216 and Mg II $\lambda$2798 emission lines. While the later results were based on samples for which much effort was made to avoid selection bias, all of these reported detections of a BE were made using heterogeneous samples. The problems inherent in this are particularly clear in the Osmer et al. (1994) results, which combined a faint $z < 1$ *IUE* sample with two bright $z \simeq 2$ and $z \simeq 3$ optically-selected samples. None of the individual samples shows a clear BE on its own, while the combined sample apparently does. In none of these studies was an absolute magnitude limit imposed to produce a luminosity-limited sample, leaving all of the results open to questions as to whether Malmquist-like biases were introduced because the high-redshift quasars tended to be the most luminous.

These deficiencies leave open the question as to whether the BE reflects an underlying physical correlation or is simply a selection effect. The ideal sample for testing the BE would be complete to some limiting luminosity, built using a homogeneous selection with correctable selection effects, and would cover a broad range of luminosities and a broad range of redshifts.

**Theoretical basis**

What physics might cause the BE? Some clues can be seen in observations of spectral variability of individual quasars, which show that the slope of the correlation between $W_\lambda$ and $L_\lambda$ for individual quasars differs from the slope for the ensemble (Kinney et al. 1990). Pogge & Peterson (1992) introduced the terms 'Intrinsic Baldwin Effect' (IBE), applied to individual quasars, and 'Global Baldwin Effect' (GBE), applied to the ensemble average behavior, as shown schematically in Fig. 7.1. The IBE variability time scale for individual quasars is of the order of days, smaller than the

136
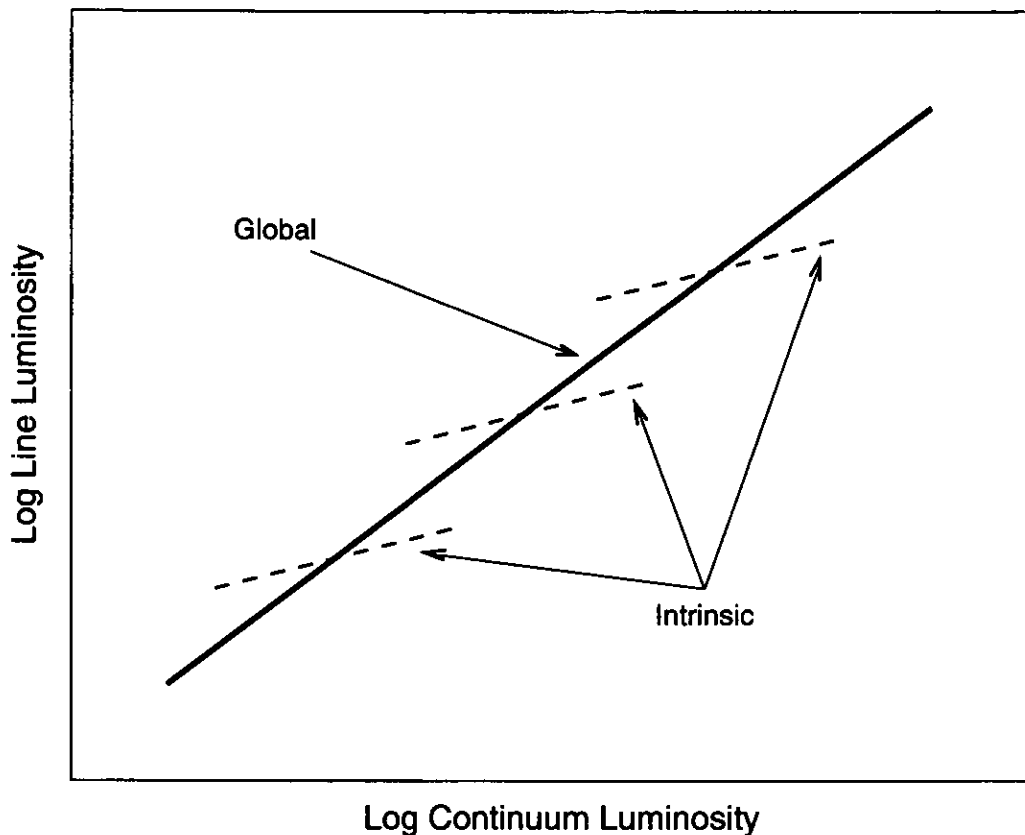
**Figure 7.1.** Schematic representation of the BE relationship between the intrinsic line luminosity and the intrinsic continuum luminosity, after Pogge & Peterson (1992, their Fig. 1). The 'intrinsic' BE is traced by variability in individual quasars (three are shown). The 'global' BE is traced by the mean of the individual quasars.

light-crossing time of $R_{\rm BLR}$. In the unified model of AGN, the broad emission lines result from the sum of emission from many individual clouds in the BLR, so rapid changes in $W_\lambda$ would more probably be expected to reflect corresponding physical changes in accretion than changes in the mean BLR cloud characteristics. The power emitted by accretion depends essentially only on $M_{\rm BH}$ and the mass accretion rate, $\dot{M} = {\rm d}M_{\rm BH}/{\rm d}t$. Even for luminous quasars, $\dot{M}$ is typically only $\sim 2~M_\odot~{\rm yr}^{-1}$ (Peterson 1997, p. 35). As $\dot{M}/M_{\rm BH}$ is therefore very small, $M_{\rm BH}$ increases very slowly, so the conclusion might be reached that the IBE reflects short-term changes in $\dot{M}$. Indeed, Pogge & Peterson (1992) have shown that a model based on time delays between variations in $L_{\rm cont}$ and $L_{\rm line}$ can be used to remove the IBE and place all quasars on the GBE locus, which supports this conclusion. On the other hand, individual quasars do not move rapidly along the GBE locus: the range of luminosities over which they exhibit the IBE is limited, so the GBE may reflect the

137

differences in $M_{\mathrm{BH}}$ between quasars.

However, it remains difficult to see why $W_\lambda$ for lines such as C IV $\lambda1549$, with high ionization potentials, should correlate in particular with the near-ultraviolet continuum luminosity as the BE suggests, or why this correlation should be in the form of a power law as in Eqn. 7.2. In addressing this problem, Green (1998) has proposed that the BE may in fact be a secondary correlation to a primary relationship between $W_\lambda$ and the X ray-to-optical continuum slope, and concluded that $W_\lambda$ depends on the *shape* of the ionizing continuum or perhaps on some third parameter characterizing quasar physics, although exactly which parameter this is remains controversial (Kuraszkiewicz et al. 1999).

## 7.3.2 Line width as a luminosity indicator

Another possible indicator of intrinsic luminosity is the intrinsic velocity FWHM of the lines, $v_{\mathrm{line}}$, which can be theoretically related to luminosity as follows. In the unified model of AGN, a principal physical difference between quasars is their central black hole mass, $M_{\mathrm{BH}}$, which defines their Eddington luminosity, $L_{\mathrm{Edd}}$. $L_{\mathrm{Edd}}$ is the luminosity at which the repulsive radiation force on a particle equals the attractive gravitational force, and is thus a good first-order estimate of the luminosity of an accretion source. In the simple case considered here, it is assumed that the source of luminosity is spherically-symmetric accretion of hydrogen gas. To derive $L_{\mathrm{Edd}}$, consider an atom of hydrogen of mass $m_{\mathrm{H}}$ falling from radius $r$ onto a black hole of mass $M_{\mathrm{BH}}$. The attractive gravitational force on the particle due to the black hole is simply

$$F_{\mathrm{attr}} = -\frac{G M_{\mathrm{BH}} m_{\mathrm{H}}}{r^2}$$

where $G$ is the gravitational constant. Now, emission from accretion will be scattered by electrons carried by the in-falling hydrogen gas. The electron scattering rate, $s$, for photons of frequency $\nu$ at radius $r$ is given by

$$s = \frac{L_\nu}{4\pi r^2 h \nu} \sigma_{\mathrm{e}}$$

where $L_\nu$ is the luminosity at frequency $\nu$, $h$ is Planck's constant and $\sigma_e$ is the Thomson electron scattering cross-section. Assuming further that the full photon

momentum is transferred, the repulsive force on a scattering electron is

$$F_{\text{rep}} = s\,\frac{h\nu}{c}$$

where $c$ is the speed of light. Hence, the luminosity at which the attractive and repulsive forces balance, so that $F_{\text{rep}} + F_{\text{attr}} = 0$, is

$$L_{\text{Edd}} = \frac{4\pi c G M_{\text{BH}} m_{\text{H}}}{\sigma_e} \simeq 3.4 \times 10^4 \frac{M_{\text{BH}}}{M_\odot}\, L_\odot \tag{7.3}$$

where $M_\odot$ is the solar mass and $L_\odot$ is the solar luminosity. At luminosities $L > L_{\text{Edd}}$, gas is repelled by luminosity more than it is attracted by gravity, so additional in-falling gas is blown away, and accretion power is thereby self-limited. A first-order approximation of the maximum luminosity of a quasar in the unified scheme is therefore $L_{\text{max}} \simeq L_{\text{Edd}} \propto M_{\text{BH}}$. If a physically-reasonable assumption is adopted that the BLR is gravitationally bound and stable (Alexander & Netzer 1997, and references therein), then the virial theorem says that the total potential energy in the BLR clouds is twice their kinetic energy. The velocity dispersion of clouds in the BLR can then be characterized by

$$v_{\text{BLR}}^2 = \frac{G M_{\text{BH}}}{R_{\text{BLR}}} \tag{7.4}$$

where $R_{\text{BLR}}$ is the effective radius of the BLR. The observed emission line profiles may then result from the sum of the emission from all of the BLR clouds, the contribution from each cloud being Doppler-shifted by the line-of-sight component of the cloud's orbital velocity, so that $v_{\text{line}} \propto v_{\text{BLR}}$. An approximation of $M_{\text{BH}}$ can then be obtained by equating $v_{\text{line}} = v_{\text{BLR}}$, giving

$$M_{\text{BH}} \simeq \frac{v_{\text{line}}^2 R_{\text{BLR}}}{G} \simeq 7 \times 10^6 \left(\frac{v_{\text{line}}}{1000\ \text{km s}^{-1}}\right)^2 M_\odot \tag{7.5}$$

using $R_{\text{BLR}} = 1$ pc (Shields 1992). Combining Eqns. 7.3 and 7.5 then gives the numerical relation

$$L_{\text{Edd}} \simeq 2.4 \times 10^{11} \left(\frac{v_{\text{line}}}{1000\ \text{km s}^{-1}}\right)^2 L_\odot. \tag{7.6}$$

While the approximation for $M_{\text{BH}}$ in Eqn. 7.5 gives values that are numerically similar to those obtained by other means (Haehnelt et al. 1998, and references therein), it is not precise, because $R_{\text{BLR}}$ will also vary with $M_{\text{BH}}$, via the gravitational potential acting on the BLR clouds and the flux of ionizing radiation that excites

them. Also, while $L_{\mathrm{Edd}}$ gives an upper bound on $L_{\mathrm{cont}}$, the Eddington efficiency, $\epsilon = L_{\mathrm{cont}}/L_{\mathrm{Edd}} \simeq 0.01\text{--}0.1$, is still not well constrained (Wandel 1999, and references therein). Nevertheless, Eqn. 7.6 does suggest that a power-law relationship between luminosity and line velocity width might be expected.

Note that the relation between the intrinsic ($z = 0$) and observed values of $W_\lambda$ and $v_{\mathrm{line}}$ is $W_\lambda(0) = W_\lambda(z)/(1 + z)$ and $v_{\mathrm{line}}(0) = v_{\mathrm{line}}(z)/(1 + z)$, which are both independent of cosmological parameters. This attribute makes $W_\lambda$ and $v_{\mathrm{line}}$ particularly attractive in determining quasar luminosities, in contrast to the standard relation between apparent magnitude and luminosity, which involves the cosmological parameters in the calculation of the luminosity distance. However, as B77 pointed out, *calibration* of any relation between intrinsic luminosity and observables still relies on assumed cosmology – it is the differences between the predicted and measured $N(m)$ relations that determine $q_0$.

## 7.4 Analysis

### 7.4.1 Measurements of $W_\lambda$, $v_{\mathrm{line}}$ and $L_{\mathrm{cont}}$

The selection of the sample analysed is described in §7.5. Each quasar spectrum was first blue-shifted from the observed redshift to $z = 0$ using the IRAF DOPCOR procedure, so that the intrinsic values of $W_\lambda$ and $v_{\mathrm{line}}$ could be measured. $W_\lambda$ and $v_{\mathrm{line}}$ were then measured automatically using the IRAF FITPROFS procedure. The parameters used are shown in table 7.1. FITPROFS simultaneously fits a straight-line continuum and a line profile to the specified spectral region. The C IV $\lambda$1549 emission line was fitted by a single Gaussian profile whose centroid was fixed at the rest wavelength of the line. Adding additional Gaussian components, to model weak adjacent lines (e.g. He II $\lambda$1640), did not reduce the uncertainties in the measurements, and led to the fit being poorly-constrained in more cases.

A possible difficulty with an analysis of CUQS spectra is that a specific continuum luminosity, $L_\lambda$, cannot properly be measured from them because we have no knowledge of the aperture correction required or, more importantly, the losses due to astrometric and telescope pointing errors for individual spectra (note that the values of $W_\lambda$ and $v_{\mathrm{line}}$ are not affected by this problem). Instead, a continuum

**Table 7.1**: Parameters for fitting the C IV line used by the FITPROFS procedure in IRAF. The continuum fitting range extends from 100 Å to the blue of the C IV $\lambda$1549 line, to 100 Å to the red of the adjacent He II $\lambda$1640 line.

| Fitting parameter | Value |
|---|---|
| Continuum region | 1449–1741 Å |
| Line centre | 1549 Å |
| Line profile | Gaussian |
| Constant noise variance, $\sigma_0^2$ | 10 |
| Inverse gain, $i$ | 1.6667 |

luminosity, $L_{\text{cont}}$, was calculated from the calibrated SuperCOSMOS photometric magnitude of the quasar using the relation (Green 1996)

$$\log L_{\text{cont}} = 28.50 - \tfrac{2}{5}\left[ b_{\text{J}} + \Delta b(z) - 5\log\frac{d_{\text{L}}}{r_{10}}\right] \tag{7.7}$$

where $b_{\text{J}}$ is the apparent magnitude of the quasar from the calibrated SuperCOS-MOS data, $d_{\text{L}}$ is the quasar's luminosity distance (see appendix B), $r_{10}$ corresponds to 10 pc, and the magnitude-to-luminosity constant is based on the nominal solar absolute magnitude and luminosity, $M_\odot = 4.8$ and $\log L_\odot = 26.58$ (for $L_\odot$ in Watts). The $\Delta b(z)$ term (effectively the $k$ correction described in appendix C) was interpolated from table 3 of Green (1996), which is reproduced in table 7.2. These $\Delta b(z)$ values are based a composite quasar spectrum with a continuum power-law index of $\alpha \simeq -0.23$ [cf. Francis et al. (1991) and Natali et al. (1998)], and include the effects of emission lines in the $B$ passband at redshift $z$. The calculated luminosities therefore do not correspond exactly to the absolute magnitudes derived in §5.2.2, where $\alpha = -1$ was used and the emission lines were ignored. Green (1996) also assumed a $B$ passband slightly different to that of the $B_{\text{J}}$ plates used here. However, the effect of including the emission lines is smaller than the uncertainties in the $b_{\text{J}}$ measurements (Wilkes 1999b), and in any case, the same $\Delta b(z)$ table has been applied to all of the quasars analysed, so the results of this analysis are self-consistent.

## 7.4.2 Estimated uncertainties in the measurements

The uncertainty in $\log L_{\text{cont}}$ used for all quasars was $\sigma_{\log L} = 0.044$, which was estimated from the combination of uncertainties in Eqn.7.7. FITPROFS makes estimates of the uncertainties on $W_\lambda$ and $v_{\text{line}}$ based on the variance of the counts in each pixel,

141

**Table 7.2:** Adopted $b$ magnitude corrections, from Green (1996).

| $z$ | $\Delta b(z)$ | $z$ | $\Delta b(z)$ | $z$ | $\Delta b(z)$ |
|-----|------|-----|------|-----|------|
| 0.0 | 0 | 1.0 | -0.574 | 2.0 | -0.823 |
| 0.1 | -0.071 | 1.1 | -0.631 | 2.1 | -0.832 |
| 0.2 | -0.171 | 1.2 | -0.671 | 2.2 | -0.870 |
| 0.3 | -0.259 | 1.3 | -0.703 | 2.3 | -0.894 |
| 0.4 | -0.349 | 1.4 | -0.733 | 2.4 | -0.879 |
| 0.5 | -0.421 | 1.5 | -0.772 | 2.5 | -0.849 |
| 0.6 | -0.475 | 1.6 | -0.811 | 2.6 | -0.813 |
| 0.7 | -0.511 | 1.7 | -0.822 | 2.7 | -0.722 |
| 0.8 | -0.529 | 1.8 | -0.828 | 2.8 | -0.724 |
| 0.9 | -0.545 | 1.9 | -0.827 | 2.9 | -0.669 |

$\sigma_{\rm p}^2$, of the spectrum being measured, given by

$$\sigma_{\rm p}^2 = \sigma_0^2 + iI$$

where $\sigma_0^2$ is a constant noise term, $I$ is the count in the pixel and $i$ is the inverse detector gain. Detector gain is difficult to define for the 2D-Frutti detector (Shectman 1984), but was estimated here as a counting efficiency of 0.6 counts per photon. The major contribution to constant noise in these spectra is sky subtraction error. The variance in the residual sky was estimated from sky-subtracted sky spectra to be $\sigma_0^2 = 10$.

No additional allowance was made for the effects of variability between the epochs of photometric and spectrographic observations, so the uncertainties in $L_{\rm cont}$, $W_\lambda$ and $v_{\rm line}$ are slightly underestimated. The uncertainty in redshift used for all quasars was $\sigma_z = 0.005$ (see §5.2.1).

### 7.4.3  Correlations

For each set of $(x, y)$ data in which linear correlations were examined, Pearson's correlation coefficient, $\rho$, was calculated using the standard formula

$$\rho = \frac{\text{cov}(x, y)}{\sigma_x \sigma_y} \tag{7.8}$$

where $\text{cov}(x, y) = \overline{xy} - \bar{x}\bar{y}$ is the covariance between $x$ and $y$. The significance of the $\rho$ values was determined by the number of standard deviations, $N_\sigma$, that $\rho$ differed from zero, estimated by (Barlow 1989, p. 80)

$$N_\sigma = \frac{\sqrt{N - 3}}{2} \ln\left[\frac{1 + \rho}{1 - \rho}\right] \tag{7.9}$$

where $N$ is the number of data points.

Three least-squares methods were used to fit straight regression lines of the form $y = mx + c$ to the data sets. Each method finds the values of $m$ and $c$ that minimizes a weighted sum of the squared distances of the $(x_i, y_i)$ points from the fitted line, but they differ in how 'distance' is defined. In the first method, $x$ is treated as the independent variable, errors on the $x_i$ are ignored and the distances are measured parallel to the $y$ axis, so that the quantity minimized is

$$\chi^2_x = \sum_i \frac{(y_i - (mx_i + c))^2}{\sigma^2_{y_i}} \qquad (7.10)$$

where $\sigma_{y_i}$ is the uncertainty on $y_i$ and the sum is over all the data points. In the second, $y$ is treated as independent, errors on the $y_i$ are ignored and the distances of the points from the fitted line are measured parallel to the $x$ axis. The quantity minimised in this case is

$$\chi^2_y = \sum_i \frac{(x_i - (y_i - c)/m)^2}{\sigma^2_{x_i}} \qquad (7.11)$$

where $\sigma_{x_i}$ is the uncertainty on $x_i$. Both of these have simple analytic solutions when the uncertainties are assumed to have a Gaussian distribution. The third method takes account of the errors on both coordinates, and the quantity to be minimised becomes the weighted sum of the squared distances of the data points from the fitted line measured orthogonally to the line,

$$\chi^2_{xy} = \sum_i \frac{(y_i - mx_i - c)^2}{(1 + m^2)\sigma_{x_i}\sigma_{y_i}}. \qquad (7.12)$$

This has no analytic solution when the measurement errors for each point are drawn from different distributions (as is strictly the case for the data analysed here), so a numerical approach must be applied (Barlow 1989, p. 110).

In most earlier studies of the BE, it is unclear exactly how power-law fitting was performed, or indeed whether the uncertainties in the measurements were accounted for at all, although in general the $\chi^2_x$ method is implied with $L_{\text{cont}}$ taken as the independent variable. Pogge & Peterson (1992) clearly demonstrated the importance of these omissions of detail, showing that all methods that do not account for uncertainty in both coordinates are inadequate for determining the 'best' fit of a straight line and estimating the uncertainties on its slope and intercept. For fair comparison with earlier results, however, all three forms of minimization were

143

applied here. The analytic solutions for minimizing $\chi_x^2$ and $\chi_y^2$ from Barlow (1989) were used by assuming a Gaussian distribution for $\sigma_{x_i}$ and $\sigma_{y_i}$. To minimize $\chi_{xy}^2$ by numerical methods, version 3.53 of the GAUSSFIT code of Jefferys et al. (1988) was used, taking the actual values of $\sigma_{x_i}$ and $\sigma_{y_i}$ into account.

## 7.5   Observed sample

A sample of CUQS spectra were examined to test the hypothesis that the correlations between $W_\lambda$, $v_{\text{line}}$ and $L_{\text{cont}}$ for the C IV $\lambda 1549$ line can be represented by power laws, as suggested by previous studies and by Eqn. 7.6. The sample was drawn from the full set of 320 quasar spectra detected in the CUQS catalogue from the 1996 and 1997 observations (chapter 5), with the following exclusions. Spectra for which the C IV $\lambda 1549$ line fell outside the observed wavelength range of $3300 \leq \lambda \leq 7000$ Å were excluded, corresponding to redshifts in the range $1.16 \leq z \leq 3.49$. Quasars with $\log L_{\text{cont}} < 38.355$, corresponding to the peak in the $N(M_{b_J})$ distribution, were excluded to produce a luminosity-limited sample. This would correspond to a volume-limited sample[2] in the absence of other selection effects (strictly, quasars with $z > 2.2$ should have been excluded to correctly construct a volume-limited sample; in fact, 6 quasars with $z > 2.2$ were included in the sample analysed). The fits to the continuum and C IV $\lambda 1549$ line were then examined visually, and spectra with obviously poor fits were excluded. These rejections were due to low signal-to-noise (s/n) ratio, or because the spectrum showed broad absorption on the blue side of the line making both the continuum and line profile fits poor. Finally, spectra for which FITPROFS could not make reliable estimates the uncertainties in the measurements of $W_\lambda$ and $v_{\text{line}}$ were excluded. This resulted in a sample of 89 spectra. The final two sets of exclusions may have introduced a small bias against weak-lined quasars.

The sample distributions of $\log L_{\text{cont}}$, $W_\lambda$ and $v_{\text{line}}$ against $z$ are shown in Fig. 7.2, and the number-count distributions are shown in Fig. 7.3. The redshift range of the sample is $1.326 \leq z \leq 2.407$ with a median of $z = 1.872$. The continuum luminosities

---

[2]The term 'volume-limited sample' is used to mean that all objects in the volume surveyed meeting the luminosity criteria are included in the sample.
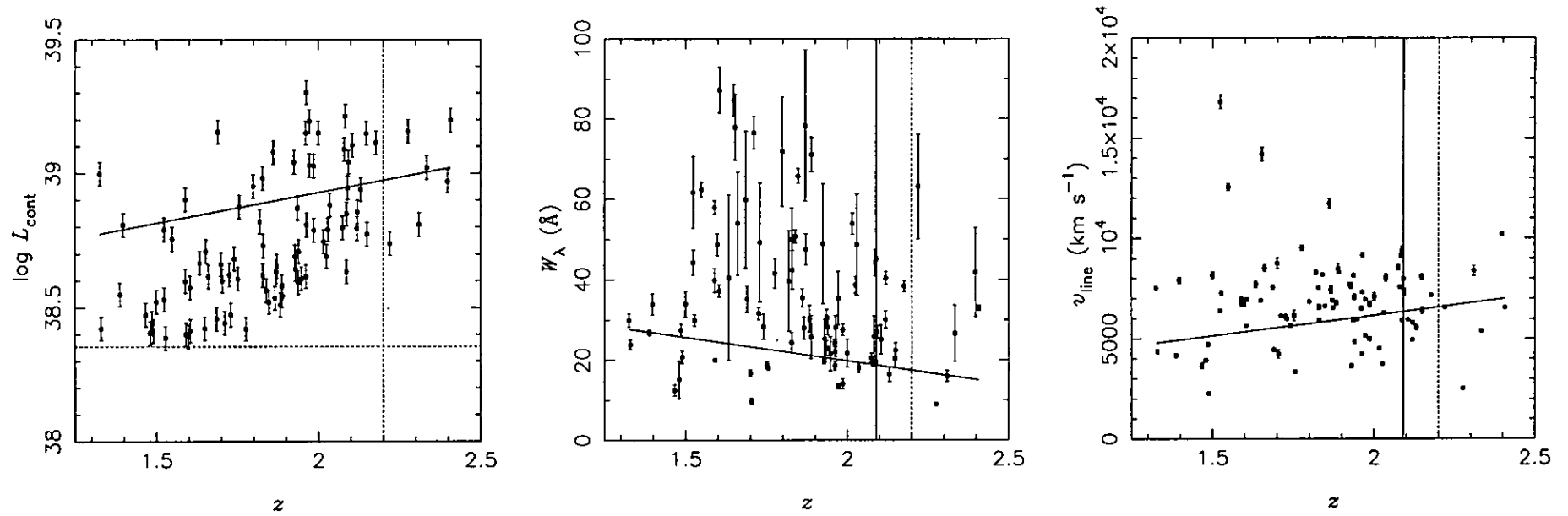
**Figure 7.2**: Distributions of $\log L_{\text{cont}}$ (left panel), $W_\lambda$ (centre panel) and $v_{\text{line}}$ (right panel) against $z$ for the sample analysed. Quasars are indicated by points. The error bars show the uncertainties in the data calculated as described in the text. Note that the error bars in $z$ are smaller than the points. The horizontal dashed line in the left panel shows the $\log L_{\text{cont}} \geq 38.355$ luminosity selection limit. The vertical dashed line at $z = 2.2$ in each panel delimits a volume-limited sample. The solid straight lines are $\chi^2_{xy}$ fits to the points, as explained in the text.
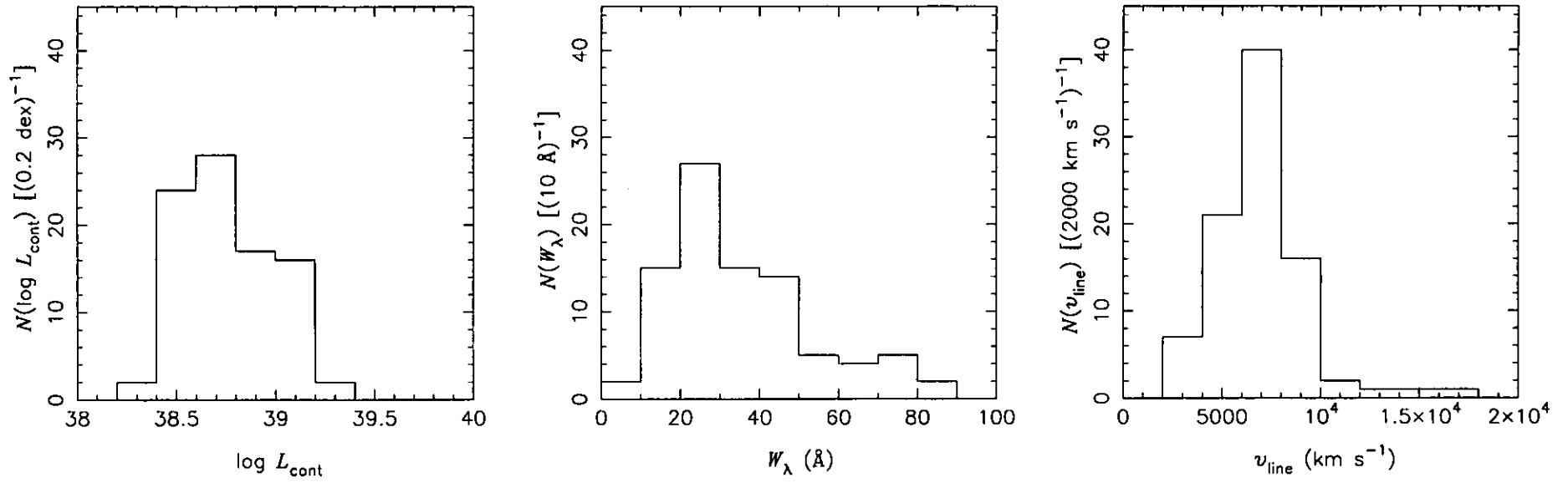
**Figure 7.3**: Number count distributions of the values of $\log L_{cont}$ (left panel), $W_\lambda$ (centre panel) and $v_{line}$ (right panel) for the sample analysed.

cover the range $38.39 \leq \log L_{\mathrm{cont}} \leq 39.30$ with a median of $\log L_{\mathrm{cont}} = 38.73$. The redshift distribution of $\log L_{\mathrm{cont}}$ is clearly not uniform, and the gap in the triangular region bounded by $38.355 \leq \log L_{\mathrm{cont}} \lesssim 38.65$ and $1.8 \lesssim z \leq 2.2$ identifies incompleteness in the sample. This is also seen in the decline in the $N(\log L_{\mathrm{cont}})$ distribution at $\log L_{\mathrm{cont}} \lesssim 38.5$. At $z = 2.2$, the gap in the $\log L_{\mathrm{cont}}$–$z$ distribution spans $\Delta(\log L_{\mathrm{cont}}) \simeq 0.3$, which is equivalent to a reduction in the limiting apparent magnitude from the nominal $b_{\mathrm{J}} = 20$ to $b_{\mathrm{J}} \simeq 19.25$ at that redshift. However, the sample selected against low s/n spectra, tending to exclude the faint, distant, quasars in this region of the distribution, so this reduction in the limiting apparent magnitude is not representative of the entire CUQS catalogue. Considering only the points above this incomplete region, with $\log L_{\mathrm{cont}} \geq 38.65$, the correlation coefficient between $z$ and $\log L_{\mathrm{cont}}$ is $\rho = 0.31$. For this correlation, $N_\sigma = 2.2$, so the correlation is weak and is not highly significant. A $\chi^2_{xy}$ fit of a straight line to the same points gives $\log L_{\mathrm{cont}} = (0.23 \pm 0.1)\, z + (38.5 \pm 0.2)$. Fig. 7.2 suggests that this probably indicates a slight deficit of luminous, low-redshift quasars in the sample.

The equivalent width distribution covers the range $8.98 \leq W_\lambda \leq 87.2$ Å, with a median of $W_\lambda = 30.1$ Å and a wide spread. Most quasars in the sample at all redshifts have $W_\lambda \gtrsim 15$ Å, marking the lower limit of confident line measurements. The correlation coefficient between $W_\lambda$ and $z$ is $\rho = -0.20$, but $N_\sigma = 1.8$, suggesting that there is no significant correlation. A $\chi^2_{xy}$ fit of a straight line to the $W_\lambda$–$z$ data gives $W_\lambda = (-11.8 \pm 4)\, z + (43 \pm 7)$. The $N(W_\lambda)$ distribution is very similar to the $1.6 \lesssim z \lesssim 2.2$ sample analysed by Osmer et al. (1994), and is slightly broader and extends to smaller $W_\lambda$ than the sample analysed by Campusano (1991a).

The $N(v_{\mathrm{line}})$ distribution covers the range $2272 \leq v_{\mathrm{line}} \leq 16808$ km s$^{-1}$, but is quite sharply peaked at $v_{\mathrm{line}} \simeq 7000 \pm 2000$ km s$^{-1}$. The distribution here is more symmetric than those of Campusano (1991a) or Wills et al. (1993) (a large optically-selected sample) and peaks at a slightly higher $v_{\mathrm{line}}$. The median velocity is $v_{\mathrm{line}} = 6782$ km s$^{-1}$. For $v_{\mathrm{line}}$ and $z$, the correlation coefficient is $\rho = -0.01$ and $N_\sigma = 0.1$, suggesting that there is no significant correlation. A $\chi^2_{xy}$ fit of a straight line to the $v_{\mathrm{line}}$–$z$ data gives $v_{\mathrm{line}} = (2046 \pm 724)\, z + (2078 \pm 1351)$.

This sample therefore achieves several of the attributes of an ideal sample listed in §7.3.1 – it is homogeneous, luminosity-limited and has no strong selection in $W_\lambda$
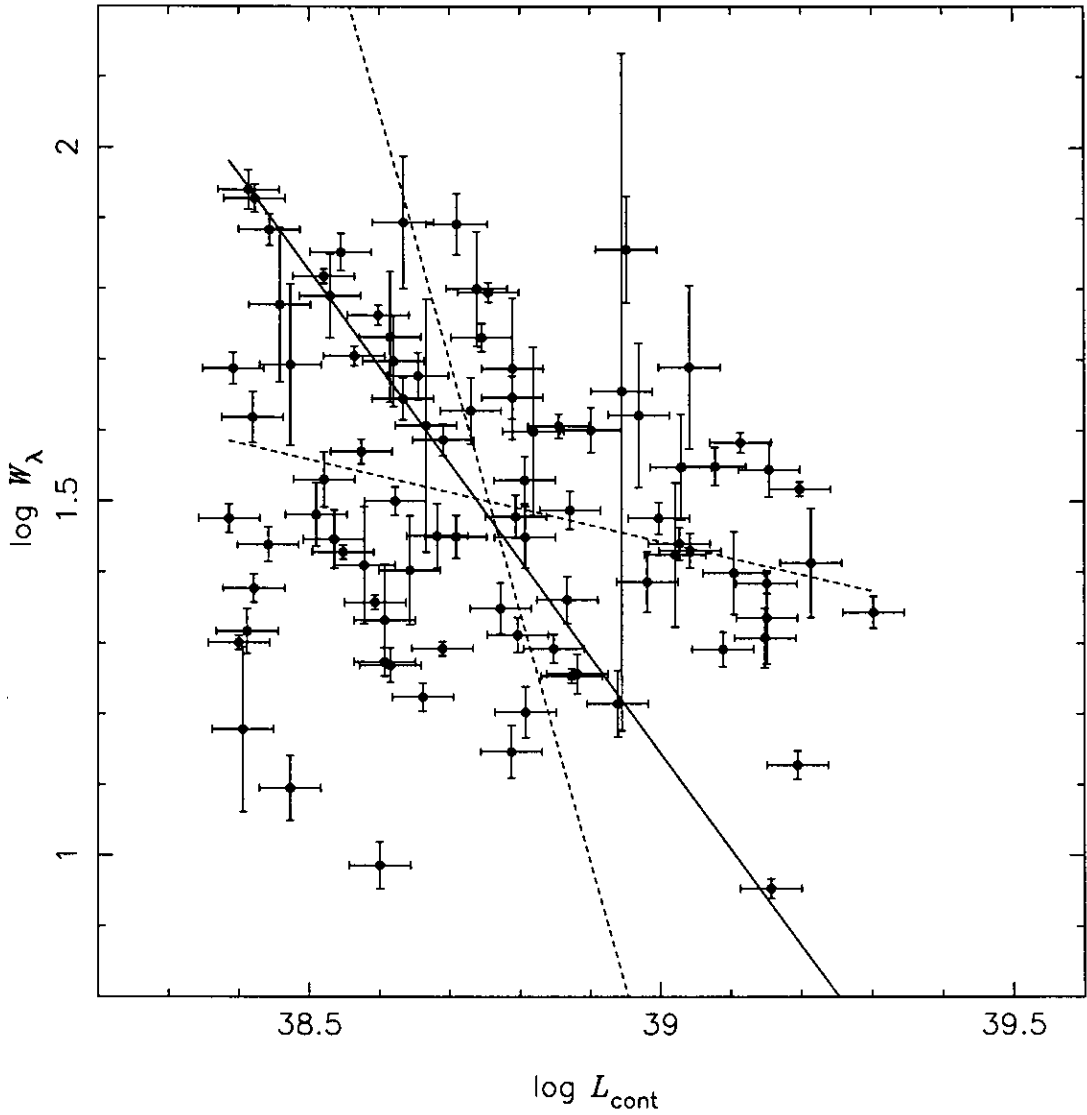
**Figure 7.4.** The distribution of the sample analysed in the $(\log L_{\text{cont}}, W_\lambda)$ plane. Quasars are shown by points. The error bars show the uncertainties in the values, calculated as described in the text. The solid straight line was fitted by minimizing $\chi^2_{xy}$. The dashed straight lines were fitted by minimizing $\chi^2_x$ (the shallower line) and $\chi^2_y$ (the steeper line).

or $v_{\text{line}}$ – but it does not cover broad ranges of luminosity or redshift. The effect of these deficiencies are discussed in §7.7.

## 7.6   Results

The correlation coefficients and the slopes and intercepts of the straight lines fitted to each of the pairs $(\log L_{\text{cont}}, \log W_\lambda)$, $(\log L_{\text{cont}}, \log v_{\text{line}})$ and $(\log v_{\text{line}}, \log W_\lambda)$ in the sample data using the methods described above are summarized in table 7.3,

Table 7.3: The correlations and fits to the measurements of $\log L_{cont}$, $\log W_\lambda$ and $\log v_{line}$. The correlation coefficient, $\rho$, was calculated using Eqn. 7.8. The slopes, $m$, and intercepts, $c$, of the straight-line fits were found by minimizing the three metrics defined in Eqns. 7.10–7.12. The straight lines are defined by $y = mx + c$. $N_\sigma$ is the estimate of the number of standard deviations that $\rho$ is from zero, calculated using Eqn. 7.9.

| | | | | $\chi^2_{xy}$ | | $\chi^2_x$ | | $\chi^2_y$ | |
| $y$ | $x$ | $\rho$ | $N_\sigma$ | $m$ | $c$ | $m$ | $c$ | $m$ | $c$ |
|---|---|---|---|---|---|---|---|---|---|
| $\log W_\lambda$ | $\log L_{cont}$ | $-0.26$ | 2.4 | $-1.4\pm0.2$ | $54\pm9$ | $-0.23\pm0.09$ | $11\pm4$ | $-3.5\pm1.5$ | $-140\pm60$ |
| $\log v_{line}$ | $\log L_{cont}$ | 0.14 | 1.3 | $3.5\pm2.3$ | $-133\pm88$ | $0.08\pm0.06$ | $0.6\pm2$ | $4.1\pm3.1$ | $155\pm115$ |
| $\log W_\lambda$ | $\log v_{line}$ | 0.39 | 3.9 | $1.2\pm0.2$ | $-3.1\pm0.6$ | $0.61\pm0.15$ | $-0.8\pm0.6$ | $3.9\pm1.1$ | $14\pm4$ |
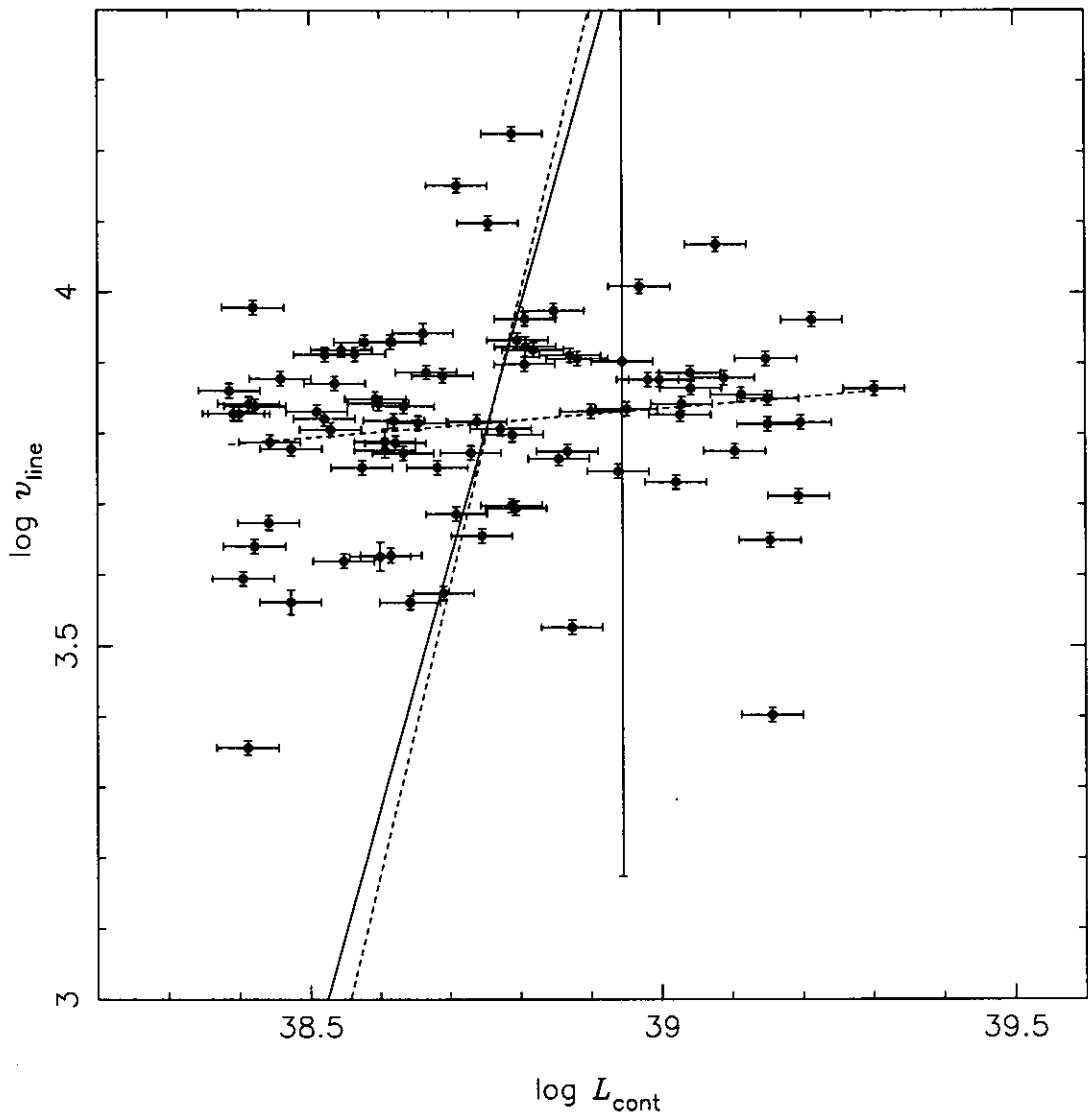
**Figure 7.5.** The distribution of the sample analysed in the $(\log L_{\text{cont}}, \log v_{\text{line}})$ plane and the straight lines fitted by the three methods. The legend is as for Fig. 7.4.

and the data points and fitted lines are shown in Figs. 7.4–7.6.

For the standard BE relation between $\log L_{\text{cont}}$ and $\log W_\lambda$, the correlation coefficient is $\rho = -0.26$, suggesting a weak correlation, and $N_\sigma = 2.4$, suggesting the correlation is marginally significant. The power-law slope found by minimizing $\chi_x^2$ (i.e. taking $\log L_{\text{cont}}$ as the independent axis) is $\beta = -0.23 \pm 0.09$, in good agreement with that found by Osmer et al. (1994) and in the same range as that found by most of the other studies cited above. However, the slope found by minimizing $\chi_{xy}^2$, $\beta = -1.4 \pm 0.2$, which is arguably more scientifically appropriate, is much steeper. Note that the difference between these slopes is $> 5$ times their formal uncertainties, demonstrating the importance of choice of fitting method.

150
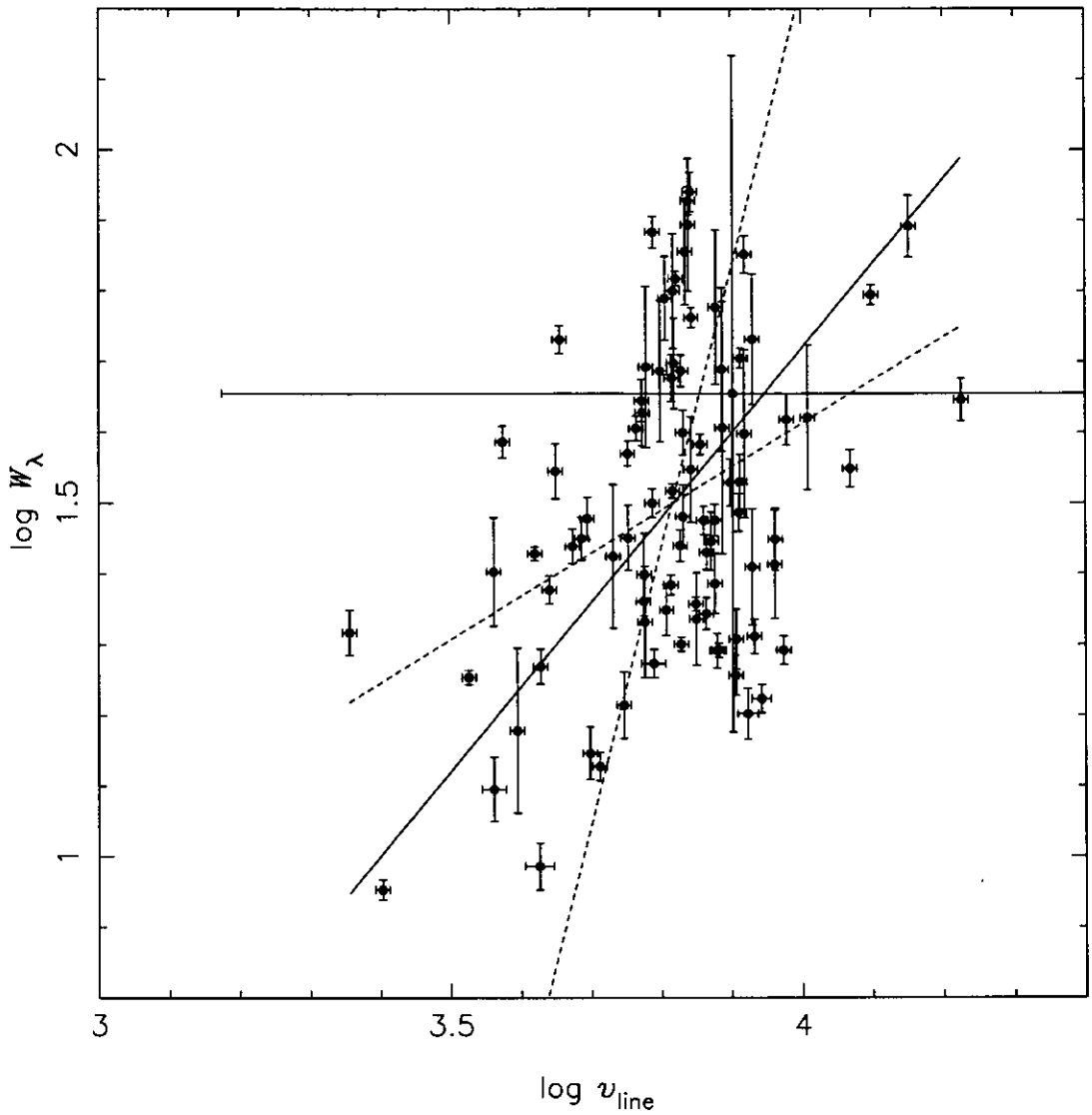
**Figure 7.6.** The distribution of the sample analysed in the $(\log W_\lambda, \log v_{\text{line}})$ plane and the straight lines fitted by the three methods. The legend is as for Fig. 7.4.

For $\log v_{\text{line}}$ and $\log L_{\text{cont}}$, the correlation coefficient is $\rho = 0.14$ and $N_\sigma = 1.4$, which suggests that there is no significant correlation in this data. However, the lines fitted by all three methods are of positive slope (that from the $\chi_x^2$ method only marginally so), which is consistent with the expectation from Eqn. 7.6 that $v_{\text{line}} \propto L_{\text{cont}}^\alpha$ with $\alpha > 0$.

Finally, the $\log W_\lambda$ and $\log v_{\text{line}}$ data were examined, for which Rudge & Raine (1998) proposed a possible theoretical relationship with a model in which $v_{\text{line}}$ depends on the inclination angle between the symmetry axis of an anisotropic BLR and the line of sight to the AGN. In this case, the sample has $\rho = 0.39$ and $N_\sigma = 3.9$, suggesting a weak but highly significant correlation. However, the positive slope of

all three fitted lines is in conflict with the predictions of Rudge & Raine, which expects $W_\lambda \propto v_{line}{}^\gamma$ with $\gamma \simeq -1$.

## 7.7 Discussion

The results found here are based on a luminosity-limited sample of 89 quasars drawn from a single homogeneous survey selected on ultraviolet excess. The correlations between $W_\lambda$, $v_{line}$ and $L_{cont}$ have been fit using a scientifically-appropriate method that fully accounts for the uncertainties in both coordinates of each data point. In these respects the results improve on previous studies.

Osmer et al. (1994) noted that a difficulty with earlier results stems from the use of samples limited by apparent magnitude. Because of the steep increase in the surface density of quasars with apparent magnitude, such samples tend to crowd up against the magnitude limit with the result that luminosity is strongly correlated with redshift. Despite knowing this, Osmer et al. did not apply a minimum luminosity limit to their data. Such a limit applied to the points in their Fig. 8 would greatly increase the uncertainties in their fitted BE relation. The sample used here, being luminosity-limited, goes some way towards avoiding this problem, although it is not immune from the effects of any possible evolution in the BE with redshift, and the slight trend to weaker lines with higher redshift seen in Fig. 7.2 may combine with the incompleteness in the sample at $z \gtrsim 1.8$ to introduce some artificial correlation between $L_{cont}$ and $W_\lambda$. The heterogeneities of the composite samples used in earlier studies, and the bias effects of selection against low-luminosity weak-lined objects inherent in samples chosen on emission line strength, have been largely avoided here. The standard criticism of the BE as a selection effect is that the correlation is enhanced by the difficulties of detecting weak, broad lines in the spectra of low-luminosity quasars (Jones & Jones 1980). Fig. 7.7 suggests that the present sample shows no such bias.

The results presented here provide weak support for the existence of a BE in the C IV $\lambda$1549 line in quasars selected on ultraviolet excess at redshifts $1.3 \lesssim z \lesssim 2.4$. The power-law slope of the BE found by minimizing $\chi^2_{xy}$, $\beta \simeq -1.4$, is much steeper than that found by other studies and, if correct, must count as evidence against the
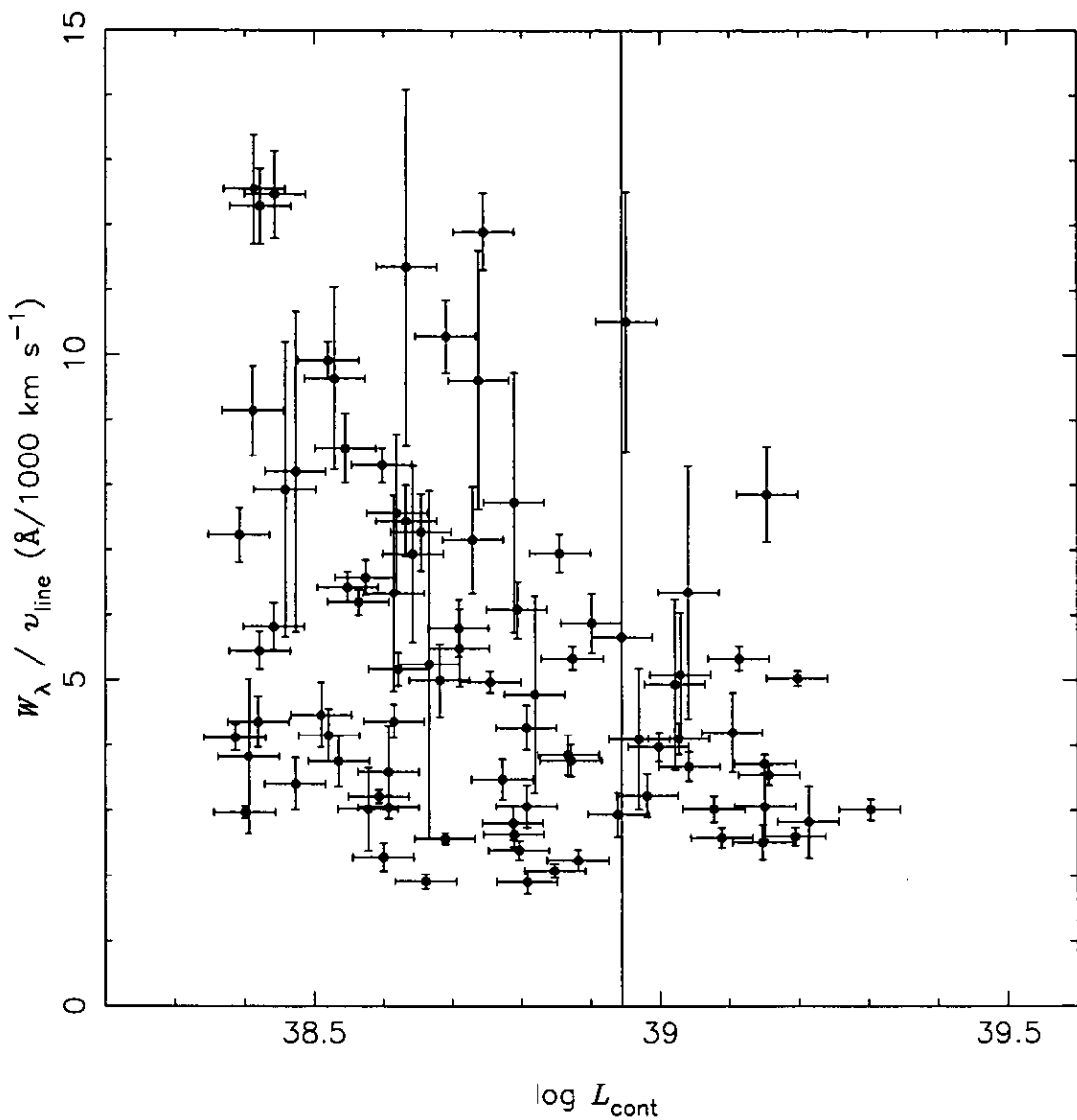
**Figure 7.7.** The distribution of $W_\lambda/v_{\text{line}}$ against $\log L_{\text{cont}}$ for the sample. The error bars on $W_\lambda/v_{\text{line}}$ were calculated by combining the individual errors on $W_\lambda$ and $v_{\text{line}}$ in quadrature, ignoring any correlation between them.

GBE model of Pogge & Peterson (1992) since $\beta < -1$ implies $b < 0$. However, the correlation is weak and the scatter in the data is very large, so the uncertainties in the slope of the BE relation remain very large. On the other hand, the slope found by minimizing $\chi_x^2$, $\beta \simeq -0.23$, is in better numerical agreement with the earlier results while being less justifiable as meaningful. If the distribution of points in Fig. 7.4 is real and not due to a hidden selection effect, then it suggests that the upper envelope of the data may be more useful than a fit to the mean (at least for samples such as this one where the IBE has not been removed) as this may tie the BE relation more closely to $L_{\text{Edd}}$ (and $M_{\text{BH}}$) and hence to the underlying physics.

The power-law correlation between $v_{\text{line}}$ and $L_{\text{cont}}$ found here weakly supports the hypothesis that the BLR clouds surround the central black hole of a quasar in a spherically-symmetric and virialized region. The slope of the significant correlation between $\log W_\lambda$ and $\log v_{\text{line}}$ found here has opposite sign to that predicted by Rudge & Raine (1998), and is based on wider ranges in both observables than was used in their analysis. This argues against their model in which $v_{\text{line}}$ depends on the inclination angle between an anisotropic axis of symmetry and the line of sight to the AGN.

All of the results here are limited by the relatively narrow ranges of intrinsic luminosity and redshift covered by the data. To achieve a much wider range of luminosities in a large homogeneous survey will be difficult not least because of the challenges presented by the requirements for accurate photometric and astrometric calibration of wide magnitude ranges, as discussed in chapter 3. Observing the C IV $\lambda1549$ line over a wider redshift range in a homogeneous sample will also remain difficult. To attempt the removal of the IBE from the results would require a long observing campaign to measure the photometric and spectral variability of a large number of objects. Combined with the large scatter still present in homogeneous samples, these difficulties argue against the BE and the $v_{\text{line}}$–$L_{\text{cont}}$ relations being generally useful for correcting quasars luminosities, such that the $m(z, q_0)$ relation could be used to determine $q_0$ from quasar spectroscopy, although detailed variability studies of these relations for individual quasars may continue to shed light on the underlying physics.

# Chapter 8

# Summary and future work

## 8.1 Chapter overview

The work reported in this thesis and the conclusions drawn from it are summarized, and some future directions are suggested.

## 8.2 Thesis summary

### 8.2.1 Calibration of digitized UKST plates

The observations for the CUQS reported here have been founded on data drawn from UK Schmidt Telescope photographic plates digitized by the SuperCOSMOS machine at the Royal Observatory Edinburgh. Many of the plate measurements were made during the development and commissioning phases of SuperCOSMOS, and much was learned about the characteristics of the plates and the digitization process. In chapter 3, it was demonstrated that the automatic star-galaxy classification of faint objects by the SuperCOSMOS and APM systems are mutually inconsistent, although it is not clear which is the more reliable.

It was shown that the astrometric accuracy required for observations of quasars (or other point sources) with fibre-input spectrographs is a function of the diameter of the optical fibres and the seeing conditions. For the 3.5-arcsec diameter fibres on the Fruit & Fiber multi-object spectrograph and the typical 1.8-arcsec FWHM seeing conditions at the Las Campanas Observatory, positions with uncertainties of

155

$\leq 1$ arcsec are sufficient to put more than 80 per cent of the light from quasars into the spectrograph fibres. It was also shown that the fibres of the 2dF spectrograph on the Anglo-Australian Telescope may be too small for efficient use of that telescope, collecting at most 60 per cent of the incident light even with 0.6-arcsec position errors in the typical 1.8-arcsec seeing at that telescope. The problems of reaching such astrometric accuracy across wide areas of digitized UKST plates remain difficult, but an r.m.s. astrometric uncertainty of $\Delta r = 0.69$ arcsec was achieved for all of the CUQS 1.5°-diameter spectroscopic fields.

By combining data from up to 5 photometric calibration regions in each plate and including calibration regions in the overlap areas of the plates, r.m.s. photometric uncertainties of $\Delta b_J = \pm 0.10$ mag, $\Delta u_J = \pm 0.12$ mag and $\Delta(u_J - b_J) = \pm 0.16$ mag were achieved over the range $15 \lesssim b_J \lesssim 21$ and $15.5 \lesssim u_J \lesssim 20.5$, with smooth residual variations across two areas of sky covered by $3 \times 3$ and $2 \times 2$ arrays of UKST fields, measuring $\sim 15° \times 15°$ and $\sim 10° \times 10°$ respectively.

## 8.2.2 The Chile-UK Quasar Survey

Chapters 4 and 5 described the spectroscopic observations, data reduction and analysis used to create the CUQS catalogue, and presented the properties of the catalogue of quasars and other objects identified.

In 12 nights of observations at Las Campanas Observatory in 1996 March, 1997 March and 1998 May, $\sim 54$ deg$^2$ of the CUQS area was observed, obtaining spectra of 4588 ultraviolet-excess quasar candidates selected on $16 \leq b_J \leq 20$ and $(u_J - b_J) \leq -0.3$. In addition, 768 spectra of objects selected on $17 \leq b_J \leq 20$ were obtained as part of a complete spectroscopic sample being made in a 1°5-diameter area in ESO/SERC survey field 345. All of the spectra obtained cover a wavelength range of at least 3300–7000 Å at 6.1 Å pixel$^{-1}$.

From the spectra obtained in 1996 and 1997, 320 quasars in the redshift range $0.228 \leq z \leq 2.768$ have been identified. In addition, 93 narrow emission-line galaxies (NELGs) in the range $0.015 \leq z \leq 0.397$ have been found. The redshifts of the quasars were measured to a typical precision of $\Delta z \simeq 0.005$ and those of the NELGs were measured to $\Delta z \simeq 0.002$. It was argued that the quasar catalogue represents a homogeneous sample of the true quasar population for $0.4 \leq z \leq 2.2$, and that

the completeness of the survey is $\sim 70$ per cent. The NELG catalogue is highly incomplete and does not yet form a homogeneous sample. Interesting, but also incomplete, samples of galactic white dwarf stars and blue galaxies lacking emission lines have also been identified.

### 8.2.3 Large quasar groups

Chapter 6 reported the results of a search for large quasar groups using a minimal spanning tree method on a homogeneous subsample of 227 quasars in the CUQS programme area. Two large quasar groups were found for which the null hypothesis of an unclustered distribution is rejected by the $(m, \sigma)$ test of Graham et al. (1995) at the 3-$\sigma$ level. The first group contains 6 quasars at median redshift $z = 1.236$ with mean separation $26 \pm 9\ h^{-1}$ Mpc. The $(m, \sigma)$ statistical significance of this group is $0.0011 \pm 0.0003$, and the probability that the group is a random significant event is $\sim 5$ per cent. Its shape suggests a single filament with length $\sim 110\ h^{-1}$ Mpc and width $\sim 15\ h^{-1}$ Mpc. The quasars in this group coincide with the core of the Clowes & Campusano (1991) group, the reality of which has now been confirmed by this independent survey.

The second group, a new discovery, ranks as one of the largest structures found so far. It contains 13 quasars with median redshift $z = 1.507$ and mean separation $32 \pm 7\ h^{-1}$ Mpc. The $(m, \sigma)$ significance of this group is $0.0020 \pm 0.0004$, and an upper limit on the probability that the group is a random significant event is $\sim 13$ per cent. The overall size of this group is $\sim 150 \times 80 \times 85\ h^{-3}$ Mpc$^3$. It lies partly outside the eastern edge of the Clowes & Campusano (1991) survey, and so would not have been detected in that survey.

These large quasar groups may have formed at such early times that they are difficult to account for as being due to the gravitational collapse of a primordial mass-density field with Gaussian fluctuations, although the uncertainties in the quasar-mass relationship at high redshift leave this question open.

## 8.2.4 Quasar luminosity indicators

Chapter 7 showed that the existence of the Baldwin Effect (BE) between the equivalent width of C IV $\lambda1549$ emission lines and the continuum luminosities of quasars is supported at the $2.4\sigma$-level by a luminosity-limited sample of quasars drawn from the survey catalogue. It was argued that the sample is free of the bias against weak, broad lines in low-luminosity quasars found in some previous studies. The BE slope found, $\beta = -1.4 \pm 0.2$, is steeper than that found in other studies. The difference in slope was shown to be at least partly due to the regression analysis used here, which it was argued is scientifically more appropriate than the methods implied by most previous studies.

It was also shown that the correlation between the velocity widths of the C IV $\lambda1549$ emission line and the continuum luminosities in the same sample has a positive slope, supporting the hypothesis that quasar broad emission lines originate in clouds occupying a spherically-symmetric and virialized region surrounding the central black hole, although the significance of the correlation coefficient is small. A significant power-law correlation with positive slope was found between the equivalent width and the velocity width of the line. This result is in conflict with the BLR model of Rudge & Raine (1998), which predicts negative slope.

## 8.3 Future work

### 8.3.1 Large-scale structure traced by quasars

The CUQS was designed to cover sufficient area to properly sample tangential structure scales of $\sim 100\ h^{-1}$ Mpc over the redshift range $0.4 \lesssim z \lesssim 2.2$ so as to provide useful measures of global clustering on those scales. The observations so far have provided evidence that significant structures on those scales exist at $z > 1$, but have not yet fully delimited those structures. It is therefore imperative that the survey be completed if the most meaningful results, both for specific structures and for the analysis of global clustering via the power spectrum, are to be obtained. Combined with the spectra already obtained, the final catalogue should contain $\sim 1330$ quasars in two continuous areas with a highly homogeneous selection function and

excellent photometric calibration, making a valuable contribution to knowledge of the Universe at high redshifts. The techniques needed to complete the survey have been established in this thesis.

The limits on fibre placement with the Fruit & Fiber spectrograph mean that quasar candidates less than 55 arcsec from an observed candidate could not be simultaneously observed. Spectra of the omitted candidates from these close candidate pairs, numbering $\sim 100$, should be obtained. The aims of these observations would be to search for quasar pairs that might link larger groups and to identify candidate gravitational lenses, as well as to slightly raise the completeness of the survey sample and remove a small bias from its angular auto-correlation function. Some 90 per cent of known gravitational lenses have separations $< 3$ arcsec, the lenses in all cases apparently being individual galaxies (Muñoz et al. 1999, and references therein). However, with $> 10^3$ quasars, the full CUQS may include one or more instances of quasars lensed by massive cluster halos with separations $> 5$ arcsec (Smith 1998, p. 99). One possible pair, with 11 arcsec separation, has already been tentatively identified in four-colour deep imaging (C.P. Haines, private communication, 1999 June 14).

Komberg & Lukash (1994) suggested that large quasar groups may be the precursors of present-epoch 'Great Attractors': very massive structures ($\sim 10^{16}\ M_\odot$) with matter falling into their deep gravitational potential wells from a radius of $\sim 50\ h^{-1}$ Mpc. If this is the case, then correlations in the redshifts of absorption lines in the spectra of quasars behind the group would be expected. Correlated absorption has already been reported at scales of $\sim 35$ and $\sim 100\ h^{-1}$ Mpc (Williger et al. 1995; Quashnock et al. 1998), and further studies using quasars behind clustered and unclustered regions in the CUQS are warranted.

## 8.3.2 Biased formation of quasars at high redshift

One of the most important outstanding questions to be resolved is how well (or indeed, if) quasars trace the mass distribution at $z > 1$. Answering this is crucial if the advantages of quasars over galaxies for wide-field high-redshift studies of large-scale structure are to be fully exploited.

The next few years will see the opening of at least two new observational av-

enues to attacking the question of quasar-mass bias at high redshift. First, the great 8-metre and 10-metre telescopes now in operation will permit direct observation of galaxies in the vicinity of high-redshift quasars. Second, the launch of the Chandra and XMM X-ray telescopes will permit determinations of the mass of clusters and superclusters of galaxies associated with quasars at higher redshifts and higher resolution than ever before, both by direct observation of emission from hot cluster gas, and by combining cluster X-ray signatures with radio observations of the imprint of the gas on the CMBR through the Sunyaev-Zeldovich effect. With these advances, there is no doubt that quasars will continue to play an important rôle in the future of cosmology.

# Appendix A

# Catalogue of emission-line objects in the CUQS

The quasars and other AGN detected in the CUQS from the 1996 and 1997 observations are listed in tables A.1–A.4. The entries in each table are sorted into the order in which the tiles were observed, as described in §4.5.

**Table A.1:** The 267 quasars detected in the CUQS programme area observations from 1996 and 1997. The first column gives the CUQS spectrum reference number, consisting of the observed year, night, tile sequence and aperture numbers. The sky positions (in J2000 coordinates) and $b_J$ and $u_J$ magnitudes are taken from the calibrated SuperCOSMOSdata, as described in chapter 3. The redshifts, $z$, were determined as described in §5.2.1. The magnitude uncertainties are $\Delta b_J = 0.10$ mag and $\Delta u_J = 0.12$ mag. The redshift uncertainties are $\Delta z = 0.005$ except where a different value is given in the final column.

| CUQS No. | $\alpha$ $\binom{\text{h.m.s}}{}$ | $\delta$ $\binom{\circ.'.''}{}$ | $u_J$ | $b_J$ | $z$ | $\Delta z$ |
|---|---|---|---|---|---|---|
| 1996.1.1.009 | 10 : 42 : 16.88 | +04 : 31 : 47.5 | 18.87 | 19.81 | 0.419 | |
| 1996.1.1.014 | 10 : 41 : 50.80 | +04 : 43 : 32.7 | 19.08 | 20.00 | 1.534 | |
| 1996.1.1.021 | 10 : 42 : 39.33 | +05 : 16 : 44.9 | 18.41 | 19.69 | 1.872 | |
| 1996.1.1.048 | 10 : 40 : 12.09 | +04 : 39 : 04.3 | 18.46 | 19.62 | 1.116 | |
| 1996.1.1.054 | 10 : 41 : 46.15 | +05 : 12 : 37.9 | 18.95 | 19.98 | 0.784 | |
| 1996.1.1.057 | 10 : 42 : 44.24 | +04 : 07 : 04.6 | 18.97 | 19.91 | 1.686 | |
| 1996.1.1.073 | 10 : 43 : 49.32 | +05 : 12 : 24.9 | 18.05 | 19.00 | 0.875 | |
| 1996.1.1.088 | 10 : 45 : 04.84 | +04 : 34 : 00.9 | 18.62 | 19.50 | 0.395 | |
| 1996.1.1.098 | 10 : 43 : 23.61 | +04 : 22 : 17.6 | 18.77 | 19.37 | 2.334 | |
| 1996.1.1.100 | 10 : 43 : 42.84 | +04 : 21 : 56.6 | 18.50 | 19.52 | 0.782 | |
| 1996.1.1.119 | 10 : 44 : 28.82 | +04 : 48 : 40.8 | 18.80 | 19.60 | 0.402 | 0.004 |
| 1996.1.1.127 | 10 : 43 : 57.81 | +04 : 38 : 24.6 | 18.28 | 18.99 | 2.407 | |
| 1996.1.1.128 | 10 : 44 : 11.87 | +04 : 45 : 37.8 | 19.01 | 19.68 | 2.417 | |
| 1996.1.2.001 | 10 : 46 : 56.72 | +05 : 41 : 50.4 | 17.62 | 18.62 | 1.236 | |
| 1996.1.2.005 | 10 : 45 : 18.87 | +05 : 24 : 55.5 | 18.07 | 19.05 | 0.701 | |
| 1996.1.2.018 | 10 : 45 : 29.87 | +06 : 23 : 39.7 | 18.31 | 19.50 | 2.120 | |
| 1996.1.2.026 | 10 : 46 : 31.87 | +05 : 20 : 09.5 | 18.63 | 19.98 | 1.426 | |
| 1996.1.2.029 | 10 : 45 : 06.45 | +05 : 16 : 27.3 | 18.57 | 19.37 | 1.100 | |
| 1996.1.2.042 | 10 : 44 : 09.49 | +05 : 31 : 34.7 | 16.68 | 18.34 | 2.090 | |
| 1996.1.2.046 | 10 : 43 : 46.29 | +05 : 23 : 31.8 | 19.32 | 19.96 | 0.649 | |
| 1996.1.2.054 | 10 : 44 : 25.80 | +06 : 09 : 25.4 | 18.32 | 19.58 | 1.251 | |
| 1996.1.2.056 | 10 : 44 : 11.99 | +06 : 07 : 09.5 | 19.23 | 19.98 | 2.340 | |
| 1996.1.2.058 | 10 : 45 : 26.22 | +04 : 52 : 55.8 | 18.24 | 19.89 | 1.355 | |
| 1996.1.2.064 | 10 : 44 : 30.27 | +05 : 18 : 57.0 | 17.37 | 18.03 | 0.890 | |
| 1996.1.2.068 | 10 : 48 : 00.44 | +05 : 22 : 09.8 | 18.42 | 19.69 | 1.232 | |
| 1996.1.2.087 | 10 : 48 : 40.12 | +05 : 35 : 51.2 | 17.72 | 18.87 | 1.972 | |
| 1996.1.2.103 | 10 : 47 : 21.59 | +05 : 13 : 48.1 | 18.53 | 19.69 | 1.733 | |
| 1996.1.2.109 | 10 : 45 : 52.74 | +06 : 24 : 36.8 | 17.24 | 18.08 | 1.507 | |
| 1996.1.2.117 | 10 : 47 : 16.42 | +05 : 51 : 59.3 | 17.71 | 18.67 | 0.895 | |
| 1996.1.2.120 | 10 : 47 : 42.78 | +05 : 49 : 59.3 | 19.05 | 19.94 | 2.220 | |
| 1996.1.2.124 | 10 : 47 : 33.19 | +05 : 24 : 54.5 | 16.84 | 17.87 | 1.326 | |
| 1996.1.3.004 | 10 : 37 : 48.30 | +04 : 02 : 40.9 | 17.20 | 18.12 | 1.088 | |
| 1996.1.3.005 | 10 : 37 : 39.42 | +03 : 49 : 45.6 | 17.94 | 19.11 | 1.030 | |
| 1996.1.3.006 | 10 : 37 : 43.90 | +04 : 02 : 32.7 | 18.86 | 19.77 | 1.087 | |
| 1996.1.3.011 | 10 : 37 : 56.97 | +03 : 50 : 22.6 | 18.43 | 19.11 | 2.160 | 0.01 |
| 1996.1.3.016 | 10 : 37 : 35.95 | +03 : 48 : 33.9 | 19.22 | 19.80 | 0.541 | |

(continued)

162

| CUQS No. | $\alpha$ (h.m.s) | $\delta$ (°.′.″) | $u_{\rm J}$ | $b_{\rm J}$ | $z$ | $\Delta z$ |
|---|---|---|---|---|---|---|
| 1996.1.3.030 | 10 : 39 : 01.52 | +03 : 07 : 13.2 | 18.85 | 19.78 | 2.106 | |
| 1996.1.3.039 | 10 : 36 : 31.62 | +03 : 57 : 07.3 | 18.26 | 18.85 | 0.813 | |
| 1996.1.3.056 | 10 : 36 : 57.77 | +04 : 12 : 22.2 | 18.27 | 19.23 | 0.630 | |
| 1996.1.3.059 | 10 : 38 : 04.61 | +03 : 13 : 19.5 | 19.29 | 19.98 | 2.370 | 0.01 |
| 1996.1.3.082 | 10 : 40 : 53.21 | +03 : 49 : 58.2 | 19.07 | 19.85 | 2.478 | |
| 1996.1.3.086 | 10 : 41 : 14.03 | +03 : 43 : 11.1 | 17.93 | 18.95 | 1.259 | |
| 1996.1.3.087 | 10 : 41 : 14.12 | +03 : 50 : 39.4 | 18.27 | 19.40 | 0.922 | |
| 1996.1.3.091 | 10 : 41 : 16.77 | +03 : 55 : 10.6 | 18.86 | 19.95 | 1.243 | |
| 1996.1.3.093 | 10 : 41 : 23.92 | +03 : 54 : 50.3 | 17.54 | 18.50 | 1.398 | |
| 1996.1.3.103 | 10 : 40 : 04.52 | +03 : 34 : 26.3 | 18.86 | 19.82 | 1.528 | |
| 1996.1.3.115 | 10 : 39 : 16.51 | +04 : 05 : 36.3 | 18.46 | 19.57 | 2.768 | |
| 1996.1.3.127 | 10 : 40 : 32.88 | +03 : 43 : 06.3 | 18.60 | 19.97 | 0.864 | |
| 1996.2.1.003 | 10 : 48 : 36.56 | +03 : 08 : 12.0 | 18.31 | 19.44 | 1.741 | |
| 1996.2.1.025 | 10 : 48 : 19.45 | +02 : 38 : 14.3 | 18.85 | 19.89 | 2.211 | |
| 1996.2.1.027 | 10 : 47 : 53.30 | +02 : 40 : 58.6 | 18.48 | 19.58 | 2.075 | |
| 1996.2.1.028 | 10 : 47 : 52.98 | +02 : 24 : 07.0 | 18.52 | 19.64 | 1.136 | |
| 1996.2.1.031 | 10 : 47 : 23.78 | +02 : 24 : 51.7 | 17.48 | 18.25 | 0.730 | |
| 1996.2.1.032 | 10 : 47 : 02.83 | +02 : 35 : 00.9 | 18.74 | 19.75 | 0.993 | |
| 1996.2.1.052 | 10 : 47 : 10.17 | +03 : 28 : 56.5 | 17.59 | 18.56 | 1.030 | |
| 1996.2.1.057 | 10 : 46 : 43.87 | +02 : 42 : 35.1 | 18.26 | 19.17 | 0.569 | |
| 1996.2.1.058 | 10 : 46 : 42.09 | +02 : 31 : 29.8 | 17.96 | 18.90 | 0.536 | |
| 1996.2.1.079 | 10 : 51 : 17.66 | +03 : 27 : 37.8 | 18.85 | 19.89 | 0.676 | |
| 1996.2.1.080 | 10 : 51 : 22.10 | +03 : 22 : 59.8 | 18.74 | 19.25 | 2.018 | |
| 1996.2.1.096 | 10 : 51 : 26.80 | +03 : 05 : 37.4 | 18.14 | 19.23 | 1.454 | |
| 1996.2.1.112 | 10 : 50 : 25.07 | +03 : 34 : 41.5 | 18.38 | 19.47 | 2.152 | |
| 1996.2.1.122 | 10 : 49 : 17.67 | +02 : 54 : 42.8 | 18.05 | 18.94 | 2.177 | |
| 1996.2.1.127 | 10 : 49 : 59.78 | +02 : 55 : 18.4 | 17.73 | 18.85 | 1.318 | |
| 1996.2.1.128 | 10 : 50 : 10.68 | +02 : 45 : 52.7 | 18.99 | 19.92 | 2.188 | |
| 1996.2.2.004 | 10 : 43 : 06.96 | +03 : 41 : 21.8 | 17.53 | 18.42 | 0.851 | |
| 1996.2.2.018 | 10 : 43 : 59.23 | +04 : 04 : 54.2 | 18.04 | 19.23 | 1.935 | |
| 1996.2.2.022 | 10 : 43 : 45.38 | +04 : 02 : 59.5 | 18.63 | 19.85 | 1.184 | |
| 1996.2.2.025 | 10 : 44 : 00.53 | +02 : 39 : 22.5 | 18.66 | 19.93 | 1.433 | |
| 1996.2.2.040 | 10 : 42 : 03.65 | +03 : 33 : 28.9 | 18.81 | 19.94 | 0.828 | |
| 1996.2.2.046 | 10 : 41 : 48.36 | +03 : 13 : 22.3 | 18.91 | 19.95 | 1.649 | |
| 1996.2.2.054 | 10 : 42 : 25.61 | +03 : 55 : 37.7 | 17.70 | 18.95 | 1.227 | |
| 1996.2.2.056 | 10 : 42 : 05.53 | +03 : 42 : 17.5 | 19.18 | 19.74 | 0.489 | |
| 1996.2.2.070 | 10 : 45 : 31.44 | +03 : 00 : 27.5 | 18.69 | 19.98 | 1.889 | |
| 1996.2.2.076 | 10 : 45 : 59.37 | +03 : 43 : 09.3 | 18.43 | 19.43 | 1.500 | |
| 1996.2.2.078 | 10 : 46 : 10.62 | +03 : 50 : 30.8 | 18.36 | 19.21 | 0.362 | |
| 1996.2.2.093 | 10 : 45 : 35.09 | +03 : 41 : 21.9 | 18.28 | 19.29 | 0.355 | |
| 1996.2.2.096 | 10 : 46 : 12.42 | +03 : 36 : 23.4 | 18.10 | 19.47 | 2.087 | |
| 1996.2.2.103 | 10 : 44 : 37.17 | +02 : 42 : 11.8 | 17.72 | 18.85 | 2.105 | |
| 1996.2.2.112 | 10 : 45 : 09.74 | +03 : 57 : 05.0 | 18.44 | 19.20 | 1.819 | |

(continued)

| CUQS No. | $\alpha$ ($^{\mathrm{h}}$:$^{\mathrm{m}}$:$^{\mathrm{s}}$) | $\delta$ ($^{\circ}$:$'$:$''$) | $u_{\mathrm{J}}$ | $b_{\mathrm{J}}$ | $z$ | $\Delta z$ |
|---|---|---|---|---|---|---|
| 1996.2.2.120 | 10 : 44 : 37.87 | +03 : 40 : 01.1 | 18.98 | 19.87 | 0.614 | |
| 1996.2.2.128 | 10 : 45 : 54.21 | +03 : 11 : 24.9 | 18.88 | 19.85 | 1.549 | |
| 1996.2.3.007 | 10 : 46 : 11.49 | +04 : 38 : 29.3 | 18.43 | 19.64 | 1.666 | |
| 1996.2.3.022 | 10 : 48 : 02.28 | +05 : 03 : 03.5 | 18.57 | 19.64 | 2.016 | |
| 1996.2.3.023 | 10 : 47 : 47.12 | +04 : 56 : 38.3 | 18.40 | 19.65 | 2.119 | |
| 1996.2.3.033 | 10 : 46 : 00.78 | +04 : 25 : 27.4 | 18.33 | 19.83 | 0.908 | |
| 1996.2.3.034 | 10 : 46 : 00.33 | +04 : 28 : 14.7 | 18.86 | 19.69 | 0.950 | 0.01 |
| 1996.2.3.036 | 10 : 45 : 51.02 | +04 : 30 : 38.4 | 18.58 | 19.79 | 0.914 | |
| 1996.2.3.038 | 10 : 45 : 45.93 | +04 : 37 : 55.1 | 19.44 | 19.91 | 2.640 | 0.01 |
| 1996.2.3.053 | 10 : 47 : 39.58 | +04 : 47 : 43.4 | 18.46 | 19.94 | 1.730 | |
| 1996.2.3.066 | 10 : 48 : 53.72 | +04 : 04 : 29.0 | 18.67 | 19.87 | 0.850 | |
| 1996.2.3.087 | 10 : 50 : 42.81 | +04 : 17 : 40.4 | 18.44 | 19.64 | 0.228 | |
| 1996.2.3.094 | 10 : 50 : 10.11 | +04 : 32 : 48.3 | 17.62 | 18.86 | 1.216 | |
| 1996.2.3.098 | 10 : 47 : 44.97 | +03 : 44 : 03.1 | 17.96 | 18.66 | 0.684 | |
| 1996.2.3.122 | 10 : 48 : 02.22 | +04 : 10 : 42.0 | 18.47 | 19.48 | 0.871 | |
| 1996.2.3.127 | 10 : 49 : 14.38 | +04 : 14 : 27.6 | 18.53 | 19.49 | 1.604 | |
| 1996.3.1.003 | 10 : 36 : 26.63 | +06 : 22 : 57.9 | 19.43 | 19.94 | 0.811 | |
| 1996.3.1.005 | 10 : 35 : 06.02 | +06 : 01 : 41.4 | 18.12 | 19.04 | 0.245 | |
| 1996.3.1.008 | 10 : 35 : 58.56 | +06 : 21 : 53.2 | 18.83 | 19.90 | 1.948 | |
| 1996.3.1.021 | 10 : 34 : 46.72 | +06 : 33 : 33.1 | 17.64 | 18.68 | 1.126 | |
| 1996.3.1.022 | 10 : 34 : 42.38 | +06 : 47 : 19.6 | 18.28 | 19.48 | 0.551 | |
| 1996.3.1.023 | 10 : 34 : 35.01 | +06 : 36 : 29.3 | 18.72 | 19.67 | 1.480 | |
| 1996.3.1.029 | 10 : 33 : 56.74 | +05 : 48 : 29.7 | 18.41 | 19.36 | 0.379 | |
| 1996.3.1.030 | 10 : 36 : 01.61 | +05 : 33 : 56.8 | 18.25 | 18.77 | 2.177 | |
| 1996.3.1.032 | 10 : 35 : 51.92 | +05 : 57 : 10.1 | 18.60 | 19.99 | 1.848 | |
| 1996.3.1.036 | 10 : 34 : 33.47 | +06 : 19 : 33.9 | 18.03 | 19.70 | 1.190 | |
| 1996.3.1.041 | 10 : 34 : 44.69 | +06 : 06 : 57.7 | 18.59 | 19.91 | 0.920 | |
| 1996.3.1.053 | 10 : 34 : 31.64 | +06 : 34 : 01.6 | 18.40 | 19.39 | 1.141 | |
| 1996.3.1.055 | 10 : 33 : 22.97 | +06 : 32 : 29.1 | 18.76 | 19.43 | 2.405 | |
| 1996.3.1.057 | 10 : 35 : 40.04 | +05 : 29 : 44.0 | 19.04 | 19.92 | 2.154 | |
| 1996.3.1.059 | 10 : 34 : 58.27 | +05 : 52 : 31.5 | 18.11 | 19.55 | 0.297 | |
| 1996.3.1.071 | 10 : 38 : 32.24 | +05 : 48 : 24.0 | 18.59 | 19.60 | 2.253 | |
| 1996.3.1.073 | 10 : 36 : 18.04 | +06 : 43 : 03.6 | 17.93 | 18.89 | 0.804 | |
| 1996.3.1.076 | 10 : 36 : 51.61 | +06 : 56 : 49.9 | 18.55 | 19.44 | 0.402 | |
| 1996.3.1.084 | 10 : 38 : 31.12 | +06 : 09 : 11.9 | 17.03 | 18.08 | 0.290 | |
| 1996.3.1.094 | 10 : 38 : 35.78 | +06 : 18 : 22.3 | 18.34 | 19.56 | 1.726 | |
| 1996.3.1.104 | 10 : 37 : 27.13 | +05 : 50 : 59.5 | 18.35 | 19.46 | 1.103 | |
| 1996.3.1.107 | 10 : 35 : 44.52 | +06 : 46 : 33.5 | 18.47 | 19.65 | 1.694 | |
| 1996.3.1.109 | 10 : 35 : 34.91 | +06 : 39 : 10.9 | 17.67 | 18.81 | 1.828 | |
| 1996.3.1.111 | 10 : 36 : 05.22 | +07 : 00 : 08.6 | 19.00 | 19.68 | 1.490 | |
| 1996.3.1.112 | 10 : 36 : 08.92 | +06 : 54 : 44.3 | 18.01 | 18.55 | 2.432 | |
| 1996.3.1.117 | 10 : 36 : 44.12 | +06 : 20 : 24.4 | 17.87 | 18.91 | 0.811 | |
| 1996.3.1.118 | 10 : 37 : 18.04 | +06 : 19 : 20.0 | 18.82 | 19.89 | 1.995 | |

(continued)

| CUQS<br>No. | $\alpha$<br>($^h$:$^m$:$^s$) | $\delta$<br>($^\circ$:$'$:$''$) | $u_J$ | $b_J$ | $z$ | $\Delta z$ |
|---|---|---|---|---|---|---|
| 1996.3.1.121 | 10 : 36 : 27.45 | +06 : 01 : 51.9 | 19.09 | 19.95 | 0.624 | |
| 1996.3.1.124 | 10 : 36 : 55.07 | +06 : 02 : 16.5 | 19.05 | 19.81 | 2.281 | |
| 1996.3.2.003 | 10 : 36 : 57.08 | +05 : 15 : 04.0 | 18.76 | 19.90 | 1.637 | |
| 1996.3.2.007 | 10 : 36 : 41.88 | +05 : 09 : 40.4 | 18.58 | 19.66 | 1.064 | |
| 1996.3.2.039 | 10 : 34 : 47.85 | +05 : 16 : 16.3 | 17.86 | 18.96 | 0.331 | |
| 1996.3.2.043 | 10 : 36 : 26.24 | +04 : 54 : 36.2 | 17.71 | 18.63 | 1.046 | |
| 1996.3.2.047 | 10 : 35 : 07.11 | +04 : 49 : 30.5 | 18.94 | 19.87 | 0.627 | |
| 1996.3.2.048 | 10 : 35 : 05.08 | +04 : 54 : 21.9 | 18.69 | 19.99 | 1.711 | |
| 1996.3.2.081 | 10 : 39 : 08.61 | +04 : 59 : 49.6 | 18.47 | 19.92 | 1.938 | |
| 1996.3.2.098 | 10 : 37 : 29.52 | +04 : 37 : 16.4 | 18.64 | 19.87 | 1.839 | |
| 1996.3.2.112 | 10 : 39 : 37.18 | +05 : 31 : 46.0 | 18.11 | 19.54 | 2.030 | |
| 1996.3.2.117 | 10 : 37 : 44.83 | +05 : 18 : 33.5 | 18.61 | 19.94 | 1.224 | |
| 1996.3.2.124 | 10 : 38 : 28.14 | +04 : 45 : 35.1 | 18.03 | 18.94 | 0.286 | |
| 1996.3.2.127 | 10 : 38 : 57.86 | +04 : 48 : 38.6 | 18.31 | 19.03 | 0.357 | |
| 1996.3.3.002 | 10 : 41 : 17.13 | +06 : 10 : 17.5 | 15.42 | 17.04 | 1.270 | |
| 1996.3.3.027 | 10 : 41 : 46.85 | +05 : 25 : 01.6 | 18.99 | 19.91 | 1.591 | |
| 1996.3.3.050 | 10 : 40 : 07.54 | +06 : 25 : 09.3 | 18.06 | 18.55 | 2.377 | |
| 1996.3.3.067 | 10 : 43 : 07.75 | +05 : 47 : 24.3 | 19.05 | 19.59 | 2.454 | |
| 1996.3.3.079 | 10 : 42 : 13.50 | +06 : 28 : 53.9 | 18.28 | 19.79 | 2.026 | |
| 1996.3.3.083 | 10 : 43 : 36.59 | +05 : 58 : 48.5 | 18.69 | 19.91 | 1.236 | |
| 1996.3.3.095 | 10 : 43 : 40.25 | +06 : 17 : 51.3 | 18.59 | 19.60 | 1.486 | |
| 1996.3.3.102 | 10 : 42 : 43.84 | +05 : 28 : 05.1 | 19.06 | 19.94 | 2.040 | |
| 1996.3.3.111 | 10 : 41 : 49.91 | +06 : 43 : 37.1 | 18.61 | 19.98 | 1.325 | |
| 1996.3.3.116 | 10 : 41 : 55.71 | +06 : 12 : 56.6 | 18.21 | 19.29 | 1.480 | |
| 1996.3.3.119 | 10 : 42 : 13.58 | +06 : 19 : 42.7 | 18.69 | 19.50 | 1.559 | |
| 1996.3.3.123 | 10 : 42 : 32.17 | +05 : 55 : 57.8 | 18.50 | 19.58 | 1.010 | 0.01 |
| 1996.3.3.127 | 10 : 42 : 41.93 | +05 : 58 : 48.4 | 19.07 | 19.95 | 1.920 | 0.03 |
| 1997.1.1.007 | 10 : 46 : 24.07 | +09 : 09 : 48.3 | 17.13 | 18.10 | 2.622 | |
| 1997.1.1.017 | 10 : 47 : 36.65 | +09 : 46 : 36.5 | 19.09 | 19.59 | 0.690 | |
| 1997.1.1.031 | 10 : 47 : 23.00 | +08 : 39 : 00.6 | 19.14 | 19.54 | 0.556 | |
| 1997.1.1.033 | 10 : 45 : 55.66 | +08 : 59 : 34.1 | 18.84 | 19.48 | 1.467 | |
| 1997.1.1.056 | 10 : 44 : 59.05 | +09 : 20 : 08.3 | 18.04 | 18.74 | 0.412 | |
| 1997.1.1.063 | 10 : 46 : 01.54 | +08 : 32 : 34.6 | 18.12 | 19.15 | 1.268 | |
| 1997.1.1.065 | 10 : 48 : 44.82 | +08 : 32 : 55.2 | 18.57 | 19.48 | 1.661 | |
| 1997.1.1.080 | 10 : 50 : 26.09 | +09 : 25 : 52.4 | 17.69 | 18.39 | 0.794 | |
| 1997.1.1.091 | 10 : 49 : 40.99 | +08 : 55 : 48.0 | 17.60 | 18.60 | 1.170 | |
| 1997.1.1.106 | 10 : 47 : 49.28 | +09 : 20 : 48.1 | 18.66 | 19.44 | 1.830 | |
| 1997.1.1.124 | 10 : 48 : 15.75 | +08 : 40 : 34.8 | 18.52 | 19.32 | 1.119 | |
| 1997.1.2.007 | 10 : 39 : 03.05 | +07 : 15 : 22.0 | 19.02 | 19.63 | 1.939 | |
| 1997.1.2.011 | 10 : 39 : 30.84 | +07 : 06 : 40.7 | 18.82 | 19.98 | 1.866 | |
| 1997.1.2.023 | 10 : 38 : 31.19 | +07 : 33 : 46.4 | 18.03 | 18.92 | 1.105 | 0.008 |
| 1997.1.2.026 | 10 : 39 : 52.18 | +06 : 33 : 22.6 | 18.42 | 19.13 | 1.388 | |
| 1997.1.2.035 | 10 : 38 : 08.09 | +07 : 17 : 06.8 | 19.12 | 19.75 | 2.150 | 0.007 |

(continued)

| CUQS<br>No. | $\alpha$<br>$(^{h}.^{m}.^{s})$ | $\delta$<br>$(^{\circ}.':'')$ | $u_J$ | $b_J$ | $z$ | $\Delta z$ |
|---|---|---|---|---|---|---|
| 1997.1.2.043 | 10 : 37 : 54.61 | +06 : 58 : 33.6 | 17.97 | 18.99 | 0.613 | |
| 1997.1.2.051 | 10 : 38 : 04.83 | +07 : 45 : 52.7 | 18.38 | 18.87 | 1.606 | |
| 1997.1.2.055 | 10 : 37 : 36.99 | +07 : 35 : 17.5 | 18.14 | 19.32 | 2.036 | |
| 1997.1.2.074 | 10 : 40 : 18.73 | +07 : 55 : 53.6 | 17.60 | 18.85 | 1.799 | |
| 1997.1.2.075 | 10 : 40 : 23.33 | +07 : 47 : 50.8 | 18.24 | 19.03 | 1.268 | |
| 1997.1.2.076 | 10 : 40 : 48.10 | +07 : 39 : 57.9 | 17.55 | 18.43 | 0.976 | |
| 1997.1.2.096 | 10 : 42 : 35.08 | +07 : 11 : 53.7 | 18.03 | 19.23 | 0.756 | |
| 1997.1.2.120 | 10 : 41 : 40.43 | +07 : 20 : 08.3 | 18.67 | 19.66 | 1.969 | |
| 1997.1.2.123 | 10 : 40 : 29.91 | +07 : 05 : 28.2 | 18.51 | 19.45 | 1.524 | |
| 1997.1.2.124 | 10 : 40 : 31.60 | +06 : 55 : 49.6 | 19.08 | 19.62 | 0.704 | |
| 1997.1.3.005 | 10 : 42 : 40.35 | +07 : 54 : 08.1 | 18.71 | 19.41 | 1.084 | |
| 1997.1.3.011 | 10 : 43 : 21.76 | +08 : 07 : 14.0 | 18.10 | 18.93 | 1.456 | |
| 1997.1.3.014 | 10 : 43 : 04.67 | +08 : 02 : 03.8 | 18.40 | 19.01 | 0.702 | |
| 1997.1.3.026 | 10 : 43 : 31.37 | +07 : 48 : 48.9 | 17.97 | 19.22 | 1.936 | |
| 1997.1.3.029 | 10 : 41 : 44.23 | +07 : 45 : 01.8 | 18.04 | 19.22 | 1.254 | |
| 1997.1.3.030 | 10 : 43 : 09.68 | +07 : 53 : 17.4 | 18.71 | 19.27 | 1.163 | |
| 1997.1.3.034 | 10 : 41 : 06.72 | +08 : 17 : 53.0 | 18.81 | 19.52 | 1.110 | |
| 1997.1.3.035 | 10 : 41 : 05.95 | +08 : 22 : 35.1 | 18.26 | 18.94 | 1.549 | |
| 1997.1.3.059 | 10 : 42 : 18.58 | +07 : 50 : 18.0 | 18.90 | 19.55 | 2.146 | |
| 1997.1.3.066 | 10 : 44 : 54.06 | +07 : 50 : 22.3 | 17.87 | 18.79 | 1.925 | |
| 1997.1.3.070 | 10 : 45 : 32.96 | +07 : 45 : 59.6 | 17.45 | 18.67 | 1.036 | |
| 1997.1.3.075 | 10 : 44 : 57.89 | +08 : 32 : 14.2 | 17.48 | 18.13 | 0.790 | |
| 1997.1.3.084 | 10 : 45 : 49.72 | +07 : 55 : 39.6 | 19.03 | 19.41 | 0.599 | |
| 1997.1.3.091 | 10 : 45 : 41.20 | +08 : 10 : 26.4 | 17.79 | 18.89 | 1.986 | |
| 1997.1.3.099 | 10 : 44 : 06.75 | +07 : 49 : 31.7 | 18.07 | 18.73 | 1.250 | |
| 1997.1.3.101 | 10 : 44 : 48.79 | +07 : 39 : 28.4 | 18.63 | 19.40 | 0.228 | |
| 1997.1.3.118 | 10 : 45 : 00.29 | +08 : 12 : 03.8 | 18.60 | 19.41 | 1.590 | |
| 1997.1.3.119 | 10 : 45 : 03.07 | +08 : 15 : 01.0 | 18.62 | 19.55 | 0.426 | |
| 1997.2.2.014 | 10 : 48 : 23.11 | +07 : 47 : 47.7 | 17.53 | 18.28 | 0.627 | |
| 1997.2.2.050 | 10 : 48 : 15.78 | +08 : 15 : 10.0 | 18.59 | 19.23 | 2.444 | 0.009 |
| 1997.2.2.051 | 10 : 47 : 51.05 | +08 : 18 : 34.5 | 19.19 | 19.55 | 0.640 | |
| 1997.2.2.053 | 10 : 48 : 36.54 | +08 : 11 : 35.1 | 17.99 | 18.81 | 2.148 | |
| 1997.2.2.067 | 10 : 49 : 47.82 | +07 : 16 : 31.8 | 18.47 | 19.23 | 1.653 | |
| 1997.2.2.078 | 10 : 51 : 10.83 | +08 : 16 : 26.8 | 18.44 | 19.88 | 1.422 | |
| 1997.2.2.108 | 10 : 50 : 53.47 | +08 : 11 : 43.3 | 17.61 | 18.64 | 0.856 | |
| 1997.2.2.109 | 10 : 50 : 18.56 | +08 : 34 : 49.4 | 17.95 | 19.05 | 1.070 | |
| 1997.2.2.115 | 10 : 49 : 35.96 | +07 : 58 : 13.6 | 17.17 | 18.18 | 1.963 | |
| 1997.2.2.120 | 10 : 50 : 08.09 | +07 : 59 : 43.2 | 18.50 | 19.35 | 1.537 | |
| 1997.2.3.006 | 10 : 50 : 22.79 | +06 : 46 : 21.6 | 17.52 | 18.45 | 1.291 | |
| 1997.2.3.012 | 10 : 50 : 59.68 | +06 : 26 : 06.1 | 18.78 | 19.95 | 0.515 | |
| 1997.2.3.058 | 10 : 48 : 40.34 | +05 : 59 : 12.4 | 18.72 | 19.85 | 1.487 | |
| 1997.2.3.063 | 10 : 47 : 52.68 | +06 : 18 : 28.6 | 18.17 | 19.38 | 0.562 | |
| 1997.3.1.010 | 10 : 52 : 45.92 | +07 : 27 : 33.4 | 18.14 | 19.30 | 2.131 | |

| CUQS No. | $\alpha$ ($^{\mathrm{h}}$:$^{\mathrm{m}}$:$^{\mathrm{s}}$) | $\delta$ ($^{\circ}$:$'$:$''$) | $u_{\mathrm{J}}$ | $b_{\mathrm{J}}$ | $z$ | $\Delta z$ |
|---|---|---|---|---|---|---|
| 1997.3.1.020 | 10 : 52 : 45.02 | +08 : 08 : 10.5 | 17.78 | 18.25 | 0.311 | |
| 1997.3.1.022 | 10 : 52 : 31.81 | +08 : 06 : 08.5 | 18.23 | 19.31 | 1.634 | |
| 1997.3.1.023 | 10 : 52 : 21.31 | +08 : 17 : 07.8 | 19.40 | 19.93 | 0.622 | |
| 1997.3.1.032 | 10 : 51 : 53.05 | +07 : 21 : 22.2 | 17.26 | 18.46 | 1.972 | |
| 1997.3.1.047 | 10 : 50 : 49.16 | +07 : 23 : 08.7 | 18.62 | 19.64 | 1.752 | |
| 1997.3.1.049 | 10 : 52 : 03.58 | +08 : 04 : 22.6 | 18.38 | 19.49 | 0.350 | |
| 1997.3.1.115 | 10 : 52 : 17.70 | +07 : 39 : 23.3 | 18.95 | 19.76 | 1.095 | |
| 1997.3.1.116 | 10 : 52 : 17.90 | +07 : 45 : 33.3 | 18.47 | 18.97 | 2.276 | |
| 1997.3.2.002 | 10 : 51 : 01.51 | +05 : 24 : 45.7 | 16.57 | 19.22 | 0.461 | |
| 1997.3.2.014 | 10 : 50 : 01.32 | +04 : 59 : 41.5 | 19.54 | 19.93 | 0.451 | |
| 1997.3.2.021 | 10 : 50 : 18.11 | +05 : 28 : 26.1 | 18.70 | 19.80 | 1.295 | |
| 1997.3.2.022 | 10 : 49 : 29.10 | +05 : 44 : 52.9 | 18.57 | 19.16 | 1.780 | |
| 1997.3.2.026 | 10 : 51 : 32.31 | +04 : 29 : 40.4 | 18.81 | 19.64 | 1.769 | |
| 1997.3.2.041 | 10 : 49 : 32.23 | +05 : 05 : 31.4 | 18.55 | 19.72 | 1.094 | |
| 1997.3.2.073 | 10 : 51 : 33.34 | +05 : 31 : 16.4 | 17.79 | 18.57 | 0.880 | |
| 1997.3.2.081 | 10 : 52 : 05.00 | +05 : 05 : 11.5 | 18.14 | 19.01 | 0.424 | |
| 1997.3.2.088 | 10 : 52 : 42.77 | +05 : 00 : 05.1 | 18.65 | 19.98 | 1.701 | |
| 1997.3.2.093 | 10 : 52 : 43.95 | +05 : 26 : 22.9 | 17.23 | 18.03 | 1.510 | |
| 1997.3.2.108 | 10 : 51 : 18.56 | +05 : 33 : 32.0 | 18.55 | 19.81 | 1.477 | |
| 1997.3.2.126 | 10 : 51 : 41.84 | +04 : 58 : 31.8 | 18.96 | 19.94 | 1.598 | |
| 1997.3.3.003 | 10 : 53 : 41.66 | +06 : 18 : 51.6 | 19.34 | 19.90 | 1.605 | |
| 1997.3.3.008 | 10 : 52 : 55.91 | +06 : 22 : 22.9 | 18.32 | 19.69 | 1.767 | |
| 1997.3.3.012 | 10 : 52 : 51.69 | +05 : 57 : 33.8 | 18.10 | 18.65 | 1.590 | |
| 1997.3.3.020 | 10 : 55 : 43.28 | +06 : 26 : 10.9 | 17.93 | 18.36 | 1.123 | |
| 1997.3.3.021 | 10 : 55 : 49.46 | +06 : 55 : 41.9 | 18.60 | 19.54 | 0.295 | |
| 1997.3.3.027 | 10 : 54 : 20.60 | +05 : 38 : 46.4 | 18.32 | 19.36 | 1.545 | |
| 1997.3.3.030 | 10 : 53 : 54.72 | +05 : 34 : 18.5 | 18.82 | 19.79 | 1.930 | |
| 1997.3.3.049 | 10 : 54 : 37.05 | +06 : 32 : 17.5 | 18.71 | 19.43 | 1.700 | |
| 1997.3.3.050 | 10 : 54 : 32.30 | +06 : 36 : 54.0 | 18.58 | 19.03 | 1.856 | |
| 1997.3.3.058 | 10 : 53 : 24.64 | +05 : 47 : 56.1 | 18.49 | 19.71 | 1.829 | |
| 1997.3.3.074 | 10 : 57 : 19.82 | +06 : 43 : 39.2 | 18.06 | 19.03 | 1.780 | |
| 1997.3.3.075 | 10 : 57 : 27.85 | +06 : 38 : 48.9 | 17.69 | 18.60 | 2.000 | |
| 1997.3.3.078 | 10 : 57 : 42.37 | +06 : 39 : 43.0 | 18.27 | 19.15 | 1.495 | |
| 1997.3.3.090 | 10 : 56 : 40.24 | +06 : 14 : 43.8 | 19.33 | 19.89 | 2.022 | |
| 1997.3.3.091 | 10 : 56 : 56.85 | +06 : 25 : 20.2 | 18.84 | 19.30 | 0.591 | |
| 1997.3.3.098 | 10 : 55 : 11.69 | +05 : 56 : 49.6 | 19.31 | 19.99 | 2.211 | |
| 1997.3.3.104 | 10 : 56 : 10.78 | +05 : 42 : 23.4 | 18.68 | 19.76 | 1.490 | |
| 1997.3.3.115 | 10 : 55 : 12.23 | +06 : 12 : 44.0 | 18.34 | 18.92 | 1.294 | |
| 1997.3.3.122 | 10 : 54 : 34.21 | +06 : 07 : 56.8 | 18.69 | 19.01 | 0.556 | |
| 1997.3.3.126 | 10 : 55 : 41.54 | +06 : 04 : 35.7 | 19.02 | 19.74 | 2.295 | |
| 1997.4.1.011 | 10 : 52 : 23.04 | +03 : 38 : 20.4 | 17.97 | 18.99 | 2.093 | |
| 1997.4.1.017 | 10 : 52 : 01.24 | +04 : 16 : 40.1 | 18.32 | 19.31 | 2.204 | 0.03 |
| 1997.4.1.055 | 10 : 49 : 56.68 | +04 : 11 : 00.0 | 18.45 | 19.26 | 0.491 | |

(continued)

| CUQS No. | $\alpha$ ($^{h}:^{m}:^{s}$) | $\delta$ ($^{\circ}:':''$) | $u_J$ | $b_J$ | $z$ | $\Delta z$ |
|---|---|---|---|---|---|---|
| 1997.4.1.076 | 10 : 54 : 08.84 | +04 : 26 : 50.2 | 16.89 | 18.03 | 1.079 | |
| 1997.4.1.078 | 10 : 54 : 12.19 | +04 : 15 : 53.6 | 18.99 | 19.60 | 2.462 | |
| 1997.4.1.083 | 10 : 54 : 00.37 | +03 : 48 : 01.1 | 17.94 | 18.55 | 2.083 | |
| 1997.4.1.120 | 10 : 52 : 49.63 | +04 : 00 : 46.2 | 18.74 | 19.60 | 1.173 | |
| 1997.4.1.123 | 10 : 53 : 01.16 | +03 : 36 : 34.0 | 18.40 | 19.13 | 1.815 | |
| 1997.4.2.009 | 10 : 56 : 15.24 | +04 : 54 : 51.7 | 19.26 | 19.99 | 0.833 | |
| 1997.4.2.034 | 10 : 53 : 52.69 | +05 : 00 : 43.7 | 18.24 | 19.28 | 1.126 | |
| 1997.4.2.035 | 10 : 53 : 44.79 | +05 : 01 : 13.3 | 17.91 | 18.61 | 1.861 | |
| 1997.4.2.040 | 10 : 53 : 10.57 | +04 : 56 : 24.5 | 18.85 | 19.98 | 2.528 | |
| 1997.4.2.050 | 10 : 54 : 23.24 | +05 : 19 : 09.6 | 18.03 | 19.31 | 0.549 | |
| 1997.4.2.070 | 10 : 57 : 41.20 | +04 : 34 : 28.2 | 18.64 | 19.79 | 2.155 | |
| 1997.4.2.074 | 10 : 56 : 39.17 | +05 : 20 : 58.5 | 19.02 | 19.90 | 1.377 | |
| 1997.4.2.078 | 10 : 56 : 54.14 | +05 : 17 : 13.0 | 17.32 | 18.38 | 0.455 | |
| 1997.4.2.080 | 10 : 57 : 03.31 | +05 : 11 : 41.4 | 19.31 | 19.89 | 2.264 | |
| 1997.4.2.081 | 10 : 57 : 19.22 | +04 : 55 : 47.9 | 18.06 | 19.32 | 1.330 | |
| 1997.4.2.120 | 10 : 57 : 16.15 | +04 : 59 : 08.1 | 17.81 | 18.77 | 0.503 | |

**Table A.2:** The 53 quasars detected in the CUQS control area observations from the 1996 and 1997. The columns are as for table A.1.

| CUQS No. | $\alpha$ ($^h:^m:^s$) | $\delta$ ($^\circ:':''$) | $u_J$ | $b_J$ | $z$ | $\Delta z$ |
|---|---|---|---|---|---|---|
| 1996.1.4.014 | 11 : 08 : 16.14 | −29 : 42 : 19.8 | 18.34 | 19.67 | 0.864 | |
| 1996.1.4.029 | 11 : 06 : 50.34 | −29 : 48 : 52.2 | 19.35 | 20.16 | 0.456 | |
| 1996.1.4.034 | 11 : 07 : 05.10 | −29 : 18 : 13.2 | 19.20 | 19.87 | 0.459 | |
| 1996.1.4.056 | 11 : 06 : 33.46 | −29 : 11 : 36.6 | 18.16 | 19.42 | 1.964 | |
| 1996.1.4.083 | 11 : 11 : 07.78 | −29 : 29 : 07.9 | 19.23 | 20.09 | 1.430 | |
| 1996.1.4.088 | 11 : 11 : 45.08 | −29 : 40 : 08.8 | 17.11 | 18.36 | 0.693 | |
| 1996.1.4.089 | 11 : 10 : 36.99 | −29 : 23 : 20.3 | 18.26 | 19.49 | 1.986 | |
| 1996.1.4.108 | 11 : 09 : 36.85 | −29 : 09 : 00.4 | 17.66 | 18.15 | 0.553 | |
| 1996.1.4.111 | 11 : 09 : 43.65 | −28 : 55 : 55.8 | 18.59 | 19.35 | 0.556 | |
| 1996.1.4.124 | 11 : 09 : 42.68 | −29 : 40 : 07.4 | 19.57 | 20.34 | 1.125 | |
| 1996.1.4.126 | 11 : 10 : 14.72 | −29 : 43 : 09.9 | 18.64 | 19.90 | 1.888 | |
| 1996.2.4.001 | 11 : 06 : 33.66 | −30 : 21 : 59.3 | 18.83 | 19.89 | 1.962 | |
| 1996.2.4.004 | 11 : 06 : 21.17 | −30 : 30 : 41.5 | 18.59 | 19.98 | 0.551 | |
| 1996.2.4.010 | 11 : 06 : 07.30 | −30 : 57 : 23.4 | 18.13 | 18.97 | 2.383 | |
| 1996.2.4.014 | 11 : 05 : 10.71 | −30 : 48 : 44.1 | 18.33 | 19.64 | 1.424 | |
| 1996.2.4.052 | 11 : 04 : 52.16 | −30 : 03 : 52.1 | 17.83 | 19.37 | 1.140 | |
| 1996.2.4.058 | 11 : 05 : 13.01 | −31 : 18 : 48.6 | 19.27 | 20.01 | 1.838 | |
| 1996.2.4.066 | 11 : 07 : 48.34 | −31 : 03 : 46.9 | 17.36 | 18.86 | 2.080 | |
| 1996.2.4.071 | 11 : 08 : 29.18 | −31 : 00 : 39.8 | 19.32 | 20.14 | 1.776 | |
| 1996.2.4.074 | 11 : 07 : 31.96 | −30 : 10 : 29.8 | 18.52 | 19.89 | 1.362 | |
| 1996.2.4.080 | 11 : 08 : 46.63 | −30 : 19 : 04.9 | 19.52 | 20.03 | 0.510 | |
| 1996.2.4.081 | 11 : 07 : 55.07 | −30 : 52 : 32.7 | 18.04 | 18.88 | 1.542 | |
| 1996.2.4.082 | 11 : 07 : 56.25 | −30 : 49 : 22.8 | 18.72 | 19.87 | 1.350 | |
| 1996.2.4.086 | 11 : 08 : 30.05 | −30 : 51 : 26.5 | 18.83 | 19.89 | 0.540 | |
| 1996.3.4.034 | 11 : 10 : 21.86 | −30 : 27 : 58.0 | 17.38 | 18.00 | 0.534 | |
| 1996.3.4.051 | 11 : 11 : 49.98 | −30 : 04 : 52.7 | 18.19 | 19.23 | 2.090 | |
| 1996.3.4.052 | 11 : 11 : 45.40 | −30 : 02 : 05.1 | 17.75 | 18.98 | 1.756 | |
| 1996.3.4.059 | 11 : 10 : 14.78 | −30 : 57 : 22.9 | 18.89 | 20.01 | 2.087 | |
| 1996.3.4.072 | 11 : 14 : 16.52 | −30 : 55 : 31.5 | 17.71 | 18.80 | 1.524 | |
| 1996.3.4.097 | 11 : 11 : 52.20 | −31 : 10 : 44.3 | 18.57 | 19.67 | 1.928 | |
| 1996.3.4.100 | 11 : 12 : 08.50 | −31 : 12 : 50.4 | 19.47 | 20.06 | 1.589 | |
| 1996.3.4.103 | 11 : 12 : 40.01 | −31 : 08 : 24.9 | 18.68 | 20.06 | 1.883 | |
| 1996.3.4.116 | 11 : 13 : 17.36 | −30 : 21 : 28.3 | 16.42 | 17.53 | 1.234 | |
| 1997.2.4.041 | 11 : 12 : 31.98 | −29 : 53 : 00.3 | 17.68 | 19.18 | 1.243 | |
| 1997.2.4.043 | 11 : 12 : 25.41 | −29 : 44 : 27.6 | 18.97 | 19.56 | 1.200 | |
| 1997.2.4.050 | 11 : 12 : 49.41 | −29 : 09 : 11.6 | 18.97 | 19.98 | 1.703 | |
| 1997.2.4.051 | 11 : 12 : 42.85 | −29 : 05 : 29.3 | 18.25 | 19.37 | 0.611 | |
| 1997.2.4.053 | 11 : 13 : 22.10 | −29 : 10 : 35.4 | 18.15 | 18.65 | 0.904 | |
| 1997.2.4.086 | 11 : 16 : 26.50 | −29 : 49 : 36.0 | 18.49 | 19.30 | 0.814 | |
| 1997.2.4.090 | 11 : 15 : 50.18 | −29 : 27 : 01.6 | 18.54 | 19.73 | 1.870 | |
| 1997.2.4.097 | 11 : 13 : 43.34 | −30 : 13 : 03.8 | 19.43 | 19.82 | 0.654 | |
| 1997.2.4.108 | 11 : 14 : 32.14 | −29 : 06 : 42.0 | 18.48 | 18.86 | 0.822 | |

(continued)

169

| CUQS No. | $\alpha$ ($^{\rm h}$:$^{\rm m}$:$^{\rm s}$) | $\delta$ ($^{\circ}$:$'$:$''$) | $u_{\rm J}$ | $b_{\rm J}$ | $z$ | $\Delta z$ |
|---|---|---|---|---|---|---|
| 1997.2.4.127 | 11 : 14 : 49.31 | $-29 : 50 : 00.5$ | 19.49 | 19.88 | 2.310 | 0.01 |
| 1997.3.4.033 | 11 : 12 : 40.23 | $-31 : 35 : 41.7$ | 17.70 | 18.65 | 0.313 | |
| 1997.3.4.047 | 11 : 12 : 27.61 | $-31 : 50 : 49.8$ | 18.63 | 19.50 | 0.821 | |
| 1997.3.4.080 | 11 : 15 : 31.21 | $-31 : 22 : 00.9$ | 18.21 | 19.07 | 0.701 | |
| 1997.3.4.094 | 11 : 16 : 14.89 | $-31 : 35 : 31.2$ | 18.77 | 19.55 | 2.398 | |
| 1997.3.4.115 | 11 : 14 : 21.38 | $-31 : 34 : 26.0$ | 18.48 | 19.09 | 2.331 | |
| 1997.3.4.117 | 11 : 14 : 07.74 | $-31 : 31 : 21.4$ | 17.15 | 18.55 | 1.961 | |
| 1997.4.4.053 | 11 : 15 : 58.77 | $-30 : 17 : 24.3$ | 18.24 | 19.00 | 1.599 | |
| 1997.4.4.094 | 11 : 19 : 31.87 | $-30 : 30 : 13.8$ | 18.62 | 19.59 | 1.704 | |
| 1997.4.4.098 | 11 : 16 : 36.90 | $-31 : 28 : 48.1$ | 17.80 | 18.97 | 2.049 | |
| 1997.4.4.110 | 11 : 18 : 25.10 | $-30 : 04 : 42.0$ | 17.09 | 18.18 | 1.690 | |

**Table A.3:** The 85 narrow emission-line galaxies and 2 low-redshift Seyfert 1 galaxies (identified in the last column) detected in the CUQS programme area observations from 1996 and 1997. The other columns are as for table A.1. The magnitude uncertainties are $\Delta b_J = 0.10$ mag and $\Delta u_J = 0.12$ mag. The redshift uncertainties are all $\Delta z \leq 0.005$ and are typically $\Delta z = 0.002$.

| CUQS No. | $\alpha$ ($^h . ^m . ^s$) | $\delta$ ($^\circ . ' . ''$) | $u_J$ | $b_J$ | $z$ | Notes |
|---|---|---|---|---|---|---|
| 1996.1.1.038 | 10 : 41 : 16.69 | +05 : 00 : 10.8 | 19.04 | 19.90 | 0.134 | |
| 1996.1.1.064 | 10 : 41 : 35.74 | +04 : 20 : 09.5 | 19.37 | 19.76 | 0.072 | |
| 1996.1.1.112 | 10 : 43 : 26.80 | +05 : 25 : 19.7 | 18.89 | 19.52 | 0.125 | |
| 1996.1.2.083 | 10 : 48 : 19.14 | +05 : 30 : 42.9 | 19.52 | 19.92 | 0.150 | |
| 1996.1.2.089 | 10 : 48 : 17.66 | +05 : 50 : 14.5 | 19.34 | 19.82 | 0.180 | |
| 1996.1.2.106 | 10 : 46 : 00.37 | +06 : 16 : 32.7 | 18.64 | 19.27 | 0.185 | |
| 1996.1.3.022 | 10 : 38 : 17.97 | +04 : 22 : 57.6 | 19.08 | 19.60 | 0.125 | |
| 1996.1.3.079 | 10 : 41 : 18.75 | +04 : 05 : 55.6 | 19.51 | 19.92 | 0.154 | |
| 1996.1.3.094 | 10 : 41 : 28.93 | +03 : 52 : 50.7 | 19.27 | 19.67 | 0.058 | |
| 1996.1.3.095 | 10 : 41 : 40.13 | +03 : 53 : 54.6 | 19.15 | 19.55 | 0.100 | |
| 1996.1.3.096 | 10 : 41 : 57.34 | +03 : 55 : 24.4 | 18.89 | 19.48 | 0.204 | |
| 1996.1.3.118 | 10 : 39 : 51.18 | +04 : 05 : 01.1 | 19.19 | 19.65 | 0.127 | |
| 1996.2.1.004 | 10 : 48 : 35.59 | +03 : 03 : 21.0 | 19.37 | 19.84 | 0.149 | |
| 1996.2.1.029 | 10 : 45 : 56.76 | +02 : 37 : 51.8 | 19.30 | 19.93 | 0.106 | |
| 1996.2.1.100 | 10 : 48 : 54.71 | +02 : 27 : 57.3 | 18.81 | 19.88 | 0.141 | |
| 1996.2.2.008 | 10 : 42 : 51.16 | +03 : 24 : 09.7 | 19.11 | 19.52 | 0.255 | |
| 1996.2.2.041 | 10 : 43 : 16.98 | +03 : 17 : 28.7 | 19.34 | 19.75 | 0.063 | |
| 1996.2.2.044 | 10 : 41 : 52.10 | +03 : 09 : 34.1 | 19.20 | 19.58 | 0.172 | |
| 1996.2.2.057 | 10 : 42 : 43.60 | +02 : 42 : 32.7 | 19.09 | 19.97 | 0.183 | |
| 1996.2.2.088 | 10 : 46 : 31.37 | +03 : 08 : 28.1 | 19.28 | 19.82 | 0.147 | |
| 1996.2.2.117 | 10 : 43 : 38.17 | +03 : 36 : 41.5 | 19.33 | 19.99 | 0.119 | |
| 1996.2.2.127 | 10 : 45 : 11.95 | +03 : 05 : 14.2 | 18.80 | 19.17 | 0.198 | |
| 1996.2.3.027 | 10 : 47 : 13.45 | +03 : 52 : 37.5 | 19.29 | 19.77 | 0.151 | |
| 1996.2.3.055 | 10 : 45 : 54.14 | +04 : 48 : 54.9 | 19.40 | 19.88 | 0.069 | |
| 1996.3.1.020 | 10 : 34 : 44.24 | +06 : 36 : 32.7 | 18.22 | 19.09 | 0.232 | |
| 1996.3.1.044 | 10 : 34 : 11.89 | +06 : 10 : 44.0 | 19.40 | 19.87 | 0.099 | |
| 1996.3.1.047 | 10 : 33 : 49.06 | +06 : 08 : 20.5 | 18.77 | 19.27 | 0.105 | |
| 1996.3.1.066 | 10 : 37 : 46.46 | +05 : 41 : 18.3 | 19.48 | 19.92 | 0.169 | |
| 1996.3.2.020 | 10 : 38 : 02.84 | +05 : 34 : 56.5 | 19.50 | 19.98 | 0.072 | |
| 1996.3.2.021 | 10 : 38 : 05.52 | +05 : 28 : 47.0 | 19.19 | 19.62 | 0.072 | |
| 1996.3.2.034 | 10 : 35 : 55.11 | +05 : 15 : 07.4 | 19.23 | 19.71 | 0.181 | |
| 1996.3.2.057 | 10 : 36 : 31.54 | +04 : 33 : 33.1 | 19.35 | 19.80 | 0.059 | |
| 1996.3.2.090 | 10 : 39 : 36.71 | +05 : 15 : 38.3 | 19.15 | 19.58 | 0.104 | |
| 1996.3.2.099 | 10 : 37 : 36.04 | +04 : 28 : 42.0 | 19.46 | 19.95 | 0.131 | |
| 1996.3.3.021 | 10 : 40 : 52.79 | +06 : 42 : 06.2 | 18.79 | 19.17 | 0.032 | |
| 1996.3.3.038 | 10 : 39 : 57.70 | +06 : 15 : 33.8 | 19.21 | 19.72 | 0.163 | |
| 1996.3.3.080 | 10 : 42 : 22.21 | +06 : 38 : 49.1 | 19.53 | 19.99 | 0.113 | |
| 1996.3.3.109 | 10 : 41 : 17.14 | +06 : 51 : 06.0 | 18.66 | 19.46 | 0.068 | |
| 1997.1.1.042 | 10 : 46 : 18.74 | +08 : 49 : 54.5 | 19.07 | 19.39 | 0.114 | |

(continued)

171

| CUQS No. | $\alpha$ $(^{h}.^{m}.^{s})$ | $\delta$ $(^{\circ}:':'')$ | $u_J$ | $b_J$ | $z$ | Notes |
|---|---|---|---|---|---|---|
| 1997.1.1.047 | 10 : 45 : 05.14 | +08 : 43 : 38.6 | 16.11 | 16.89 | 0.123 | Seyfert 1 |
| 1997.1.1.082 | 10 : 48 : 51.85 | +08 : 42 : 05.4 | 18.57 | 19.36 | 0.090 | |
| 1997.1.1.103 | 10 : 48 : 38.37 | +08 : 33 : 31.0 | 19.14 | 19.60 | 0.083 | |
| 1997.1.2.012 | 10 : 39 : 24.57 | +07 : 04 : 47.6 | 19.03 | 19.42 | 0.167 | Seyfert 1 |
| 1997.1.2.080 | 10 : 41 : 24.71 | +07 : 44 : 15.8 | 19.16 | 19.48 | 0.175 | |
| 1997.1.2.082 | 10 : 41 : 25.58 | +06 : 56 : 25.4 | 18.95 | 19.25 | 0.154 | |
| 1997.1.2.106 | 10 : 39 : 14.40 | +07 : 48 : 58.7 | 19.20 | 19.50 | 0.052 | |
| 1997.1.2.116 | 10 : 40 : 27.60 | +07 : 24 : 33.1 | 18.90 | 19.49 | 0.187 | |
| 1997.1.3.002 | 10 : 43 : 19.19 | +08 : 16 : 19.7 | 18.62 | 19.11 | 0.065 | |
| 1997.1.3.025 | 10 : 43 : 39.02 | +07 : 37 : 50.9 | 18.92 | 19.60 | 0.100 | |
| 1997.1.3.048 | 10 : 40 : 36.84 | +08 : 08 : 41.4 | 19.14 | 19.45 | 0.214 | |
| 1997.1.3.115 | 10 : 44 : 50.20 | +08 : 12 : 33.5 | 18.11 | 19.08 | 0.065 | |
| 1997.2.2.026 | 10 : 48 : 11.25 | +07 : 25 : 31.7 | 19.33 | 19.88 | 0.151 | |
| 1997.2.2.029 | 10 : 46 : 42.18 | +07 : 26 : 01.5 | 19.12 | 19.55 | 0.171 | |
| 1997.2.2.057 | 10 : 47 : 28.49 | +07 : 12 : 55.3 | 18.91 | 19.31 | 0.136 | |
| 1997.2.2.058 | 10 : 47 : 27.85 | +07 : 22 : 38.1 | 18.64 | 19.43 | 0.166 | |
| 1997.2.2.071 | 10 : 50 : 25.77 | +07 : 34 : 37.9 | 18.93 | 19.59 | 0.105 | |
| 1997.2.3.029 | 10 : 48 : 11.99 | +06 : 24 : 20.3 | 19.30 | 19.70 | 0.151 | |
| 1997.2.3.034 | 10 : 49 : 36.94 | +06 : 49 : 22.2 | 16.95 | 19.12 | 0.099 | |
| 1997.2.3.047 | 10 : 47 : 51.01 | +06 : 38 : 21.1 | 16.82 | 17.19 | 0.100 | |
| 1997.2.3.064 | 10 : 47 : 51.31 | +06 : 09 : 46.4 | 18.55 | 18.87 | 0.100 | |
| 1997.2.3.119 | 10 : 51 : 23.15 | +06 : 42 : 25.6 | 18.87 | 19.97 | 0.263 | |
| 1997.3.2.033 | 10 : 49 : 50.01 | +05 : 14 : 08.9 | 19.11 | 19.68 | 0.192 | |
| 1997.3.2.075 | 10 : 51 : 43.89 | +05 : 33 : 08.5 | 19.10 | 19.71 | 0.235 | |
| 1997.3.2.079 | 10 : 52 : 14.58 | +05 : 29 : 08.9 | 17.53 | 18.80 | 0.054 | |
| 1997.3.2.122 | 10 : 51 : 06.46 | +05 : 06 : 27.1 | 19.22 | 19.92 | 0.118 | |
| 1997.3.3.005 | 10 : 52 : 25.96 | +06 : 06 : 17.0 | 18.74 | 19.31 | 0.126 | |
| 1997.3.3.026 | 10 : 54 : 25.16 | +05 : 42 : 59.3 | 19.67 | 19.98 | 0.076 | |
| 1997.3.3.052 | 10 : 53 : 54.53 | +06 : 48 : 06.1 | 19.44 | 19.76 | 0.173 | |
| 1997.3.3.053 | 10 : 55 : 15.13 | +06 : 30 : 46.7 | 19.09 | 19.47 | 0.132 | |
| 1997.3.3.055 | 10 : 53 : 18.87 | +06 : 46 : 37.4 | 16.67 | 17.27 | 0.053 | |
| 1997.3.3.060 | 10 : 53 : 02.63 | +05 : 56 : 31.7 | 17.61 | 18.30 | 0.129 | |
| 1997.3.3.064 | 10 : 51 : 51.34 | +05 : 55 : 41.5 | 17.82 | 18.90 | 0.040 | |
| 1997.3.3.067 | 10 : 56 : 26.82 | +05 : 52 : 15.2 | 17.40 | 18.21 | 0.145 | |
| 1997.3.3.087 | 10 : 57 : 03.01 | +06 : 10 : 27.9 | 17.91 | 19.29 | 0.122 | |
| 1997.4.1.066 | 10 : 52 : 10.38 | +03 : 27 : 12.9 | 18.73 | 19.51 | 0.149 | |
| 1997.4.1.081 | 10 : 53 : 31.97 | +03 : 49 : 21.8 | 17.50 | 19.55 | 0.077 | |
| 1997.4.1.091 | 10 : 53 : 36.46 | +04 : 07 : 03.4 | 19.49 | 19.90 | 0.015 | |
| 1997.4.1.108 | 10 : 52 : 51.66 | +04 : 24 : 56.0 | 17.51 | 19.20 | 0.018 | |
| 1997.4.1.111 | 10 : 52 : 53.53 | +04 : 30 : 22.1 | 17.90 | 18.53 | 0.018 | |
| 1997.4.1.112 | 10 : 53 : 08.94 | +04 : 10 : 36.0 | 18.55 | 19.16 | 0.397 | |
| 1997.4.2.006 | 10 : 54 : 35.87 | +04 : 59 : 26.4 | 19.55 | 19.96 | 0.170 | |
| 1997.4.2.010 | 10 : 55 : 55.02 | +04 : 47 : 50.2 | 18.21 | 19.14 | 0.170 | |

(continued)

| CUQS No. | $\alpha$ ($^{\mathrm{h}}.^{\mathrm{m}}.^{\mathrm{s}}$) | $\delta$ ($^{\circ}.'.''$) | $u_{\mathrm{J}}$ | $b_{\mathrm{J}}$ | $z$ | Notes |
|---|---|---|---|---|---|---|
| 1997.4.2.033 | 10 : 53 : 54.55 | +04 : 57 : 21.0 | 19.17 | 19.83 | 0.117 | |
| 1997.4.2.046 | 10 : 54 : 09.48 | +04 : 42 : 43.1 | 16.51 | 17.84 | 0.069 | |
| 1997.4.2.056 | 10 : 53 : 33.56 | +05 : 21 : 21.6 | 17.34 | 19.11 | 0.070 | |
| 1997.4.2.076 | 10 : 56 : 46.70 | +05 : 22 : 25.6 | 16.56 | 19.85 | 0.038 | |
| 1997.4.2.123 | 10 : 56 : 28.92 | +04 : 53 : 24.0 | 18.73 | 19.57 | 0.230 | |

**Table A.4:** The 6 narrow emission-line galaxies detected in the CUQS control area observations from 1996 and 1997. The columns are as for table A.1.

| CUQS No. | $\alpha$ $(^{\mathrm{h}}:^{\mathrm{m}}:^{\mathrm{s}})$ | $\delta$ $(^{\circ}:':'')$ | $u_{\mathrm{J}}$ | $b_{\mathrm{J}}$ | $z$ |
|---|---|---|---|---|---|
| 1996.1.4.001 | $11:09:11.69$ | $-29:19:35.2$ | 19.50 | 20.08 | 0.339 |
| 1996.1.4.055 | $11:06:52.42$ | $-29:12:11.3$ | 17.76 | 18.31 | 0.145 |
| 1996.2.4.075 | $11:07:33.60$ | $-29:59:18.7$ | 18.99 | 19.70 | 0.211 |
| 1996.3.4.047 | $11:09:58.21$ | $-30:38:52.9$ | 19.48 | 20.16 | 0.243 |
| 1997.3.4.006 | $11:13:26.55$ | $-31:27:57.4$ | 19.10 | 19.51 | 0.291 |
| 1997.4.4.087 | $11:19:40.69$ | $-30:48:46.9$ | 19.09 | 19.42 | 0.227 |

# Appendix B

# Calculation of cosmological distances

## B.1 Comoving distance and separation

To fairly compare the clustering of objects at different redshifts, it is important to discount the changes in separation between objects that are solely due to the expansion of the Universe. It is therefore convenient to define a "comoving" coordinate system which expands with the Universe such that objects at rest maintain constant coordinates. In the common analogy that likens the change in separation of galaxies due to the expansion of the Universe to the change in separation of dots on an inflating balloon, a comoving coordinate system might be represented by a mesh of lines on the surface of the balloon. Since the coordinate mesh expands at the same rate as the separation between pairs of dots, the coordinate separation between pairs of dots remains constant. Separations measured in comoving coordinates are therefore independent of the time-dependent scale factor, $a(t)$, of the Universe in conventional cosmology. This appendix shows how to calculate the comoving separation, $d_{ab}$, of two objects observed at redshifts $z_a$ and $z_b$ with angular separation $\theta$ in terms of the standard cosmological parameters, and expressed in physical units as the distance would appear at redshift $z = 0$. The derivation largely follows Weinberg (1972, hereafter W72) and Osmer (1981). The subscript 0 is used to indicate values at the time of observation (i.e. $z = 0$).

A start is made by noting that the assumption of the Cosmological Principle

implies that the spatial curvature of the Universe is uniform. This means that spacetime intervals may be measured using the Robertson-Walker (RW) metric, which takes the general form

$$d\tau^2 = dt^2 - a^2(t)[d\eta^2 + g^2(\eta)(d\theta^2 + \sin^2\theta d\phi^2)]$$

(B.1)

where $d\tau$ is the spacetime interval, $dt$ is the clock time interval and $(\eta, \theta, \phi)$ define a dimensionless comoving spherical polar coordinate system. The choice of physical dimensions are absorbed by the $a(t)$ term, which is a time-dependent scale factor. The $g(\eta)$ term can take three forms depending on the type of curvature,

$$g(\eta) = \begin{cases} \sin\eta & \text{for uniform positive curvature (spherical geometry)} \\ \eta & \text{for zero curvature (Euclidean geometry)} \\ \sinh\eta & \text{for uniform negative curvature (hyperbolic geometry).} \end{cases}$$

Eqn. B.1 can be rewritten in terms of a different radial coordinate, $r = g(\eta)$, by noting that

$$r = \sin\eta \quad \Rightarrow \quad d\eta^2 = \frac{dr^2}{(1 - r^2)}$$
$$r = \eta \quad \Rightarrow \quad d\eta^2 = dr^2$$
$$r = \sinh\eta \quad \Rightarrow \quad d\eta^2 = \frac{dr^2}{(1 + r^2)}$$

giving the commonly-used form of the RW metric,

$$d\tau^2 = dt^2 - a^2(t)\left[\frac{dr^2}{(1 - kr^2)} + r^2(d\theta^2 + \sin^2\theta d\phi^2)\right]$$

(B.2)

where $k = +1, 0, -1$ corresponding to the spherical, Euclidean and hyperbolic geometries respectively. Applying the RW metric from Eqn. B.2 to Einstein's gravitational field equations (W72, Eqns. 15.2.1, 15.2.2 and 16.2.5) then gives

$$8\pi G\rho = \frac{3}{a^2}(k + \dot{a}^2) - \Lambda$$
$$8\pi G p = -\frac{2\ddot{a}}{a} - \left(\frac{\dot{a}}{a}\right)^2 - \frac{k}{a^2} + \Lambda$$

(B.3)

where $G$ is the gravitational constant, $\rho$ is energy density, $p$ is the pressure and $\Lambda$ is the cosmological constant. The energy density of the present Universe is dominated by non-relativistic matter, so $p \ll \rho$ and so $p = 0$ may be used. The standard cosmological parameters are then introduced: $H = \dot{a}/a$ (the Hubble parameter); $\Omega = 8\pi G\rho/3H^2$ (the matter density parameter); $q = -\ddot{a}/aH^2$ (the deceleration

parameter); $\lambda = \Lambda/3H^2$ (the normalized cosmological constant). Eqn. B.3 is then rearranged to get

$$
\begin{aligned}
q &= \frac{\Omega}{2} - \lambda \\
\frac{k}{a^2 H^2} &= \Omega + \lambda - 1.
\end{aligned}
\tag{B.4}
$$

Now, for a photon, $d\tau = 0$, and for travel on a radial path, $d\theta = d\phi = 0$, so Eqn. B.2 reduces to

$$
\frac{dt^2}{a^2(t)} = \frac{dr^2}{(1 - kr^2)}.
\tag{B.5}
$$

A photon from an object at comoving radial distance $r_{01}$ emitted at at time $t_1$ will therefore reach the observer at time $t_0$, given by integrating Eqn. B.5

$$
\int_{t_1}^{t_0} \frac{dt}{a(t)} = f(r_{01})
$$

where

$$
f(r_{01}) = \int_{a(t_1)}^{a(t_0)} \frac{da}{a\dot{a}} = \int_0^{r_{01}} \frac{dr}{\sqrt{1 - kr^2}} = \begin{cases} \sin^{-1} r_{01} & k = +1 \\ r_{01} & k = 0 \\ \sinh^{-1} r_{01} & k = -1 \end{cases}
\tag{B.6}
$$

Note that $f(r_{01}) = g^{-1}(r_{01}) = \eta_{01}$, and this is time-independent as expected from the definition of comoving coordinates. Redshift is now defined in the usual way as $z = a(t_0)/a(t_1) - 1$ and Eqn. B.6 is rewritten in terms of redshift and the standard cosmological parameters to obtain the dimensionless comoving radial separation of an object at redshift $z_1$ from the observer (Refsdal 1966; Peacock 1999)

$$
\eta_{01} = \frac{1}{a_0} \int_0^{z_1} \frac{dz}{\sqrt{\Omega_r(1+z)^4 + \Omega_0(1+z)^3 + (1 - \Omega_0 - \lambda_0)(1+z)^2 + \lambda_0}},
\tag{B.7}
$$

where $\Omega_r$ is the density parameter for radiation. During the matter dominated epoch, $z \lesssim 600$, the radiation energy density is much smaller than the matter density, so $\Omega_r = 0$ can be used (Peacock 1999). Note that Eqns. B.4 can be used to substitute $q_0$ terms for $\lambda_0$ terms, etc. Next, the comoving separation between two objects at redshifts $z_1$ and $z_2$ with angular separation $\theta$ is calculated, using the method of Osmer (1981). A rectangular comoving coordinate system is defined with the observer at the origin $(0,0,0)$ such that the first object is at coordinates $\boldsymbol{a} = (0,0,r_1)$ and the second is at $\boldsymbol{x} = (r_2 \sin\theta, 0, r_2 \cos\theta)$. The vector, $\boldsymbol{x}'$, from

object 1 to object 2 is given by translating the origin from the observer to object 1 using (W72, Eqn. 14.2.7)

$$\boldsymbol{x}' = \boldsymbol{x} - \boldsymbol{a}\left\{(1 - k\boldsymbol{x}^2)^{1/2} - \left[1 - (1 - k\boldsymbol{a}^2)^{1/2}\right]\left(\frac{\boldsymbol{x} \cdot \boldsymbol{a}}{\boldsymbol{a}^2}\right)\right\}. \tag{B.8}$$

The dimensionless comoving separation of objects 1 and 2 is then given by the length of $\boldsymbol{x}'$ as

$$\eta_{12} = \begin{cases} \sin^{-1}|\boldsymbol{x}'| & k = +1 \\ |\boldsymbol{x}'| & k = 0 \\ \sinh^{-1}|\boldsymbol{x}'| & k = -1. \end{cases} \tag{B.9}$$

Finally, conversion to physical coordinates is made by adopting the Hubble scale $a_0 = c/H_0$, giving the desired result,

$$d_{12} = \frac{c}{H_0}\eta_{12}, \tag{B.10}$$

where $c$ is the speed of light and $H_0 = 100\,h$ km s$^{-1}$ Mpc$^{-1}$ is the present value of the Hubble constant. Evaluation of $d_{12}$ is made by numerical integration of Eqn. B.7 and substitution of the appropriate parameter values into Eqns. B.8–B.10.

# B.2 Luminosity distance

The luminosity distance of an object, $d_{\rm L}$, is defined in terms of the total intrinsic (i.e. rest-frame) bolometric luminosity, $L_{\rm bol}$, and the detected bolometric luminosity density, $\ell_{\rm bol}$, by

$$\ell_{\rm bol} = \frac{L_{\rm bol}}{4\pi d_{\rm L}{}^2}.$$

If redshift is due to the expansion of the Universe, and not some other physical cause, it can be shown (Robertson 1938) that $\ell_{\rm bol}$ and $L_{\rm bol}$ can also be simply related to the comoving distance of the emitter from the observer by

$$\ell_{\rm bol} = \frac{L_{\rm bol}}{4\pi d_{01}^2(1 + z_1)^2}. \tag{B.11}$$

A physical explanation of Eqn. B.11 is that $L_{\rm bol}$ is detected on the surface of a sphere of radius $4\pi d_{01}^2$. One factor of $(1 + z)$ then accounts for the decrease in energy per photon between emission and detection due to redshift, and a second factor of $(1 + z)$

accounts for the time dilation that decreases the rate at which photons are detected. We can then easily calculate the luminosity distance of an object at redshift $z_1$ as

$$d_{\mathrm{L}} = d_{01}(1 + z_1)$$

using the definition of comoving distance given above.

# Appendix C

# The $k$ correction

If measurements are made of the bolometric (i.e. total-spectrum) intensity of radiation in power per unit area received from a redshifted object, $\ell_{bol}$, then its emitted bolometric luminosity, $L_{bol}$, can be calculated from the area of a sphere with radius equal to the object's luminosity distance, $d_L$, as $L_{bol} = 4\pi d_L^2 \ell_{bol}$, as described in appendix B. However, if the measurements are of the intensity, $\ell_f$, filtered by the combined transmission function due to the atmosphere, telescope and detector system, then the measurements must be corrected for the redshift of the spectral energy distribution (SED) with respect to the filter passband. This is known as the $k$ (or sometimes $K$) correction after the term first introduced (incorrectly) by Hubble (1936).

For clarity, the $k$ correction is derived here for the general case of classes of objects whose SEDs do not evolve with time, and for the specific case of objects with power-law SEDs of the form $f_\nu \propto \nu^\alpha$ (where $\nu$ is frequency, $f_\nu$ is the flux density in power per unit area per unit frequency and $\alpha$ is a constant). The subscript $z$ is used to indicate measurements of an object's SED at redshift $z$, and subscript 0 to indicate measurements of the intrinsic SED (i.e. as it would be observed at $z = 0$). For the case of objects whose SED evolves with time, see e.g. Humason et al. (1956).

Qualitatively, following Oke & Sandage (1968) and Sandage et al. (1995), it must be noted that there are two components required to the $k$ correction. First, the effective frequency bandwidth, $\Delta\nu$, of a given filter is increased in the rest-frame of a redshifted object by a factor of $(1 + z)$. This component is independent of the SED. Secondly, the filter bandwidth covers a different portion of the SED, so that

the observed effective frequency of the filter falls on an emitted frequency that is higher by a factor of $(1 + z)$. This component depends on the SED of the object.

Quantitatively, largely following Humason et al. (1956), a start is made by assuming that the objects to be observed all have the same, non-evolving, intrinsic SED. The bolometric and filtered intensities of an object at redshift $z$ are then defined by the integrals

$$
\begin{aligned}
\ell_{\text{bol}}(z) &= \int_0^\infty f_{\nu z}(\nu)\, d\nu \\
\ell_f(z) &= \int_0^\infty T(\nu) f_{\nu z}(\nu)\, d\nu
\end{aligned}
\tag{C.1}
$$

where $T(\nu)$ is the transmission function of the filtered observation. The bolometric magnitude correction for an object at redshift $z$, $\Delta m(z)$, is defined by

$$
\Delta m(z) = \tfrac{5}{2} \log \frac{\ell_{\text{bol}}(z)}{\ell_f(z)}.
$$

The $k$ correction is now defined as the difference between the bolometric corrections at redshift $z$ and redshift 0, i.e.

$$
k = \Delta m(z) - \Delta m(0) = \tfrac{5}{2} \log \frac{\ell_{\text{bol}}(z)}{\ell_f(z)} - \tfrac{5}{2} \log \frac{\ell_{\text{bol}}(0)}{\ell_f(0)}.
\tag{C.2}
$$

The apparent bolometric magnitude, $m_{\text{bol}}$, of an object at redshift $z$, which is the value sought, is then related to its apparent filtered magnitude, $m_f$, by

$$
m_{\text{bol}}(z) = m_f(z) + \Delta m(0) - k.
$$

$\Delta m(0)$ is assumed constant for a given type of object. If the $\Delta m(0)$ is not known, then $m_{\text{bol}}(z)$ can still be calculated to within a constant term, so that the magnitudes of similar objects at different redshifts can be fairly compared. Eqns. C.1 and C.2 are now rearranged to give

$$
k = \tfrac{5}{2} \log \frac{\ell_{\text{bol}}(z)}{\ell_{\text{bol}}(0)} + \tfrac{5}{2} \log \frac{\int_0^\infty T(\nu) f_{\nu 0}(\nu)\, d\nu}{\int_0^\infty T(\nu) f_{\nu z}(\nu)\, d\nu}
\tag{C.3}
$$

If the emitted SED, $f_{\nu 0}$, is known, then the observed SED, $f_{\nu z}$, can be constructed by noting that $\nu_z = \nu_0/(1 + z)$, so that $f_{\nu z}(\nu) = f_{\nu 0}(\nu(1 + z))$. This changes the total area under the SED in Eqn. C.1 by a factor of $(1 + z)^{-1}$, so the first term in Eqn. C.3 must be $-\tfrac{5}{2} \log(1 + z)$. Hence the final form of the $k$ correction where the SED is measured in terms of frequency is

$$
k = -\tfrac{5}{2} \log(1 + z) + \tfrac{5}{2} \log \frac{\int_0^\infty T(\nu) f_{\nu 0}(\nu)\, d\nu}{\int_0^\infty T(\nu) f_{\nu 0}(\nu(1 + z))\, d\nu}.
\tag{C.4}
$$

If this derivation is repeated for SEDs measured in terms of wavelength, $\lambda$, then a similar expression is arrived at, with the differences that $\lambda_z = \lambda_0(1+z)$, so that $f_{\lambda z}(\lambda) = f_{\lambda 0}(\lambda/(1+z))$. This changes the area under SED curve (in the $\lambda$ form of Eqn. C.1) by a factor of $(1+z)$, and so changes the sign of the first term, giving

$$k = +\tfrac{5}{2}\log(1+z) + \tfrac{5}{2}\log \frac{\int_0^\infty T(\lambda) f_{\lambda 0}(\lambda)\, d\lambda}{\int_0^\infty T(\lambda) f_{\lambda 0}(\lambda/(1+z))\, d\lambda}. \tag{C.5}$$

In fact, these two forms of the $k$ correction are equivalent, since $f_\nu \propto \lambda^2 f_\lambda$. For arbitrary SEDs, Eqns. C.4 and C.5 must be evaluated by numerical integration using a known transmission function $T$. However, the SEDs of AGN are commonly modelled as having a power-law form, $f_\nu \propto \nu^\alpha$, over the observed bandwidth. In this case, Eqn. C.4 reduces to

$$\begin{aligned} k &= -\tfrac{5}{2}\log(1+z) + \tfrac{5}{2}\log \frac{\int_0^\infty T(\nu)\nu^\alpha\, d\nu}{\int_0^\infty T(\nu)\nu^\alpha(1+z)^\alpha\, d\nu} \\ &= -\tfrac{5}{2}(1+\alpha)\log(1+z). \end{aligned} \tag{C.6}$$

# Appendix D

# Abbreviations, symbols and units

AGN     Active galactic nucleus/nuclei. The abnormally luminous centre of an otherwise normal galaxy.

ADU     Analogue-to-digital units. The integer counting unit of the data read from a CCD camera.

CMBR     Cosmic microwave background radiation. All-sky blackbody radiation with a mean temperature of $\sim 2.73$K and isotropic to $\sim 10^{-5}$.

$h$     The dimensionless Hubble parameter, defined in terms of the Hubble constant $H_0 = 100\ h$ km s$^{-1}$ Mpc$^{-1}$. The Hubble constant relates apparent recession velocity of an object to its distance.

FWHM     Full width at half maximum, a measure of the spread of a distribution.

IRAF     Image Reduction and Analysis Facility software.

$\Lambda$     The cosmological constant that appears in the solutions to the equations of general relativity.

$\lambda$     Wavelength, normally expressed in Ångstrom units (1 Å $= 10^{-10}$ m) for emission and absorption lines, e.g. C IV $\lambda 1549$ means the triply-ionized carbon line with wavelength 1549 Å.

Mpc     Megaparsec $\simeq 3.262 \times 10^6$ light years $\simeq 3.09 \times 10^{22}$ m.

NELG     Narrow emission-line galaxy, with narrow ($v < 1000$ km s$^{-1}$) emission lines and line-strength ratios suggesting a higher than normal state of ionization.

183

$\Omega$        The ratio $\rho/\rho_{\mathrm{crit}}$, where $\rho$ is the mean mass density, and $\rho_{\mathrm{crit}}$ is the critical mass density just necessary to halt the expansion of the Universe after infinite time.

Seeing       The combined effects of turbulence and temperature variations in the atmosphere, through which a celestial object is observed.

UKST       United Kingdom Schmidt Telescope, Australia. A 1.8 m Schmidt camera with an unvignetted field of $5°.4$ diameter, producing photographic plates 356 mm square with images detectable to $B \simeq 23$.

$z$        Redshift. The redshift of a body emitting photons is defined by $1 + z = \lambda_{\mathrm{obs}}/\lambda_{\mathrm{emit}}$, where $\lambda_{\mathrm{obs}}$ is the observed wavelength of a photon and $\lambda_{\mathrm{emit}}$ is the emitted wavelength.

# References

Abell G.O., Chincarini G., eds, 1983, Early Evolution of the Universe and Its Present Structure, Proc. IAU Symp. 104, Reidel, Dordrecht

Adami C., Mazure A., 1998, A&AS, 134, 393-400

Aghanim N., Désert F.X., Puget J.L., Gispert R., 1996 A&A, 311, 1

Alexander T., Netzer H., 1997, MNRAS, 284, 967

Allen C.W., 1976, Astrophysical Quantities (third edition revised), The Athlone Press, London

Alpher R.A., Bethe H.A., Gamow G., 1948, Physical Review, 73, 803

Antonucci R., 1993, ARA&A, 31, 473

Bagla J.S., 1998, MNRAS, 297, 251

Bahcall N.A., 1992, in Fabian (1992), q.v., p. 275

Bahcall N.A., Chokshi A., 1991, ApJ, 380, L9

Bahcall N.A., Soneira R.M., 1984, ApJ, 277, 27

Baldwin J.A., 1977, ApJ, 214, 679

Baldwin J.A., Burke W.L., Gaskell C.M., Wampler E.J., 1978, Nat, 273, 431

Bardeen J.M., Bond J.R., Kaiser N., Szalay A.S., 1986, ApJ, 304, 15

Barden S.C., Massey P., 1988, in Barden S.C., ed, Fiber Optics in Astronomy, ASP Conf. Ser. vol. 3, ASP, San Francisco, p. 140

Barlow R.J., 1989, Statistics, Wiley, Chichester

Barrow J.D., Bhavsar S.P., Sonoda D.H., 1985, MNRAS, 216, 17

Bastian U., Röser S., 1993, Catalogue of Positions and Proper Motions - South, Astronomishes Rechen-Institut, Heidelberg

Bazell D., Peng Y., 1998, ApJS, 116, 47

Beard S.M., MacGillivray H.T., Thanisch P.F., 1990, MNRAS, 247, 311

Benn C.R., Vigotti M., Carballo R., Gonzalez-Serrano J.I., Sánchez S.F., 1998,

MNRAS, 295, 451

Bertin E., Arnouts S., 1996, A&AS, 117, 393

Bessell M.S., 1990, PASP, 102, 1181

Bhavsar S.P., Ling E.N., 1988, ApJ, 331, L63

Bhavsar S.P., Splinter R.J., 1996, MNRAS, 282, 1461

Blair M., Gilmore G., 1982, PASP, 94, 742

Blanton M., Cen R., Ostriker J.P., Strauss M.A., 1998, preprint astro-ph/9807029, ApJ submitted

Bond J.R., Kofmann L., Pogosyan D., 1996, Nat, 380, 603

Börner G., 1993, The Early Universe, Springer–Verlag, Berlin, p. 70

Boyle B.J., 1986, PhD thesis, University of Durham

Boyle B.J., di Matteo T., 1995, MNRAS, 277, L63

Boyle B.J., Fong R., Shanks T., Peterson B.A., 1987, MNRAS, 227, 717

Boyle B.J., Fong R., Shanks T., Peterson B.A., 1990, MNRAS, 243, 1

Boyle B.J., Smith R.J., Shanks T., Croom S.M., Miller L., 1999, in Sato K., ed, Cosmological Parameters and the Evolution of the Universe, Proc. IAU Symp. 183, Kluwer, Dordrecht

Broadhurst T.J., Ellis R.S., Koo D.C., Szalay A.S., 1990, Nat, 343, 726

Brodbeck D., Hellinger D., Nolthenius R., Primack J., Klypin A., 1998, ApJ, 491, 1

Burbidge E.M., Junkkarinen V.T., Koski A.T., Smith H.E., Hogg A.A., 1980, ApJ, 242, L55

Campusano L.E., 1991a, AJ, 102, 502

Campusano L.E., 1991b, A&A, 250, 9

Cannon R.D., Hawarden T.G., Sim M.E., Tritton S.B., 1985, The U.K. 1.2m Schmidt Telescope and the Southern Sky Survey-II Photographic Techniques, Occasional Reports of the Royal Observatory Edinburgh No 4

Cheriton D., Tarjan R.E., 1976, SIAM J. Comput., 5, 724

Clowes R.G., Campusano L.E., 1991, MNRAS, 249, 218

Clowes R.G., Campusano L.E., Graham M.J., 1995, in Maddox & Aragón-Salamanca (1995), q.v., p. 400

Coles P., Davies A., Pearson R.C., 1996, MNRAS, 281, 1375

Coles P., Lucchin F., 1995, Cosmology : the Origin and Evolution of Cosmic Struc-

ture, Wiley, Chichester, p. 332 ff

Coles P., Pearson R.C., Borgani S., Plionis M., Moscardini L., 1998, MNRAS, 29, 245

Colless M., 1997, in Kontizas E., Kontizas M., Morgan D.H., Vettolani G.P., eds, Wide Field Spectroscopy, Kluwer, Dordrecht

Colombi S., Mellier Y., Raban B., eds, 1998, Wide Field Surveys in Cosmology, Proceedings of the 14th IAP Cosmology Colloquium, Editions Frontières

Connolly A.J., Szalay A.S., Koo D., Romer A.K., Holden B., Nichol R.C., Miyaji T., 1996, ApJ, 473, L67

Conway J.H., Sloane N.J.A, 1993, Sphere packings, lattices and groups (2nd ed.), Springer-Verlag, New York

Copi C.J., Olive K.A., Schramm D.N., 1995, ApJ, 451, 51

Corbin M.R., 1990, ApJ, 357, 346

Crampton D., Cowley A.P., Hartwick F.D.A., 1987, ApJ, 314, 129

Crampton D., Cowley A.P., Hartwick F.D.A., 1989, ApJ, 345, 59

Crampton D., ed, 1991, The Space Distribution of Quasars, ASP, San Francisco ASP Conf. Ser. vol. 21, ASP, San Francisco

Croom S.M., 1997, PhD thesis, University of Durham

Cuby J.G., Mignoli M., 1994, in Instrumentation in Astronomy III, Proc. SPIE, 2198, 98

Davé R., Hellinger D., Primack J., Nolthenius R., Klypin A., 1997, MNRAS, 284, 607

Davenhall A.C., 1998a, CURSA User's Manual, Starlink User Note SUN/190.6

Davenhall A.C., 1998b, Programmer's Note for XYTORADEC, Institute for Astronomy, Edinburgh

Dekel A., West M.J., 1985, ApJ, 288, 411

Deng Z., Xia X., Fang L.Z., 1994, ApJ, 431, 506

de Vaucouleurs G., 1971, PASP, 83, 113

Dicke R.H., Peebles P.J.E., Roll P.G., Wilkinson D.T., 1965, ApJ, 142, 414

Dijkstra E.W., 1959, Numer. Math., 1, 269

Doroshkevich A.G., Tucker D.L., Oemler A., Kirshner R.P., Lin H., Shectman S.A., Landy S.D., Fong R., 1996, MNRAS, 283, 1281

Dussert C., Rasigni M., Palmari J., Rasigni G., Llebaria A., Marty F., 1986a, J. Theor. Biol., 125, 317

Dussert C., Rasigni G., Rasigni M., Palmari J., Llebaria A., 1986b, Phys. Rev. B., 34, 3528

Eichhorn H., 1960, Astr. Nach., 285, 233

Einasto M., Einasto J., Tago E., Dalton G.B., Andernach H., 1994, MNRAS, 269, 301

Einasto J., Klypin A.A., Saar E., Shandarin S.F., 1984, MNRAS, 206, 529

Einasto M., Tago E., Jaaniste J., Einasto J., Andernach H., 1997, A&AS, 123, 119

Engels D., Tesch F., Ledoux C., Wei J., Ugryumov A., Valls-Gabaud D., Hu J., Voges W., 1999, preprint astro-ph/9811182, to appear in Aschenbach B., Freyberg M., eds, Highlights of X-ray Astronomy, MPE Report, Garching

Ettori S., Guzzo L., Tarenghi M., 1997, MNRAS, 285, 218

Evans D.W., 1988, PhD thesis, University of Cambridge

Fabian A.C., ed, 1992, Clusters and Superclusters of Galaxies, Proceedings of the NATO Advanced Study Institute, Kluwer, Dordrecht

Falcke H., Gopal-Krishna, Biermann P.L., 1995, A&A, 298, 395

Fang L.Z., Jing Y.P., 1998, ApJ, 502, L95

Feldman H.A., Kaiser N., Peacock J.A., 1994, ApJ, 426, 23

Ferland G., Baldwin J., eds, 1999, Quasars and Cosmology, ASP Conf. Ser. vol. 162, San Franciso

Filipenko A.V., 1984, PhD thesis, California Institute of Technology

Fisher K.B., Bahcall J.N., Kirhakos S., Schneider D.P., 1996, ApJ, 468, 469

Francis P.J., Hewett P.C., Foltz C.B., Chaffee F.H., Weymann R.J., Morris S.L., 1991, ApJ, 373, 465

Gaztañaga E., Fosalba P., Elizalde E., 1998, MNRAS, 295, L35

Geller M.J., Huchra J.P., 1989, Science, 246, 897

Geller M.J. et al., 1997, AJ, 114, 2205

Giveon U., Maoz D., Kaspi S., Netzer H., Smith P.S., 1999, MNRAS, 306, 637

Goldschmidt et al., 1991, in Crampton (1991), q.v., p. 93

Górski K.M., 1992, ApJ, 398, L5

Graham M.J., 1997, PhD thesis, University of Central Lancashire

Graham M.J., Clowes R.G., Campusano L.E., 1995, MNRAS, 275, 790

Graham M.J., Clowes R.G., Campusano L.E., 1999, ApJ, 513, 69

Green P.J., 1996, ApJ, 467, 61

Green P.J., 1998, ApJ, 498, 170

Green R.F., Yee H.K.C., 1988, in Osmer et al. (1988), q.v., p. 233

Gregg M.D., Becker R.H., White R.L., Helfand D.J., McMahon R.G., Hook I.M., 1996, AJ, 119, 407

Guth A.H., 1981, Phys. Rev. D, 23, 347

Haehnelt M.G., Natarajan P., Rees M.J., 1998, MNRAS, 300, 817

Hambly N.C., Miller L., 1997, SuperCOSMOS Technical Manual, available from http://www.roe.ac.uk/cosmos/manuals/tm.ps.gz

Hambly N.C., 1998a, The SuperCOSMOS data processing guides: Introduction, available from http://www.roe.ac.uk/cosmos/manuals/intro.ps.gz

Hambly N.C., 1998b, The SuperCOSMOS data processing guides: Photometry, available from http://www.roe.ac.uk/cosmos/manuals/photometry.ps.gz

Hambly N.C., Miller L., MacGillivray H.T., Herd J.T., Cormack W.A., 1998, MNRAS, 298, 897

Hamuy M., Walker A.R., Suntzeff N.B., Gigoux P., Heathcote S.R., Phillips M.M., 1992, PASP, 104, 533

Hazard C., Mackey M.B., Shimmins A.J., 1963, Nat, 197, 1037

Hewett P.C., Foltz C.B., Chaffee F.H., 1995, AJ, 109, 1498

Heydon-Dumbleton N.H., Collins C.A., MacGillivray H.T., 1989, MNRAS, 238, 379

Hog E. et al., 1997, A&A, 323, L57

Hubble E.P., 1929, Proc. Nat. Acad. Sci., 15, 168

Hubble E.P., 1934, ApJ, 79, 8

Hubble E.P., 1936, ApJ, 84, 517

Humason M.L., Mayall N.U., Sandage A.R., 1956, AJ, 61, 97

Iovino A., Shaver P.A., 1988, ApJ, 330, L13

Iovino A., Shaver P.A., Cristiani S. 1991, in Crampton (1991), q.v., p. 202

Jedamzik K., Mathews G.F., Fuller G.M., 1995, ApJ, 441, 465

Jefferys W.H., Fitzpatrick M.J., McArthur B.E., 1988, Celestial Mechanics, 41, 39

Jenkins A. et al., 1998, ApJ, 499, 20

189

Jones B.J.T., Jones J.E., 1980, MNRAS, 193, 537

Kaiser N., 1984, ApJ, 284, L9

Kaiser N., Peacock J.A., 1991, ApJ, 379, 482

Kelly D., 1995, Accessing SuperCOSMOS IAM Data, SuperCOSMOS User Note 22.0, Royal Observatory Edinburgh

Kerscher M., 1998, A&A, 336, 29

Kershner R., 1939, Amer. Jnl. Mathematics, 61, 665

Kibblewhite E.J., Bridgeland M.T., Bunclark P., Irwin M., 1984, in Klinglesmith D.A., ed, Astronomical Microdensitometry Conference, NASA Conf. Publ., 2317, 277

Kinney A.L., Rivolo A.R., Koratkar A.P., 1990, ApJ, 357, 338

Kirsner R.P., Oemler A., Schechter P.L., Shectman S.A., 1981, ApJ, 248, L57

Köhler T., Groote D., Reimers D., Wisotzki L., 1997, A&A, 325, 502

Komberg B.V., Kravtsov A.V., Lukash V.N., 1996, MNRAS, 282, 713

Komberg B.V., Lukash V.N., 1994, MNRAS, 269, 277

Krzewina L.G., Saslaw W.C., 1996, MNRAS, 278, 869

Kron R.G., ed, 1990, Evolution of the Universe of Galaxies, ASP Conf. Ser. vol. 10, San Francisco

Kuraszkiewicz J., Wilkes B.J., Green P.J., Mathur S., McDowell J.C., Czerny B., 1999, in Ferland & Baldwin (1999), q.v., p. 325

La Franca F., Andreani P., Cristiani S., 1998, ApJ, 497, 529

Landy S.D., Szalay A.S., 1993, ApJ, 412, 64

Lasker B.M., Sturch C.R., McLean B.J., Russell J.L., Jenkner H., 1990, AJ, 99, 2019

Leibundgut B. et al., 1996, ApJ, 466, L21

Lewis I., Glazebrook K., 1997, AAO Newsletter, 83, 10

Lissandrini C., Cristiani S., La Franca F., 1994, PASP, 106, 1157

Liu Y.Z., 1995, A&A, 304, 317

Loeb A., 1997, in Smith E.P., Koratkar A., eds, Science with the Next Generation Space Telescope, ASP Conf. Ser. vol. 133, San Francisco, p. 73

Longo M.J., 1991, ApJ, 372, L59

Luo S., Vishniac E., 1995, ApJS, 96, 429

MacGillivray H.T., 1998, Publ. Astron. Soc. Australia, 15, 42

Maddox S.J., Sutherland W.J., Efstathiou G., Loveday J., 1990, MNRAS, 243, 692

Maddox S.J., Aragón–Salamanca A., eds, 1995, Wide Field Spectroscopy and the Distant Universe, Proceedings of the 35$^{th}$ Herstmonceux Conference, World Scientific, Singapore

Margon B., 1999, Phil. Trans. R. Soc. Lond. A, 357, 93

Maran S.P., 1992, ed, The Astronomy and Astrophysics Encyclopedia, CUP, Cambridge

Martínez V.J., Jones B.J.T., Domínguez-Tenreiro R., van de Weygaert R., 1990, ApJ, 357, 50

Massey P., Davis L.E., 1992, A User's Guide to Stellar CCD Photometry with IRAF, NOAO, p.38

Mecke K.R., Buchert T., Wagner H., 1994, A&A, 288, 697

Miller J.S., 1995, Proc. Nat. Acad. Sci., 92(25), 11422

Miller L., Cormack W., Paterson M., Beard S., Lawrence L., 1992, in MacGillivray H.T., Thomson E.B., eds, Digitised Optical Sky Surveys, Kluwer, Dordrecht, p. 133

Mo H.J., Fang L.Z., 1993, ApJ, 410, 493

Monet D., 1996, BAAS, 28(2), 54.04

Monet D., 1997, BAAS, 29(5), 16.08

Monet D. et al., 1996, USNO-A V1.0 A Catalogue of Astrometric Standards, U.S. Naval Observatory, Washington DC

Moreau O., Reboul H., 1995, A&A, 111, 169

Muñoz J.A., Falco E.E., Kochanek C.S., Lehár J., McLeod B.A., Impey C.D., Rix H.W., Peng C.Y., 1999, preprint astro-ph/9902131, to appear in Gorgas J., Zamorano J., eds, Astrophysics & Space Science, special issue: Proceedings of the III Scientific Meeting of the SEA (Spanish Astronomical Society)

Murdoch H.S., 1983, MNRAS, 202, 987

Natali F., Giallongo E., Cristiani S., La Franca F., 1998, ApJ, 115, 397

Newman P.R., Clowes R.G., Campusano L.E., Graham M.J., 1998a, in Muller V., Gottlöber S., Mücker J.P., Wambsganss J., eds, Large-Scale Structures: Tracks and Traces – Proceedings of the 12th Potsdam Cosmology Workshop, p. 133

191

Newman P.R., Clowes R.G., Campusano L.E., Graham M.J., 1998b, in Colombi et al. (1998), q.v., p. 408

Odewahn S.C., Humphreys R.M., Aldering G., Thurmes P., 1993, PASP, 105, 1354

Oke J.B., Sandage A., 1968, ApJ, 154, 21

Olino A.V., Frieman J.A., Schramm D.N., eds, 1998, Proceedings of the 18th Texas Symposium on Relativistic Astrophysics, World Scientific Press, New Jersey

Oort J.H., 1983, ARA&A, 21, 373

Oort J.H., Arp H., de Ruiter H., 1981, A&A, 95, 7

Öpik E., 1922, ApJ, 55, 406

Osmer P.S., 1981, ApJ, 247, 762

Osmer P.S., Hewett P.C., 1991, ApJS, 75, 273

Osmer P.S., Porter A.C., Green R.F, Foltz C.B., eds, 1988, Optical surveys for quasars, ASP Conf. Ser. vol. 2, San Francisco

Osmer P.S., Porter A.C., Green R.F., 1994, ApJ, 436, 678

Osmer P.S., Shields J.C., 1999, in Ferland & Baldwin (1999), q.v., p. 235

Ostriker J.P., 1993, ARA&A, 31, 689

Peacock J.A., 1991, MNRAS, 253, 1P

Peacock J.A., 1999, Cosmological Physics, CUP, Cambridge

Peebles P.J.E., 1993, Principles of Physical Cosmology, Princeton University Press, Princeton

Peebles P.J.E., 1998, preprint astro-ph/9806201, to appear in Greco M., ed, les Recontres de Physique de la Valle d'Aosta

Penzias A.A., Wilson R.W., 1965, ApJ, 142, 419

Peterson B.M., 1997, An Introduction to Active Galactic Nuclei, CUP, Cambridge

Pogge R.W., Peterson B.M., 1992, ApJ, 103, 1084

Prim R.C., 1957, Bell Sys. Tech. J., 36, 1389

Protogeros Z.A.M., Weinberg D.H., 1997, ApJ, 489, 457

Quashnock J.M., Vanden Berk D.E., York D.G., 1998, in Olino et al. (1998), q.v.

Ratcliffe A., Shanks T., Broadbent A., Parker Q.A., Watson F.G., Oates A.P., Fong R., Collins C.A., 1996, MNRAS, 281, L47

Rees M.J., 1992, in Fabian (1992), q.v., p. 1

Refsdal S., 1966, MNRAS, 132, 101

Robertson H.P., 1928, Philosophical Magazine, 5, 835

Robertson H.P., 1938, Zeitschrift für Astrophysik, 15, 69

Robichon N. et al., 1995, A&A, 304, 132

Röser S., Bastian U., 1991, PPM Star Catalogue, Astronomishes Rechen-Institut, Heidelberg

Rudge C.M., Raine D.J., 1998, MNRAS, 297, L1

Ryan S.G., Wood P.R., 1995, Publ. Astron. Soc. Australia, 12, 89

Sandage A.R., Kron R.G., Longair M.S., 1995, The Deep Universe, Saas-Fee Advanced Course 23, Springer, New York

Sahni V., Sathyaprakash B.S., Shandarin S.F., 1997, ApJ, 476, L1

Scharf C.A., Lahav O., 1993, MNRAS, 264, 439

Schlegel D.J., Finkbeiner D.P., Davis M., 1998, ApJ, 500, 525

Schmalzing J., Kerscher M., Buchert T., 1997, in Bonometto S., Primack J, Provenzale A, eds, Dark Matter in the Universe, Proceeding of the International School of Physics Enrico Fermi, vol. 132, IOS Press, Amsterdam

Schmidt M., 1963, Nat, 197, 1040

Schmidt M., Green R.F., 1983, ApJ, 269, 352

Schramm D.N., 1993, in Prantzos N., Vangioni-Flam E., Cassé M., eds, Origin and Evolution of the Elements, CUP, Cambridge, p. 112

Sciama D.W., 1993, Modern Cosmology and the Dark Matter Problem, CUP, Cambridge

Shanks T., Boyle B.J., Peterson B.A., 1988 in Osmer et al. (1988), q.v., p. 244

Shanks T., Boyle B.J., 1994, MNRAS, 271, 753

Shaver P.A., Robertson J.G., 1983, in Abell & Chincarini (1983), q.v., p. 369

Shectman S.A., 1984, Proc. SPIE, 445, 128

Shectman S.A., 1993, in Gray P.M., ed, Fiber Optics in Astronomy II, ASP Conf. Ser. vol. 37, San Francisco, p. 26

Shectman S.A., Schechter P.L., Oemler A.A., Tucker D., Kirshner R.P., Lin H., 1992, in Fabian (1992), q.v., p. 351

Shectman S.A., Landy S.D., Oemler A., Tucker D.L., Lin H., Kershner R.P., Schechter P.L., 1996, ApJ, 470, 172

Shields G.A., 1992, in Maran (1992), q.v., p. 9

Silk J., Weinberg D., 1991, Nat, 350, 272

Smith M.G., 1983, in Quasars and Gravitational Lenses, 24th Liège Astrophysical Colloquium, Institut d'Astrophysique, Liège, p. 4

Smith R.J., 1998, PhD thesis, University of Cambridge

Smith R.J., Boyle B.J., Maddox S.J., 1995, MNRAS, 277, 270

Steidel C., Adelberger K., Dickenson M., Giavalisco M., Pettini M., Kellogg M., 1998a, ApJ, 492, 428

Steidel C., Adelberger K., Giavalisco M., Dickenson M., Pettini M., Kellogg M., 1998b, in d'Odorico S., Fontana A., Giallongo E., eds, The Young Universe, ASP Conf. Ser. vol. 146, p. 428

Szalay A.S., 1999, Phil. Trans. R. Soc. Lond. A, 357, 117

Szapudi I., Szalay A.S., 1998, ApJ, 494, L41

Taff L.G., Lattanzi M.G., Bucciarelli B., 1990 ApJ, 358, 359

Tago E., Einasto J., Saar E., 1984, MNRAS, 206, 559

Tegmark M., 1995, ApJ, 455, 429

Tegmark M., Bromley B.C., 1999, ApJ, 518, L69

Tegmark M., Peebles P.J.E., 1998, ApJ, 500, L79

Tegmark M., Silk J., Rees M.J., Blanchard A., Abel T., Palla F., 1997, ApJ, 474, 1

Thackrah A.D., 1996, PhD thesis, University of Edinburgh

Tucker D.L. et al., 1997, MNRAS, 285, L5

Tully R.B., Fisher J.R., 1977, A&A, 54, 661

Turner M.S., 1997, in Schramm D.N., Galeoti P., eds, Generation of Cosmological Large-scale Structure, Kluwer, Dordrecht, p. 153

Urry C.M., Padovani P., 1995, PASP, 107, 803

Valdes F., 1992, Guide to the Multifiber Reduction Task DOFIBERS, National Optical Astronomy Observatories IRAF Group

Véron P., 1983, in Quasars and Gravitational Lenses, 24th Liège Astrophysical Colloquium, Institut d'Astrophysique, Liège

Véron-Cetty M-P. & Véron P., 1991, Catalogue of Quasars and Active Nuclei, ESO Scientific Report No. 10

Vogeley M.S., 1995, in Maddox & Aragón–Salamanca (1995), q.v., p. 142

Wallace P.T., 1994, Starlink User Note SUN/5.14

Wandel A., 1999, in Ferland & Baldwin (1999), q.v., p. 335

Wang Y., Bahcall N., Turner E.L., 1998, AJ, 116, 2081

Webster A., 1982, MNRAS, 199, 683

Webster R.L., Francis, P.J., Peterson B.A., Drinkwater M.J., Masci F.J., 1995, Nat, 375, 469

Wechsler R.H., Gross M.A.K., Primack J.R., Blumenthal G.R., Dekel A., 1998, ApJ, 506, 19

Weinberg S., 1972, Graviation and Cosmology, Wiley, New York

Weinberg D.H., 1995, in Maddox & Aragón–Salamanca (1995), q.v., p. 129

West M.J., 1991, ApJ, 379, 19

West M.J., 1994, MNRAS, 268, 79

White A.T., 1984, Graphs, Groups and Surfaces, Elsevier, Amsterdam

White M., Scott D., Silk J., 1994, ARA&A, 32, 319

White S.D.M., 1997, in Bergeron E., ed, The Early Universe with the VLT, Springer, Berlin, p. 219

Wilkes B.J., 1999a, in Ferland & Baldwin (1999), q.v., p. 99

Wilkes B.J., 1999b, preprint http://hea-www.harvard.edu/QEDT/, to appear in Cox A., ed, Astrophysical Quantities, Springer, in press

Williams R.E. et al., 1996, AJ, 112, 1335

Willick J.A., 1999, in Dekel A., Ostriker J.P., eds, Formation of Structure in the Universe, CUP, Cambridge, chapter 6

Williger G.M., Hazard C., Baldwin J.A., McMahon R.G., 1995, in Maddox & Aragón–Salamanca (1995), q.v., p. 374

Wills B.J., 1992, Quasistellar Objects, Spectroscopic and Photometric Properties, in Maran (1992), q.v., p. 575

Wills B.J., Brotherton M.S., Fang D., Steidel C.C., Sargent W.L.W., 1993, ApJ, 415, 563

Wirtz C., 1924, Astr. Nach., 222, 21

Wyse R.F.G., Gilmore G., 1992, MNRAS, 257, 1

Yee H.K.C., 1990, in Kron (1990), q.v., p. 322

Yess C., Shandarin S.F., 1996, ApJ, 465, 2

Zamorani G., Marano B., Mignoli M., Zitelli V., Boyle B.J., 1992, MNRAS, 256,

238

Zeldovich Ya.B., Einasto J., Shandarin S.F., 1982, Nat, 300, 407

Zheng W., Kriss G.A., Telfer R.C., Grimes J.P., Davidsen A.F., 1997, ApJ, 475, 469